

OCULAR DISTORTION MEASUREMENT AND RELATIONSHIP WITH REFRACTIVE
ERROR

by

Edward Anthony LaVilla

Copyright © Edward Anthony LaVilla 2018

A Dissertation Submitted to the Faculty of the

COLLEGE OF OPTICAL SCIENCES

In Partial Fulfillment of the Requirements

For the Degree of

DOCTOR OF PHILOSOPHY


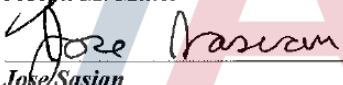
In the Graduate College

THE UNIVERSITY OF ARIZONA

2018

THE UNIVERSITY OF ARIZONA
GRADUATE COLLEGE

As members of the Dissertation Committee, we certify that we have read the dissertation prepared by *Student Name*, titled *Dissertation Title* and recommend that it be accepted as fulfilling the dissertation requirement for the Degree of Doctor of Philosophy.

 _____	Date: 11/19/2018
<i>James T. Schwiegerling</i>	
 _____	Date: 11-19-2018
<i>Joseph M. Miller</i>	
 _____	Date: 11-19-18
<i>Jose Sasian</i>	

Final approval and acceptance of this dissertation is contingent upon the candidate's submission of the final copies of the dissertation to the Graduate College.

I hereby certify that I have read this dissertation prepared under my direction and recommend that it be accepted as fulfilling the dissertation requirement.

 _____	Date: 11/19/2018
<i>James T. Schwiegerling</i> Professor Optical Sciences	

STATEMENT BY THE AUTHOR

This dissertation has been submitted in partial fulfillment of requirements for an advanced degree at the University of Arizona and is deposited in the University Library to be made available to borrowers under rules of the Library.

Brief quotations from this dissertation are allowable without special permission, provided that accurate acknowledgment of source is made. Requests for permission for extended quotation from or reproduction of this manuscript in whole or in part may be granted by the head of the major department or the Dean of Graduate College when in his or her judgment the proposed use of the material is in the interest of scholarship. In all other instances, however, permission must be obtained from the author.

SIGNED: Edward A. LaVilla

ACKNOWLEDGEMENTS

I was extremely fortunate to have such a wide net of support throughout this dissertation process. This small section is woefully inadequate at describing my love and appreciation for the persons and groups listed below for helping me reach this point. A tremendous thanks to my mother and father, brother Charlie and sister Vicky for the love given to me and sacrifices made for me across the country for all these years. My lab mates, Dulce Gonzalez, Brian Redman, Bill Duncan, Ashley Valdez, Carl Chauncy and many others for their technical and mental support. My friends near and far, Pat Kieffer, Marc Zempare, Logan Graves, Lindsay Guzman, Eddie Donovan, Nick Lasarso, Cody Nizolek, Bob MacDonald, and many, many more.

I'd like to acknowledge the financial support I've received over the years that allowed this unfunded body of work to become a reality. A tremendous thanks to the College of Optical Sciences for the myriad of scholarship, fellowship, RA and TA funding opportunities. We students of the college are lucky to be a part of such an accomplished and dedicated college. Dr. Robert Norwood for years of mentorship on business and diversity as a researcher. Dr. Jon Ellis for guidance in being a senior graduate student and transitioning as a Ph. D in Optics. My committee members Dr. Jose Sasian and Dr. Joseph Miller for their input on this dissertation work.

Finally, the person, whom I owe the biggest debt of gratitude, is my advisor Jim Schwiegerling. I've never met someone as brilliant or caring as him, qualities that he passes through to all students of his without second thought. Thank you so very much for all your lessons, patience, and guidance to see me through this process. To all persons and groups mentioned, and those who were not, I extend my sincerest admiration for all your support.

TABLE OF CONTENTS

LIST OF FIGURES	6
LIST OF TABLES	9
ABSTRACT	10
CHAPTER 1: Refractive Error Development and Myopia Review	11
CHAPTER 2: Fundus Camera Imaging and Theory of Ocular Distortion	40
CHAPTER 3: Ocular Distortion Simulation for a Representative Population	70
CHAPTER 4: Measurement of Ocular Distortion in Human Subjects	90
CHAPTER 5: Error Analysis, Observations, and Future Work	131
APPENDIX A: Fifth and Sixth Order Wavefront Expansion	150
APPENDIX B: Crude Eye Model Verification	151
APPENDIX C: Retinal Irradiance Calculation for Modified Fundus Camera	160
APPENDIX D: Distortion Coefficient Values for All Human Trial Subjects	166
REFERENCES	204

LIST OF FIGURES

Figure 1-1:	Illustrations of various refractive states of the eye [2]	12
Figure 1-2:	Illustration of rat eye defining axial direction along line of site [38]	18
Figure 1-3:	Illustrations of various off-axis refractive states [42]	20
Figure 1-4:	Anatomy of the human eye [59]	24
Figure 1-5:	Peripheral aberration of the eye for various refractive states [79]	28
Figure 1-6:	Illustrations of multi-focal soft contact lens classification [82]	34
Figure 2-1:	Internal and external illumination design for fundus camera [132]	42
Figure 2-2:	Illustration of illumination path of modified fundus camera	43
Figure 2-3:	Relay path of modified fundus camera	45
Figure 2-4:	Microscope image of grid target dot	46
Figure 2-5:	3D printed target holder for modified fundus camera	46
Figure 2-6:	Retinal projection path of modified fundus camera	48
Figure 2-7:	Field curvature effect on focus spots in fundus imaging [132]	49
Figure 2-8:	Imaging path of modified fundus camera	50
Figure 2-9:	Zeiss fundus camera layout according to Bengsston [136]	51
Figure 2-10:	Zeiss fundus camera magnification [136]	52
Figure 2-11:	Representation of Hamilton's mixed characteristic function W [138] ...	54
Figure 2-12:	Barrel and pincushion distortion examples	57
Figure 2-13:	Illustrations of second order distortion (B_6, B_7) terms	58
Figure 2-14:	Illustrations of third order distortion (C_7, C_{13}) terms	60
Figure 2-15:	Illustrations of third order distortion (C_8, C_{12}) terms	61
Figure 2-16:	Illustrations of third order distortion (C_9, C_{14}) terms	61
Figure 2-17:	Illustrations of fourth order distortion (D_{23}, D_{26}) terms	63
Figure 2-18:	Illustrations of third order distortion (D_{24}, D_{25}) terms	64
Figure 2-19:	Illustrations of third order distortion (D_{27}, D_{29}) terms	64
Figure 2-20:	Illustrations of third order distortion (D_{28}, D_{30}) terms	65
Figure 3-1:	Zemax Arizona eye model ray trace example	72

Figure 3-2:	Illustration of globe radius definition	75
Figure 3-3:	Ocular distortion percentage of simulated population vs Tscherning 1 lenses	81
Figure 3-4:	Ocular distortion percentage of simulated population vs Tscherning 2 lenses	82
Figure 3-5:	Ocular distortion percentage of simulated population vs soft contact lenses	83
Figure 3-6:	MiSight multi-focal SCL power profile fit	87
Figure 3-7:	Ocular distortion percentage of simulated population vs multi- focal SCLs	88
Figure 4-1:	Modified fundus camera calibration setup	91
Figure 4-2:	Modified fundus camera illumination path calibration image example	93
Figure 4-3:	Modified fundus camera imaging path calibration image example	94
Figure 4-4:	Example retinal imaging with grid target using modified fundus camera	98
Figure 4-5:	Example retinal imaging with grid target using modified fundus camera	99
Figure 4-6:	Example retinal imaging with grid target using modified fundus camera	100
Figure 4-7:	Example retinal imaging with grid target using modified fundus camera	101
Figure 4-8:	Example retinal imaging with grid target using modified fundus camera	102
Figure 4-9:	Image processing candidates	104
Figure 4-10:	Fourier domain filtering on retinal images	105
Figure 4-11:	Automatic centroid detection from Fourier filter analysis	106
Figure 4-12:	Final centroid locations and nominal comparative grid definition	107
Figure 4-13:	Mean nominal grid spacing for human trial subjects	109
Figure 4-14:	Second order distortion coefficient values of subject 10	111
Figure 4-15:	Third order distortion coefficient values of subject 10	112

Figure 4-16:	Fourth order distortion coefficient values of subject 10	113
Figure 4-17:	Mean value for D_{23} coefficient for human trial subjects	114
Figure 4-18:	Mean value for D_{26} coefficient for human trial subjects	115
Figure 4-19:	Mean value for D_{28} coefficient for human trial subjects	115
Figure 4-20:	Mean value for D_{30} coefficient for human trial subjects	116
Figure 4-21:	Mean radial distortion percentage from simulation and human trial subjects	118
Figure 4-22:	Second order error fitting of coefficients to final centroids	121
Figure 4-23:	Third order error fitting of coefficients to final centroids	122
Figure 4-24:	Fourth order error fitting of coefficients to final centroids	123
Figure 4-25:	Mean fitting error for human trial subjects	125
Figure 4-26:	Example images of subject 27 with and without spectacle lenses	126
Figure 4-27:	Second order distortion coefficient values of subject 17 with glasses ...	127
Figure 4-28:	Third order distortion coefficient values of subject 17 with glasses	128
Figure 4-29:	Fourth order distortion coefficient values of subject 17 with glasses ...	129
Figure 5-1:	Lens flare imaging artifact examples in fundus camera imaging	132
Figure 5-2:	Vignetting induced imaging artifact examples in fundus camera imaging	133
Figure 5-3:	Lateral misalignment imaging error examples	135
Figure 5-4:	Fourth order distortion coefficient values calibration lateral misalignment	136
Figure 5-5:	Fourth order distortion coefficient values human subject lateral misalignment	137
Figure 5-6:	Weak dot contrast examples	139
Figure 5-7:	Blood vessel deviation in retinal imaging	141
Figure 5-8:	Central dot blurring examples in retinal imaging	142

LIST OF TABLES

Table 1-1:	Optical parameters considered for various animal models	15
Table 1-2:	Atropine retardation efficacy on myopic progression	38
Table 3-1:	Mean and standard deviation of simulation radial distortion percentage	79
Table 4-1:	Human trial subject data	95
Table 4-2:	User clicked centroid point repeatability test results	108

ABSTRACT

The underlying drivers of refractive error development in the human eye remain open areas of research. Axial elongation, peripheral ametropia, neurotransmitters at the retinal surface and environmental stimuli are a few factors that have been studied to describe the onset and progression of refractive error development. However, the ametropia puzzle remains unsolved and the number of people afflicted by ametropia is growing.

One possible driver for refractive error development is distortion in the retinal image. However, no systems are available to objectively measure ocular distortion. To enable the measurement of ocular distortion, a novel imaging system is created and tested in a sample population. Using a modified fundus camera, a target is projected onto the retinal surface and imaged to a detector. A distortion criterion for a rotationally non-symmetric optical system is used to analyze the resulting distortion pattern.

A simulated population of one thousand different configurations, for a model eye spanning -20 to +9 D, is used to investigate ocular distortion prior to human trials. A small human trial cohort was imaged using the modified fundus camera and compared to the simulated data set. The repeatability of the distortion measurements and its relationship to refractive error is investigated.

Chapter 1: Refractive Error Development and Myopia Review

Introduction

Visual acuity is the measure of the human eye's ability to resolve images from the real world onto the retina of the eye. To resolve these images in space, the main determinants of refraction are the focusing power of the cornea, the crystalline lens and the length of the eye [1]. A reduction in visual acuity from images being focused in front of the retinal plane, due to a higher curvature in the cornea or the length of the eye being too long, is defined as foveal or axial myopia [1]. When images are perfectly formed on the retina, a person is in the state of emmetropia and an image focused behind the retinal plane is defined as hyperopia [1]. The focusing power of the eye is often defined in units of diopters (D).

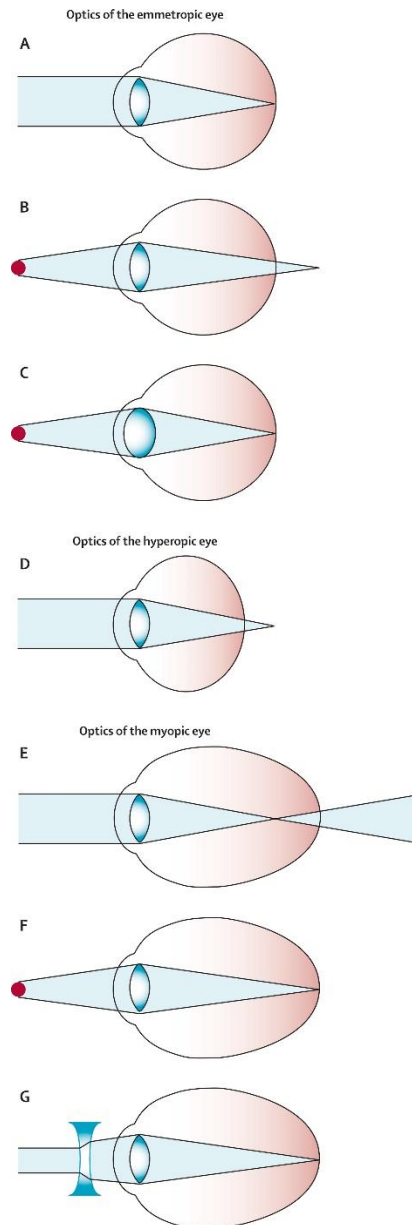


Figure 1- 1: (A) An emmetropic eye focused objects at a distance or infinity to the retina. (B) Objects brought near to the eye are focused behind the retinal plane due to the optics of the eye. (C) Accommodation of the eye brings the image of the near object into focus at the retina. (D) Hyperopic eyes are too short which causes images to be presented behind the retina. Accommodation can bring these distant objects into focus. (E) Myopic eyes are too long and present distant objects before the retina. Accommodation cannot correct for this effect. (F) Near objects presented to the myopic eye can be focused on the retina through accommodation. (G) Corrective lenses that reduce the refractive power of the optics of the eye can bring distant objects to focus on the retina in the myopic eye. [2]

The human visual system places a high priority on achieving a high visual acuity. A whole host of scientific research has been devoted to how a refractive state outside of emmetropia regulates eye growth. At birth, most babies are hyperopic and experience a process call emmetropization

where the eye grows and reduces the magnitude and variance of hyperopia [1]. However, this process can be over-driven, leading to a myopic state, the opposite of the hyperopic state. The drivers for the emmetropization process remain an active area of research as genetic or physiological means, ocular aberration or environmental stimuli have been proposed but not conclusively linked to the over compensation of this process leading to myopic development. Corrective measures are rarely introduced to subjects exhibiting less than -1 D of spherical equivalent refractive error (SER). The term myopic progression refers to the increase in SER beyond the arbitrary -1 D definition of axial myopia and the understanding of mechanisms associated with this progression are of critical importance.

Of growing concern is the increase in diagnosed myopia cases of children and young adults over the last few decades [3]. Myopia and slight hyperopia were found to be the predominant refractive state in teenagers [4] and myopia has become 1.6 times more prevalent in the United States over a 34-year period from 1971-2005 [5]. Mid to high levels of myopia may increase the risk for ophthalmic complications such as cataracts, glaucoma, and chorioretinal abnormalities [6]. These are serious medical conditions that increase healthcare costs and further reduce the quality of life for myopic subjects. With the growing number of myopic subjects, understanding the mechanisms of myopia onset and progression has continued to be a key research question in ophthalmology and optical engineering.

Suggested Factors for the Development and Progression of Myopia

There is an ever-growing body of scientific research related to the onset and progression of myopia. Myopia is likely a multivariable condition that has long been theorized to be a

combination of genetic and environmental factors. Identifying key mechanisms in refractive development remains challenging as correlations between multiple factors are often present. Furthermore, variability in age, gender, ethnicity, and unique optical components add additional complexity in drawing conclusions about the significance of these various mechanisms. Solving the myopia puzzle is a grand endeavor but through individual studies and insights into new variables, researchers are moving closer to piecing together the blurry picture of myopia.

The primary focus of Chapter 1 is the introduction of the myopia puzzle, factors involved in refractive error development and methods designed to correct myopia or retard myopic progression. Three categories of interest will be touched upon throughout this chapter. The first category will be defined as physical ocular parameters or mechanisms and ocular aberrations such as axial length, accommodation, or peripheral refractive error. The second category will describe genetic or biological signaling in the human eye related to ocular growth. And the third category will touch on environmental factors related to myopia such as light intensity or exposed visual environments. It must be noted that myopia onset and progression variables likely cross more than one of these definitions and the interplay between them remains an active area of research.

Animal Models

In an effort to uncover the mysteries of myopia development, researchers have benefited greatly from studies conducted with various species of animals. Schaeffel and Feldkaemper produced a review of animal model studies related to myopia research in 2015 [7]. The focus of this section will be to briefly highlight four animal study groups, the chick, tree shrew, marmoset and rhesus

monkey, and comment on some very useful insights that have helped mold and shape the current understanding of myopia.

Table 1-1 details some common optical parameters of the eye related to these different animal species. Animal models provide a means to test specific variable and their relation to the emmetropization process and myopic development, but the optics and mechanical function of these animal eye models must also be acknowledged. Results from these studies can lead to interesting investigative leads with respect to human children.

Animal	Eye Size [mm]	Visual Acuity [cyl/deg]	Active Accommodation	Fovea
Chick	8-14	7	Yes – 17 D	No
Tree Shrew	7.8	2	No	No
Marmoset	-	30	Yes – 20 D	Yes
Rhesus Monkey	-	30	Yes	Yes

Table 1- 1: Optical parameters measured in various animal species research on refractive error development.

One of the most interesting results of these studies is that myopia can be induced in young animals through two methods. First, deprivation myopia, defined as any degradation to the retinal image, can be accomplished by placing occluders or frosted diffusers over the animal's eye for example [7]–[11]. Second, lens induced myopia, where the addition of a positive or negative spectacle lens creates myopic or hyperopic defocus, stimulating eye growth [7], [12]–[15]. Furthermore, imposing a localized defocus, such as one hemisphere of the retina, can modulate eye growth [7], [16]–[19]. However, the triggering of eye growth from either deprivation or the use of spectacle lenses is different with respect to visual input. For example, chicks and tree shrews that have had the optic nerve cut or neurotoxins blocking the retinal

signaling pathways, still saw local myopia develop during induced defocus [20], [21]. On the contrary, rhesus monkeys who had their lids sutured required visual input or that rearing these monkeys in the dark, did not induce myopia [11].

Given that visual input and retinal signaling was different for certain species, a host of research has been devoted to retinal pathways and their responsibility in regulating eye growth. When looking at chicks, tree shrews and rhesus monkeys, two retinal signaling mechanisms of note were found to modulate eye growth [22]–[26]. ZENK is a transcription factor found in amacrine cells in the retina that is responsible for expressing a whole host of genes related to the retinal signaling pathway [7]. The release of dopamine in response to bright light or image contrast at the retina has also been a common connection amongst these animal models [27]. The effects of retinal signaling offer a rich research environment regarding the biomechanisms associated with eye growth.

Setting commonalities aside from the various animal species, striking observational results in specific animal studies adds further weight to the postulate that myopia development and the emmetropization process is a highly interconnected and complex process. In chicks, it has been shown that the ability to detect the sign of defocus is possible by observing that amacrine cells, expressing the ZENK transcript, see an upregulation with myopic defocus and a down regulation with hyperopic defocus [28]. Also in chicks, interrupting deprivation myopia for as little as thirty minutes can cause a retardation in myopic development up to half of its original progress [29]. Insight to the emmetropization process could be gleaned from rhesus monkeys who have had their fovea ablated but are still able to recover from deprivation induced myopia, suggesting that various processes may or may not require visual input [30]. Furthermore, bright light has been shown to inhibit the effects of both deprivation and lens induced myopia [31]–

[36]. Thus, it is possible to see that the processes regulating eye growth may vary from species to species but more importantly, the modulation of eye growth relies on a combination of factors and stimuli from the environment, biological regulators and optical signals present in the eye.

Axial Elongation

It is well known that the length of the human eye as well as ocular components of the eye are tied to refractive error. Axial elongation is one physical observation often associated with myopic subjects where the length of the eye relative to the corneal surface has grown beyond the focusing power of the cornea and crystalline lens. Figure 1-2 details a schematic rat eye with the purpose of defining the axial direction and equatorial direction. Studies often report a change in SER and the change in axial length to detail myopic progression. While axial elongation is a common partner to myopia, other factors may play a significant role in reaching balance between ocular power and the length of the eye [37]. Mutti et. al. found that when controlling for vitreous chamber depth (VCD), the area between the crystalline lens and the retinal surface, that children who became myopic from the start of the study, did not experience crystalline lens flattening, thinning and losing power where their emmetropic counterparts did [37]. Thus, axial elongation in describing refractive error only paints a one-dimensional view of myopia and the overall degraded visual acuity state of the eye.

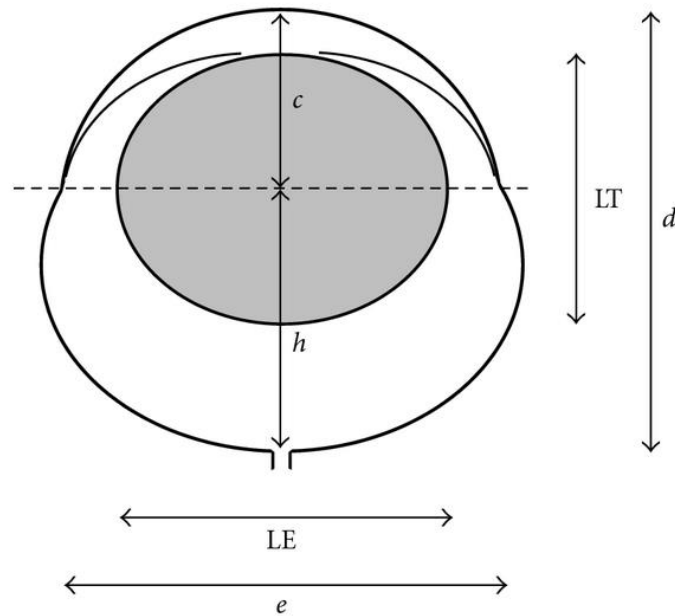


Figure 1- 2: The axial dimension is denoted by length d and the equatorial dimension is denoted by length e in this eye schematic [38].

Flitcroft in his review of the complexities surrounding myopia aetiology effectively summarizes the underlying message of this chapter, namely that the simple definition of on-axis foveal myopia lacks the depth to tie together decades worth of observation [39]. A concise view of literature to date would suggest that “the retina has a central role in optically regulating eye growth and that each area of retina processes the retinal image and influences the growth and/or the biomechanics of the overlying sclera” [39]. These observations point towards a complex interaction between the optics of the eye, the shape of the posterior segment and the physiological mechanisms of eye growth [39].

Refraction in the Retinal Periphery

The region surrounding the fovea, the peripheral retinal region, has garnered significant interest related to refractive development in both human and animal subjects. Investigation of the refractive error in the peripheral retina has uncovered several insights into the role of the retina as a signal driver for refractive development. Peripheral refractive error provides a window into the complex interplay between biological mechanisms of retinal signaling, environmental stimuli and retinal image quality.

Locally imposed hyperopic or myopic defocus in certain animal species and the associated response of local refractive development, indicate a connection between peripheral retinal signaling and scleral growth [7], [16]. An observation of this kind suggests a global eye growth mechanism comprising of two or more ocular regions through some signaling pathway. Smith et. al. has shown that peripheral retinal imaging can influence eye growth in rhesus monkeys though the neural image processing governing this task remains uncertain [30], [40], [41]. Another interesting result that separates the classical on-axis myopia definition and the influences of the peripheral retina is that the induction of peripheral hyperopia causes foveal myopia with and without visual input [19]. Given these results, it is reasonable to conclude that the full visual field and ocular regions other than the fovea can contribute to global eye growth.

While there is a clear complexity in the variables related to the periphery, Schaeffel and Feldkaemper provide a concise conclusion in a review of animal studies and myopia, stating that emmetropization is likely controlled in the retinal periphery and accommodation is likely controlled by the fovea [7]. Discussion of accommodation related to myopia will be presented later.

In humans, the interplay between foveal refraction and peripheral refraction related to eye growth has been well documented [39]. In 2000, Mutti et. al. found an interesting result in off-

axis refractive error where myopes tend to have more relative hyperopia off-axis, emmetropes remain emmetropic off-axis and hyperopes tend to have more relative myopia off-axis [42]. An example image of these three cases can be seen in Figure 1-3. Using a single field point of 30° off-axis, this study shows that the shape of eye in each refractive category is quite different with hyperopes having a larger equatorial diameter and myopes having a longer axial diameter, consistent with other ocular shape observations [42]. Atchison et. al. has shown a confirmation of retinal shape in one study [43] but interestingly found a counter to these observations in a cohort of 87 subjects [44]. Of the 66 myopic eyes measured, only 12% were found to have a prolate shape, that is an elongation in the axial dimension from the cornea was longer than that of the equatorial planes [44]. The inclusion of asphericity and a departure from simple spherical representation of the eye to an ellipsoid, creates a much more interesting landscape to investigate the mechanisms behind a degraded emmetropic state.

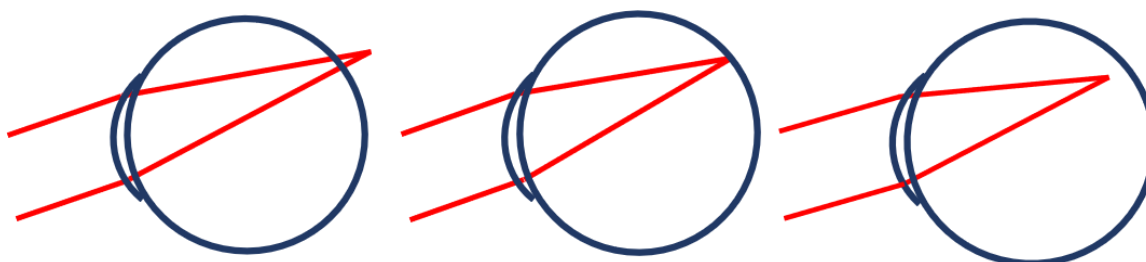


Figure 1- 3: Illustration of off-axis refractive error. Mutti et. al. showed that myopic eyes tend to exhibit off-axis hyperopia (left), emmetropic eyes were emmetropic off-axis (center), and hyperopic eyes were myopic off-axis (right)[42] .

Human studies of the retinal periphery indicate that ocular shape may be a significant factor in myopic development and not simply an outcome of eye growth towards myopia [39]. Combining the complexity of ocular shape and the apparent signaling pathways of the retina to various

regions of the eye; it is clear that the retinal periphery plays a significant role in refractive development.

Accommodative Convergence-Accommodation Ratio (AC/A) and Accommodative Lag

The accommodative mechanism and the role it plays in myopia onset or progression has been investigated in both animals and humans. Interest in the accommodative convergence-accommodation ratio increased after data showed that myopic children have a reduced accommodative response compared to emmetropic children [45], [46]. The AC/A ratio detail expresses the amount of accommodative convergence, the amount the eyes turn inward in response to a change in power from the crystalline lens deformation, per unit diopter of accommodation. Mutti et. al. expanded on previous studies to investigate the AC/A ratio 5 years before and after myopic onset [47]. This work saw an increase in the AC/A ratio in subjects who became myopic compared to subjects who remained emmetropic 4 years prior to myopia onset [47]. At onset, the AC/A ratio leveled off for became-myopic subjects [47]. Comparing the results to CLEERE data previously reported, the results of the AC/A ratio study indicate that an increase in this ratio seems to play a role in becoming myopic but does not predict myopic development [47], [48].

Another closely studied variable related to myopia development and progression is accommodative lag. When trying to focus the eyes at the plane of an object, a lag is said to occur if the plane of focus lies behind the object under view.

Mutti et. al. found no signs of accommodative lag in either became-myopic children prior to the onset of myopia [49]. However, an increase in accommodative lag was seen in one or more years

after the year of onset for became-myopic children [49]. This suggests that accommodative lag may be a result of myopia rather than a cause [49]. While the AC/A ratio and accommodative lag are dubious as predictor of myopia onset, the relationship between accommodation and ocular shape may hold a key to understanding refractive development and remains an active area of research [47].

Genetics

It is well established that the risk of myopic onset increases if there is parental myopia present [50]. Children born to parents who are both myopic are five to six times more likely to develop myopia than their counterparts who have one or no myopic parents [50]–[52]. There is some suggestion that an established parental history of myopia plays a predominant role in early onset myopia but no genetic link has yet been proven, only correlation between one or more myopic parents and development of myopia in offspring [51]. While Wojciechowski and Cheng found evidence that syndromic and high myopia may be closely tied to inheritance, non-syndromic myopia related to gene or gene variants accounts for only a small percentage of myopia cases [53]. Exploration into genetic markers linked to myopia onset and progression remains an open area of research.

Ethnicity

For some parts of the world, myopia and myopic progression have risen to staggering proportions. In East Asia, countries such as Singapore, China, Japan, Hong Kong, Taiwan and Korea have seen a dramatic increase in myopia over the last 50-60 years [2]. 80-90% of children

completing high school have myopia with 10-20% of this population having high levels of myopia [2]. There has been a clear difference in the uptake and effect of myopia on these populations compared to other ethnicities. However, the reasoning as to why remains unclear. A difference in peripheral hyperopia for moderate myopic persons of East Asian ethnicity compared to whites with similar central refractive error is one such factor that has been studied to understand the ethnicity discrepancy [54]. While ocular shape was different between the two study groups, corneal shape and power were not significantly different, which suggests that local visual environments may play a more significant development in ocular growth [54]. Thus, the link between various ethnic groups and myopia prevalence remains open.

Coupled Mechanisms

The visual environment has long been thought to play an important role in refractive development. Over many years, effects of light intensity, spectral content, and spatial frequency variation have been studied alongside the development of myopia. Often these environmental signals correlate with biological or optical mechanisms that form the interpretation of the visual environment. This section will look to explore several studies of these coupled mechanisms and the relationship to myopia.

A surprising observation was uncovered in both human and animal models where a bi-directional change in choroid thickness in response to imposed defocus [55]–[57]. The change in thickness moves the retinal plane relative to the sign of the imposed defocus over a very short time scale [55]–[57]. These observations suggest that the retina may be able to interpret the sign of defocus present. Wallman et. al. showed that this defocus detection can take place in as little as two

minutes [58]. In animal models, the effect of choroidal thinning or thickening has been associated with long term eye growth accompanied by myopia or hyperopia [55].

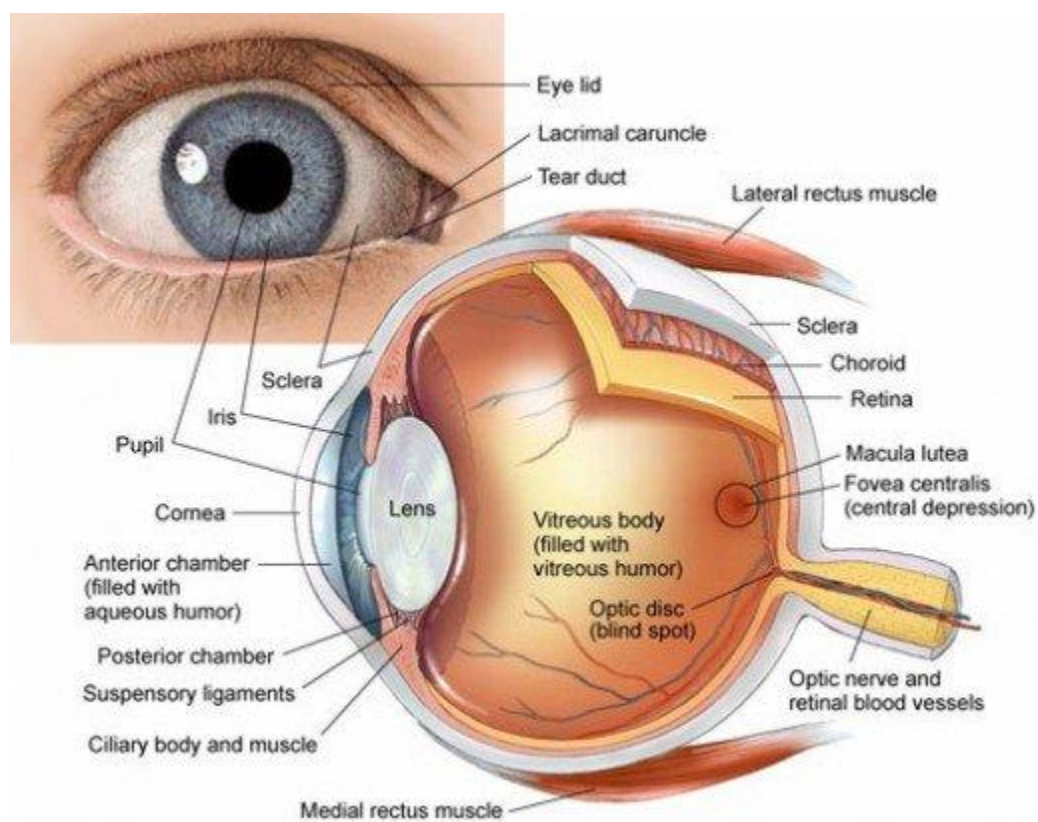


Figure 1- 4: Anatomy of the human eye. The cross section is looking top-down of the right eye [59].

The role of muscarinic blockers such as atropine, homatropine and pirenzepine in the retardation of myopic progression remains unclear [55]. However, work in this area has reached a consensus where the effect of these blockers is not a paralysis of ciliary muscles controlling accommodation [60]. Instead, these agents appear to disrupt receptors located in the retina [61], retinal epithelium or choroid [62], [63]. Coupling an optical input such as the sign of defocus, with a biological agent affecting ocular receptors, causes an observable physical change in ocular structure. In fact, Sander et. al. showed that in as little as 60 minutes, homatropine could block

choroidal thinning due to hyperopic defocus but did not alter choroidal thickening in the presence of myopic defocus [55].

Chakraborty et. al. has compiled a review containing several coupled mechanisms related to ocular length and other physiological variables that are connected to the circadian biology of the eye [53]. Work in this area has shown that ocular components undergo significant diurnal variations including choroidal thinning and thickening [53]. Axial length of the eye varied from 25-45 μm during this diurnal cycle [64], [65]. While this change in axial length only corresponds to a power change of 0.06-0.11 D [66], which is visually insignificant, this observation challenges the understanding of the impact of these short scale variations in relation to long term refractive development.

The retinal clock potentially regulates the diurnal or circadian rhythms in eye growth or ocular components, impacting the overall refractive development of the eye [53]. In chicks, under form deprivation induced myopia, there is an interruption in the diurnal rhythm such that instead of shrinking at night, the eye continues to grow as during the day [53], [67]. Similarly, studies have shown that an introduction of light for two hours during mid-night causes acute growth for a period of six hours following the exposure, breaking the axial length rhythm and ultimately lead to longer eye development [68]. Introducing hyperopic defocus in the morning hours has been observed to increase eye growth in chicks [69] suggesting that go or stop signals related to refractive development may be influenced by this light and dark cycle [53].

Relating to the light and dark cycle, ambient light spectrum, intensity and duration has also been investigated in the context of myopia inhibition. It is believed that the protective mechanism in myopia in ambient light is due to the light intensity [53]. The coupled interaction between light and photoreceptors or neurotransmitters, specifically dopamine, has been studied extensively [7].

Dopamine acts as a circadian regulator [70] that modifies different aspects of visual function as well as light adaptation [71], [72]. Under form deprivation myopia, dopamine levels are seen to decrease alongside a decrease in dopamine biosynthesis [24], [73]. Dopamine implication in disparate animal models strongly encourage the notion that environmental stimuli coupled to biomechanisms can cascade into more complex signaling for refractive development [7].

Though not specifically commented on in this section, the role of environments spatially rich in information, light spectrum, age, gender, and other well-known variables associated with myopia or myopia development may have complex interactions with one another. The notion of coupled mechanisms related to global refractive development is an important consideration in understanding the nature of myopia onset and progression.

Ocular Aberrations

The degradation of retinal image quality due to axial monochromatic aberrations and higher order aberrations (HOA) has been investigated in connection to refractive development. Methods used in adaptive optics were adapted to investigate wavefront error and HOAs, bringing a high repeatability measurement technique to the investigation of ocular aberrations [74]. Still, finding correlations between myopia or hyperopia and HOAs remains an ongoing effort. To illustrate the difficulty in drawing conclusions for ocular aberrations, a study from Cheng et. al. measured 200 eyes from 100 subjects that exhibited high variability in individuals and measured monochromatic aberrations [75]. Llorente et. al. point out that the discrepancies found amongst studies of ocular aberration may be due to age, refractive error range, populations and ethnicities, statistical power of subjects in each study, and differences in the measurement of corneal radius of curvature, asphericity and aberrations [76].

Assessing the tolerances of an optical system is an important exercise in optical engineering to understand how deviations from a perfect system introduce optical aberrations. With a curved image plane and immersed media optical elements, the eye presents a challenging landscape in investigating aberrations at a system level.

Marcos et. al. investigated the sources of variability in ocular aberrations and again found high inter-subject and inter-eye variations [77]. However, the effects of element tilt, decenter, and misalignment, which are typical parameter that lead to increased aberrations in a conventional optical system, were found to have little effect on ocular aberrations [77]. Thus, interpreting correlations between myopia and high order axial aberrations from various studies have been inconsistent suggesting that the argument for high levels of axial aberration in myopic subjects is weak [78].

Departing from axial aberrations Mathur, Atchison and Charman investigated the HOAs of the peripheral retina over a $42^\circ \times 32^\circ$ (horizontal, vertical) visual field [79]. A few interesting results came from this study. First, the study found that the relative peripheral refractive error (RPRE) was found to be myopic for both emmetropes and myopes [79]. This observation deviates from previous studies [42] and may be due to measurement taking place over a reduced field angle [79]. The results of RPRE in the Atchison study suggest that for myopes and emmetropes this refractive error across this 20° radial field is insufficient to explain myopia development [79]. Another interesting result was that coma dominated the HOAs in the periphery field, increasing from center visual field out to the periphery and in an approximate radial orientation seen in Figure 1-5 [79]. This observation was seen in both myopes and emmetropes with one difference being that the increase in magnitude of coma off-axis is more rapid in myopic subjects [79].

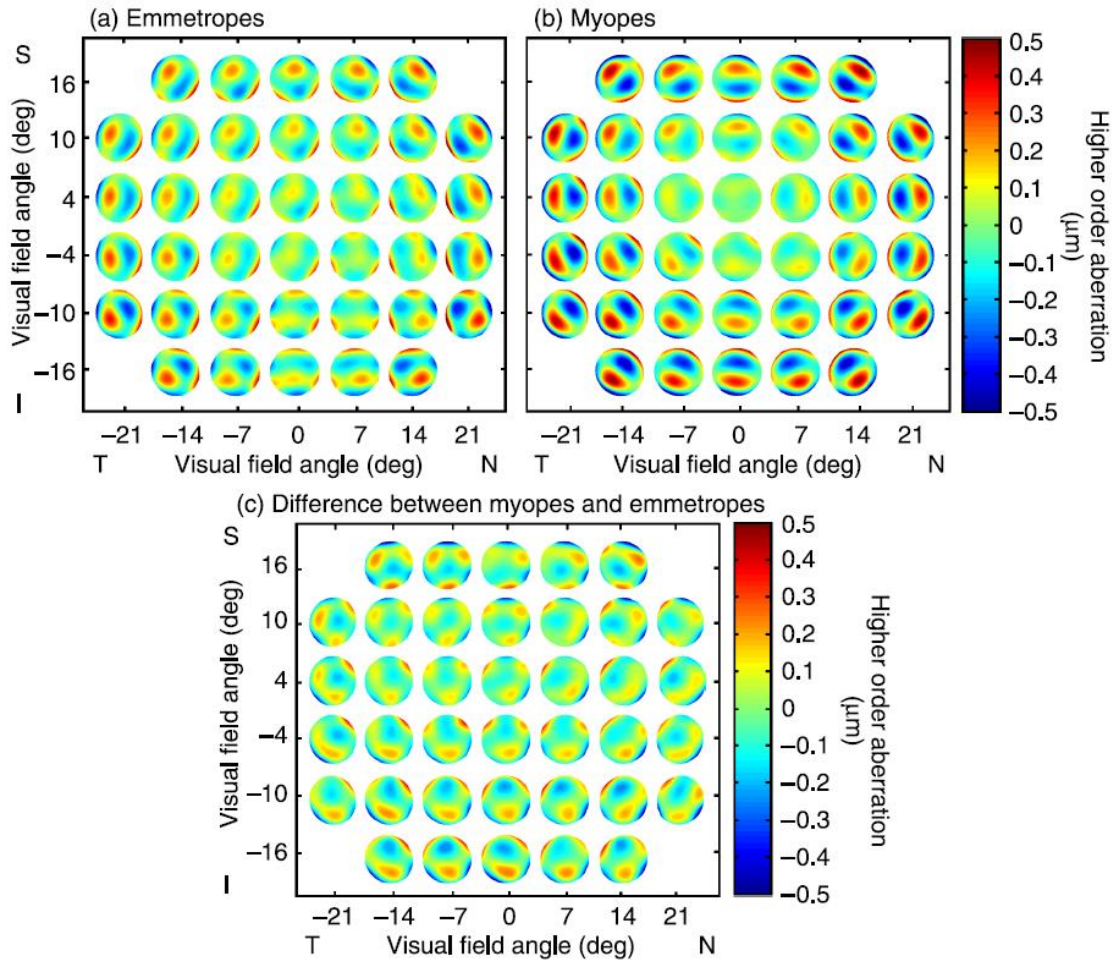


Figure 1- 5: Peripheral aberration as a function of visual field angle for emmetropes (top left), myopes (top right) and a difference between the two refractive groups (bottom center) [79].

While it is difficult to account for the effect introduced by internal ocular elements such as the crystalline lens, the aberrations due to the cornea can be measured with high accuracy [76].

Hartwig and Atchison found myopes tend to have negative spherical aberration in the cornea compared to emmetropes and hyperopes [80]. When coma was removed from wavefront maps in the Atchison study [79], an asymmetry in HOAs was observed between emmetropes and myopes across the visual field [79]. Corneal deformations due to lid pressure and forces produced by extraocular muscles were suggested as potential mechanisms for this asymmetry [79]. Another

study by Buehren et. al. looked at corneal deformations post-blink and found variations up to 1D in refractive error, post-blink, at corneal diameters of 8 mm [81]. Therefore, it may be of great interest to study large aperture and large field effects on retinal image quality. The inclusion of the retinal periphery in the discussion of ocular aberrations and investigation into mechanical deformation of ocular components leaves open a tremendous area of research into new ideas in myopia development.

Methods to Control Myopic Progression

With any complex, multivariable problem, the solution space is often large and diverse. Intervention methods for myopia control and treatment are no different. The following section of this chapter will provide an overview on a variety of myopia control methods and the efficacy in controlling myopic progression for each. Myopia progression will be defined as an increase in negative SER error from the time of baseline measurement to the end of a given intervention period. These intervention methods include wearables such as spectacle lenses or contact lenses as well as pharmacological treatments such as atropine.

While there is currently no preventative technique for myopia onset, intervention methods often attempt to limit or reduce the amount of myopic progression in susceptible subjects. Intervention methods can be classified in two ways. First, a control intervention is that which limits the amount of myopic progression over time in a repeatable amount compared to no intervention at all. A second classification would be intervention methods that actively seek to treat myopia, where progression over time is either reduced or eliminated completely compared to no intervention or another intervention method. Thus, studies will often report the efficacy of an

intervention method in reducing axial elongation or SER myopia development with respect to a control intervention method. A well conducted review of optical and pharmacological methods for myopia control by Kang will serve as a guidance for this chapter section [82].

Single Vision Spectacle Lenses (SVL) and Single Vision Contact Lenses

Single vision lenses, in the form of spectacle lenses or soft contact lenses (SCL), that correct for the on-axis refractive error are typically the first control method introduced for myopic refractive error around -1 D. SVLs are effective at controlling on-axis refractive error and off-axis astigmatism as gaze direction changes, making them a widely deployed solution. However, the effectiveness at reducing or eliminating myopic progression is highly variable on an individual basis. Age of intervention, ethnicity, genetics, gender, ocular shape, and habits during near or distance viewing, all variables associated with myopia onset and progression in general, account for the variability in effectiveness.

Since these methods are usually the first line of treatment for myopia, SVLs often serve as the control mechanism to evaluate new intervention designs [83]. A slight deviation from conventional SVLs methods was the introduction of rigid gas-permeable (RGP) lenses. Early investigations of rigid lenses hypothesized an increase in retinal image quality compared to SVLs or SCLs but a recent study by Katz, Schein and Ley found no effect on axial elongation or myopic progression compared to SVLs [84]. The Contact Lens and Myopia Progression (CLAMP) study by Walline et. al. found similar rates of axial elongation between randomly fitted RGP or SCL groups but also observed increased myopic progression in RGP users [85].

Under-correction

Two theories from previous works have created interest in under correcting myopic defocus to reduce the amount of myopic progression. The first theory suggests that inducing myopic defocus leads to a decreased rate of axial elongation in chicks [41]. A second theory proposes that allowing for myopic defocus through under correction, the accommodative burden and error at near viewing distances will be less, thus a reduction in progression [82]. However, over a two-year study, Chung et. al. found that compared to fully corrected subject, those who were under-corrected for axial myopia by 0.75 D, saw an increase in the rate of myopic progression [86]. Further work still needs to be done in understanding the effects of no correction or under correction compared to fully corrected myopia and the rate of progression.

Multifocal Spectacle Lenses

Theories driving the investigation of under-correction have also been explored in another intervention method classified as multifocal spectacle lenses. Providing a correction for on-axis foveal vision as well as peripheral correction in a single lens package in the form of bifocals, progressive addition lenses (PAL), or radial refractive gradient (RRG) lenses [83], [87], [88]. These designs have typically tried to balance near and distance vision by introducing a section of a lens that has a +1 D or +2 D addition power to the base correction [82]. The targeted mechanisms for controlling myopia in multifocal spectacle lenses are three-fold. First, the addition of a near add power reduces the accommodative demand and increases the convergence demand during near viewing [89]. Second is a reduction in peripheral blur and the related retinal signaling mechanisms [90]. The third control mechanism is related to accommodative lag based

on an observation from Cheng et. al. that showed a reduction in accommodative lag during near viewing of 0.39 D per +1 D add power [91].

The Correction of Myopia Evaluation Trial (COMET) was the largest randomized study investigating PALs as a control for myopia. The study included 469 children, ages 6-11 years old that were prescribed a +2 D add PAL lens and compared against SVLs as a control. A positive effect on myopia progression appeared to occur only in the first year of the three-year study. The result of the trial found a statistically significant difference in myopic progression compared to SVLs, but was deemed clinically insignificant as the retardation of refractive error development was 0.09 D in PALs [90]. A follow-up study, COMET2, investigated the efficacy of PALs with the inclusion criteria that subjects has high levels of accommodative lag, near esophoria which involves the eyes turning more inward than necessary during convergence, and low levels of myopia (-0.75 D to -2 D). This three-year study observed a reduction in myopic progression of 0.28 D compared to SVLs [92].

Unfortunately, a number of other studies investigating the efficacy of bifocal spectacle lenses on myopic progression were found to have minimal effects [93]–[96]. However, a more recent study that included a 3 prism diopter (PD) add inside the +1.5 D near addition zone showed strong effects on myopic progression compared to SVLs [97]. The prism addition displaces the image in near viewing, avoiding double vision and reducing the convergence demand. Myopic progression was measured to be half of that observed in the SVL controls with a net reduction of -1.05 D [97].

The desire for multifocal spectacle lenses to correct foveal and peripheral refractive error is a tall order for lens designers. The eye can rotate up to 45°, but under natural conditions, the eye-head coordination often limits this rotation to 20° at final gaze position, offering some flexibility in

design trade-offs [98]. RRG lenses that use a change in refractive index to create near add zones must also adhere to these design limitations. Barbero and Fario-Ribiero found that the variability peripheral refractive profiles of individuals may severely limit the feasibility of RRG designs [88]. Furthermore, it has been shown that for PALs, differences in the amount and distribution of add power plays a significant role in the behavior of accommodative responses [99]. However, a study using a multifocal soft contact lens design found that tailoring the add power to a given individual saw a reduction in myopic progression of 72 percent and a reduction of axial elongation of 80 percent compared to a single-vision soft contact lens control group [100]. Thus, given the high variance in ocular shape, ocular components, and other factors in individuals, it may be that one-size-fits-all approaches in myopia interventions affect combined refractive development mechanisms adversely, calling for more tailored intervention considerations.

Multifocal Contact Lenses (MFCL) and Novel Lens Design

Like multifocal spectacle lens designs, multifocal soft contact lenses (MFSCCL), multifocal RGP lenses, as well as myopia treatment-specific spectacle lenses [101], have been extensively studied [102]–[109]. Again the main focus in the design philosophy of these MFSCCLs is to alter the peripheral retinal defocus in an effort to control myopia [83], [110], [111]. In reviews of myopia control contact lenses, two classes of MFCL designs are presented as shown by the illustration in Figure 1-6 [82], [111].

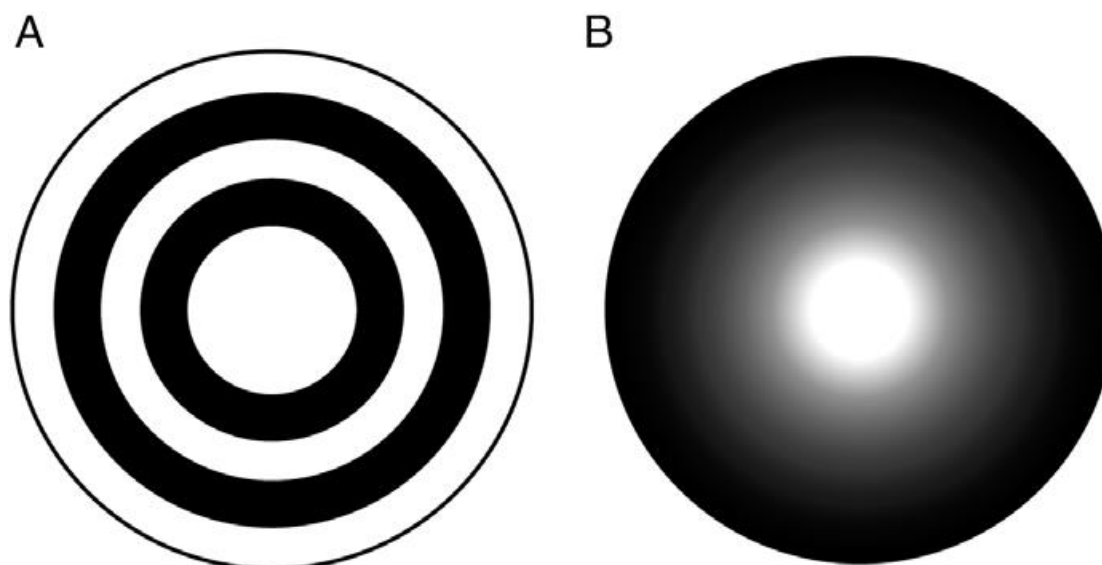


Figure 1- 6: Illustration from Kang of MFCL classifications. The design labeled A corresponds to concentric MFCLs and the design labeled B corresponds to progressive MFCLs [82]. The grayscale seen B represents the local power of the lens.

The concentric ring or bifocal design features alternating distance correction zones shown in white in Figure 1-6a and treatment zones of positive add power shown in black in Figure 1-6a [82]. By providing two planes of distance and near focus simultaneously, the concentric ring design aims to create strong visual acuity for the foveal center while inflicting myopic defocus in the retinal periphery [82], [108]. This methodology is adopted from animal studies that observed the exacerbation or slowing of ocular growth in animals relative to hyperopic or myopic peripheral refractive error respectively [7], [19]. The progressive power or peripheral add power design typically features a gradual change in distance correction by means of curvature change or index change in the central region of the lens, shown in white to gray in Figure 1-6b [82]. The periphery of the progressive power design is typically a relative plus power add as shown in black of Figure 1-6b [82]. A design goal of clear corrected vision as well as induced myopic defocus in the periphery separates the progressive power design from the concentric ring design where the simultaneous imaging of two in focus plans leads to a reduction in contrast of the binocular image [82].

Overall the introduction of novel lens designs and MFCL in the treatment of myopia progression has shown positive results. When comparing to a control group, Kang summarizes that the mean annual myopic refractive error progression is reduced by 0.22 D and 0.31 D for the progressive power and concentric ring designs respectively, while the mean annual reduction of axial elongation was -0.11 mm and -0.12 mm respectively. These values suggest a moderate effect on myopic progression and that the variability in efficacy for a given design may be due to some of the common difference between them, listed below.

1. Base curvature
2. Index of refraction in the lens
3. Total treatment zone diameter
4. Total add power or rate of add power addition in the periphery
5. Aspheric or optical zone prescription

A further criticism of these studies has been the length of time studied for a given intervention as well as the time of positive effect on myopia progression from the onset time of intervention [82].

A few studies have even turned to off-label intervention methods such as commercially available MFSCs designed for presbyopia [112]–[114]. In presbyopia, the ability to accommodate during near viewing is lost, leading to lens design philosophies that rely on the principle of simultaneous vision from multiple in focus planes as seen in the concentric ring design approach. A study by Walline et. al. used a commercially available Proclear Multifocal (center D) (CooperVision,

Pleasanton,CA) and observed a reduction of myopic refractive error of 50% and a reduction of axial elongation of 29% compared to the control group [102]. While long term studies are needed to understand the mechanisms and effectiveness of MFCL designs, indicators point at a positive correlation between balancing high visual acuity with retinal peripheral refractive error and a reduction in myopic progression.

Orthokeratology (OK)

Orthokeratology (OK) is a treatment methodology for correcting refractive error through corneal reshaping. In OK use, subjects wear a specialized rigid lens over night that creates clear, unaided vision during the daytime. The use of OK as a treatment for myopia has been studied and found to be one of the most effective optical treatment methods for retarding the progression of myopia [115]. Recent meta-analyses have reported a 41-45% reduction in myopic progression against controls [116], [117]. The myopic control effect of OK is believed to be linked to a reduction in retinal peripheral defocus [82]. Whether this change is related to induced myopic defocus or accommodative function requires further investigation [82].

Hiraoka and colleagues have investigated OK lens wear and the effects on myopia progression extensively. Following 22 OK lens wearers, ages 8-12 years old, over a 5-year period, they found a reduction of myopic progression of 50% in the first year compared to SVL spectacle control, and a 21% reduction in the second year [118]. However, after three years of treatment, no significant difference in myopia progression was seen [118]. As with other intervention methods, questions are raised surrounding the optimal age of intervention and the long-term effects of OK treatment. Cho and Cheung investigated the effects of discontinuing OK treatment, where the first phase of the study considered a spectacle control group, continuous OK users and

interrupted OK users that switched to spectacle lens correction [119]. In this phase, the discontinued OK user group experienced a faster progression of axial elongation than the other two groups. The second phase had the discontinued group resume OK use but interestingly found that all three groups progressed approximately the same in this second phase. The suggested outcome is that similar to Hiraoka's observations, that there appears to be an attenuation of myopic control effect after 2 years [118], [119]. Cho and Cheung suggest that intervention of OK lens wear not be prescribed to children younger than 14 years old [119]. Hiraoka, in a recent retrospective study, investigated 10 years of medical records related to OK users and the treatment of myopia [118]. This study also found that a faster rate of myopic progression was found in children with a younger baseline age than older children [118].

Though the efficacy of OK lens wear has shown promising treatment results [116], [117] and the long-term safety of OK lens wear was investigated [118], the mechanism of control needs further investigation. Most of the optical effect of OK lens is derived from an altered anterior corneal topography and in the case of myopia control, a corneal flattening reducing lens power is induced. The effect on curvature of the posterior cornea is seen immediately after lens removal, but quickly returns to well observed values after a few hours [120]. Thus, it is plausible to assume that effects at the edge of cornea may contribute to the influence of myopia control in OK lens users. Mathur and Atchison investigated the higher order aberrations present in the periphery of OK lens users and found significant increases in 3rd order aberrations including coma magnitude and orientation, as well as spherical aberration [121]. Further exploration of the effects of OK lens wear may lead to more complex OK lens design or provide insights into more advanced control mechanisms for myopic progression.

Pharmacological Agents

Topical or eye-drop treatments containing non-selective muscarinic inhibiting agents (atropine) or selective muscarinic agents (pirenzepine) have been investigated in animal and human models for control in myopic progression [122]–[125]. These agents bind to muscle receptors M1-M5 in the pupillary sphincter or ciliary muscle, though these muscle receptors are found in various concentrations in the retina, choroid and sclera, making the action site for these agents an open area of research [122]. Side effects of high dose atropine have raised concerns for deploying this intervention method widely. These side effects include photophobia and blurred vision due to pupil dilation and inhibited accommodation from use of atropine [82]. However, these agents have shown some of the strongest reduction effects on myopia progression compared to other intervention methods [115].

The Atropine for Treatment of Myopia (ATOM1) and the follow- up ATOM2 study, investigated the effects of atropine on myopic progression in children [126], [127]. The ATOM2 study looked at dose dependent effects of atropine with 0.5%, 0.1%, and 0.01% concentrations, where it was shown that higher concentrations of atropine corresponded to a higher myopic control [127].

Following the table presented by Kang [82], the impact on SER and axial length is shown from these two studies.

Concentration	Study	SER Change (D)	Axial length change (mm)
1%	ATOM1	-0.28 ± 0.92	-0.02 ± 0.35
0.5%	ATOM2	-0.30 ± 0.60	+0.24 ± 0.25
0.1%	ATOM2	-0.38 ± 0.60	+0.28 ± 0.28
0.01%	ATOM1	-0.49 ± 0.63	+0.41 ± 0.32
Control	ATOM1	-1.20 ± 0.69	+0.38 ± 0.38

Table 1- 2: Myopic progression from ATOM1 and ATOM2 studies using atropine. Various concentrations in the form eye drops were tested. Myopia progression appears to slow with atropine treatment.

Following the cessation of atropine from subjects in the ATOM1 and ATOM2 studies, a troubling rebound effect was observed, again with a dose dependence, on year following atropine use [128], [129]. While the site of action and combined effect on myopic progression while using these pharmacological agents is still being investigated, further analysis on the long-term efficacy and safety need to be addressed as a viable myopia control intervention.

Summary

There are a wide variety of theories about the cause of refractive error development and myopia, as well as theories on the various treatment efficacies. It is still unclear the validity of these theories. In the next chapter a new, novel theory for the cause or influencer of refractive error development is proposed. This theory may or may not prove correct, but the aim of this dissertation is to develop an instrument that will enable the validation or invalidation of the new theory. Specific research goals to evaluate the effectiveness of this instrument will be laid out and addressed as well.

Chapter 2: Fundus Camera Imaging and Theory of Ocular Distortion

Introduction

The primary purpose of this chapter is to familiarize the reader with fundus camera photography and introduce a metric for ocular distortion. Modifications to a base fundus camera package are detailed in this chapter to provide the context for measuring ocular distortion. Later in this chapter, details regarding the representation of distortion in a rotationally non-symmetric optical system are presented.

Background

In 1895, Hermann von Helmholtz produced the first direct ophthalmoscope that could directly measure the retinal surface of a patient [130]. Several designs exist in both patent literature and the public domain for retinal imaging and one method, primarily adopted by ophthalmologists for clinical use, is the fundus camera. The first instance of the modern fundus camera, for retinal imaging, was created in 1925 by Dr. J.W. Nordenson with the help of the Zeiss Company, that used the Gullstrand principle of illumination [130]. By separating the illumination path and imaging path, a more uniform illumination and sharper image resolution were achieved. In 1955, Dr. Hans Littmann, working for the Zeiss Company, created the embodiment of the modern fundus camera that is most used today [131]. The advancement of this design allowed for the direct measurement of objects on the retinal surface by creating a telecentric beam in image

space [130]. Points on the retina are imaged to a common detector plane and the system is insensitive to ametropia or accommodation of the eye under test [131].

Work by DeHoog and Schwiegerling outline the two major classifications of fundus camera photography as either an internal or external illumination configuration based on literature and patent review [132]. Figure 2-1a illustrates the external illumination configuration where an image of the light source is imaged on the retinal surface by elements 8 and 10. An annulus, element 9, is located conjugate to the pupil of the eye and is guided into the eye by a beam splitter, element 2, that combines the illumination and imaging pathways. Element 9 is crucial to the design of the fundus camera as the central obscuration eliminates the back reflection from the anterior corneal surface as well as the anterior crystalline lens surface. The image of the retinal surface is created by several aspheric objective elements at location 3, a relay lens system, elements 5 and 6 and a baffle element 4 which limits the entrance pupil diameter of the imaging path and further controls corneal back reflections.

The internal illumination system more closely resembles the configuration used in the Zeiss FF3 camera design and is illustrated in Figure 2-1b. In this configuration, elements 7,9 and 10 are responsible for creating an intermediate image of the illumination source on a holed mirror, element 3. The holed mirror is conjugate to the pupil of the eye, passing the illumination source image through element 2, an aspheric objective, and this holed mirror also serves as the limiting entrance pupil diameter for the imaging path. Element 8 is a single black dot that is conjugate to the back surface of the aspheric objective at 2 and is responsible for eliminating the back reflections from this objective. Further control over the entrance pupil diameter of the imaging path, as well as control over corneal and crystalline lens back reflections can be accomplished by placing an iris behind the holed mirror at 3. An intermediate image of the retinal surface is

formed before the holed mirror at 3 by the aspheric objective at 2 before being imaged by a relay lens system of elements 4 and 5 to the detection plane. It should be noted that the relay lens system in both imaging pathways serves as the correction of refractive error for any ametropic eye under test.

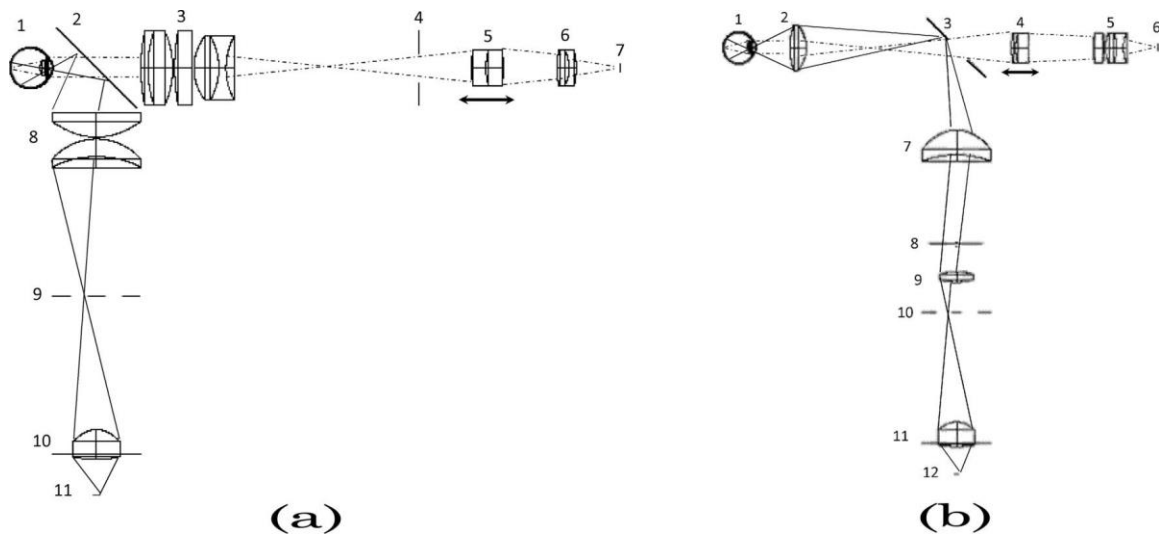


Figure 2- 1: An external illumination fundus camera design (a) and an internal fundus camera design (b). Main differences are seen in how the illumination and imaging pathways are combined into a single functionality. [132]

The following sections will detail the various elements and modifications made to a Zeiss FF3 fundus camera to measure ocular distortion. Considerations for improvement as well as camera calibration, performance and sources of error will be discussed elsewhere. For the remainder of this section and document, the modified Zeiss FF3 system will be referred to as the “fundus camera”.

Illumination Intermediate Image Path

Illumination Source Relay Path

The second arm of the illumination pathway of the fundus camera, illustrated in Figure 2-3, creates an intermediate image of the source and annulus of light at a conjugate plane with a holed mirror seen at location 8. After being redirected by a fold mirror at location 4, a second modification to the fundus camera, a grid pattern for measuring ocular distortion, is picked up by the illumination path at location 5. The grid pattern at location 5 is conjugate to the retinal surface, or equivalently, the location of the intermediate image of the retina, which forms before the holed mirror and is shown in red. The legacy system has a small fixation target located at the same location as plane 5, which was used to fix the subjects gaze during measurement and served as the intended target plane location. Objective elements at location 6 complete the relay path to the holed mirror. There is a central black dot obscuration at location 7 that is conjugate to the back surface of the aspheric objective lens. The obscuration eliminates the back reflections from the two objective surfaces from entering the imaging path.

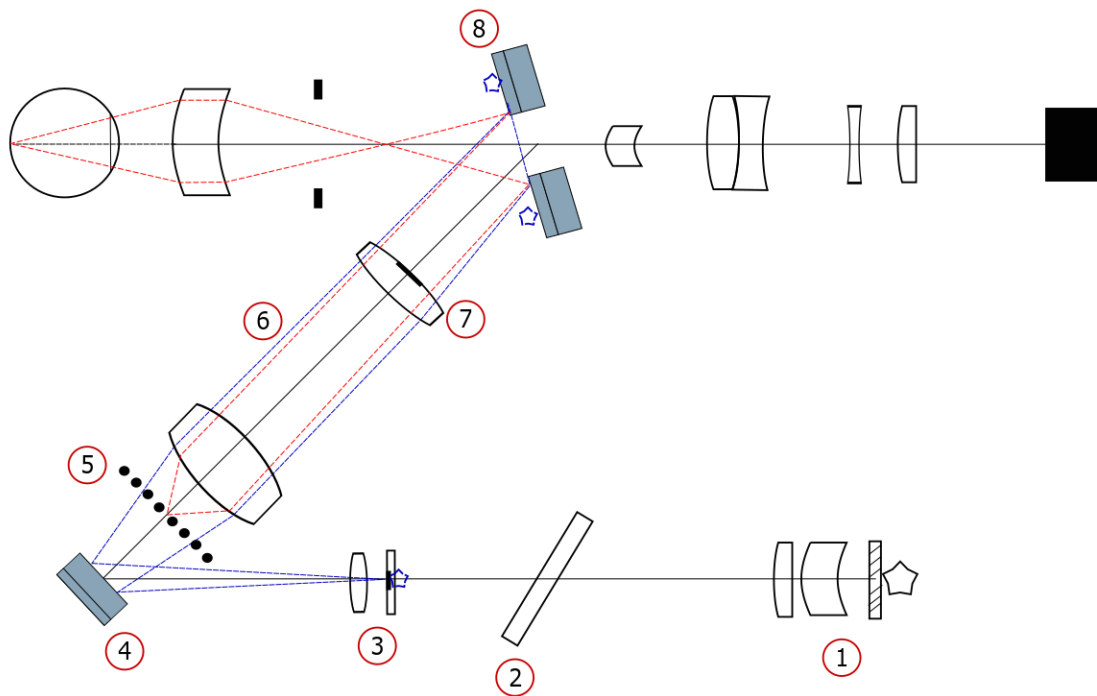


Figure 2- 3: The source image and annulus mask at location 3 are conjugate to the holed mirror at location 8 (blue) and conjugate to the pupil of the eye. The dot grid pattern at location 5 is picked up along the illumination path and is conjugate to the retina by the holed mirror (red).

The grid target used in this body of work was chosen to be a rectilinear grid of dots with a diameter of 0.5 mm and spacing of 1 mm. The actual dot diameter and spacing was measured on a Zygo NewView 8300 interferometer, used primarily as a microscope in this case. The true dot diameter is approximately 0.642 mm and spacing of 1 mm, seen in Figure 2-4. A laser printer was used to print the pattern on a transparency, causing the mismatch in diameter as well as deformed shape. A piece of glass supported the grid target, and both were fixed to a 3D printed mount. The mount arm fixed to the existing body of the fundus camera through a set of three screws and was secured in place at location 5. The target was aligned using a model eye on an optical bench and the Z location corresponding to the distance away from the fold mirror at

location 4 was determined by imaging an emmetropic subject and finding the plane of best focus for the grid pattern. Figure 2-5 shows the mounting scheme for the grid target.



Figure 2- 4: The printed dot diameter and shape (left) is approximately 0.642 mm and the nominal center to center dot spacing (right) is approximately 1 mm.



Figure 2- 5: 3D printed cover and grid target holder. The grid target, fixed to a glass plate, is located inside the red circle of the image and placed conjugate to the retina.

Retinal Projection and Return Path

Figure 2-6 illustrates the retinal illumination and return path of the fundus camera. The grid pattern projection onto the retina is accomplished by making the holed mirror conjugate to the pupil plane of the eye at location 11. A baffle at location 9 helps to further control the corneal back reflections returned into the imaging path way. The aspheric objective lens at location 11 serves a critical role in the fundus camera design. A fast objective, approximately $f/2$, is responsible for bringing the annulus of light into focus at the pupil of the eye. A uniform illumination covers the retinal surface and effectively creates a virtual object of the retina and grid pattern at infinity to be recorded by the imaging pathway [133].

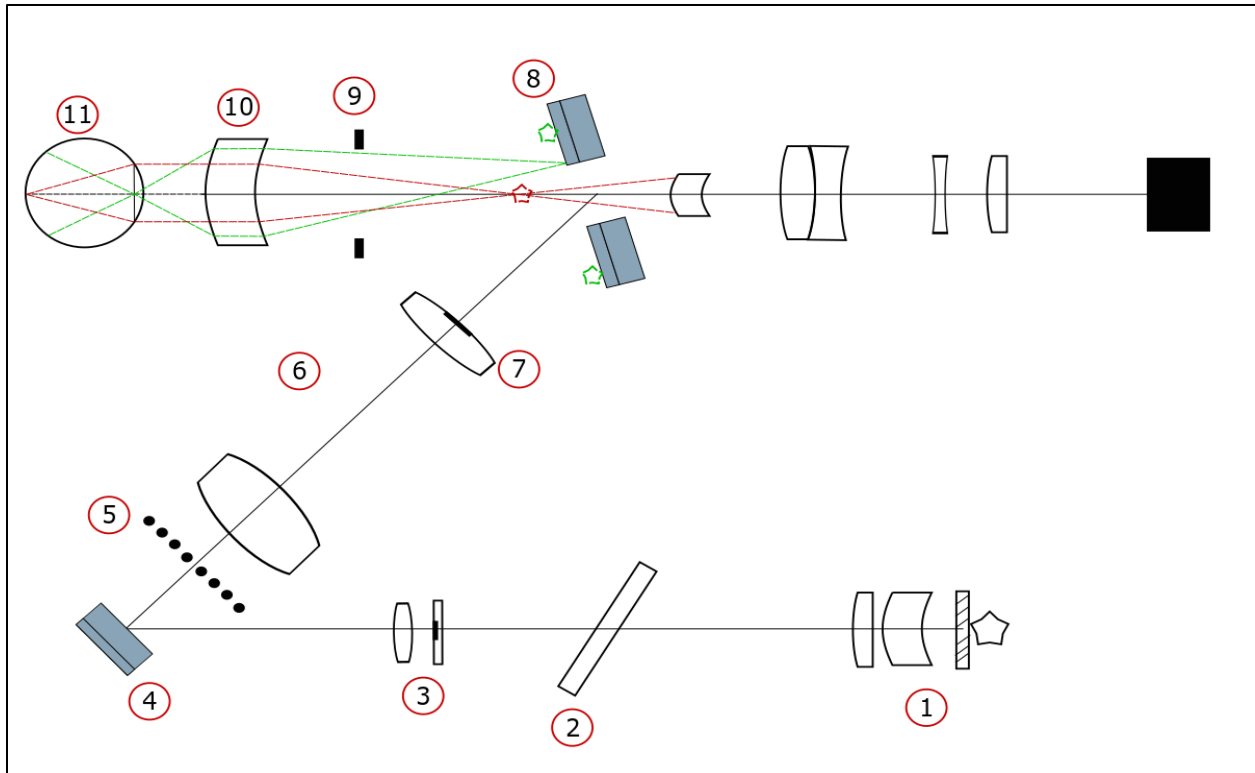


Figure 2- 6: The holed mirror image at location 8 is conjugate to the pupil of the eye located at 11 (green). An intermediate image of the retina with the grid target projection becomes the object presented to the imaging pathway for detection (red).

The retinal surface can be considered a Lambertian scatterer [134] that has different reflectance values for wavelengths in the visual band, with red light having the highest value around 40% [135]. Thus, a strong illumination source is required to have sufficient intensity of the retinal image compared to return signals from unwanted surfaces such as the anterior cornea. The light exiting the eye is telecentric when passing back into the aspheric objective. Here the objective must flatten the curvature of the retina to ensure plane to plane imaging. Pomerantzeff et. al. illustrates in Figure 2-7, the difficulty in flattening the curvature of the retina for large angles to a common flat focus plane [133]. Therefore, careful attention to the optical design of such an objective as well as additional lens components may serve as an improvement to the legacy fundus imaging system.

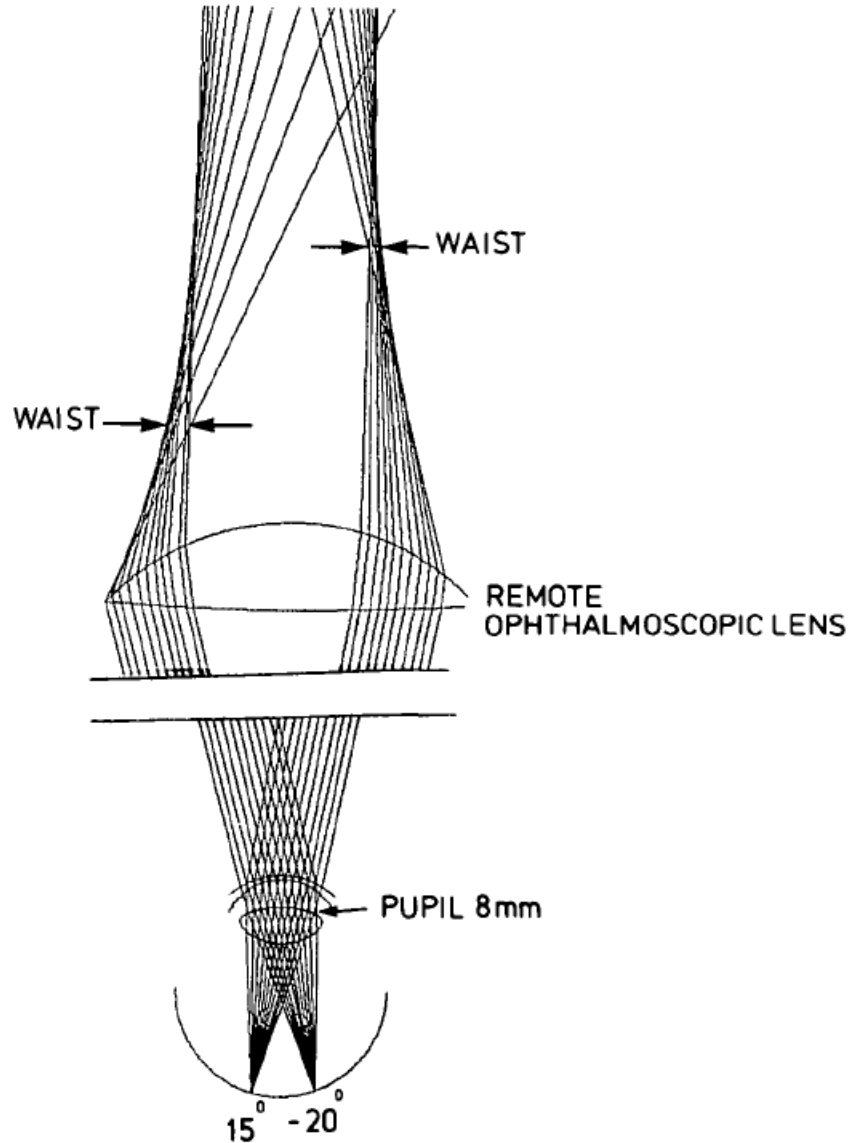


Figure 2- 7: Aspheric objective lens attempts to correct the high curvature, virtual retinal object but various planes of best focus exist for a range of field points on the retina [133].

Retinal Imaging Path

Figure 2-8 illustrates the final optical path that relays the intermediate image of the retinal surface to a detection plane at location 13. The imaging path, shown in orange, consists of a relay lens configuration marked by location 12. Various degrees of ametropia will cause the

intermediate image of the retina to form at different points along the optical axis in front of the holed mirror. The retinal image is passed through a series of lenses to correct the ametropia of the eye including two astigmatic lenses that combine to form a cylindrical lens of variable axis and power to correct for patient astigmatism [131]. From the correction lenses the object pattern is sent to a doublet that begins a typical relay lens system. Changing the spacing between the doublet, negative lens and positive lens, it is possible to compensate for the varied axial position of the intermediate retinal image. Thus, the focal length to the detection plane is altered to present a sharp image of the retina at the detection plane.

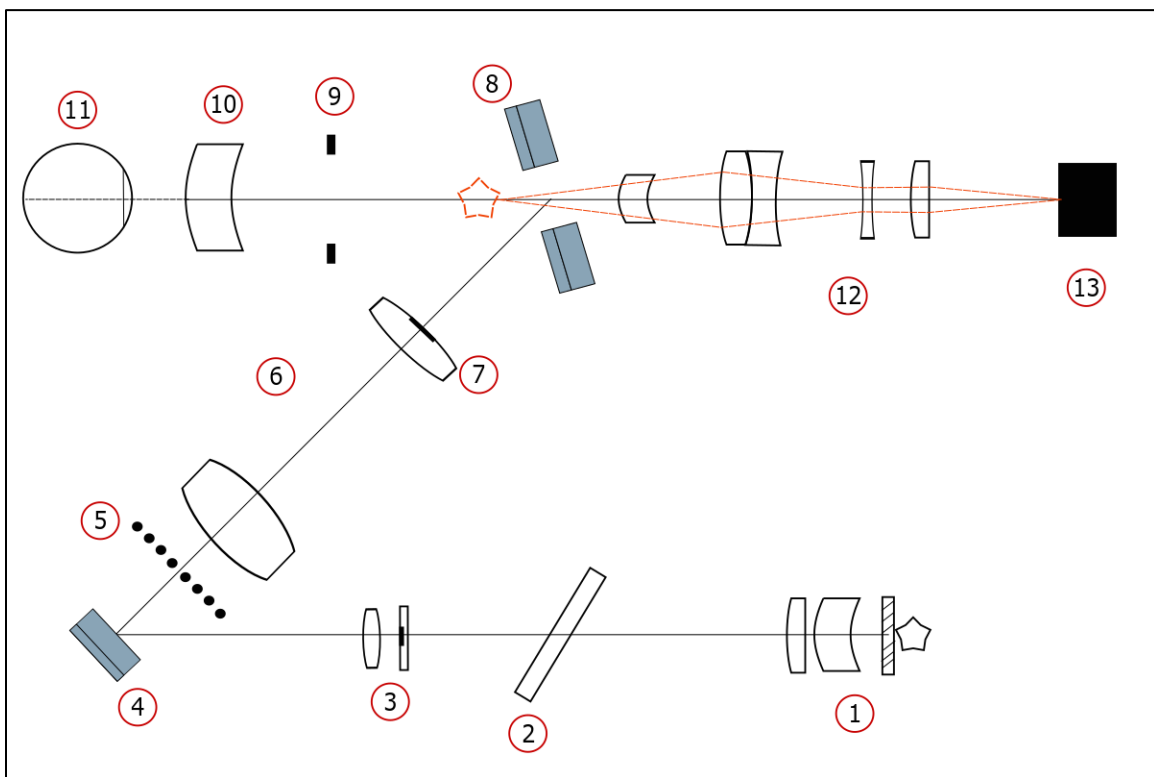


Figure 2- 8: Final imaging path for the fundus camera. An intermediate image of the retinal surface and grid target is located before holed mirror at location 8. The location of this intermediate image is different for subjects with any refractive error. A relay lens system corrects for any added power induced by the eye under test.

Work conducted by Bengtsson and Krakau details that the total magnification of the fundus image M_{tot} is related to the combined magnifications of the eye, aspheric objective lens and the imaging objective (M_e, M_f, M_c) [136]. Figure 2-9 illustrates the Zeiss imaging system [136].

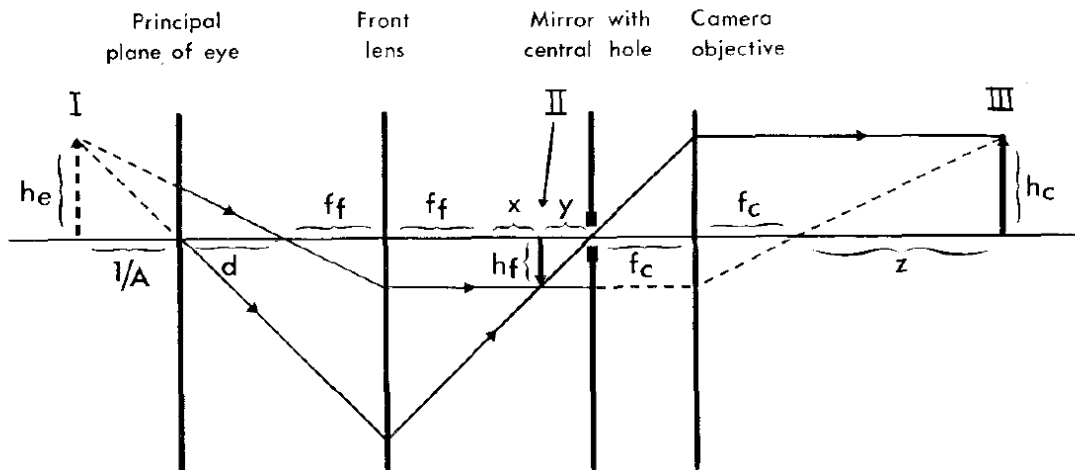


Figure 2-9: Layout of the imaging path for the Zeiss fundus camera [136].

The total magnification is given by Equation 2.1 where f_c, f_f and d are all constants; d is a constant if the camera is correctly positioned for each subject [136].

$$M_{tot} = M_e * M_f * M_c = \frac{f_c * d}{f_f} \left(A + \frac{1}{f'} \right) \quad 2.1$$

A is equivalent to the refractive power of the eye under test in diopters and f' is the focal location of the intermediate retinal image. The emmetropic eye ($A = 0$), has the “nominal power” of $1/\bar{f}'$, such that we can define a relative magnification M_{rel} by Equation 2.2 [136].

$$M_{rel} = \frac{M}{1/\bar{f}'} = \left(A + \frac{1}{\bar{f}'}\right)\bar{f}' \quad 2.2$$

In the case of pure axial emmetropia, $f' = \bar{f}'$, such that M_{rel} can be described by Equation 2.3 [136].

$$M_{rel} = 1 + A\bar{f}' \quad 2.3$$

Gullstrand used a specific schematic eye where $\bar{f}' = 0.017055 \text{ m}$ and plugging into Equation 2.3, a table in strong agreement with manufacture provided values from Zeiss was achieved by Bengtsson and Krakau shown in Figure 2-10. Thus, a map of retinal magnifications can be built for various degrees of ametropia.

A	Zeiss' values		$1 + A\bar{f}'$
	M	M_{rel}	
+16	3.10	1.28	1.27
+12	2.93	1.21	1.20
+ 8	2.76	1.14	1.14
+ 4	2.60	1.07	1.07
0	2.43	1.00	1.00
- 4	2.27	0.93	0.93
- 8	2.11	0.87	0.86
-12	1.95	0.80	0.80
-16	1.79	0.74	0.73

Figure 2- 10: Manufacture compared values of relative retinal magnification of the Zeiss fundus camera [136].

The remainder of this chapter will serve to introduce how distortion of the eye will be evaluated, thus describing the concept of ocular distortion. Measurement of this ocular distortion using the

modified fundus camera is a first step approach to validating or invalidating the postulate of ocular distortion causing or influencing refractive error development.

Aberration Background

For an optical system, where all lens surfaces are free from aberration, the ability to form an image of an object, with a given height and location, is described by paraxial optics. In the case of real world optical systems with finite apertures and a finite field of view (FOV), aberrations exist such that the paraxial image point is displaced at the image plane. Seidel was crucial in investigating and describing the primary imaging defects and these aberrations are referred to as the *Seidel aberrations* [137].

The most common optical system is one that exhibits rotational symmetry about the optical axis. However, optical configurations can deviate from this symmetry leaving only one, two or zero axes of symmetry. An example of a zero axis of symmetry optical system could be a freeform lens, a single axis of symmetry optical system would be a decentered lens from the optical axis and a two axis of symmetry example would be an on axis cylindrical lens. Barakat and Houston explored the mathematics describing aberrations for optical systems with one, two or no axes of symmetry [138]. Their work will serve as a basis to describe the aberrations of the human eye, as an optical system with no axes of symmetry.

Barakat and Houston work from Luneberg's formulation of Kirchhoff's diffraction theory where the complex amplitude of a point source located in object space at (x_o, y_o, z_o) can be described at the Fraunhofer image plane by Equation 2.4.

$$a(x, y) = \iint_{\text{aper}} \phi(p, q) \exp[ikW(x_o, y_o, p, q)] \exp[ik(px + qy)] dpdq \quad 2.4$$

Equation 2.4 is a wavefront representation of the optical path from a point in object space and contains $W(x_o, y_o, p, q)$, that turns out to be the Hamilton mixed characteristic function. In a system without aberrations, $W(x_o, y_o, p, q)$ will vanish and thus makes it the description of the optical path of light from object to image plane, illustrated in Figure 2-11. The aperture or pupil coordinates (p, q) represent the direction cosines of the normals to the converging wavefront, where the third direction cosine is described using the Law of Cosines.

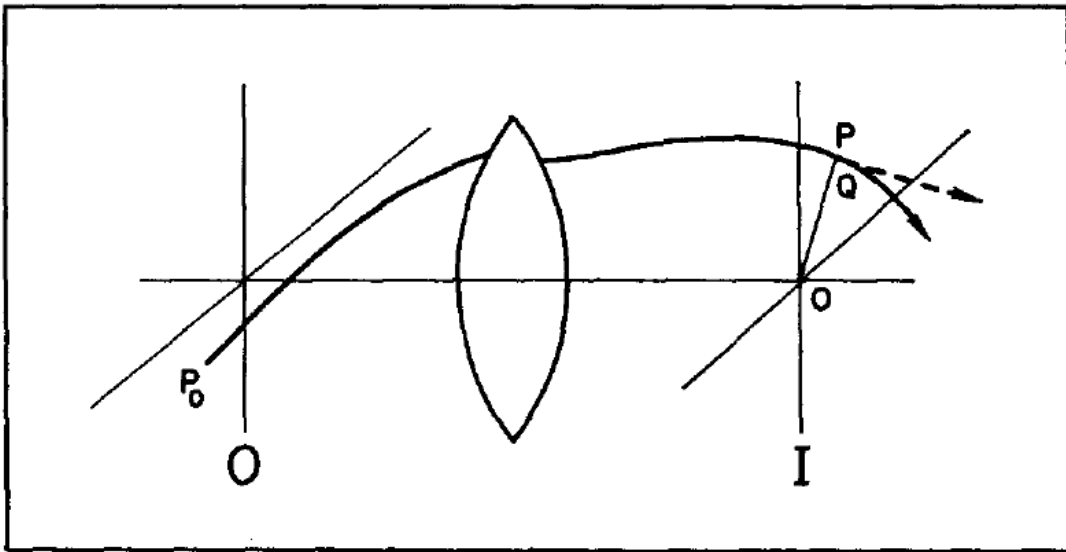


Figure 2- 11: Representation of W characteristic function. The optical length of light from the object plane O to the foot Q dropped from the perpendicular to the tangent of the light ray at P. Thus, W in a system with aberrations is a displacement of the paraxial description of image plane I coordinates [138].

The optical path difference for a set of rays can be readily found through several raytracing schemes which in turn describes the aberrations of the optical system. Using a power series

representation of $W(x_o, y_o, p, q)$ the intersection points of rays at the paraxial Fraunhofer image plane ($x, y, z = 0$) can be described with homogenous polynomial functions of increasing order. The intersection points (x, y) of the aberrated wavefront at this image plane are found by taking the derivative of the wavefront with respect to the exit pupil coordinates detailed in Equation 2.5 and the power series expansion assumed by Hamilton for $W(x_o, y_o, p, q)$ is described by Equation 2.6. Wavefront error and the respective wavefront error power will denote the displacement of the imaging coordinates found in Equation 2.5.

$$x = -\frac{\partial W}{\partial p} \quad y = -\frac{\partial W}{\partial q} \quad 2.5$$

$$-W = W^0 + W^1 + W^2 + W^3 + W^4 + \dots W^n \quad 2.6$$

For systems with rotational symmetry or even two planes of symmetry, it can be shown that W^n when n is an odd integer, will disappear. In the remainder of this chapter, the aberrations of increasing order n will be described and the assumption that the human eye contains no planes of symmetry will be carried forward. In assuming no planes of symmetry, all combinations of the independent variables (x_o, y_o, p, q) are necessary to describe W and thus the aberrations of the human eye. It will be noted now and described later, but terms in the expansion of W that contain only (x_o, y_o) are related to the pupil aberrations of the system.

Distortion and Aberration Classification

Distortion is the primary aberration of interest in this body of work. The relationship between ocular distortion and refractive development, if any, forms the motivation for the works derived

here. At the image plane of a rotationally symmetric optical system where distortion is present, object points are perfectly focused and free from blur but appear warped since distortion displaces the paraxial imaging coordinates in the plane of focus. Distortion is therefore a non-linear change in magnification with respect to object field position. The description of this aberration can be found in Seidel notation shown in Equation 2.7, where the magnitude of distortion scales as the cube of the normalized object field coordinate (h), linearly with the normalized pupil coordinate (ρ) and the cosine of the pupil azimuthal angle (θ) [137].

$$\Delta W = W_{311} h^3 \rho \cos \theta \quad 2.7$$

The 4th order wavefront error term in Equation 2.7 is commonly called pincushion or barrel distortion, the rotationally symmetric distortion terms, are illustrated in Figure 2-12. However, given the non-symmetric nature of the human eye, it is possible that a complex distortion of the wavefront exists, created by the curvatures, indices, and spacing of the ocular components. Thus, the formulation by Barakat and Houston of wavefront error, provides a useful tool in describing complex distortion of various orders from fundus camera imaging. These distortion terms are classified below in order of their respective wavefront error power. Given that the wavefront error is the derivative of the wavefront with respect to the exit pupil direction cosines, Barakat and Houston expansion terms for (x, y) that contain only (x_o, y_o) independent variables are considered in this text, as these are the distortion terms of interest.

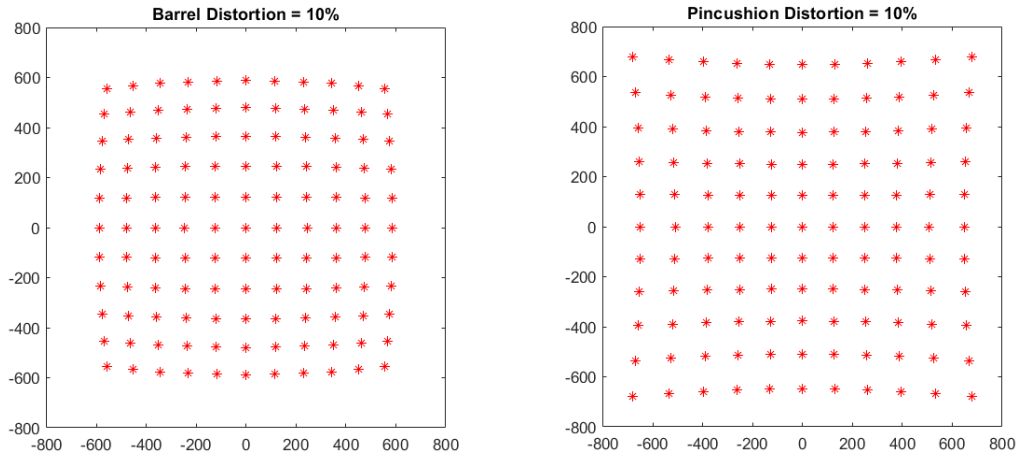


Figure 2- 12: Barrel distortion (left) arises when W_{311} is negative and pincushion distortion (right) occurs when W_{311} is positive. Points in the image plane are displaced according to Equation 2.7.

Second Order Wavefront Error

The W^1 expansion term is ignored in this text since the wavefront error associated with this expansion term represents a shift of image coordinates laterally or longitudinally in the image plane. An expansion of the W^2 term, excluding cross terms containing only (x_o, y_o) independent variables, is shown in Equation 2.8 below.

$$W^2 = B_1 p^2 + B_2 p x_o + B_3 q y_o + B_4 q^2 + B_5 p q + B_6 q x_o + B_7 p y_o \quad 2.8$$

Applying Equation 2.5 to the mixed characterization function yields the wavefront error as the location of the image space coordinates (x, y) . As noted before, the wavefront error terms that contain only (x_o, y_o) independent variables, represent geometric distortions. The wavefront error terms for W^2 are represented in Equation 2.9 below.

$$x = B_2 x_o \quad 2.9$$

$$y = B_3 y_o$$

$$B_6: \begin{cases} x = B_6 y_o \\ y = 0 \end{cases}$$

$$B_7: \begin{cases} x = 0 \\ y = B_7 x_o \end{cases}$$

The terms (B_2, B_3) represent paraxial magnification in the x and y directions respectively, where the object size is either grown or shrunk in image space depending on the sign of the coefficients. Coefficients (B_6, B_7) represent skew distortion in the x and y directions respectively; shown as illustrations in Figure 2-13.

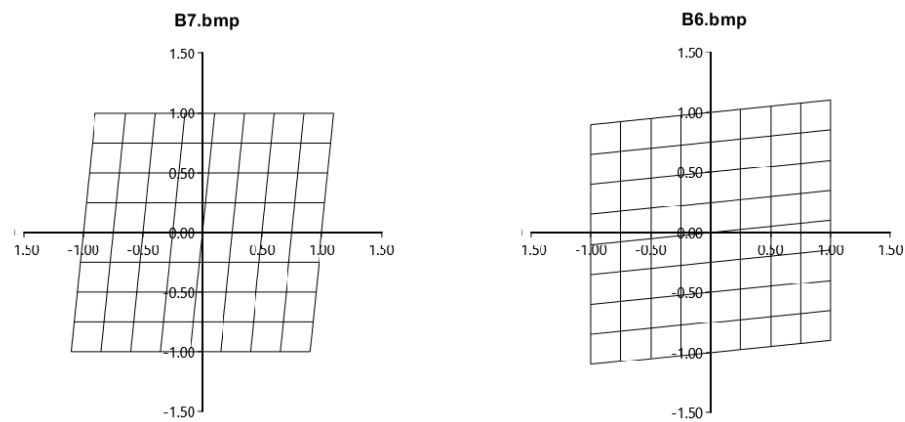


Figure 2- 13: Skew distortion in the y direction (B_7 ,left) and in the x direction (B_6 ,right).

Third Order Wavefront Error

The expansion of the W^3 term, excluding cross terms containing only (x_o, y_o) independent variables, is shown in Equation 2.10 below.

$$\begin{aligned}
 W^3 = & C_1 p^3 + C_2 p^2 q + C_3 p q^2 + C_4 q^3 + C_5 p^2 x_o + C_6 p^2 y_o + C_7 p x_o^2 + C_8 p y_o^2 \\
 & + C_9 p x_o y_o + C_{10} q^2 x_o + C_{11} q^2 y_o + C_{12} q x_o^2 + C_{13} q y_o^2 + C_{14} q x_o y_o \\
 & + C_{15} p q x_o + C_{16} p q y_o
 \end{aligned} \tag{2.10}$$

Differentiating with respect to the wavefront direction cosines and collecting all the distortion terms, yields the third order wavefront error expressed as image coordinates (x, y) shown in Equation 2.11 below.

$$\begin{aligned}
 C_7: & \begin{aligned} x &= C_7 x_o^2 \\ y &= 0 \end{aligned} \\
 C_8: & \begin{aligned} x &= C_8 y_o^2 \\ y &= 0 \end{aligned} \\
 C_9: & \begin{aligned} x &= C_9 x_o y_o \\ y &= 0 \end{aligned} \\
 C_{12}: & \begin{aligned} x &= 0 \\ y &= C_{12} x_o^2 \end{aligned} \\
 C_{13}: & \begin{aligned} x &= 0 \\ y &= C_{13} y_o^2 \end{aligned} \\
 C_{14}: & \begin{aligned} x &= 0 \\ y &= C_{14} x_o y_o \end{aligned}
 \end{aligned} \tag{2.11}$$

Coefficients (C_7, C_{13}) represent quadratic compression and expansion about the y and x axes respectively; Figure 2-14 illustrates these distortion patterns. Quadratic curvature distortion about the x and y axes is represented by coefficients (C_8, C_{12}) respectively; illustrated Figure 2-15. Finally, the last third order distortion terms represent a well-known distortion called

keystone. Coefficients (C_9, C_{14}), illustrated in Figure 2-16 are the x and y direction keystone distortions respectively.

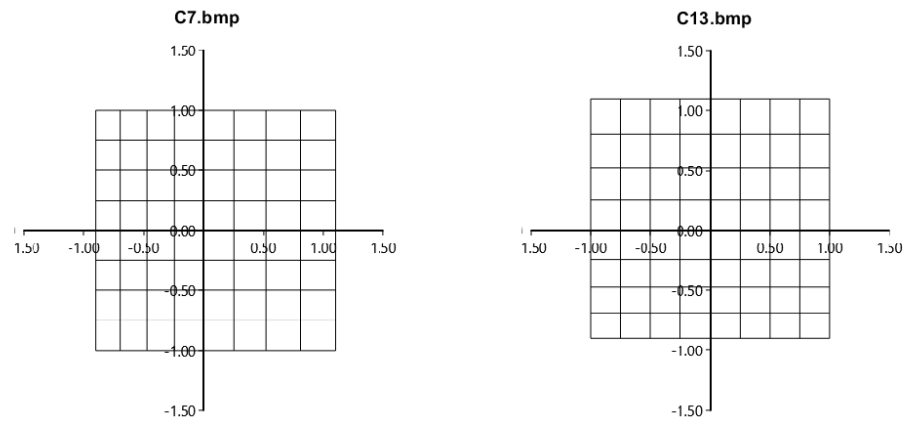


Figure 2- 14: Quadratic compression and expansion distortion in the x direction (C_7 ,left) and in the y direction (C_{13} ,right).

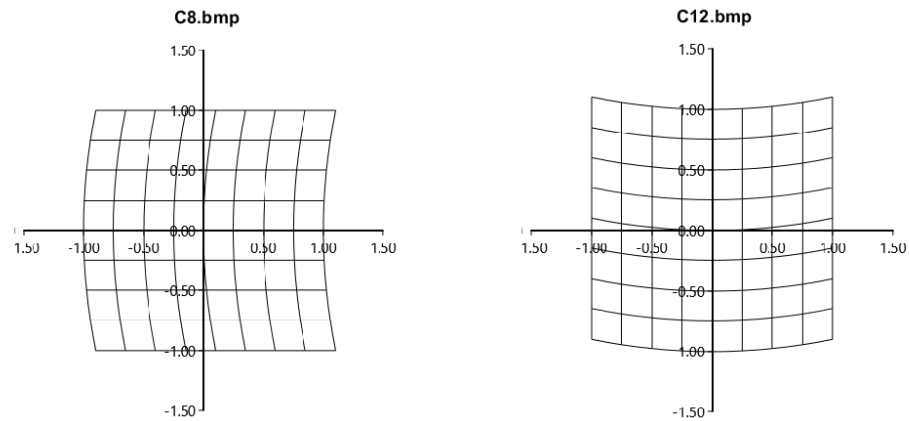


Figure 2- 15: Quadratic distortion in the x direction (C_8 ,left) and in the y direction (C_{12} ,right).

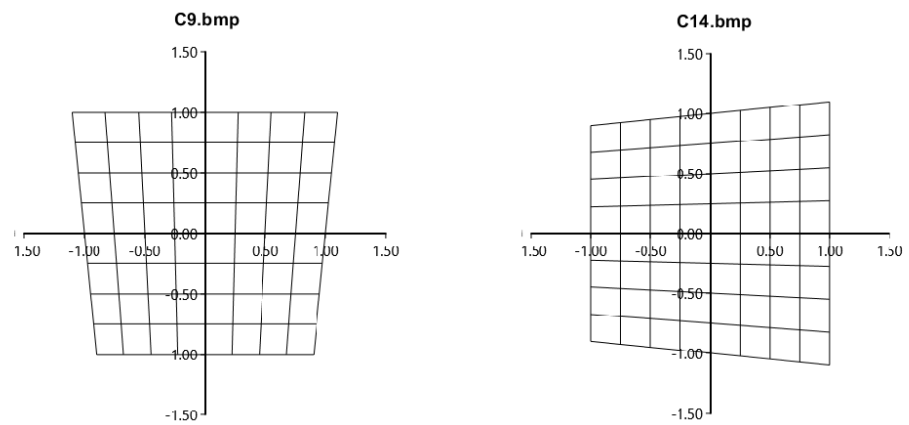


Figure 2- 16: Keystone distortion in the x direction (C_9 ,left) and in the y direction (C_{14} ,right).

Fourth Order Wavefront Error

The last expansion to be represented in the main body of this text is the W^4 term, shown in Equation 2.12 below. Appendix A contains the expansions of W^5 and W^6 as well as the collected distortion terms for the 5th and 6th order wavefront errors.

$$\begin{aligned}
W^4 = & D_1 p^4 + D_2 p^3 q + D_3 p^2 q^2 + D_4 p q^3 + D_5 q^4 + D_6 p^3 x_o + D_7 p^2 q x_o + D_8 p q^2 x_o \\
& + D_9 q^3 x_o + D_{10} p^3 y_o + D_{11} p^2 q y_o + D_{12} p q^2 y_o + D_{13} q^3 y_o + D_{14} p^2 x_o^2 \\
& + D_{15} q^2 x_o^2 + D_{16} p q x_o^2 + D_{17} q^2 y_o^2 + D_{18} p^2 y_o^2 + D_{19} p q y_o^2 + D_{20} p^2 x_o y_o \\
& + D_{21} q^2 x_o y_o + D_{22} p q x_o y_o + D_{23} p x_o^3 + D_{24} q x_o^3 + D_{25} p y_o^3 + D_{26} q y_o^3 \\
& + D_{27} p x_o^2 y_o + D_{28} q x_o^2 y_o + D_{29} q x_o y_o^2 + D_{30} p x_o y_o^2
\end{aligned} \quad 2.12$$

The fourth order wavefront error functions are collected in Equation 2.13 below.

$$\begin{aligned}
D_{23}: & \begin{aligned} x &= D_{23} x_o^3 \\ y &= 0 \end{aligned} \\
D_{25}: & \begin{aligned} x &= D_{25} y_o^3 \\ y &= 0 \end{aligned} \\
D_{27}: & \begin{aligned} x &= D_{27} x_o^2 y_o \\ y &= 0 \end{aligned} \\
D_{30}: & \begin{aligned} x &= D_{30} x_o y_o^2 \\ y &= 0 \end{aligned} \\
D_{24}: & \begin{aligned} x &= 0 \\ y &= D_{24} x_o^3 \end{aligned} \\
D_{26}: & \begin{aligned} x &= 0 \\ y &= D_{26} y_o^3 \end{aligned} \\
D_{28}: & \begin{aligned} x &= 0 \\ y &= D_{28} x_o^2 y_o \end{aligned} \\
D_{29}: & \begin{aligned} x &= 0 \\ y &= D_{29} x_o y_o^2 \end{aligned}
\end{aligned} \quad 2.13$$

Coefficients (D_{23}, D_{26}) represent cubic expansion in the x and y directions respectively; Figure 2-17 shows these distortion patterns. Cubic curvature distortion about the x and y axes is

represented by coefficients (D_{24}, D_{25}) respectively; illustrated in Figure 2-18. Coefficients (D_{27}, D_{29}) represent an interesting distortion pattern of skew combined with quadratic compression and expansion in the x and y directions respectively; illustrated in Figure 2-19. Finally, coefficients (D_{28}, D_{30}) represent linearly increasing quadratic curvature distortion about the x and y axes respectively and are illustrated in Figure 2-20.

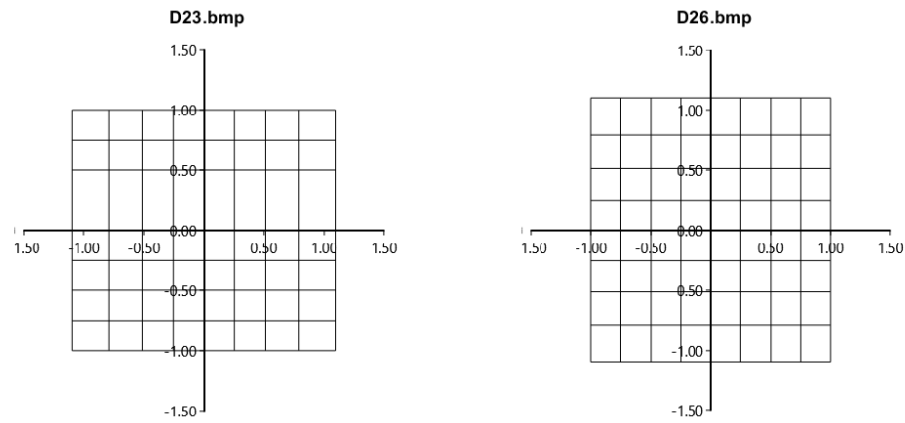


Figure 2- 17: Quadratic expansion distortion in the x direction (D_{23} ,left) and in the y direction (D_{26} ,right).

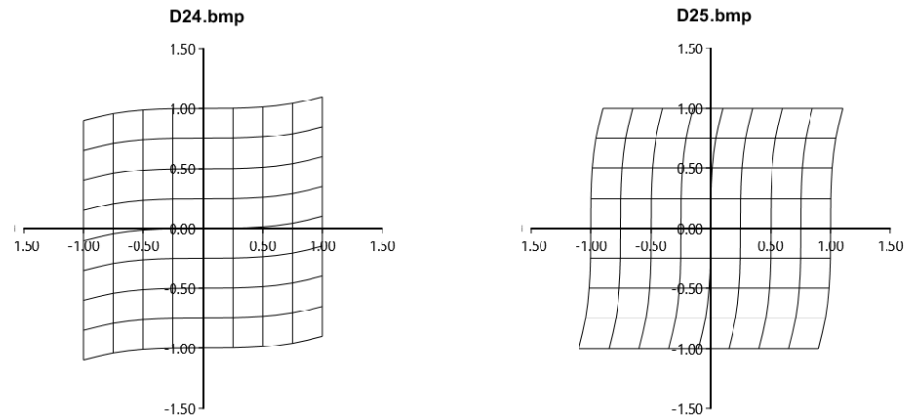


Figure 2- 18: Cubic curvature distortion about the x axis (D_{24} ,left) and the y axis (D_{25} ,right).

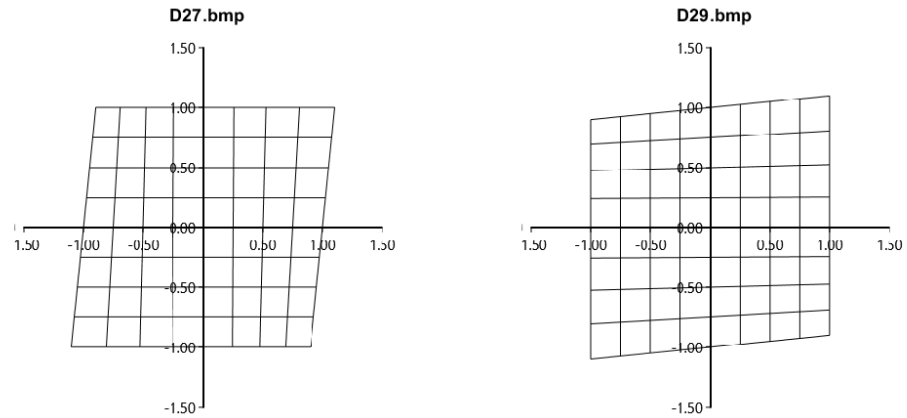


Figure 2- 19: Quadratic compression and expansion with skew distortion in the x direction (D_{27} ,left) and in the y direction (D_{29} ,right).

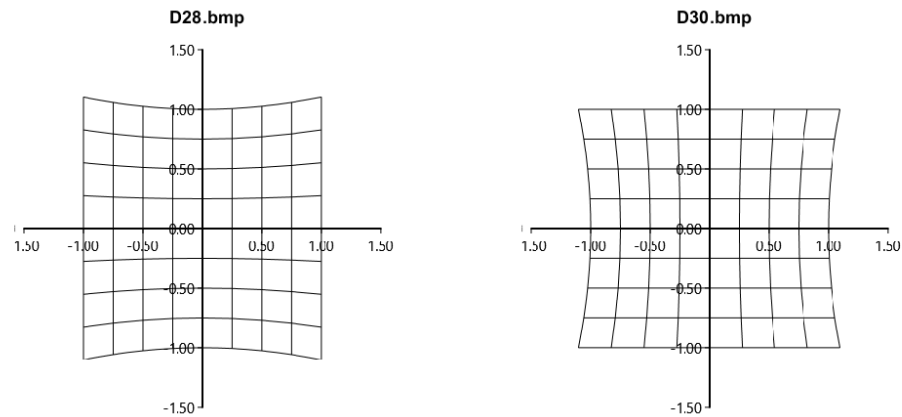


Figure 2- 20: Linearly increasing quadratic curvature distortion about the x axis (D_{28} ,left) and the y axis (D_{30} ,right).

Radial Distortion Metric

At the time of writing, it is unclear which, if any, distortion terms influence the development or progression of refractive error in human eyes. The ability to break down complex distortion up to 6th order wavefront error provides a robust basis to investigate distortion in the human eye but creates a non-trivial approach to data analysis. In the fully generalized representation of distortion out to 6th order wavefront error, twenty unique coefficients in both x and y would require correlation and observation. However, it is possible to combine a few of these independent terms together to represent well-known distortion patterns such as barrel or pincushion, described earlier in this chapter. A commentary, accompanied by the mathematics involved in combining and defining the radial distortion coefficient will be presented in this section. The investigation of the third order rotationally symmetric distortion term for myopes,

emmetropes, and hyperopes can also be connected to simulation results of human eye models presented in Chapter 3.

Barakat and Houston express, as others have, the wavefront direction cosines (p, q) in polar coordinates described by Equation 2.14 below, where ρ is the normalized exit pupil radial coordinate and θ is the exit pupil azimuthal angle coordinate [138].

$$\begin{aligned} p &= \rho \cos \theta \\ q &= \rho \sin \theta \end{aligned} \tag{2.14}$$

Equation 2.15 below relates the (x_o, y_o) object space independent variables to the normalized object field coordinate h . With Equation 2.14 and Equation 2.15 in hand, it is possible to find terms in the 4th order wavefront error that combine to give the rotationally symmetric Seidel distortion aberration seen in Equation 2.7.

$$h = \frac{\sqrt{x_o^2 + y_o^2}}{h_{max}} \tag{2.15}$$

To begin, Barakat and Houston provide a combination of the four independent variables (p, q, x_o, y_o) for a system with rotational symmetry to a new set of independent variables (u_1, u_2, u_3) shown in Equation 2.16 below.

$$\begin{aligned} u_1 &= x_o^2 + y_o^2 \\ u_2 &= p^2 + q^2 \\ u_3 &= x_o p + y_o q \end{aligned} \tag{2.16}$$

Given the symmetry of a system with this description, $y_o = 0$ provides no loss of information but for the general case with no axes of symmetry, all four independent variables will remain in

this representation. Taking the square of the three new independent variable sets will return an equivalent statement of the W^4 wavefront term. This step is shown in Equation 2.17 below, where the inner product terms (u_1u_2, u_1u_3, u_2u_3) are left unexpanded.

$$\begin{aligned}
 (u_1 + u_2 + u_3)^2 &= x_o^4 + 2x_o^2y_o^2 + y_o^4 + p^4 + 2p^2q^2 + q^4 + x_o^2p^2 + 2x_oy_0pq + y_o^2q^2 \\
 &+ [(x_o^2 + y_o^2)(p^2 + q^2)] + [(x_o^2 + y_o^2)(x_0p + y_0q)] \\
 &+ [(p^2 + q^2)(x_0p + y_0q)]
 \end{aligned} \tag{2.17}$$

By visual inspection, only the inner product term of (u_1u_3) will yield expansion terms that are linear with respect to the direction cosines (p, q), and therefore, 4th order wavefront error distortion terms. The expansion of this inner product is shown in Equation 2.18.

$$(x_o^2 + y_o^2)(x_0p + y_0q) = x_o^3p + x_oy_o^2p + x_o^2y_0q + y_o^3q \tag{2.18}$$

The four corresponding distortion terms from Equation 2.18 are ($D_{23}, D_{26}, D_{28}, D_{30}$) and that a linear combination of these terms will reproduce the rotationally symmetric third order barrel or pincushion distortion found by Seidel.

Representing radial distortion from the general, zero symmetry terms, leaves a degree of freedom when choosing how to combine these four distortion terms. The combination of terms can be thought of as a constant distortion term D_o together with a residual term ΔD from each of the four (x, y) distortion values. The radial distortion value is shown in Equation 2.19 below.

$$D_R = D_o(\Delta D_{23} + \Delta D_{26} + \Delta D_{28} + \Delta D_{30}) \tag{2.19}$$

In this body of work, the choice for D_o is the mean of the four distortion terms such that $D_R = D_o$ when reporting radial distortion values for hyperopes, emmetropes, and myopes in future sections. It is unclear, whether choosing the minimum or maximum of each term for D_o is a more appropriate measure in building the D_R distortion metric and is likely outside of the noise confidence level for the given system proposed here. Of further note, it is unclear whether the residuals of each term have significance between the various refractive groups. Both considerations require further analysis.

Ocular Distortion as an Influencer of Refractive Error Development

It should be stated that the following section is a purely conceptual body of writing and has not been tested or scrutinized at the time of writing. The statements here are meant to provide possible modalities as to how or why distortion might affect human refractive error development, that may be tested in future studies.

There may be no connection between ocular distortion and refractive error development, but some real-world consequences of human eyesight might make ocular distortion an influencer. For example, humans see keystone distortion at all times during the day. Staring out far into the horizon creates a pinch point at the center of focus, thanks to the accommodative-convergence response. In the periphery of vision, straight lines are bent toward the center of vision. Perhaps, when humans combine images from the left and right eyes, a complex radial and keystone distortion is being presented to the brain. Over or under correcting one image with respect to the other, to flatten the 3D world, may be a driving signal for eye growth. Depth perception may be closely related to this keystone phenomena where the eye attempts to fit the perfect amount of

keystone distortion for each person to properly assess depth location of objects in the field-of-view.

Another thought may be related to the changing lifestyle and environmental conditions in humans. Living in urban centers and a significant increase in daily screen time may be presenting demanding visual processing conditions in the brain. With a high density of straight line objects, high spatial frequency information, it may be that the brain prioritizes keeping objects straight in the periphery by growing the eye in response to this stimulus. Rather than in a resting position, focused at infinity, the visual system is being asked to accommodate, converge and process stationary straight-line information for extended periods of time. It may be that the brain can't correctly undistort all of the visual environment, requiring eye growth to compensate. All of these postulates would need to be rigorously tested and scrutinized but outline some interesting concepts related to ocular distortion and human vision.

Summary

Fundus camera imaging has been reviewed along with the modifications implemented in this body of work to measure ocular distortion. Barakat and Houston provide a method to break down complex distortion in the rotationally non-symmetric optical system of the eye. This method allows for a radial distortion metric to be applied to retinal images from human test subjects. The next chapter will outline simulation work related to ocular distortion in simulated human eyes by raytracing.

Chapter 3: Ocular Distortion Simulation for a Representative Population

Retinal Ray Tracing and Ocular Distortion Simulation

Ocular distortion of the human eye requires careful consideration and insight in how to define distortion. For a rotationally symmetric optical system in air, where the imaging condition is planar to planar, the traditional Seidel representation of radial distortion is sufficient. In the human eye, the index immersed, and curved image plane of the retina breaks these conditions, requiring more thought in quantifying or measuring ocular distortion. Simulation of a reasonably complex eye model provides the most realistic approach to understand and characterize ocular distortion in the human population.

First, a model eye must be chosen to represent the optical surfaces found in human eyes. Navarro describes the considerations and assumptions necessary for modeling the human eye as an optical system [139]. Corneal surfaces, crystalline lens surfaces and the retinal surface are the key areas when considering the design of the optical system. The corneal surface is a meniscus lens that varies in topographical nature across the population [139]. The description of the corneal surfaces may be modeled to varied complexity with the application of a bi-conic sag equation or more robustly with Zernike polynomials [139]. However, actual topography and variations across the population leave true fitting a difficult simulation challenge. The optics of the crystalline lens present a further design challenge due to the gradient index of refraction (GRIN) present in this lens. The change in index of refraction from the outer layer to inner layer of the crystalline lens adds complexity to the model in the number of surfaces as well as ensuring correct layer spacing and index values. The age of a person also contributes to the design of the

crystalline structure as layers change separation and size with increasing age [139]. Finally, measurement of the retinal radius of curvature remains an open area of research with limited information on population variations to retinal curvature. Each of these areas must be considered when developing a human eye model.

The simulation work presented in the following text was done in Zemax optical design software (Zemax LLC, Kirkland, WA) using the Arizona eye model as a baseline. The AZ eye model provides a reasonable complexity of the human eye while matching clinical levels of on and off-axis aberration [140]. From the background in Chapter 1, this eye model successfully represents many clinical aberrations that have been studied in connection with refractive development. The model fits with the longitudinal chromatic aberration of the eye as well as, for fields under 40° , clinical levels of oblique astigmatism in the human eye as reported by Atchison and Smith [141]. Furthermore, for a 5.7 mm pupil, the AZ eye model matches clinical levels of longitudinal spherical aberration reported by Porter et. al. [142]. Even in areas of concession, such as the single index of refraction applied to the crystalline lens, optical characteristics such as dispersion and conic constants provide accurate depictions of clinical levels of aberrations [140].

Thus, the AZ eye model provides a sufficiently complex model of the human eye while more importantly, tailoring its design to match clinical aberrations. These conditions justify the use of this eye model in the investigation of a yet unmeasured ocular aberration in ocular distortion. For this body of work, the model consists of an anterior and posterior conic corneal surface, iris stop, anterior and posterior conic crystalline lens surface and a spherical retinal surface. Commentary on the construction of the spherical retinal surface will be listed later in this chapter. The current rotationally symmetric eye model allows for an appropriate first step characterization of ocular distortion in a human population. Further complexity can be added to the model to introduce the

effects of accommodation, increased complexity in crystalline lens structure as well as moving to a rotationally non-symmetric optical system. Figure 3-1 illustrates an example version of the model human eye in Zemax software.

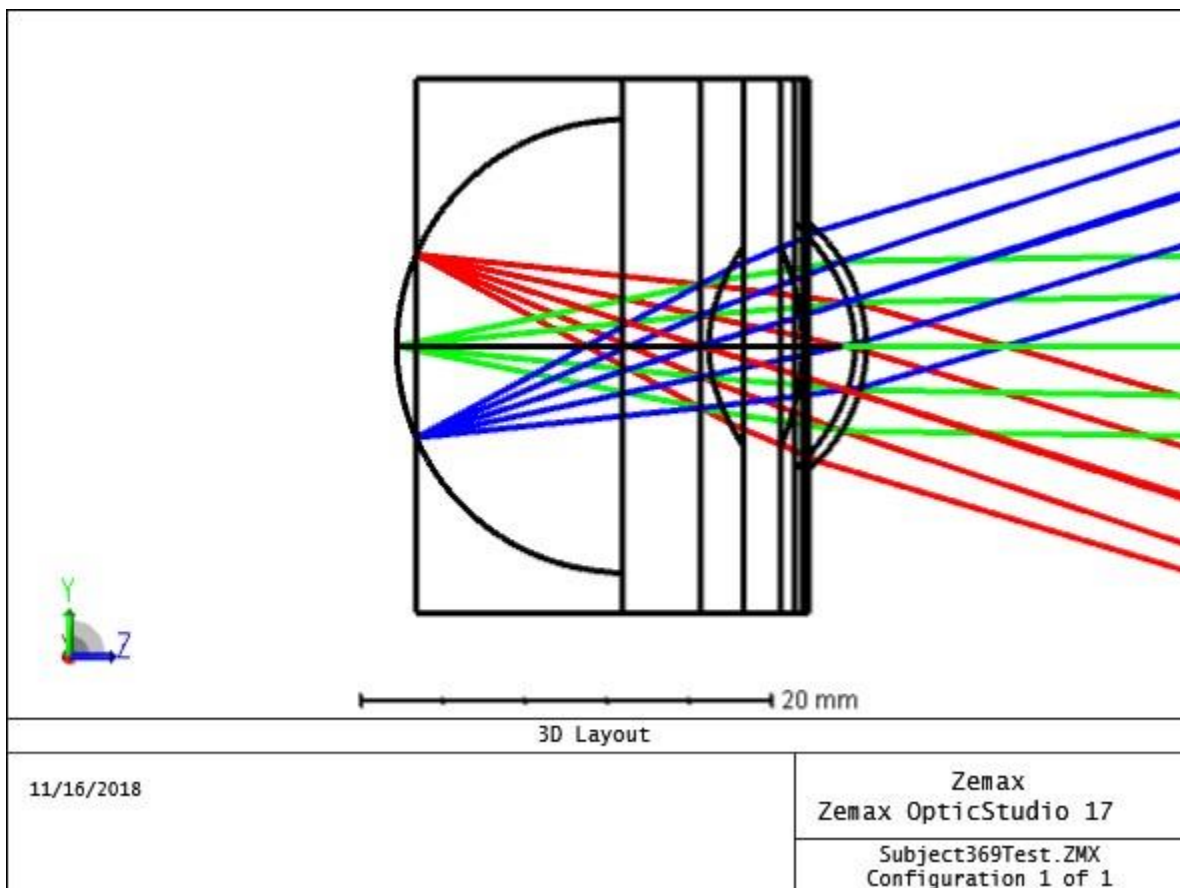


Figure 3- 1: AZ eye model illustration three field points traced from the back of the retina. Several configurations with corrective modalities added are also considered.

Simulated Population Generator

Before entering human trials to attempt the measurement of ocular distortion, the simulation work in this chapter aimed to uncover any trends or distributions for ocular distortion in a simulated population. A large population size was desired to interpret any potential findings related to this distortion pattern. To create this representative population, work from Rozema et.

al. [143] and Schwiegerling [144] was adapted to generate a randomized population set of 1000 eyes with refractive error between -20 D and +9 D, based on measured optical parameters. The term “simulated population” will be used for the remainder of this text to describe the 1000 eye generated data set. To accurately analyze results derived from this simulated population it is important to understand how these values were found.

For a given set of random variables denoted by \vec{a} and observables for these random variables denoted N , a covariance matrix X_N can be created. The mean vectors for each random variable $\vec{\mu}_a$ are also calculated to construct the covariance matrix. The diagonals of the matrix X_N are the variance of the random variables \vec{a} [144]. The remaining cells of the matrix are calculated such that the difference between a random variable and its mean $(a_{ji} - \bar{a}_j)$ is multiplied by another random variable and the difference of its mean $(a_{j'i} - \bar{a}_{j'})$, shown in Equation 3.1 below [144].

$$X_N(a_j, a_{j'}) = \sum_{i=1}^N (a_{ji} - \bar{a}_j) * (a_{j'i} - \bar{a}_{j'}) \quad 3.1$$

Cholesky decomposition, shown in Equation 3.2, creates a lower triangular matrix C , that is used to find a vector of random values given the variable set \vec{a} , while drastically reducing computation time when using the covariance matrix [144].

$$CC^T = X_N \quad 3.2$$

Thus, for any given statistical distribution that one desires, a random vector \vec{n} can be created.

With this, a new set of random variables \vec{b} can be created from the measured parameter means of

the seed population, $\vec{\mu}_a$, applied to a chosen distribution, \vec{n} , and decomposed covariance matrix, C , as shown in Equation 3.3 below [144].

$$\vec{b} = \vec{\mu}_a + C\vec{n} \quad 3.3$$

Rozema et. al. created a covariance matrix and mean value vector for 39 ocular parameters from a seed population of 127 subjects using biometry data found in Project Gullstrand, a European multicenter study [143]. The assumption of the Gaussian Multivariate Model created in this work assumes that if a given ocular parameter has a gaussian distribution and the mean and standard deviation are known, then a large number of random values can be generated with the same distribution as that parameter [143]. This body of work uses 10 of the 39 parameters investigated by Rozema. The anterior and posterior corneal keratometry, the anterior and posterior corneal eccentricity, central corneal thickness, the anterior and posterior crystalline lens radius of curvature, the crystalline lens thickness, the anterior chamber depth and the ocular length were selected to build the simulated population.

A few comments must be considered regarding the biometry data collected in the Rozema work. First, crystalline lens biometry data was not collected in Project Gullstrand, so a population reported by Atchison et. al. [145] of 66 age matched emmetropic patients formulated the crystalline lens parameters found in the Rozema paper [143]. Second, the observations gathered on the sample population greatly affect the outcome of the generated random parameters [143]. For instance, the subjects of Project Gullstrand were 70% women and 30% men [143]. Women statistically have shorter eyes, a higher crystalline lens power and other gender separated ocular parameters than men. The influence of these differences are highlighted in the data set [143], [145]. Therefore, the characteristics of the simulated population generated by these values should

be interpreted with these biases in mind as well as how the distribution of each ocular variable is chosen. Still, this simulated population generator makes for a powerful investigatory tool for the population differences related to ocular aberrations even with this seed population influence.

Following the method proposed by Schwiegerling [144], the covariance matrix and mean values of the 10 above mentioned ocular parameters, selected from the work of Rozema et. al. [143], were converted to parameters found in the AZ eye model. In this body of work, the assumption is made that the retinal surface is rotationally symmetric and spherical. The AZ eye model was designed to split the tangential and sagittal off-axis foci [140], but this simulation instead uses a globe radius R_g approximation based on values created from the simulated population. Given that there is little to no clinical work done on mean retinal curvature, an approximation based on available data was created and is illustrated in Figure 3-2 below.

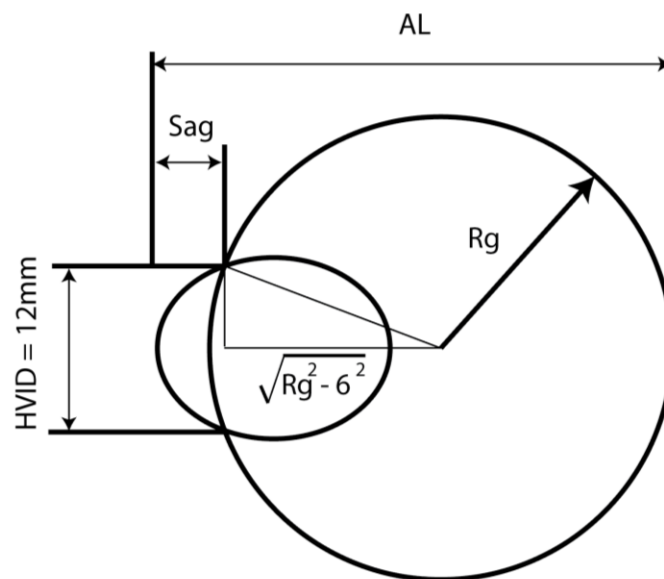


Figure 3- 2: Globe radius (R_g) illustration used as the base curvature for the retina in the simulated population eye models. The corneal sag (Sag) and axial length (AL) are derived from the converted ocular parameters in Rozema. $HVID$ is the assumed open diameter of the pupil.

The derivation of the globe radius relies on two assumptions. First, the cornea is an ellipsoid with a conic constant $CC = -0.25$ and second, the horizontal visible iris diameter $HVID$ is 12 mm.

With these two assumptions, measured values from the biometry data of the average Keratometry K and axial length AL , can be used to calculate the radius of curvature for the cornea R_c shown in Equation 3.4 below.

$$R_c = \frac{337.5}{K} \quad 3.4$$

Next, the corneal sag at the limbus of the eye is calculated using the sag equation for an ellipsoid shown in Equation 3.5, where $r = HVID/2$.

$$sag = \frac{1}{CC + 1} \left[R_c - \sqrt{R_c^2 - (CC + 1)r^2} \right] \quad 3.5$$

From the illustration in Figure 3-2 the axial length can be written as Equation 3.6 and thus rearranged to arrive at the equation for the globe radius in Equation 3.7.

$$AL = sag + R_g + \sqrt{R_g^2 - r^2} \quad 3.6$$

$$R_g = \frac{AL - sag}{r/3} + \frac{3r}{AL - sag} \quad 3.7$$

Raytracing Scheme, Environmental Parameters and Ocular Distortion Metric

Understanding that the first approach to measuring ocular distortion would be with the use of a modified fundus camera system, a raytracing scheme was created to represent how the target pattern would be imaged by the camera system. The AZ eye model was reversed, and the object plane curved to match the globe radius for each subject in the simulated population. Rays were monochromatic at a wavelength of $0.5876 \mu\text{m}$.

A total of 121 chief rays were traced from various field points by updating the normalized object space coordinates h_x and h_y from $[-1,1]$. This allowed equally spaced rays in field to be launched from the retinal surface. In the modified fundus camera system, the target pattern is projected conjugate to the retinal surface, making an intermediate object of the curved retinal surface with the target dots scattered back toward the aspheric objective and finally imaged.

As mentioned previously in this chapter, the difficulty in simulating ocular distortion is that the traditional imaging conditions do not apply to the human eye. Without the prescriptions for the optical components in the fundus camera, one to one simulation was impossible. However, it was understood that the function of the camera system was to flatten the retinal plane to create a plane to plane imaging scenario. Tracing true chief rays from the curved retinal plane to a flat plane in air, would result in large amounts of barrel or pincushion distortion depending on the location of the image plane. This is due to the angular magnification between object space and image space for the chief ray.

Ocular distortion was then treated in a different manner for the unique case of reverse raytracing in the eye. The question became, what, if any, distorted field coordinates entering the eye, produces equally spaced angles on the retinal surface? Treating ocular distortion in this manner removes the contribution of the curved retinal plane, analogous to the aspheric objective flattening the field. By tracing a chief ray through the nodal point of the eye and relating the

object space and image space ray angles, a metric for ocular distortion can be created. Ideally, the angle going into the nodal point in object space should equal the exiting angle in image space. Any deviation of these two angles would suggest uneven angular magnification with respect to field, or the inherent distortion of the optics of the eye. This percent distortion metric using these two ray angles is defined in Equation 3.8 below. Commentary on the “nodal” description is found below.

$$\% \text{ Ocular Distortion } (OD) \equiv \frac{\theta_{nodal}' - \theta_{nodal}}{\theta_{nodal}} * 100 \quad 3.8$$

To trace a ray through the nodal plane of the eye, a few steps were required. First, the nodal plane location was found from cardinal point data in Zemax. Next, a dummy surface was placed at this nodal plane location and was updated to become the new system stop. Finally, the cosine of the field angle with respect to the optical axis, leaving the retinal surface and leaving the front corneal surface were recorded to find the inherent population percent distortion. Since the AZ eye model is a rotationally symmetric system, only the direction cosine with respect to the optical axis was necessary to capture. This method can be generalized to a rotationally non-symmetric optical system by accounting for all 3 direction cosines.

It should be noted here that this method of tracing a chief ray through the new stop location is the simplest way to ensure a ray is passing through the nodal point of the eye but, this ray is no longer the true chief ray of the eye. A definition of this newly traced ray will be called a “nodal ray” and the angle of this ray with respect to the optical axis is being captured in the ocular distortion calculation. Only the maximum diagonal field was used to calculate the percent ocular distortion. The maximum diagonal field in this case was 25° which is approximately the half

angle of the fundus camera field of view. Given that the target grid in test schemes fills almost the entire camera field of view, the maximum angle of inspection for this simulation was justified.

Refractive Correction Modalities and the Effect on Ocular Distortion

It was also a research goal to understand if there is any effect on ocular distortion when a correction modality is placed on the eye. Three different refractive error correction modalities were simulated in this body of work including, spectacle lenses, soft contact lenses (SCL) and multi-focal soft contact lenses (MFSCCL). To characterize the population refractive error, a paraxial lens surface was placed in front of each subject simulated eye and the power was optimized until the RMS spot size at the retina, on-axis, was minimized. The power of the paraxial lens became the refractive error of the given simulated subject and corrective modalities were optimized to correct this refractive error. Below is a summary of each correction modality and the resultant ocular distortion measure. Table 3-1 below summarizes the mean and standard deviation of ocular distortion for each modality and the general population.

Ocular Distortion %		
	Mean	STD
Population	-0.32	0.35
Tscherning 1	-0.60	4.96
Tscherning 2	-0.55	3.92
SCL	-0.38	1.21
MFSCCL	11.47	1.79

Table 3- 1: Mean and standard deviation of ocular distortion percentage for each corrective modality and the simulated population.

Single Vision Spectacle Lens Correction

Perhaps the simplest myopic control mechanism is the single vision spectacle lens (SVLS). SVLS are introduced at varying ages of the population to correct for central refractive error and off-axis astigmatism. To correct central refraction a single solution to the Tscherning ellipse can be chosen for one lens surface that corresponds to the case of zero astigmatism [146]. Modelling the spectacle lens as a thin lens system, the front surface power can be found from Equation 3.9 below.

$$\phi_1^2(n+2) - \phi_1 \left[\frac{2}{q'}(n^2-1) + \Phi(n+2) \right] + n \left[\Phi + \frac{n-1}{q'} \right]^2 = 0 \quad 3.9$$

In Equation 3.9, ϕ_1 is the power of the anterior surface of the lens, Φ is the total power of the lens, n is the index of refraction, and q' is the spectacle lens distance from the center of rotation of the eye (~27 mm). For aesthetic reasons, the smaller of the two solutions to the quadratic is typically chosen when assigning base curvature of a SVL. These two solutions are labeled as “Tscherning 1” and “Tscherning 2” in this text.

The lens material was chosen as N-BK7 and SVL lens thickness was 5 mm, distance from cornea was 14 mm, with the clear aperture of the lenses set to 40 mm. The radius of curvature for the back surface was left to vary and a second optimization of RMS spot radius was completed to find this curvature. It is worth noting that the merit function of the optimization is looking for the case where the RMS spot radius is minimized for all fields. In the distortion metric, the image space direction cosine was found at the posterior surface of the spectacle lens. Figure 3-3 below shows the plot of the simulated population ocular distortion with the Tscherning 1 spectacle lens ocular distortion superimposed.

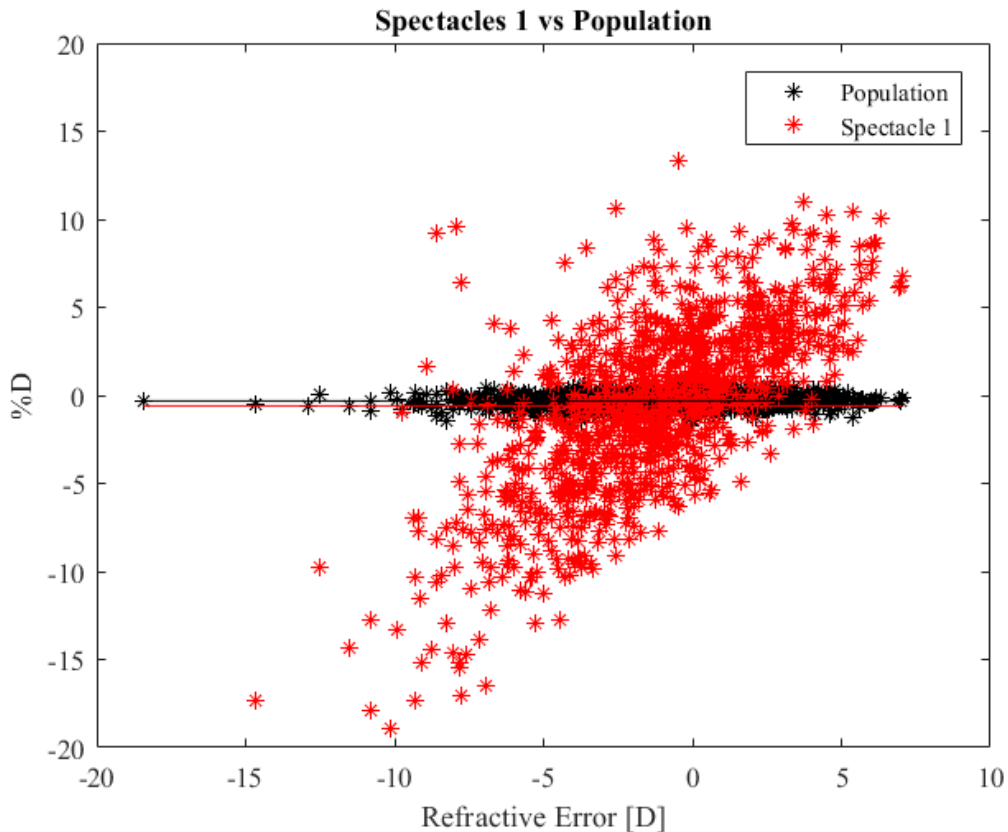


Figure 3- 3: The population ocular distortion (black) plotted against simulated subject refractive error with the Tscherning 1 solution ocular distortion (red) super imposed. The mean value lines are also shown. When spectacle lenses are used as a corrective modality, a significant shift toward barrel ocular distortion occurs as the amount of myopia increases.

The mean value for the Tscherning 1 solutions is -0.6% ocular distortion ($\sigma = 4.96$), a slight increase from the population mean. A major shift toward barrel distortion is induced as myopia increases and that pincushion is introduced as refractive error becomes more hyperopic. Furthermore, it appears that the data spread also increases when introducing spectacle lens correction. While the biometric data used to create the simulated population was taken from adult subjects, it may be that in children, where the refractive development is still on-going and eye growth on-going, that the trend changes. If ocular distortion plays a role in refractive development, then this trend suggests that spectacle lens correction may be beneficial or

detrimental in retarding refractive error development in individual cases. The Tscherning 2 solution is plotted below in Figure 3-4.

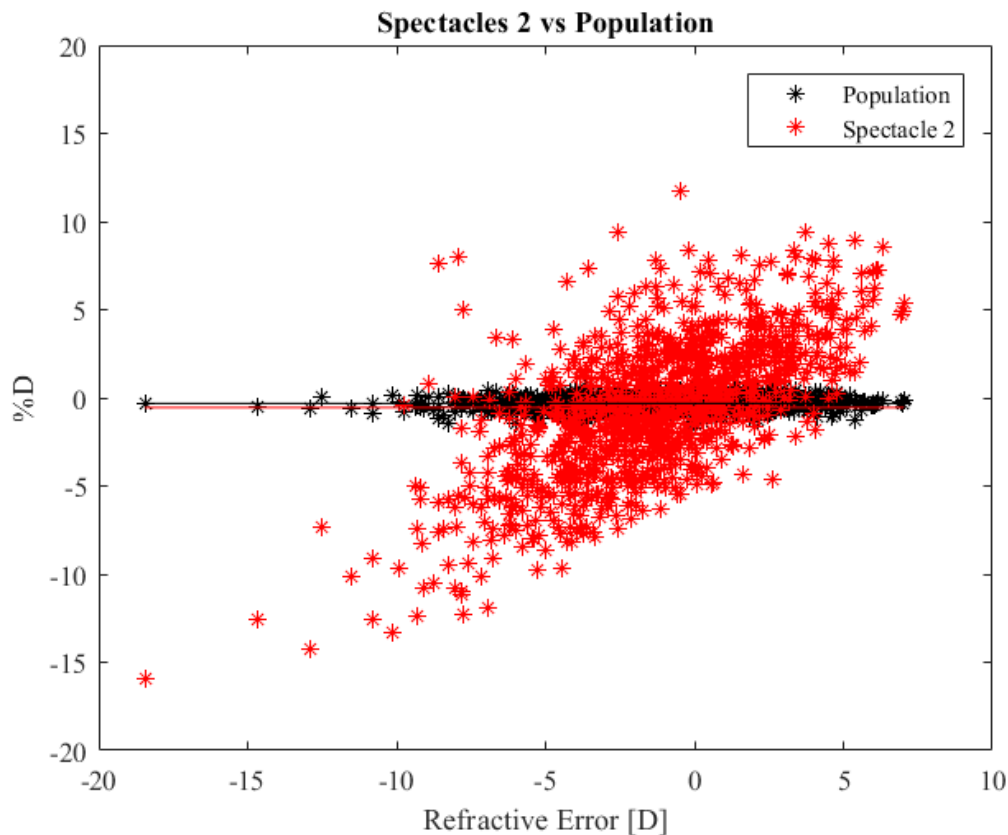


Figure 3- 4: The population ocular distortion (black) plotted against simulated subject refractive error with the Tscherning 2 solution ocular distortion (red) super imposed. The mean value lines are also shown. When spectacle lenses are used as a corrective modality, a significant shift toward barrel ocular distortion occurs as the amount of myopia increases. This shift is less dramatic than in the case of the Tscherning 1 solution.

The mean value for the Tscherning 1 solutions is -0.55% ocular distortion ($\sigma = 3.92$), a slight increase from the population mean. The Tscherning 2 solution has a smaller effect on the shift toward barrel or pincushion, as well as data spread, but still exhibits the same overall trend as the Tscherning 1 solution. Interestingly, the Tscherning 2 solution is often not used in spectacle lens

fabrication because the cosmetic effects are undesirable. However, it may prove to be a better solution for retarding myopic progression than the traditional prescription.

Soft Contact Lens (SCL) Correction

To simulate the effect of a hydrogel soft contact lens on distortion, a two-surface spherical element was modeled in Zemax. Both surfaces were chosen to be 6 mm in diameter due to the limit of the open aperture of the eye model. A thickness of 0.8 mm was given to the SCL and an index of refraction of 1.416, simulating one hour of wear in the eye [147]. The posterior radius of curvature was fit to the anterior corneal radius of curvature. The anterior SCL surface was optimized to correct for RMS spot radius on the retinal surface for all fields. The SCL results are plotted below in Figure 3-5.

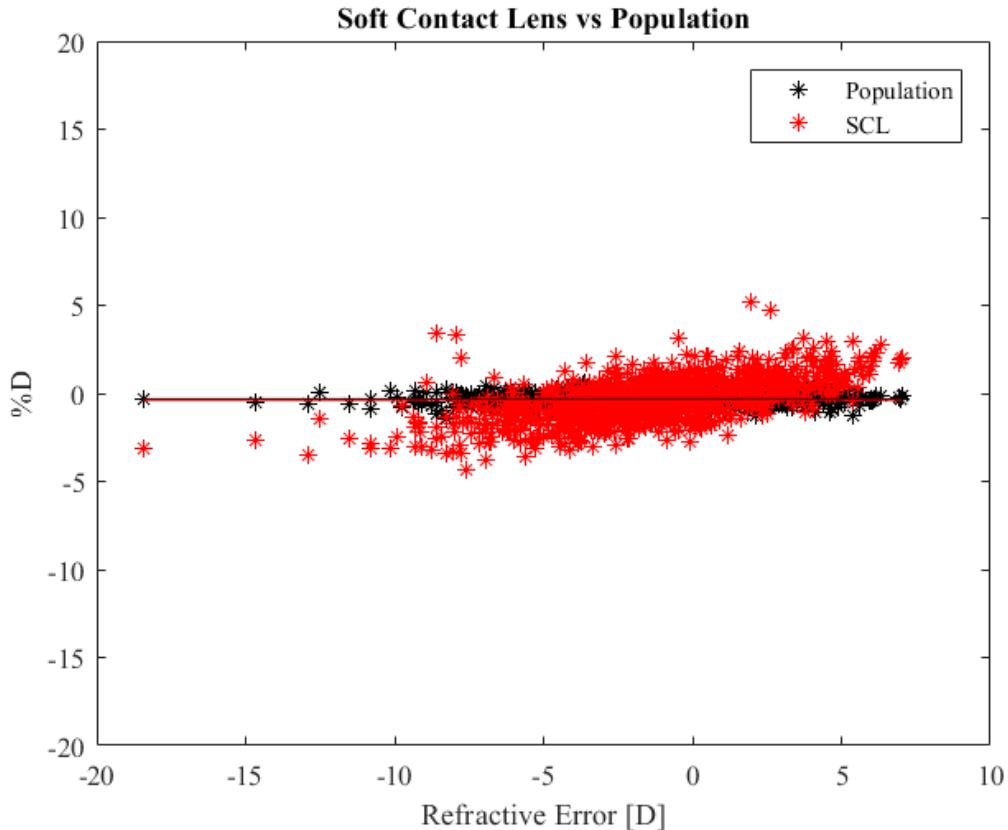


Figure 3- 5: The population ocular distortion (black) plotted against simulated subject refractive error with the SCL ocular distortion (red) super imposed. The mean value lines are also shown. The SCL does not induce large changes to the magnitude of ocular distortion but still exhibits a general trend to making ocular distortion more barrel as myopia increases.

The ocular distortion induced by the addition of SCL correction is very close to the values of the population inherent ocular distortion. The mean value for the SCL addition is -0.38 % ocular distortion ($\sigma = 1.21$). Surprisingly, this effect on ocular distortion that is within the range of the natural ocular distortion of the population fits with literature on SCL wear and myopia retardation. SCLs have been shown to be more effective than SVLs at retarding myopic progression. A postulate can be posed that given a unique set of ocular components for a person, eye growth tries to minimize or achieve a “ideal” value of ocular distortion. If the postulate is true, then it may explain why a modality like the SCL is more effective at regulating the signal for eye growth than compared to SVLs. The variance for individuals that are introduced to a

corrective modality is much lower in SCL such that the optimal ocular distortion value isn't under or over driven. Simulation results near the population mean encourage further work related to ocular distortion, corrective modalities, and refractive development.

Multi-Focal Soft Contact Lens (MFSCCL) Correction

Kim et. al. used a Shack-Hartmann technique to investigate the power profiles of several commercially available MFSCCLs [148]. Following work from Nam et. al. it was possible to convert these power profiles into surface maps for simulation in Zemax. Nam et. al. represent the local curvature $\kappa(r, \theta)$ of a wavefront $W(r, \theta)$ by Equation 3.10 below [149].

$$\kappa(r, \theta) = \frac{1}{2} \left[\frac{\partial^2 W}{\partial r^2} + \frac{1}{r} \frac{\partial W}{\partial r} + \frac{1}{r^2} \frac{\partial^2 W}{\partial \theta^2} \right] \quad 3.10$$

The axial vergence of the wavefront, where different power zones come to focus on-axis can be expressed by Equation 3.11, where n is the index of refraction.

$$V(r, \theta) = \frac{n}{r} \frac{\partial W}{\partial r} \quad 3.11$$

Finally, understanding that results from the Shack-Hartmann technique on power profiles is a direct measure of the axial wavefront vergence, the wavefront can be recreated as shown in Equation 3.12 below, where $\phi(r, \theta)$ is the power profile found from Kim et. al. and r is the radius of the clear aperture on the MFSCCL.

$$W(r, \theta) = \int_0^{r/2} \frac{\phi(r, \theta) \cdot r}{n} dr \quad 3.12$$

MFSCs often feature zones of power that present multiple focal planes to the wearer. The MiSight MFSC power profile was investigated by Rodriguez et. al. [150] and served as the MFSC of choice for this simulation work. This design features a -3 D central correction zone and base power, with two more additional treatment zones, which are used for presbyopia correction. The power profile $\phi(r, \theta)$ was fit to a 11th order polynomial function in MATLAB (MathWorks, Natick, MA), where upon integration would yield 12th order coefficients. A central power region was calculated, describing a spherical surface serving as the base power. In Zemax, the surface was treated as an even asphere with coefficients out to the 12th power. The clear aperture of the MFSC was 7 mm. Figure 3-6 shows the fit of the power profile to the 11th order coefficient terms.

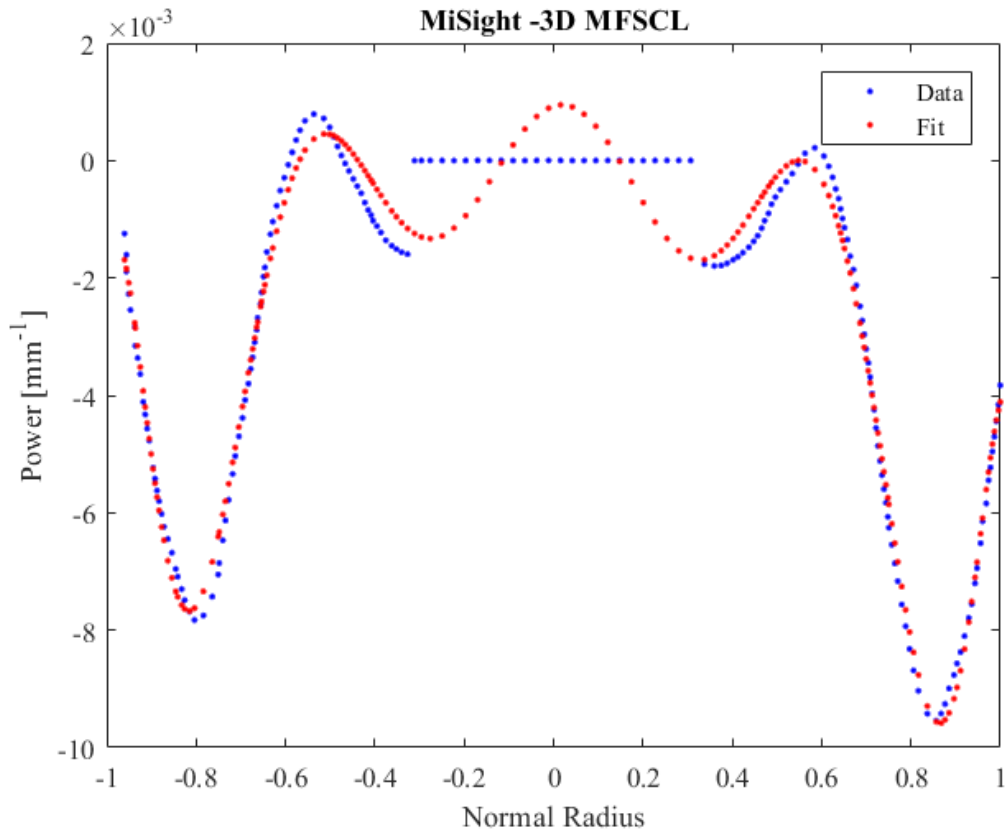


Figure 3- 6: Power profile fit of the MiSight MFSCl to an 11th order polynomial to be represented as an even asphere surface in Zemax. The center fit points where the blue horizontal line is seen are removed in the Zemax model. The base sphere has the aspheric power terms added on at the 0.3 normalized radial position.

Given that the addition power zones create multiple planes of focus at the retina, using the ocular distortion metric related to the ray direction cosines does not effectively capture the true distortion metric. The large increase in mean ocular distortion is likely due to these multiple planes of focus present which are not accounted for. While the ability to turn power profiles into usable simulation surfaces is available, the distortion metric for this modality is not adequately suited to describe the change in ocular distortion. No inferences were drawn from the data produced by the MFSCl on the simulated population. Nevertheless, Figure 3-7 shows the new ocular distortion for the MFSCl, but significant future work remains to understand the impact of multiple power zones on ocular distortion.

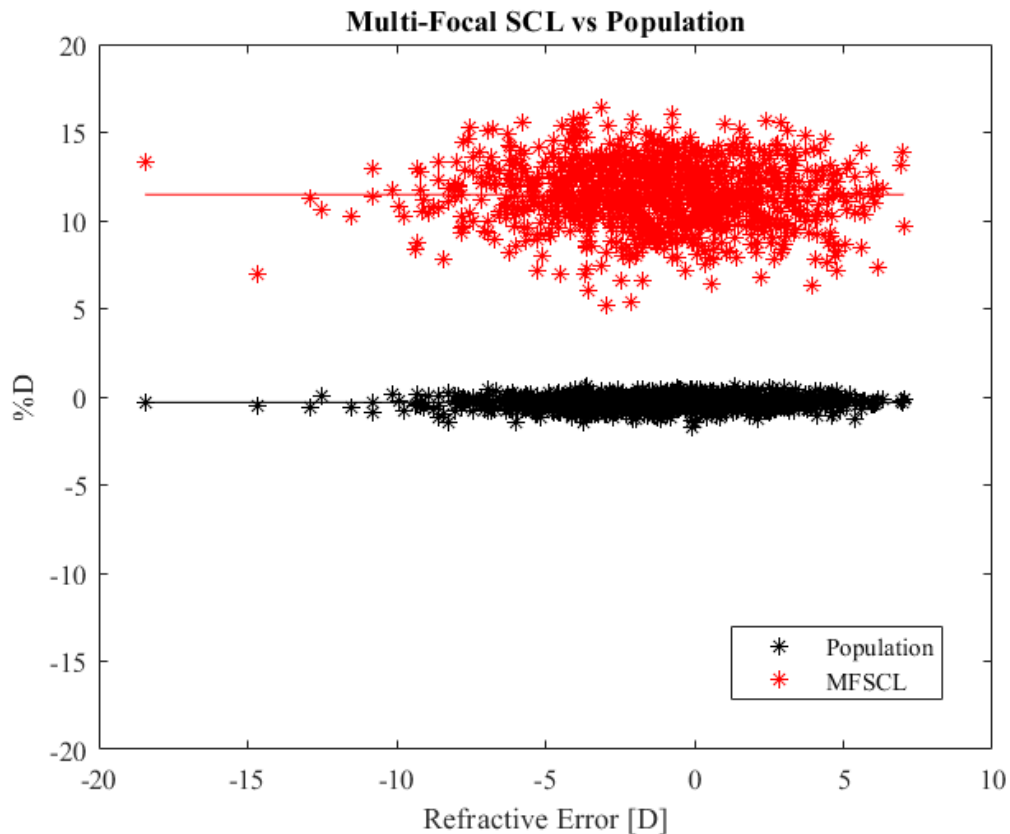


Figure 3- 7: The population ocular distortion (black) plotted against simulated subject refractive error with the SCL ocular distortion (red) super imposed. The mean value lines are also shown. No inferences are drawn from this data set and interpretation should be omitted at the time of writing.

Summary

The measurement of ocular distortion and even further, the definition of ocular distortion are brand new research challenges that need further exploration. However, early simulation work provides a potential window into ocular distortion in the general population. Furthermore, interesting trends emerge when viewing ocular distortion as a function of population refractive error. This simulation technique for investigating ocular distortion is a novel approach and shows encouraging signs to continue this scientific investigation. In the next chapter, a small cohort of human subject will have their eye's measured with the modified fundus camera. Comparisons

between the simulation and human trials will offer new insight on ocular distortion in the population.

Chapter 4: Measurement of Ocular Distortion in Human Subjects

Introduction

The modified fundus camera proposed in this body of work is a novel measuring modality for ocular distortion. However, the ability of this fundus camera to measure ocular distortion and to what certainty, was unknown prior to the writing of this document. Therefore, a calibration method, human subject testing, and the creation of a custom data processing package were created to gain insight on the performance capabilities of the fundus camera. Details on each section of this research plan are laid out in this chapter as well as some commentary on error analysis. Further sources of error will be commented on in Chapter 5 in relation to future improvements of this ocular distortion camera.

Calibration Method

Distortion correction by means of calibration is routinely done in imaging systems of all kinds. It was of interest in this body of work to quantify the amount of distortion introduced by both the illumination and imaging paths of the fundus camera. The residual distortion of the camera system would be an offset parameter for the measured ocular distortion of human subjects. To investigate the two optical paths separately, a crude eye model was proposed to simulate the most realistic scenario of imaging of the human eye during this calibration process. Appendix B contains a write up commenting on the validity of this crude eye model as a calibration tool. Also, contained in Appendix B is a verification that chief ray height locations from Zemax

simulation should serve as an equivalent comparison to centroid locations of the projected dot patterns in experimental images. The modeling has been updated since the time of writing of Appendix B related to verification using chief ray heights but the justification of the crude eye model as a calibration tool still stands.

The amount of distortion in the illumination and imaging paths were investigated separately but these paths share some common setup parameters. An optical breadboard was raised, secured and leveled on two rigid posts connected to L-brackets to match the height of the aspheric objective on the fundus camera. The crude eye model was placed on a rotation stage connected to a linear translation stage for repeated movement testing. Centering the nodal plane of the crude eye model over the center of rotation of the stage ensured that images with rotation would mimic the response of the human eye. Figure 4-1 shows the testing setup for calibration using the crude eye model.

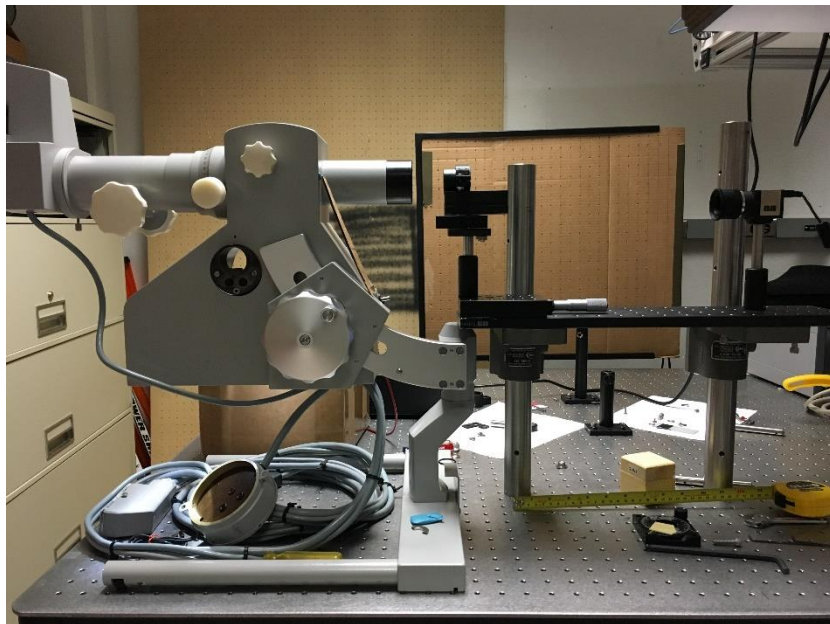


Figure 4- 1: Calibration setup with crude eye model. Both illumination and imaging paths were calibrated under the same setup with slight variations in detectors and configuration.

Illumination Path Calibration

Using the internal LED suite as the illumination as well as the internal grid target of 1 mm spaced dots, the illumination path of the fundus camera could be calibrated by imaging the back of the curved fiber bundle (CFB). The method to capture images was similar to actual fundus camera operation when imaging a human subject. Fundus camera operation and associated imaging artifacts will be discussed later in the chapter. By visual inspection, the crude eye model was aligned to the holes of the optical breadboard and leveled to make the anterior doublet surface parallel with the optical table level. The fundus camera was displaced laterally with respect to the open aperture of the doublet where the illumination patch could be shown on the aperture surrounding the doublet. From this position, the fundus camera was translated toward or away from the crude eye model until the annulus of light was in focus. Then the camera was laterally moved such that the entire achromatic doublet was filled with the annulus of light.

Typically, the annulus of light would be focused to the stop of the eye which is about 3 mm behind the first power surface or anterior cornea of the eye, but here the stop is at approximately the front surface of the achromatic doublet. The internal dot pattern was projected into the crude eye model and captured using a Point Grey USB camera with a zoom lens shown in Figure 4-2. Analysis of the dot patterns will be commented on in a later section of this chapter. The method of image capture described above was repeated three times to determine that -1.5% barrel distortion, the average amount radial distortion in the illumination path, was present.

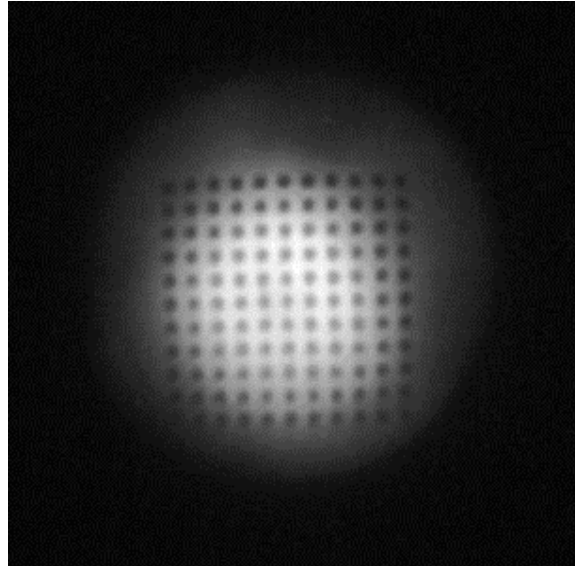


Figure 4- 2: Super imposed image of high and low illumination pattern projection on the back of the CFB for illumination path calibration. An average of -1.5% radial distortion determined for this path.

Imaging Path Calibration

For the imaging path calibration, an equivalent grid of 1 mm spaced dots was taped to the back of the CFB. A marker was used to indicate the center of the dot pattern and a diffuse bar source was placed behind the CFB to illuminate the grid pattern. A similar alignment scheme for the camera was used as in the illumination path calibration to ensure, to some extent that the relative distance and alignment of the camera and crude eye model were the same in each configuration.

The legacy configuration of the fundus camera featured a 35 mm x 35 mm film imaging plane for detection. A digital camera was originally used to replace the film plane but failed to capture the full field of view when imaging the eye model due to the sensor size mismatch. A 3D printed cellphone mount held an iPhone 6s at the eyepiece reticle to capture both the imaging path calibration and the subsequent human subjects. The cellphone and reticle combination achieved a full field of view capture of the retinal while allowing for real time alignment. The projected dot pattern can be through the cellphone camera in Figure 4-3. Processing of three test run

images in this optical path yielded an average of 2% pincushion distortion, inherent to the camera system.

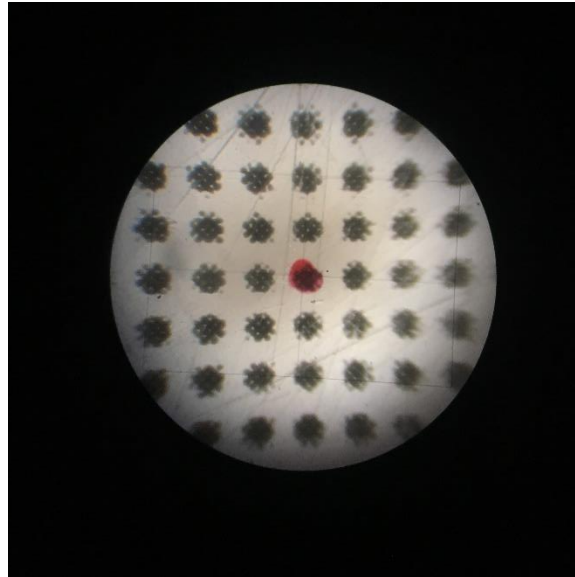


Figure 4- 3: Imaging path calibration of grid target through cellphone camera. An average of 2% radial distortion determined for this path.

Thus, the overall residual distortion in the fundus camera system was determined to be 0.5 % radial distortion. Residual distortion of the fundus system was applied as a constant offset for the subsequent human trial population.

Human Trials

The first step in realizing an imaging modality to quantify ocular distortion and the potential connection to refractive error development was undertaken through a small cohort human trial. To investigate the effectiveness of the modified fundus camera as a distortion measurement system, two straightforward questions were proposed before the trial and serve as the main research questions guiding this work. The first question was whether a grid pattern could be repeatably projected onto the retina of the eye and imaged to process dot centroids for a measure

of ocular distortion. Second, after processing the image, is there a difference or trend between ocular distortion in hyperopes, emmetropes, or myopes?

The human trial testing conformed to the tenets of the Declaration of Helsinki and the research procedure was approved by the University of Arizona Institutional Review Board. Seventeen subjects (n = 17), ages 19-33 years old (mean = 25.2) voluntarily agreed to participate in this ocular distortion measurement. Table 4-1 lists demographic information of the 17 subjects.

Age	Gender	Ethnicity	Refractive Error [D]
24	F	Hispanic	-0.5
24	F	Asian	-7
30	M	Asian	-8
19	F	Caucasian	-1.25
27	F	Hispanic	-0.5
24	F	Asian	0
20	F	Caucasian	1.25
25	M	Caucasian	-1
27	M	Caucasian	0
33	F	Hispanic	0
21	F	Caucasian	-1
25	F	Asian	-5.75
23	M	Caucasian	-4.25
30	M	Asian	-4
27	F	Caucasian	-4.5
27	M	Caucasian	-2.5
22	M	Caucasian	2

Table 4- 1:Demographic information on human cohort. Refractive error values are self-reported by the patients and may be inaccurate. The normal distribution of refractive error of the population is well represented in this small cohort.

It should be noted that the refractive error listed in Table 3-1 are self-reported values from the participants. Some participants had recently received their prescription from an outside ophthalmologist, other subjects reported their refractive error to the best of their recollection. The subject cohort does represent the general refractive error seen in the population with 8

myopic subjects (-1D to -8D), 7 emmetropic subjects ($-1D \leq E < 1D$) and 2 hyperopic subjects (1D to 2D). All subjects reported little to no astigmatism ($>1D$). 53% of the subjects were of Caucasian descent, 29% of Asian descent, and 18% of Hispanic descent with 10 out of the 17 subjects being female. Testing of the right eye was done for all except one patient who was hyperopic in the left eye. The anisometropia of the exempted subject was less than 1D so the left eye was used for measurement to provide depth to the experiment.

Subjects were scheduled for imaging via an email recruitment to the College of Optical Sciences at the University of Arizona where a consent session was held detailing the following imaging procedure. After collecting background information, subjects were sat in a chair in front of the fundus camera. 2% phenylephrine dilating solution was placed in a small pocket under the bottom eyelid. The subjects were allowed 20 minutes to sit and relax until full mydriasis was reached. Previously, a series of tests were conducted under guidelines for ISO Standard 15004-2 which addressed light hazard levels for ophthalmic instruments. It can be shown in Appendix C that the modified fundus camera operates at worst, two times less than the aphakic damage threshold for a white light source, making this an eye safe imaging technique.

The imaging procedure for human subjects follows very closely to that of the procedure described for the crude eye model in calibration. Subjects seated in front of the camera placed their chin and forehead on a chinrest which was adjusted to the height of the camera. The camera system was placed on an ophthalmic imaging bench where the camera could easily be moved forward, back or laterally with respect to the subject's eye. Alignment and image capture was performed in real time by first aligning to the human eye by operator sight and more fine positioning while inspecting a live camera feed from the cellphone camera. Typically, refractive error is corrected by moving the detection plane toward or away from the zoom lens elements in

the fundus camera. In this instance, the cellphone zoom function was used to bring blood vessels on the retina into sharp focus. The focus plane for the camera was then locked for all subsequent images of the target and retina.

Figure 4-4 to Figure 4-8 show representative images the projected target and retina for each test subject. Challenges and imaging error will be reported in Chapter 5, but no subjects were unable to reach full mydriasis and all subjects are included in the study. A brief commentary related to the two proposed study questions follow the images.

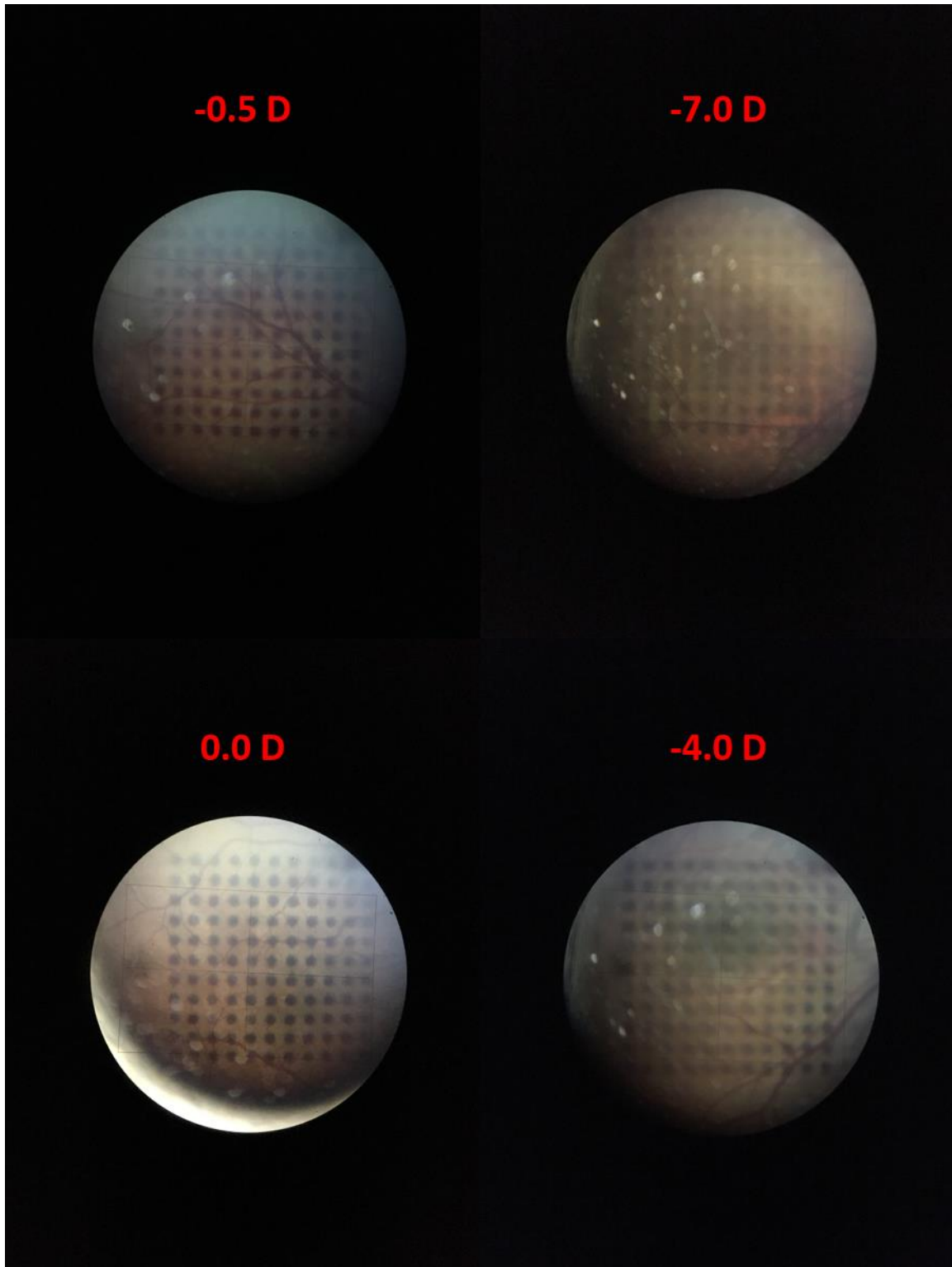


Figure 4- 4: Four retinal images with the projected grid pattern from cohort subjects. Self-reported refractive error is listed above each image.

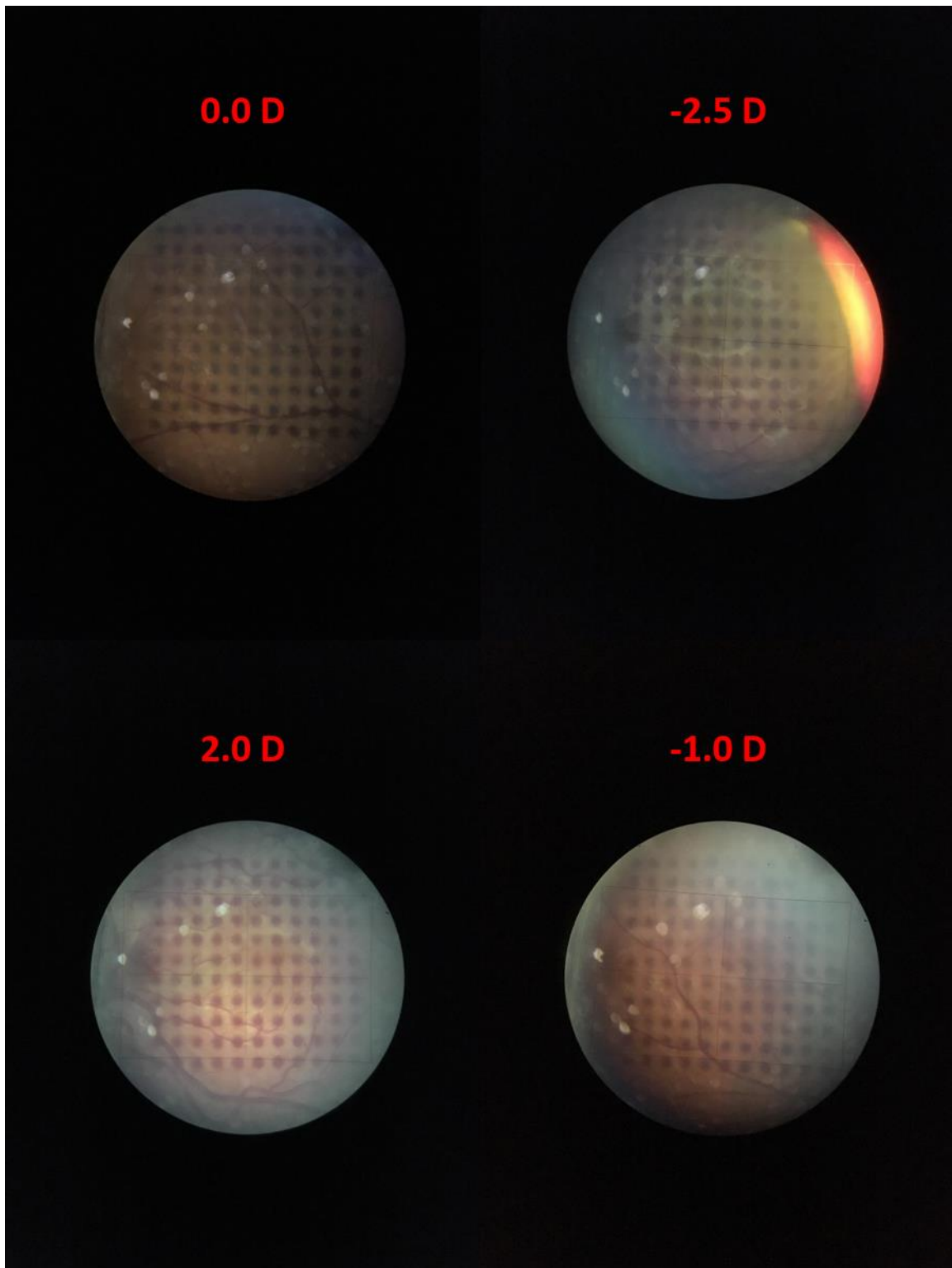


Figure 4- 5: Four retinal images with the projected grid pattern from cohort subjects. Self-reported refractive error is listed above each image.

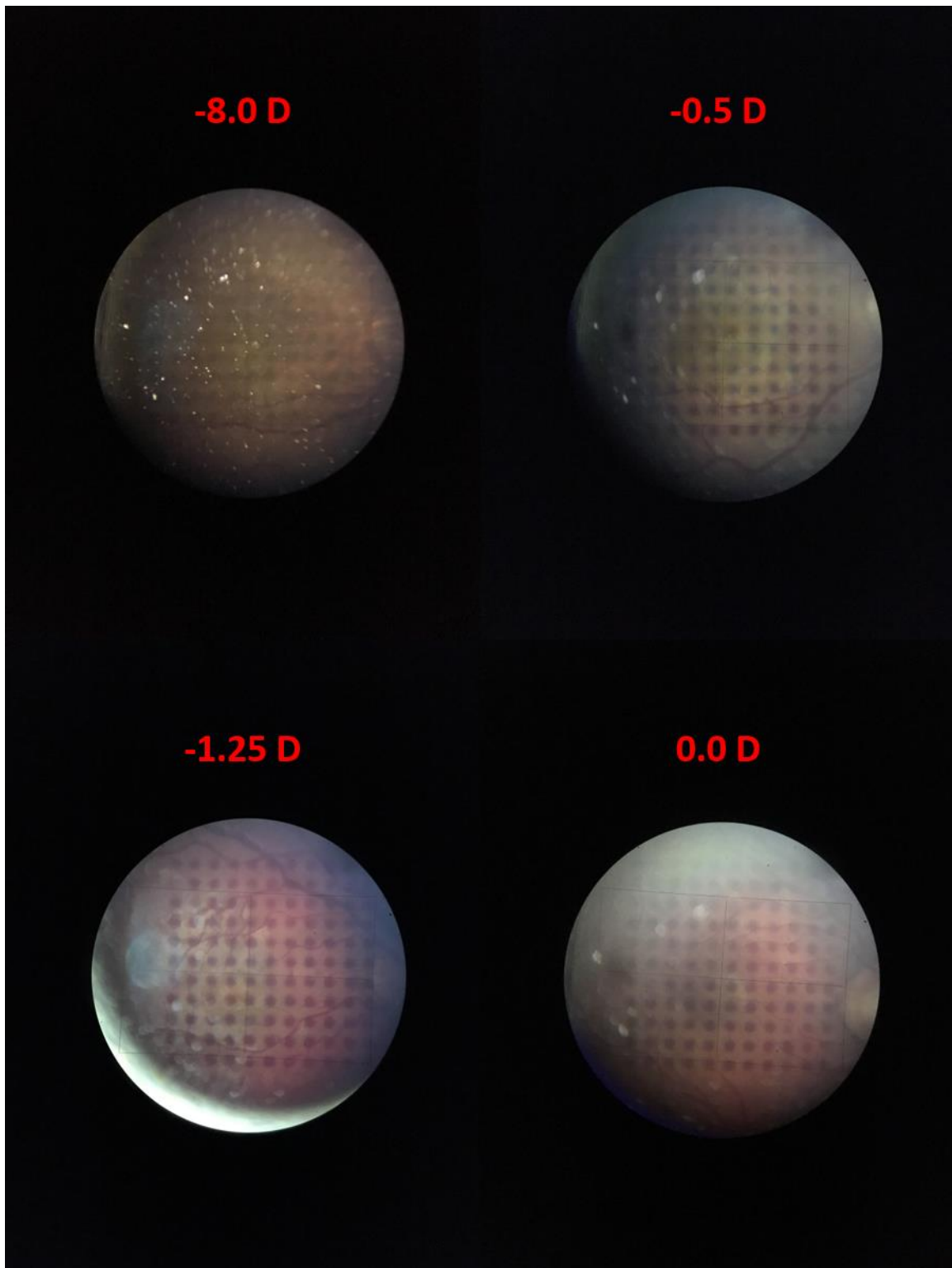


Figure 4- 6: Four retinal images with the projected grid pattern from cohort subjects. Self-reported refractive error is listed above each image.

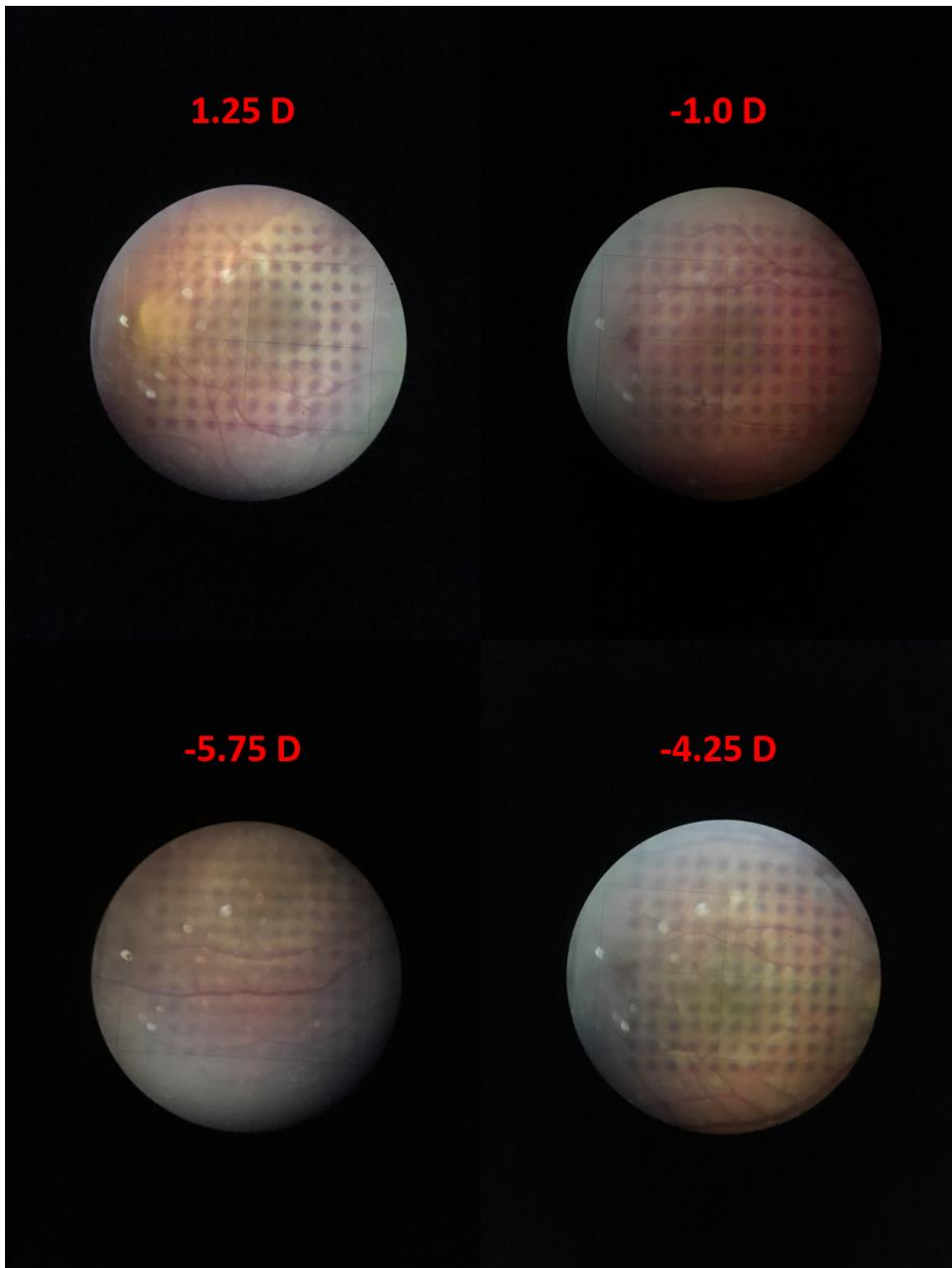


Figure 4- 7: Four retinal images with the projected grid pattern from cohort subjects. Self-reported refractive error is listed above each image.

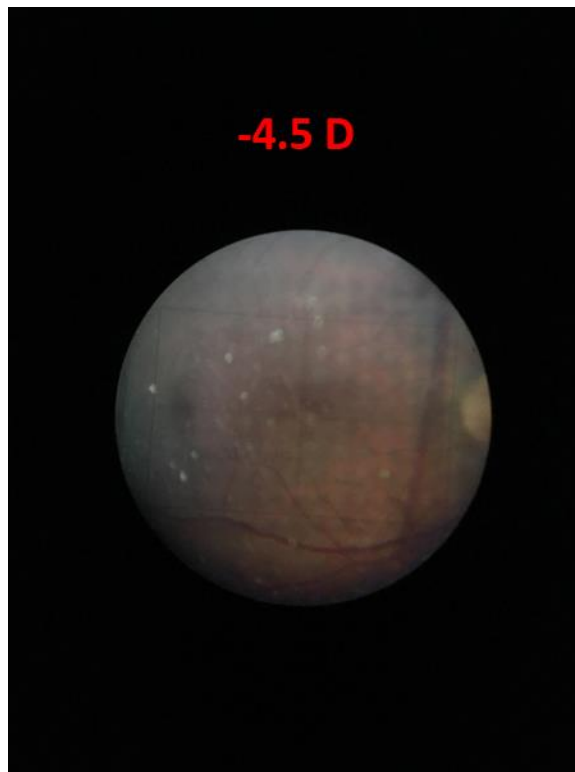


Figure 4- 8: The final retinal image with the projected grid pattern of a cohort subject. Self-reported refractive error is listed above the image.

Figure 4-4 to Figure 4-8 demonstrate qualitative answers to the two proposed research questions. Given that the location of the grid pattern is conjugate to the retina in the fundus camera system, it is indeed possible to resolve reasonably sharp target features for distortion measurement in human eyes. Second, by visual inspection, there appear to be differences between hyperopic, emmetropic, and myopic individuals in both ocular distortion patterns and overall image resolution of the grid pattern. Figure 4-5 demonstrates this difference most clearly, where the +2 D subject appears to have more barrel distortion in the grid pattern than the more pincushion 0 D subject in the sub image above. The patterns of emmetropic and myopic subjects tend to show a more pincushion effect toward the periphery, but in some cases shown a collapsing together of points in the central region. Figure 4-6 demonstrates this effect of point collapse in the center for

the -0.5 D subject and compared to the 0 D subject in the sub image below. Motivation for expanding the wavefront representation out to higher orders lies in reviewing the experimental data and seeing these combinations of distortion terms, creating complex distortion patterns. Further commentary on the influence of alignment, camera sensitivity with respect to system error, and imaging artifacts will be discussed further in Chapter 5.

Data Processing

In an effort to quantitatively answer if there is variability between hyperopic, emmetropic, and myopic subjects, a testing criterion was created for the data processing of the grid pattern centroids. First, each image selected for processing required the optic disc to appear on the right side of the image. Given that the right eye for each subject under test was used, this provides a roughly equivalent retinal area for investigation for each subject. In the case of the +2 D subject, whose left eye was imaged, the image was rotated about the vertical axis to place the optic disc on the right side of the image. Second, it was decided that three images of each subject would be processed to create a mean for the fit distortion values. Lastly, in each of the three images, the eye must not have rotated more than 3.5° between subsequent images.

The approximate field of view of the fundus camera is around 50° or 2020 pixels on the cellphone sensor. By tracking a portion of a blood vessel in each of the selected images, the average pixel movement of the eye was recorded. Therefore, images where blood vessel jumps were less than 175 pixels and met the criterion of optic disc location, were selected as processing candidates for distortion fitting. A sample set of three images is shown in Figure 4-9.

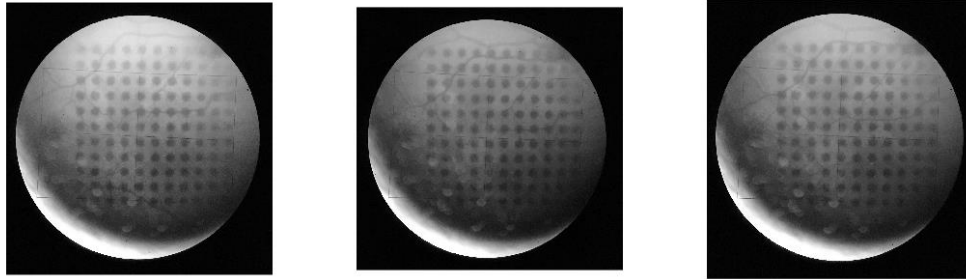


Figure 4- 9: Three processing candidate images that meet the criterion for post-processing. It is of important note that the pattern does not deviate significantly even with small eye rotations. The conjecture that a stable, repeatable target can be imaged on the retina is further supported here.

The data processing scheme to find the grid pattern centroids and fit to the distortion wavefront errors discussed in Chapter 2 follows a series of post processing steps that are completed using MATLAB numerical software. Processing dot centroids in the human subject images is done in two steps, an automatic Fourier based method and a user defined clicking procedure.

A candidate image was loaded, cropped and resized to perform a computationally efficient Discrete Fourier Transform (DFT). Pixel coordinate space was transformed to real space with knowledge of the cellphone sensor parameters. Similarly, the Fourier or frequency space domain was created from the real space coordinates and in consideration with Nyquist sampling theorem. A complex filtering function was incorporated in the raw image DFT to reduce intensity variation and suppress noise artifacts found on the retina. Figure 4-10 shows the filtered Fourier space image as well as the resultant binary image of a human subject.

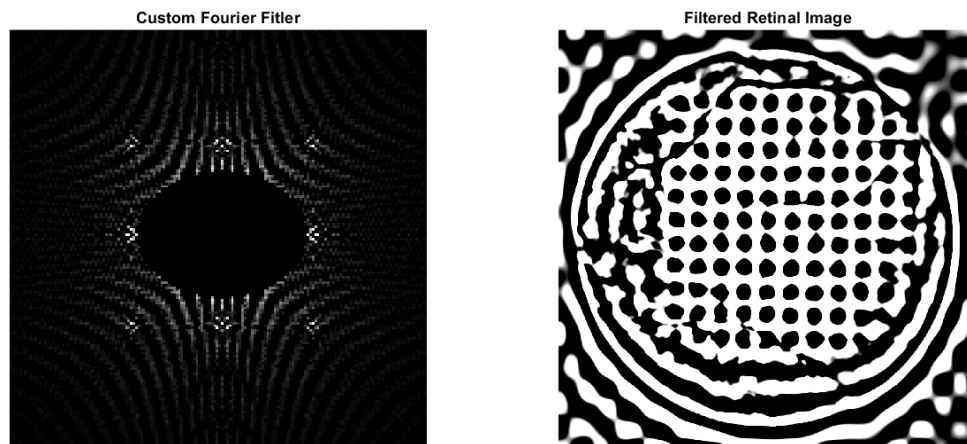


Figure 4- 10: A filtered Fourier Transform (FT) shown on the left with the binary resultant image of the retina shown on the right.

The Fourier domain shows the frequency separation of the grid pattern related to the dot pitch, which is the critical information necessary to calculate centroid center locations. Uneven illumination, color, and noise artifacts such as blood vessels can be suppressed relatively well through this method. Optimization of the complex filter function was not performed as each subject case had varied levels of dot image quality. Furthermore, no image enhancement related to dot shape or size was performed due to the variability in resolution capability for each subject. Once the binary image was formed, an internal MATLAB algorithm was used to identify centroid locations. Contiguous matrices use a nearest neighbor approach to identify connected components in the binary image. Careful selection of component size would yield locations of dot centers as shown in Figure 4-11. Approximately, 25%-50% of image points can be captured automatically sign this automated method.

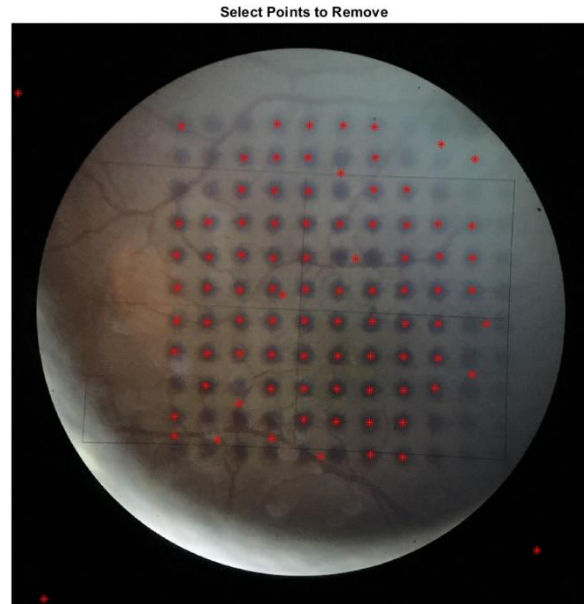


Figure 4- 11: Centroid centers marked in red that were found by the internal centroid algorithm. Incorrect or misinterpreted centroid values are also present in the image and indicate false positive centers.

The false positives for centroids seen in Figure 4-11 provide the motivation for the second centroid center locating procedure, user hand clicked points. While automatic detection relies on mathematical weighting to determine centroids, the reality of false positives requires the aid of the human eye. While also correcting for these erroneous centroid locations, it is possible to expand the data set by user clicking the remaining centers for increased point sampling in the image. Once the final center coordinate location has been recorded, points are passed through a sorting algorithm to orient point (1,1) in the matrix as the upper left most point all the way through point (11,11). This ensures that proper field coordinates can be identified.

Typically, distortion values are reported such that the distorted image or target is referenced to a nominal or undistorted object. To create a nominal or undistorted reference grid, where the center location of centroids should have been located, a center spacing value was calculated for

each image processed. The spacing between the center dot of the grid pattern at position (6,6) and the four nearest neighbors were averaged to create the nominal grid spacing, centered at the (6,6) position and illustrated in Figure 4-12. The assumption made for the reference grid is that the distortion around the (6,6) point should be low given that this is close to the optical axis of the fundus camera system.

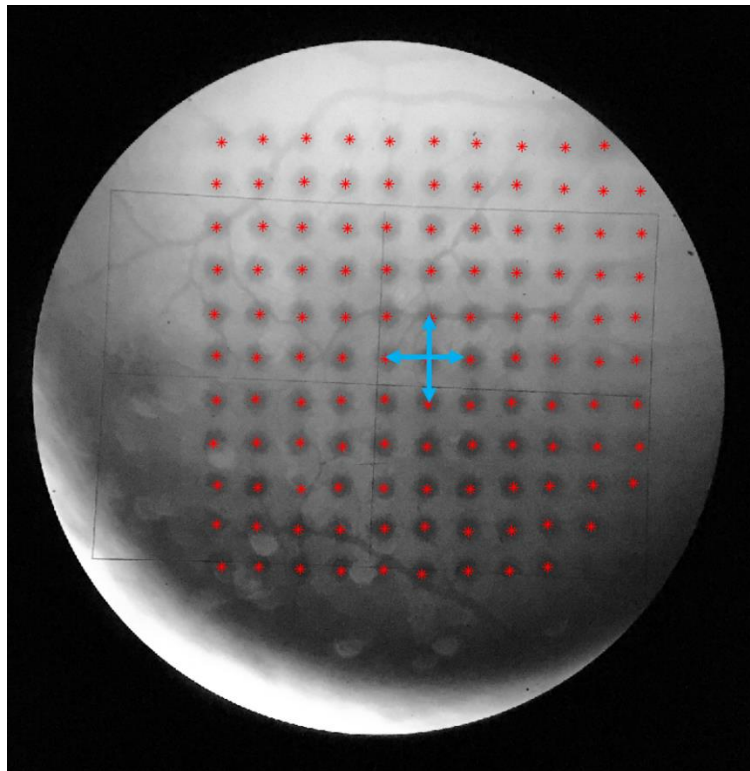


Figure 4- 12: The method for determining the undistorted reference grid is done by taking the center dot of the grid pattern at (6,6) and average the four nearest neighbor distances seen in light blue. Removed false-positive points (yellow) can be viewed with the automatically found centers (red) and the user hand-clicked centers (blue).

The center hand clicking method can raise concerns of error in center location values. User bias, accuracy, fatigue and image noise all contribute to potential error. To understand the type of error that could be induced during the hand clicked processing a repeatability test was devised. Using a nominal image like the one shown in Figure 4-12. the automated and manual processing was completed back to back six times. In each of the six runs, the number of automatically found

points was increased or decreased to see if there was influence on having a majority of the found centers come from hand clicking. Table 4-2 reports the number of automatically found points and the center spacing of the resulting distorted center locations. It was determined that the two-stage process of center location was sufficient for processing the entirety of the human retina dataset.

	Run 1	Run 2	Run 3	Run 4	Run 5	Run 6
Points Found Automatically	63	33	69	77	46	42
Spacing	124.2	122.2	124.1	126.5	124.8	123.2
Mean Spacing	124.2					
STD Spacing	1.45					

Table 4- 2: Repeatability results for automatic and manual center dot processing. All number are in units of pixel space coordinates. Commentary on fit errors related to spacing values is presented later.

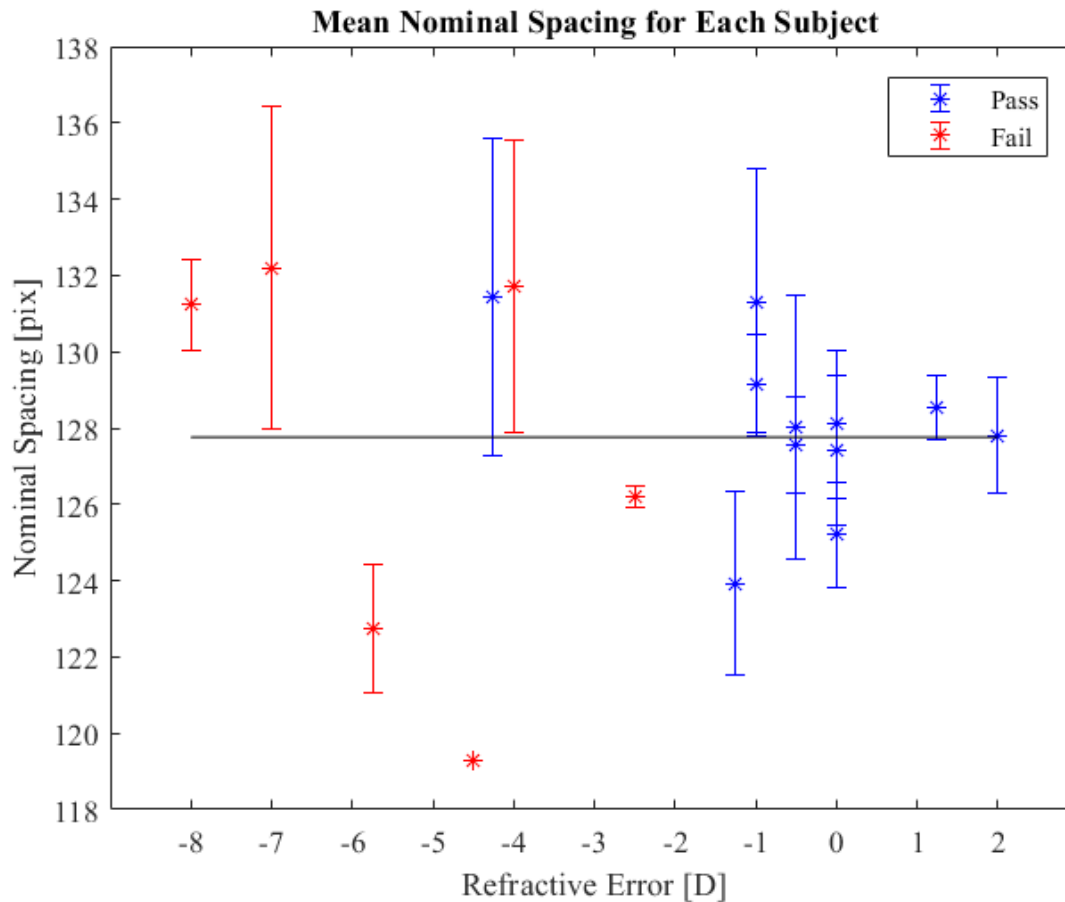


Figure 4- 13: Mean nominal spacing for each subject. The mean spacing for all refractive powers is 127.76 pixels, shown in black. Points indicated in red have low dot contrast in image processing and should be viewed as weak data sets. Error bars around points correspond to standard deviation ($\sigma = 1$).

Mean nominal spacing for each subject is shown in Figure 4-13. The mean nominal spacing for all subjects was found to be 127.76 pixels. Referring to Figures 4-4 through 4-8, it is clear to see that some subjects have well defined, high contrast dots where others, typically myopic subjects, have deformed and blurred dots. A visual inspection for all subjects created a subjective pass/fail criterion for the data sets. All data sets were considered for analysis but datasets with weak grid points are highlighted for the reader's attention. Further discussion of this pass/fail criterion will be mentioned in Chapter 5. For the remainder of this chapter, the "nominal grid" or "nominal points" of a subject is related to an 11x11 grid formed from these nominal spacing values.

Coefficient Fitting and Results

With the assumption that the human eye is a rotationally non-symmetric optical system and using the wavefront expansion from Barakat described in Chapter 2, the processed centers from each subject was fit to 4th order distortion coefficients in x and y. Though this text extends the wavefront error out to the 6th order, it was found that the least squares fitting was over constrained causing numerical error in lower fit orders. Thus, the radial distortion metric described in Chapter 2 will be used to characterize ocular distortion in this text due to the convergence of fit error using 4th order distortion coefficients.

Using the nominal spacing value to determine nominal grid coordinates (x_o, y_o) a polynomial matrix A , is formed to evaluate the distorted center coordinates (x, y) . The nominal grid points (x_o, y_o) and the distorted grid points (x, y) share a common center point which is (x_6, y_6) . Subtracting the center point from both sets of coordinates creates a Cartesian pixel space of positive and negative coordinates. The following least-squares minimization equation to find the distortion coefficients for (x, y) is shown in Equation 4.1 below.

$$\begin{aligned}
 A_x \setminus b_x &= \begin{bmatrix} x_{o,1} & y_{o,1} & x_{o,1}^2 & \dots & x_{o,1}^3 \\ \vdots & \vdots & \vdots & \ddots & \vdots \\ x_{o,n} & y_{o,n} & x_{o,n}^2 & \dots & x_{o,n}^3 \end{bmatrix} \begin{bmatrix} x_1 \\ \vdots \\ x_n \end{bmatrix} = \begin{bmatrix} F_{x,1} \\ \vdots \\ F_{x,9} \end{bmatrix} \\
 A_y \setminus b_y &= \begin{bmatrix} x_{o,1} & y_{o,1} & x_{o,1}^2 & \dots & x_{o,1}^3 \\ \vdots & \vdots & \vdots & \ddots & \vdots \\ x_{o,n} & y_{o,n} & x_{o,n}^2 & \dots & x_{o,n}^3 \end{bmatrix} \begin{bmatrix} y_1 \\ \vdots \\ y_n \end{bmatrix} = \begin{bmatrix} F_{y,1} \\ \vdots \\ F_{y,9} \end{bmatrix}
 \end{aligned} \tag{4.1}$$

In Equation 4.1, n is equal to the number of dot centers found, with a maximum of 121 found centers for the 11x11 target grid but the number of points varies between subjects. $F_{x,y}$ represent

the x and y distortion terms for the 4th order wavefront error expansion. These $F_{x,y}$ coefficients represent the Barakat B-D labeling coefficients and will be reported as such. Thus, 18 independent coefficients are fit in this process.

The 10th subject of this study was chosen at random to demonstrate the variance in coefficient values across the three processed images. The coefficient values for each processed image for all 18 coefficients are shown in Figures 4-14 to 4-16 below.

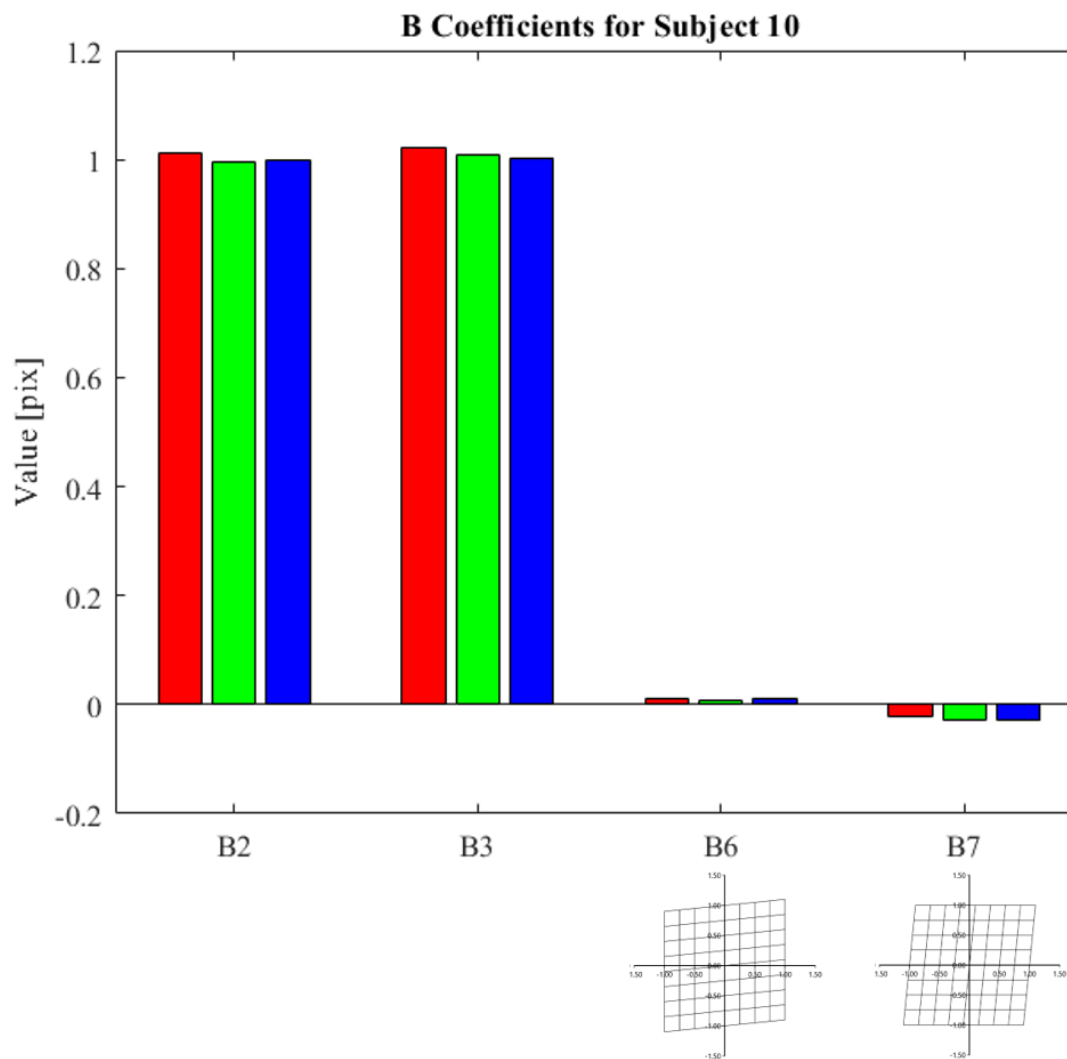


Figure 4- 14: Linear B coefficient values for subject 10. Note B_2 and B_3 correspond to x and y linear magnification respectively. Fit values are stable and of reasonable magnitude for each processed image.

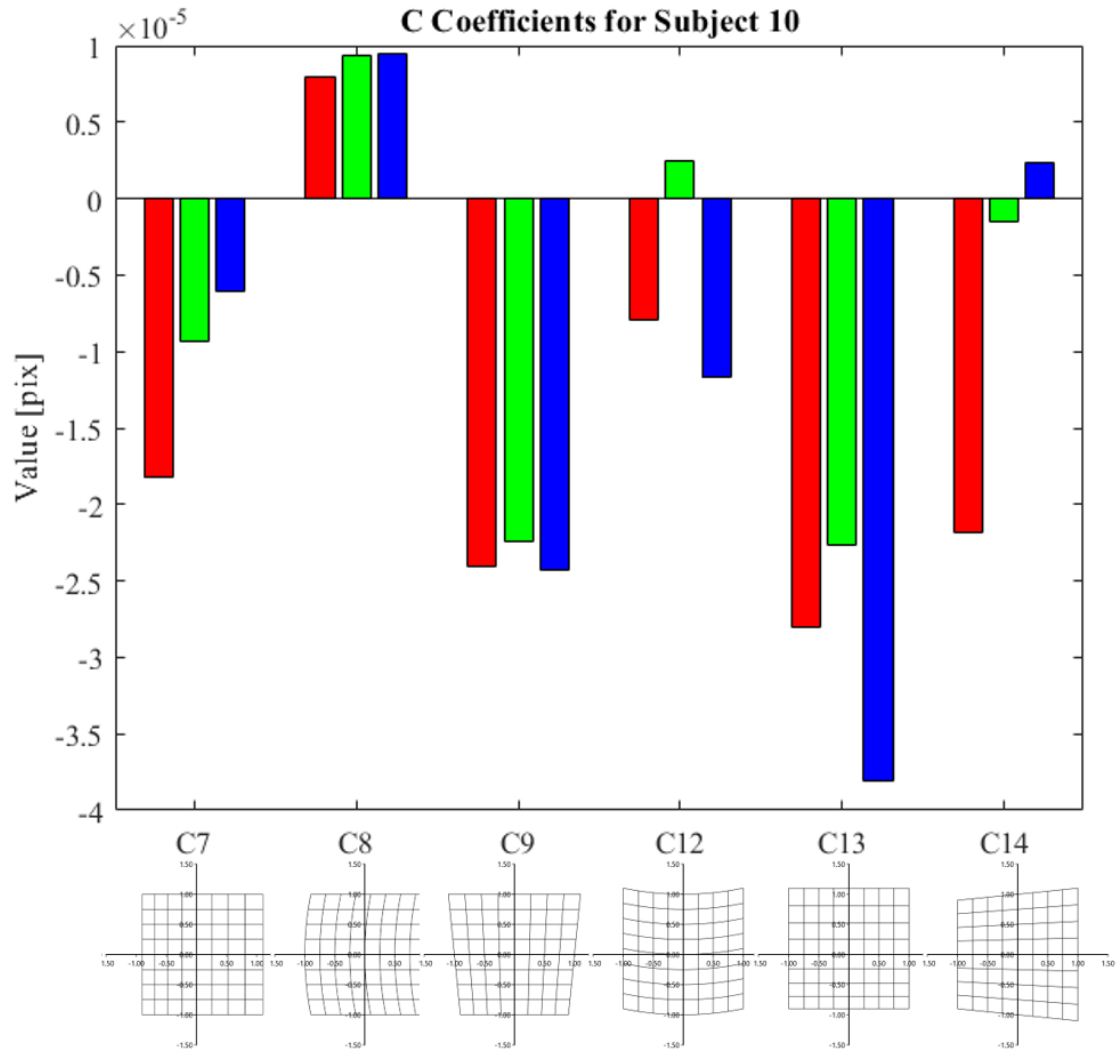


Figure 4- 15: Quadratic C coefficient values for subject 10. Fit values for (C_7, C_8, C_9, C_{13}) are stable and of reasonable magnitude for each processed image. Fit values for (C_{12}, C_{14}) are unstable in sign and magnitude, making them inconclusive representations of image distortion.

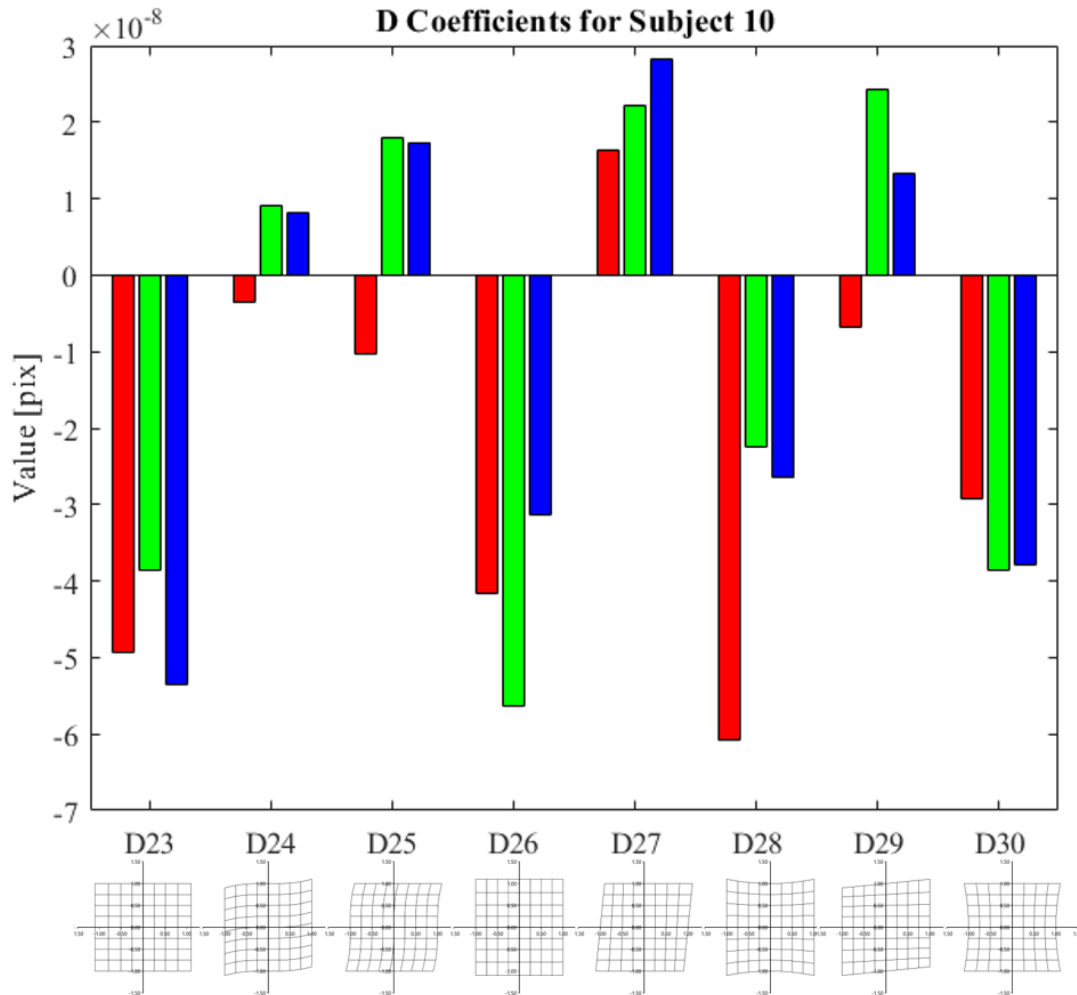


Figure 4- 16: Cubic D coefficient values for subject 10. Fit values for ($D_{23}, D_{26}, D_{27}, D_{28}, D_{30}$) are stable and of reasonable magnitude for each processed image. Fit values for (D_{24}, D_{25}, D_{29}) are unstable in sign and magnitude making them inconclusive representations of image distortion.

An important take away of Figures 4-14 to 4-16, is that over the three processed images, some coefficients flip sign or span zero. The trustworthiness of these coefficients at representing their corresponding distortion is therefore inconclusive. However, most coefficients appear to be stable across the three images, bringing confidence to the fitting as well as understanding ocular distortion through component distortion of complex nature. Appendix D contains a matrix for each human subject indicating whether a sign flip for a given coefficient was found. Obviously,

individuals with a high number of coefficient value flips would represent inconclusive or weak data.

From the three images processed for each subject, the mean and standard deviation of each coefficient was found. Mean values for each subject are plotted against their self-reported refractive error. Given the system sensitivity and low number of processed images, only four distortion terms related to building 3rd order Seidel radial distortion will be discussed in this chapter for the entire subject population. Appendix D contains all coefficient values plotted against refractive error. It should be noted that beyond the four terms discussed in this chapter, a few other distortion term values exhibited potential trends with respect to refractive error. The four terms related to 3rd order radial distortion ($D_{23}, D_{26}, D_{28}, D_{30}$) are shown in Figure 4-17 through 4-20 below.

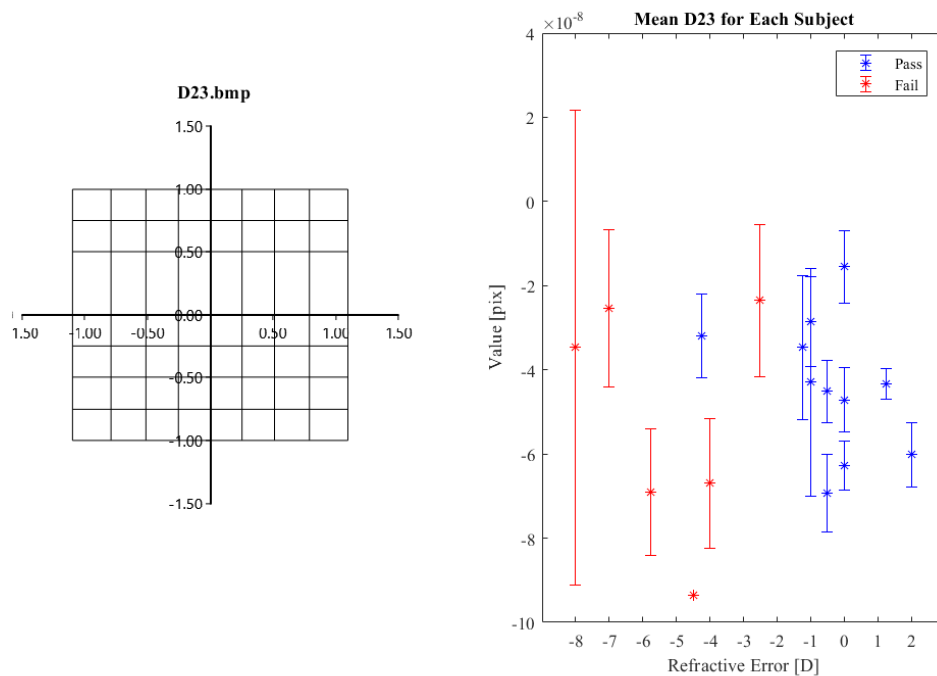


Figure 4- 17: An illustration of D_{23} (left) with the mean D_{23} value for each subject against refractive error (right). The red marks correspond to severely blurred or weak contrast dots on the retina and blue marks are well resolved dots. Error bars correspond to $\pm\sigma = 1$. While no global trend can be seen in the data, it appears that two groups form around separate values of D_{23} .

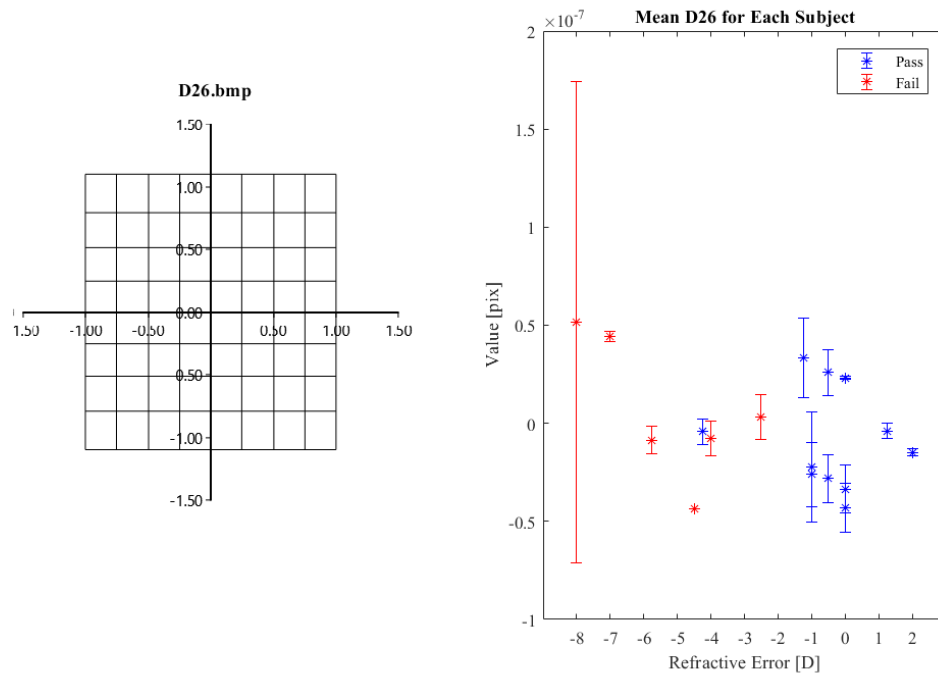


Figure 4- 18: An illustration of D_{26} (left) with the mean D_{26} value for each subject against refractive error (right). The red marks correspond to severely blurred or weak contrast dots on the retina and blue marks are well resolved dots. Error bars correspond to $\pm\sigma = 1$. No global trend is seen in the D_{26} data set as most of the values span zero.

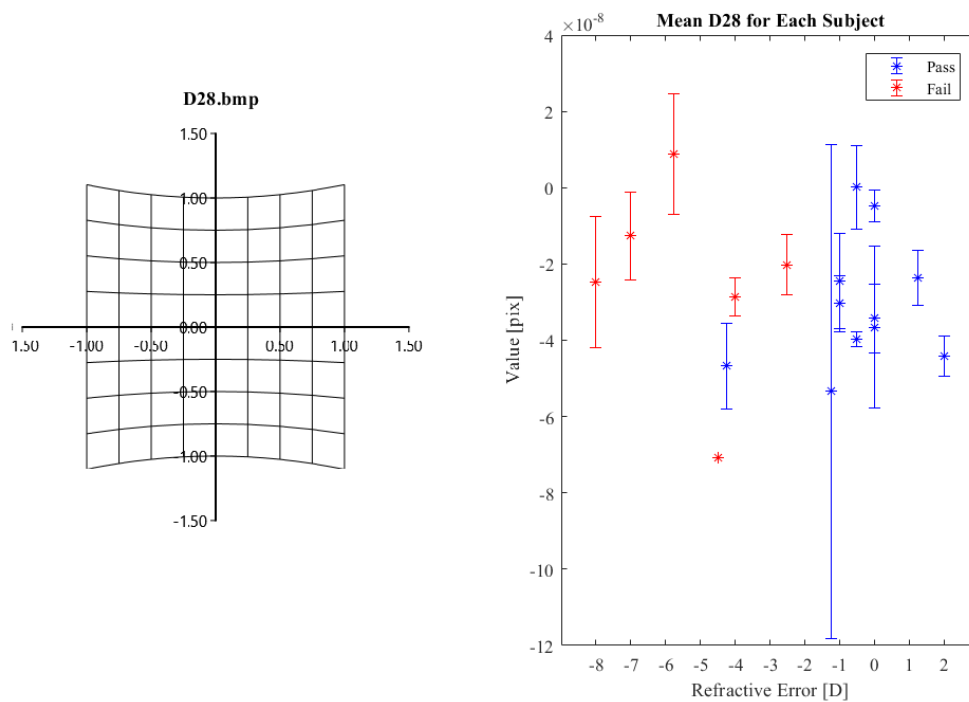


Figure 4- 19: An illustration of D_{28} (left) with the mean D_{28} value for each subject against refractive error (right). The red marks correspond to severely blurred or weak contrast dots on the retina and blue marks are well resolved dots. Error bars correspond to $\pm\sigma = 1$. No global trend is seen in the D_{28} data set.

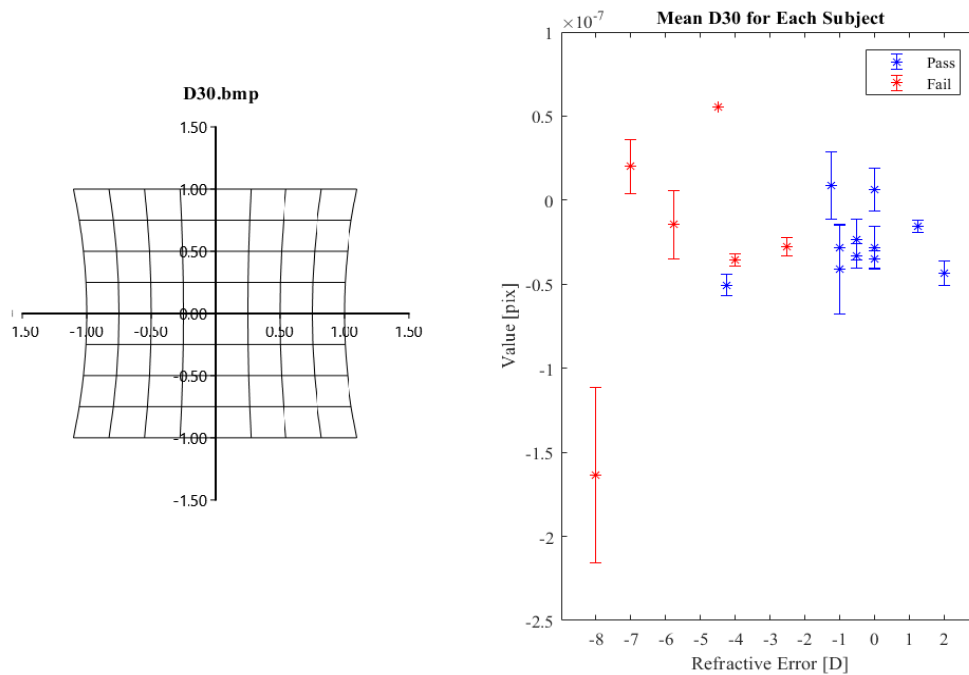


Figure 4- 20: An illustration of D_{30} (left) with the mean D_{30} value for each subject against refractive error (right). The red marks correspond to severely blurred or weak contrast dots on the retina and blue marks are well resolved dots. Error bars correspond to $\pm\sigma = 1$. No global trend appears for the D_{30} coefficient.

It appears that for the D_{26} and D_{28} coefficients that no significant trend occurs in the mean data set across the population. The D_{23} coefficients exhibits an interesting nature of two pooled value groups, one around $-3e^{-07}$ and another around $-6.5e^{-07}$. This distortion coefficient can be thought of as an increase in point spacing in the nasal-temporal meridian, where separation is largest at the maximum field extent. Determining the cause of the spread related to ocular parameters remains an open question at the time of writing. Lastly, D_{30} coefficients exhibit a grouping around a value of $-5e^{-08}$ which would suggest a population centered around some common level of barrel distortion in the nasal-temporal meridian.

The next logical step combines the four distortion terms above into a relative value of radial distortion. In most literature and in practice, radial distortion is calculated as a percentage in the form of a distance ratio of the residual movement. The distance from a center location to the nominal location of the maximum field point is compared to the distance from center of the distorted maximum field coordinate. Equation 4.2 below describes the formula used to calculate the percent distortion, where $r = \sqrt{x^2 - y^2}$.

$$\%D = \frac{r_{distorted} - r_{nominal}}{r_{nominal}} * 100 \quad 4.2$$

The nominal spacing for each run was used to build the nominal grid points. The mean of $(D_{23}, D_{26}, D_{28}, D_{30})$ was, according to the radial distortion metric detailed in Chapter 2, applied to the 4th order wavefront error equation with $(B_2 = B_3 = 1)$ and the nominal grid points as seed (x_o, y_o) coordinates. The maximum field coordinate along the diagonal of the square grid of points was used to calculate the radial distortion percentage. A plot of the mean percent distortion for the entire refractive population is shown in Figure 4-21 below along with the percent distortion found from the simulated population.

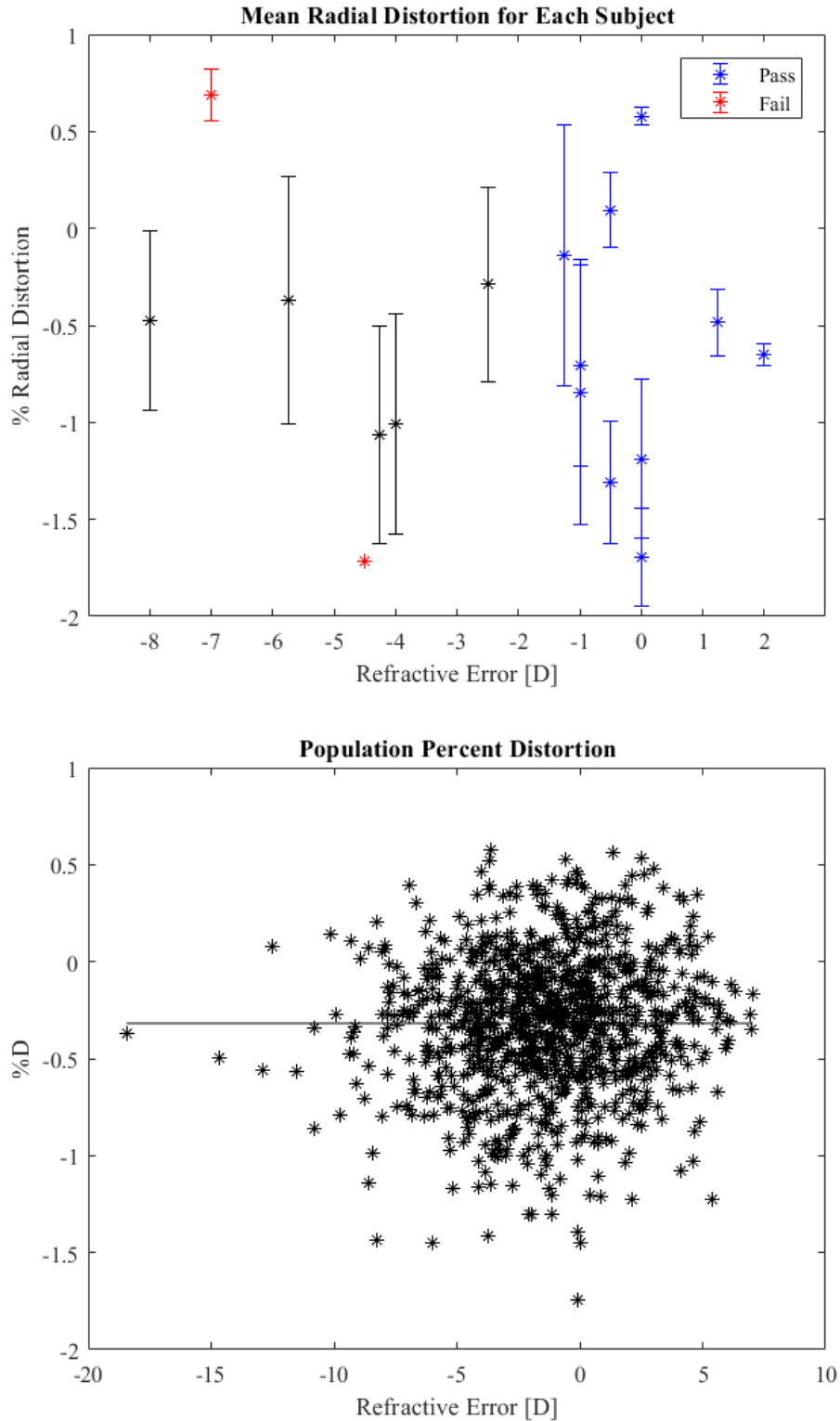


Figure 4- 21: Mean radial distortion as a percentage plotted against the subject refractive error (top) and the simulated population radial distortion plotted against the subject refractive error (bottom). For the human trials, the blue and red markings indicate strongly resolved and weak or blurred dot patterns respectively. The markers in black correspond to subjects who had one or more radial distortion coefficient values span zero, indicating inconclusive results.

The amount of radial distortion for the population appears to be around -0.5% barrel distortion after the 0.5% pincushion camera distortion offset is applied from calibration. Perhaps unsurprisingly, subjects who had one or more of their radial distortion terms be both positive and negative over the three processed images, were found in subjects of higher levels of myopia. The off the shelf camera configuration clearly has limitations in measuring ocular distortion for individuals of higher myopia. An encouraging sign is that the data set from the human trials appears to match that of the simulated population.

It is important to understand that the images processed, and the amount of radial distortion measured, is likely residual ocular distortion due to the imaging modality used in this body of work. The retina becomes a new intermediate object placed at infinity relative to the imaging arm of the fundus camera. Points are pre-distorted through the cornea and crystalline lens respectively before being projected onto the retina. The fundus camera imaging path, attempts to correct the retinal curvature for flat plane imaging by means of the aspheric objective. Therefore, the residual distortion patterns being imaged are most likely the remnants of the pre-distorted points locations and un-corrected retinal curvature from some base value.

Two new postulates can be raised from inspection of the radial distortion in Figure 4-21. First, it may be that the eye grows, reshaping ocular components, to reach zero radial distortion or some minute value of barrel distortion in older age. Given that humans see a 3D world in only 2D, perhaps a similar compensation to null distortion is occurring in the brain for flat plane imaging as this fundus camera system does, where distortion values slightly out of some threshold set into motion mechanisms for eye growth. Second, the influence of retinal curvature may play an important role in local distortion and visual perception. The variability of retinal curvatures

coupled with the variability in ocular components could be an indicator for the data spread seen in the emmetropic and hyperopic subjects. Perhaps, the size, shape, and spacing of ocular components for each individual needs to reach minimum level for that given individual. It may be the case that some individuals can tolerate higher or lower levels of ocular distortion without causing eye growth leading to refractive error development. Nevertheless, strong correlation between simulated ocular distortion and experimentally measured ocular distortion was found.

Fitting Error

To evaluate the effectiveness of least squares fitting of distortion points to the 4th order wavefront error function, RMS distance error was calculated for the fit points of all subjects. The 2nd order fit, rebuilds the distorted wavefront points using only the linear B coefficients and nominal grid point locations. The 3rd order fit and 4th order fit are found using the same procedure but with the quadratic C coefficients and cubic D coefficients respectively. The convergence of the fitting points to the processed distortion points can be seen graphically in Figures 4-22 through 4-24 below for a single subject on a single image.

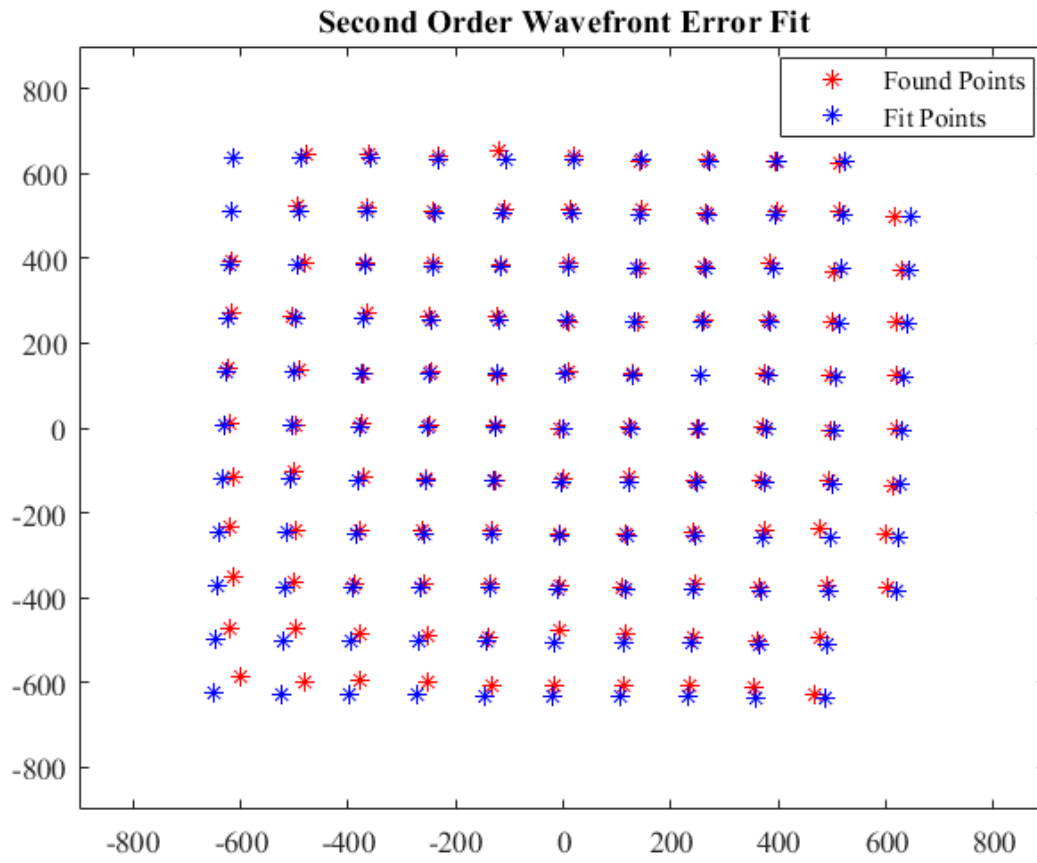


Figure 4- 22: 2nd order wavefront error point fitting. The 2nd order fit is successful at fitting most inner points but loses strength as field coordinates increase at the periphery.



Figure 4- 23: 3rd order wavefront error point fitting. The 3rd order fit is successful at fitting most field points but deviates at the very edge of the field. The mild barrel distortion remains uncaptured in the fitting at second order.

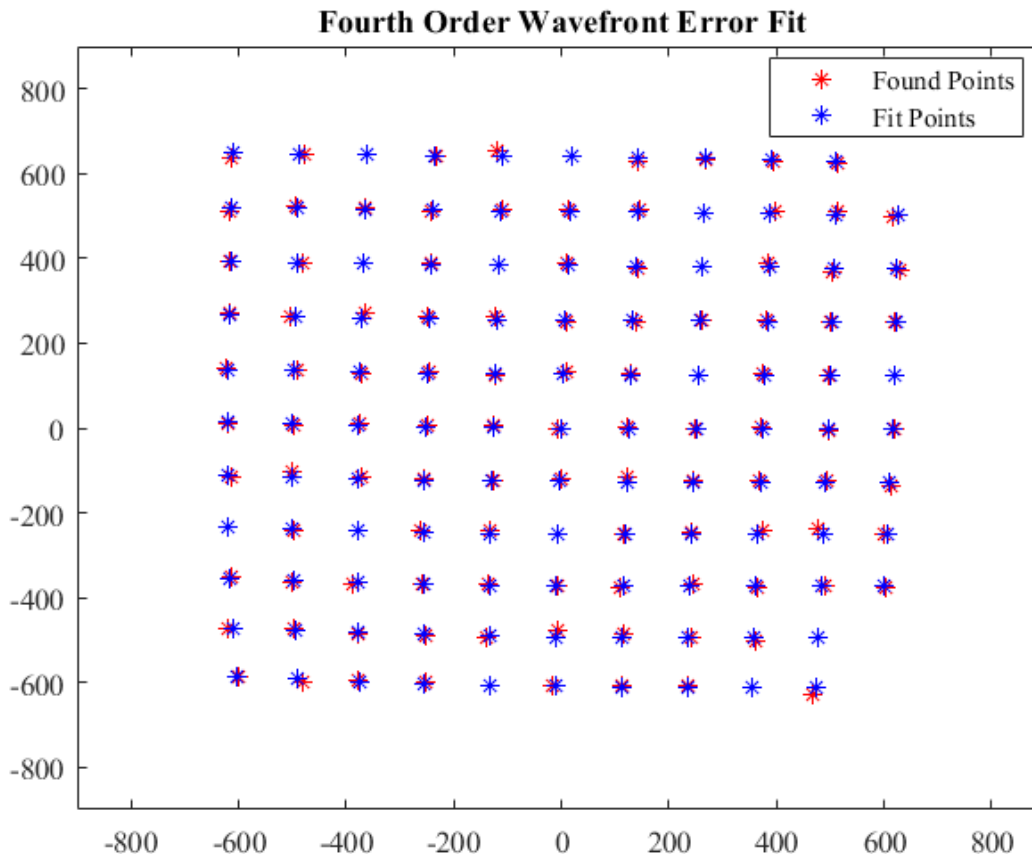


Figure 4- 24: 4th order wavefront error point fitting. The 4th order fit is successful at fitting almost all field points to the distortion pattern of the eye. Note that local variation and high frequency shifts are not captured by the 4th order fitting, suggesting higher orders may be needed in future work.

The convergence is quite strong at the 4th order wavefront error, leaving only higher frequency shifts present at certain field locations. This high order distortion is likely caused by local retinal curvature deviations and will be discussed further in Chapter 5. Though the representative coefficients for the 5th and 6th order wavefront error were calculated, it was discovered that the fitting was not numerically stable at these orders. Increasing the number of sampling points on the grid would potentially allow of numerical stability in the least squares fitting to higher orders, capturing the high frequency distortion. Transitioning to a normalized coordinate space may also improve numerical stability.

A numerical measure of fit was performed for all subjects related to the distance separation in pixels of fit points and distorted points. The residual distance between these two coordinates is reported as mean RMS error described by Equation 4.3 and shown graphically in Figure 4-25. All subjects monotonically decrease as fit order increases with some subjects fitting much stronger than others. The deviation between subjects is related to the uncertainty in determining dot location due to blurred or weak dots, low resolved distortion point count, or presence of high order distortion beyond the 4th order.

$$RMS \text{ Fit Error} = \sqrt{\frac{\sum \left(\sqrt{(x_{fit} - x_{distort})^2 + (y_{fit} - y_{distort})^2} \right)^2}{\# \text{ of points found}}} \quad 4.3$$

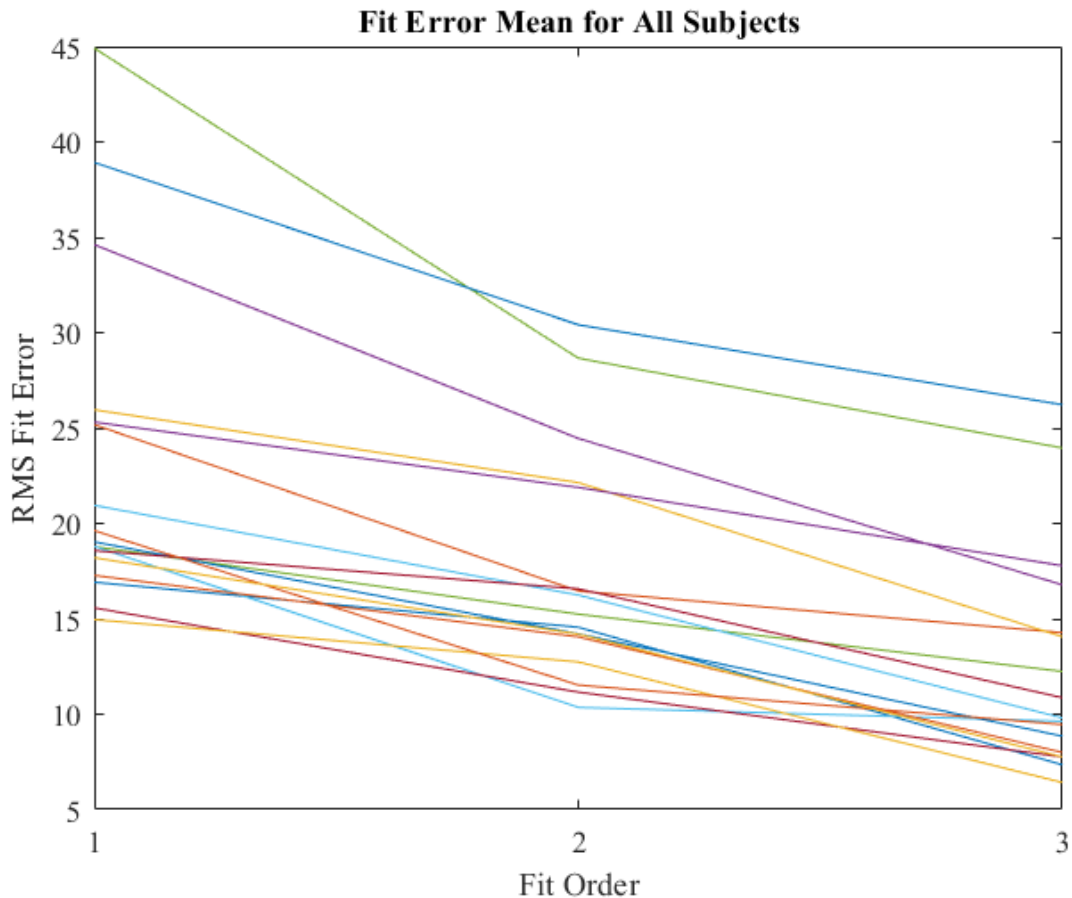


Figure 4- 25: Mean RMS Fit error for all subjects. All subjects see improved fitting out the 4th order wavefront error. Error units are in pixels. Larger error is attributed to weak dot contrast, low numbers of points found, and higher order distortion.

Ocular Distortion with Spectacles in Fundus Camera Imaging

One final test was run to understand the effect that a corrective modality, such as spectacle lenses, might have on the residual ocular distortion pattern. Subject 17 of this study had their eye measured using the modified fundus camera while leaving their corrective spectacle lenses on. A comparison of the fundus image with and without glassed is shown in Figure 4-26 below.

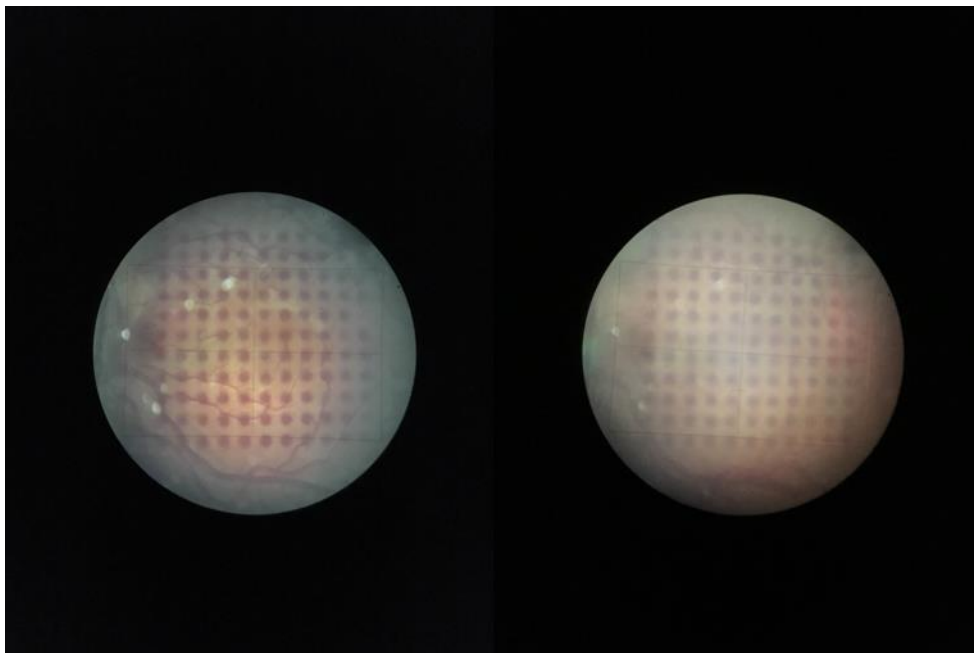


Figure 4- 26: Subject 17 without glasses (left) and with spectacles (right). Ignoring the tilt term, it is visibly apparent that the grid pattern under spectacles appears more barreled than without spectacles.

Running the same image capture and data processing scheme, three images were measured with spectacle lenses in place. A coefficient comparison, where the mean and standard deviation error bars for each coefficient are presented in Figures 4-27 to 4-29 below.

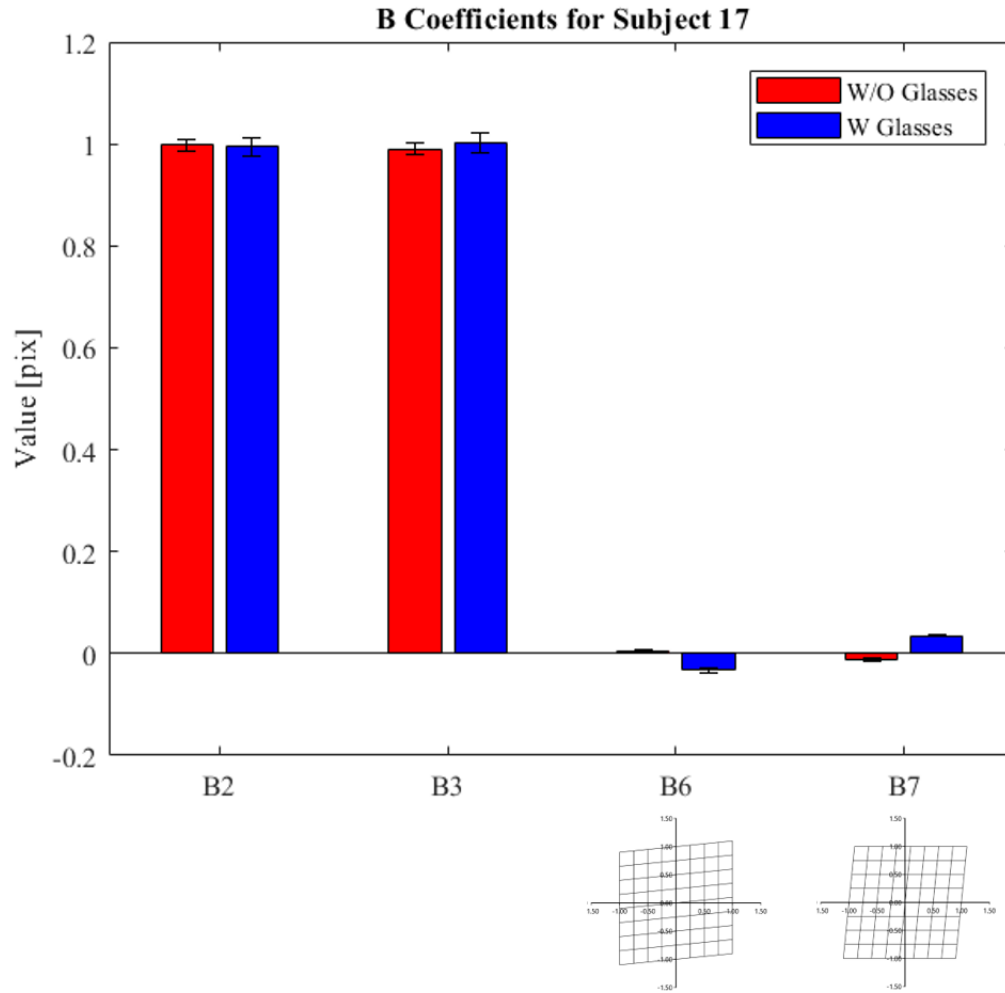


Figure 4- 27: Mean values for the linear B coefficient terms for subject 17 with and without spectacle lenses on. The skew values are off which is expected due to the visible grid pattern tilt.

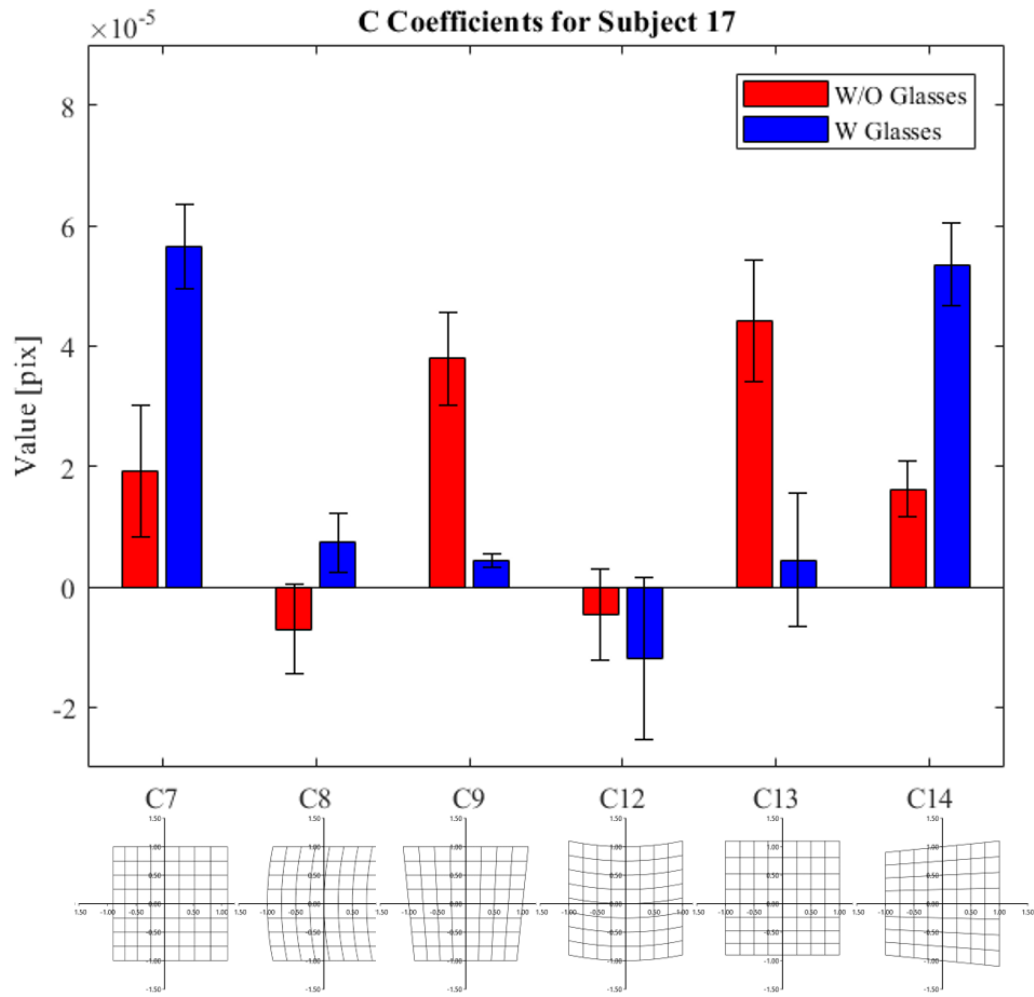


Figure 4- 28: Mean values for the quadratic C coefficient terms for subject 17, with and without spectacle lenses on. Values for $(C_7, C_9, C_{13}, C_{14})$ show significant changes in magnitude and C_8 shows a sign change.

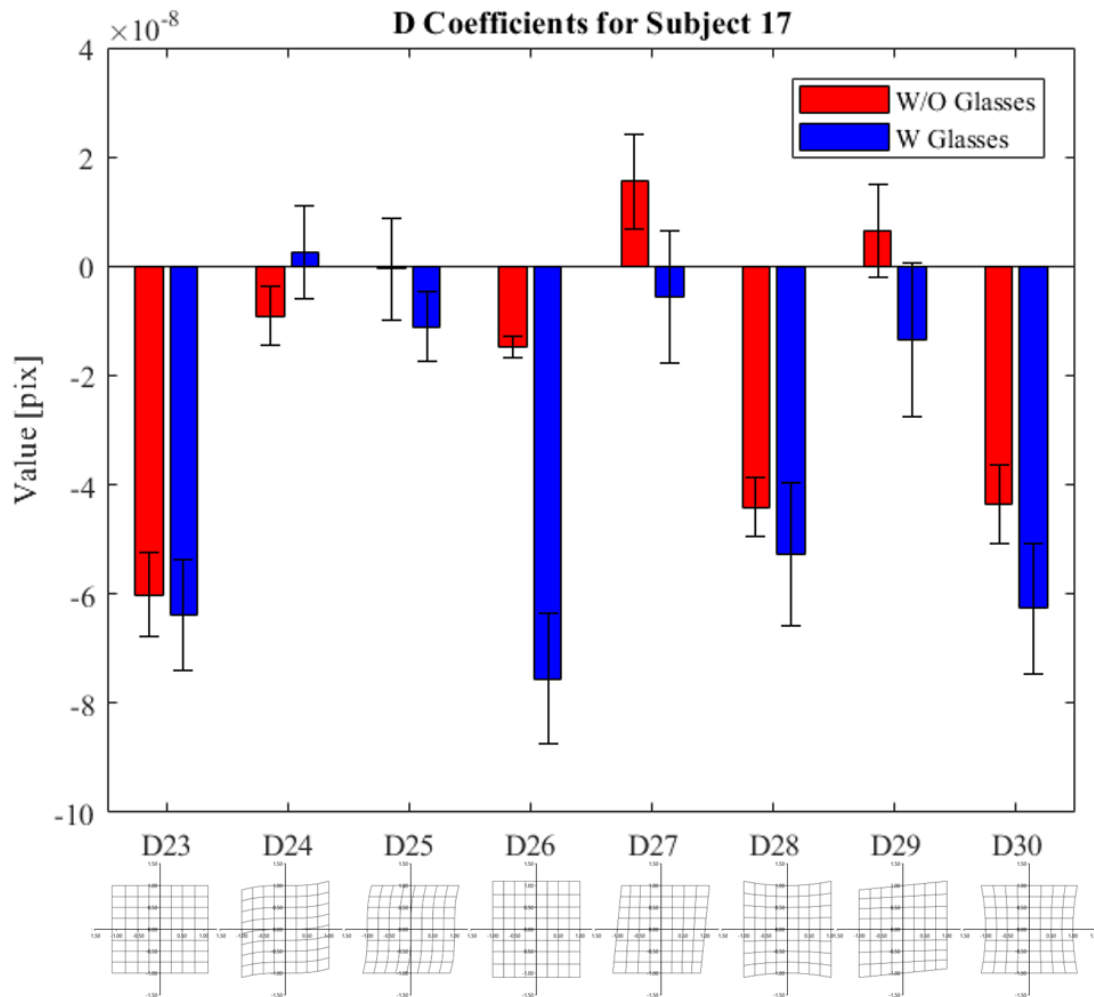


Figure 4- 29: Mean values for the cubic D coefficient terms for subject 17, with and without spectacle lenses on. The value for D_{26} and D_{25} showing a significant change in magnitude, with (D_{23}, D_{28}, D_{30}) values remaining within similar ranges. (D_{24}, D_{27}, D_{29}) all show a sign change.

It can be seen in Figures 4-27 through 4-29 that significant changes in coefficient magnitude and even in orientation occur when adding a refractive error correcting modality. The mean percent radial distortion without glasses for subject 17 was found to be $-1.15\% \pm 0.06$ but when spectacle lenses were added this value changed to a mean of $-2.21\% \pm 0.26$. The largest contributing factor to this is likely the change in magnitude seen in D_{26} . Given the results of this test, it may be possible that corrective modalities for refractive error indeed alter the amount of residual ocular distortion present in people, similar to effects seen in simulation. Further work

with more subjects and various corrective modalities will need to be investigated. This line of inquiry may be able to shed light on why certain corrective modalities inhibit further refractive error development once applied to a patient or why weak retardation on refractive error development occurs.

Summary

Relating back to the two proposed research questions, the fundus camera system was shown to repeatably place a target pattern on the back of the retina and have it imaged. It appears that the sample subjects from this human trial mostly exhibit mild barrel distortion under this imaging modality. Simulation and experimental results on the magnitude of ocular distortion appear to agree with one another. Distinguishing ocular distortion between various refractive error groups remains inconclusive at the time of writing. However, interesting variation between subjects can be seen and new postulates raised from this data set. It is likely that this off the shelf configuration generates errors at the signal level of detection for null ocular distortion. Improvements, sources of error, the influences of error on the data sets and other commentary is presented in Chapter 5 of this work.

Chapter 5: Error Analysis, Observations, and Future Work

Introduction

In this chapter, attention will be given to known errors in the fundus camera system related to measuring ocular distortion. Repurposing an “off-the-shelf” system to investigate a new property has advantages and disadvantages. It is important to understand what the physical limits in the measurement of ocular distortion are and if these limitations can be overcome in future works. Furthermore, discussion related to camera improvement, future studies and interesting observations will also be presented. Thus, the format of this chapter will focus on system error sources and effects, observations and commentary, and finally future improvements and research goals.

Camera Misalignment and Imaging Artifacts

Perhaps the largest source of error in this investigation is due to camera misalignment between the subject’s eye and the fundus camera. Several conditions lead to changes in the ocular distortion pattern or well-known imaging artifacts from fundus camera imaging. Most of these errors influence distortion measurements or reduce the confidence in data sets when processing retinal images. Examples and commentary will follow each of the topics.

One of the most common imaging artifacts seen in retinal images are flares of either blue or red light. The ideal imaging plane for the Gullstrand condition exists when the annulus of

illumination is located at the stop plane of the eye. However, small shifts around this plane can cause the above-mentioned flares in the retinal image. A blue flare occurs when the camera is too far away from the subject's eye and the red flare occurs when the camera is too close to the subject's eye, considered the Z direction of the optical system. These color patches arise from dispersion in the cornea from the inner band of light on the annulus. Imaging examples of these two errors are shown in Figure 5-1 below. Usually, these two artifacts serve as an alignment tool for the operator to move the camera system into the correct plane, but in cases of weak mydriasis or uniquely shaped corneas, removal of this artifact may not be possible. The major concern of this error is the occlusion of the target pattern in image processing, while other aberration effects may be present due to the Z displacement.

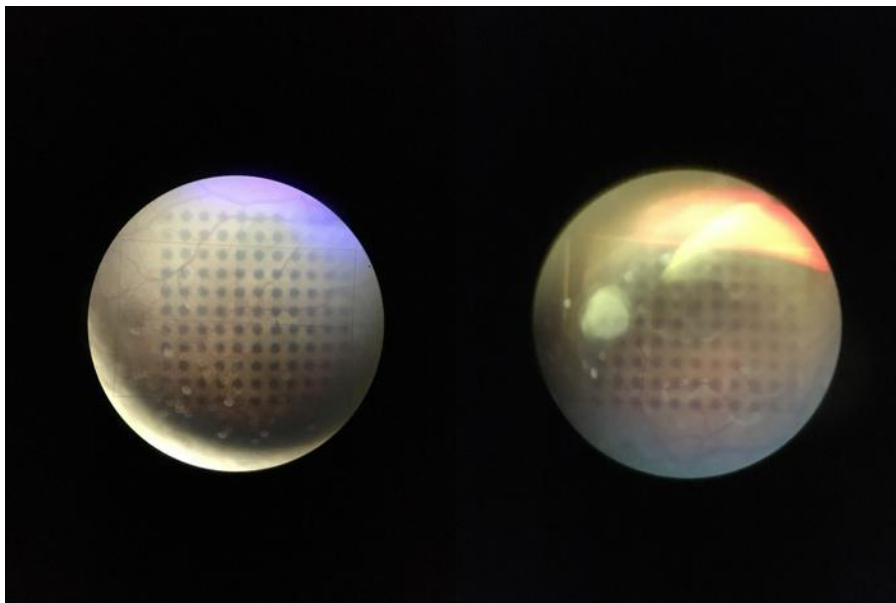


Figure 5- 1: Examples of corneal dispersion effects in fundus imaging. Blue flare (left) occurs when the camera and eye separation is too large. Red flare (right) occurs when the camera and eye separation is too small.

Another common alignment error seen in the retinal images is vignetting from the iris or the aspheric objective. In rare cases, the aspheric objective can become tilted relative to the optical axis of the imaging path of the fundus camera. Six screw pins create the aligning mechanism for

the aspheric objective that sits in a contained housing that can be threaded on and off the camera face. Cleaning of the front surface of the objective may be necessary and the insertion back onto the camera after cleaning can lead to this tilt. The vignetting by the iris is usually due to weak mydriasis or exposure to ambient light sources during imaging. A greenish-blue haze appears on the side or edge where the vignetting occurs. Eye shape and sensitivity to the dilating drop also play a role in the stop response of the iris during imaging. In the small cohort human trial, it was challenging to avoid these errors. Both cases of vignetting likely cause a shift to the distortion pattern, represented as skew or some version of keystone distortion. In either case, altered distortion of the target points would yield misinformation when considering all the of the independent distortion terms. Figure 5-2 shows an example of each of these vignetting cases.

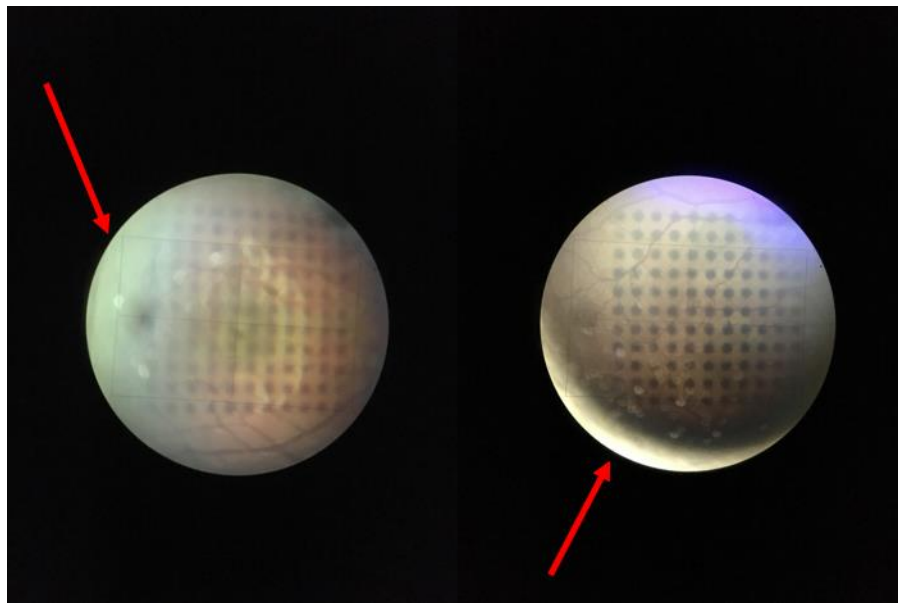


Figure 5- 2: Vignetting caused by the iris (left) and aspheric objective vignetting or tilt (right) in human subject imaging. Red arrows indicate the vignetting areas in both cases. Occlusion of target dots as well as pattern shifting are primary concerns for this error.

The major misalignment error found in this imaging technique is most likely related to pupil aberrations. Given that two optical systems are being coupled together to both illuminate and

image, it would be reasonable to suggest that pupil aberrations were present and mixed with imaging aberrations in the retinal images. Pupil aberrations arise when the exit pupil of one optical system has a third order misalignment with the entrance pupil of another optical system [151]. The beam deformation due to these pupil aberrations can cause a pre-distortion of the target point before striking the retina or create a displacement of the target points at the image plane. Without knowledge of the camera lens components, simulation could not be done to investigate the effects of pupil aberration and limitation in camera system modification would make control over these aberrations challenging.

However, when attempting to calibrate the system with a crude eye model, the first indication of target pattern influence due to misalignment or pupil aberrations was uncovered. Subsequent testing in the human eye confirmed similar pattern influence was observed with misaligning the camera system with respect to the stop. Lateral displacement of the camera from the center of the stop induces significant keystone distortion along with vignetting. The amount of displacement needed to see this effect is approximately 2-3 mm. In most cases, the operator can see and undo the influence of this misalignment, but eye or head shifts from the subject can cause the same misalignment. Example images for this lateral displacement error are shown in Figure 5-3.

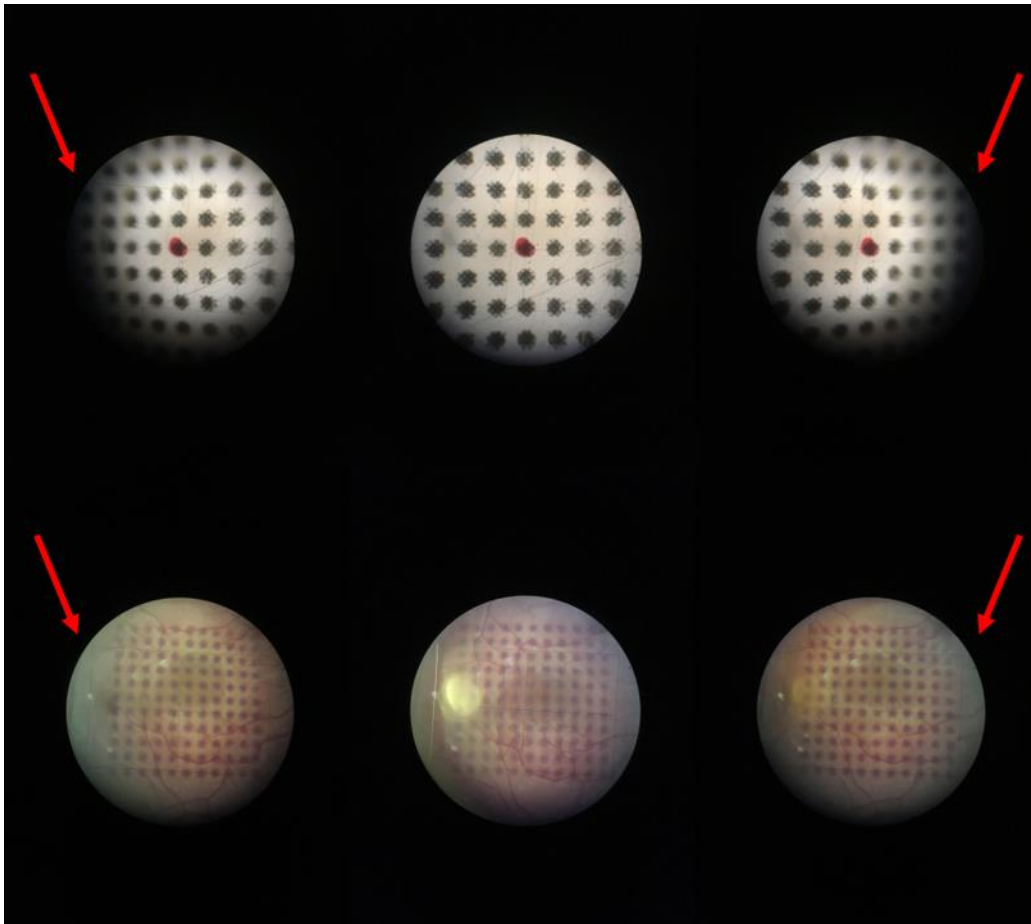


Figure 5- 3: Lateral misalignment with respect to the eye stop causes keystone distortion. Example images for the calibration system (top) and in a human subject (bottom). Notice in the human subject that the corner opposite the vignetting side appears to pinch and blur.

Since the observed shift in the pattern was so strong and understanding that in an imaging session, this is a realistic error to occur, a test was run on the calibration images to see the effect of this misalignment on the distortion coefficients after image processing. A centrally aligned image as well as a left and right laterally decentered image were processed from the calibration crude eye model photos along with a human example. The two human images from 5-3 were processed and compared to a centrally aligned image for the same subject as reported in Chapter 4. Only the 4th order distortion coefficients are shown for the calibration and human misalignment tests.

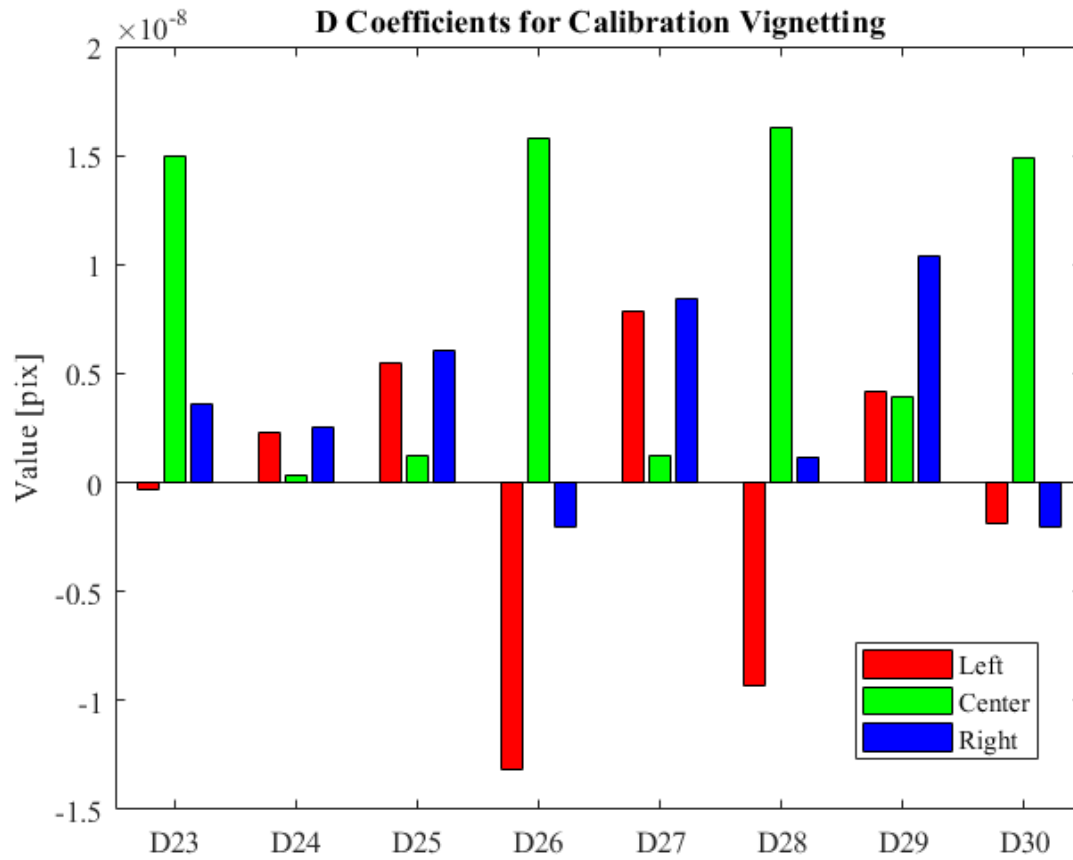


Figure 5- 4: 4th order distortion coefficient values for a camera displacement to the left of the eye stop (red), to the right of the eye stop (blue) and in a centrally aligned situation (green) for the imaging path calibration configuration. There is a significant increase in coefficient magnitude or in sign for the left and right displacements.

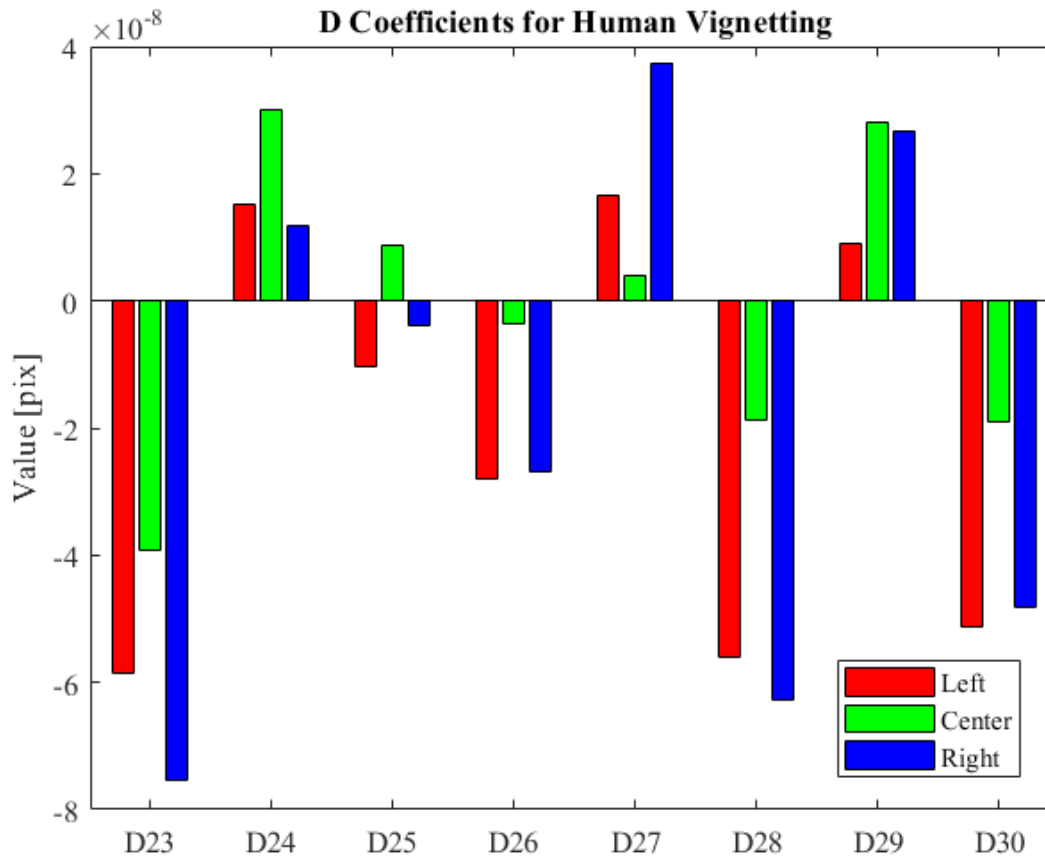


Figure 5- 5: 4th order distortion coefficient values for a camera displacement to the left of the eye stop (red), to the right of the eye stop (blue) and in a centrally aligned situation (green) for a human test subject. Again, there is a significant increase in coefficient magnitude or in sign for the left and right displacements.

Figure 5-4 and Figure 5-5 demonstrate that this misalignment error significantly changes the coefficient values found in fitting. When calculating the radial percent distortion for each of the three human cases, the values were found to be -2.21%, -0.92%, and -2.24% for the left, center, and right processed images respectively. The misalignment error appears to drive the converted radial distortion towards a more barrel value. The conclusion from this test must be that the addition of pupil aberration in the image distortion pattern increases the magnitude of radial percent distortion and increases the spread of values seen in the mean radial distortion for the human trial population (Figure 4-21). It should be noted that these processed cases for the

calibration path and in a human subject are drastic cases of misalignment but still any alignment errors or introduction of pupil aberration will affect the measured coefficients. This influence is likely present in the data sets presented in Chapter 4 and must be addressed in future work.

Pass Fail Criterion for Blurred or Weak Target Dots

As mentioned in Chapter 4, a pass/fail criterion was created separate data sets from individuals with high contrast and well resolved target patterns from individuals without. Most of the subjects that exhibited challenges in processing centroids were of the moderate to high myopic refractive error group. The pass/fail determination was a subjective measure of the three processing candidate images. While this subjective analysis of images was important to understand the strength of processing for each subject, some interesting variations between refractive errors emerged.

For example, two subjects with approximately the same self-reported refractive error of -4 D showed very different retinal dot patterns. Figure 5-6 below shows the candidate who passed the visual inspection on the left and one with the same refractive error who failed on the right. Two postulates can be raised from this example regarding refractive error and resolving ocular distortion targets. First, it may be possible that two people may have very similar on-axis refractive error, but their retinal shapes may differ such as variable mean curvatures along eye meridians or different order of asphericity. The ellipsoid shape of the eye may be significantly different in the two cases and balancing off-axis astigmatism and field curvature by the aspheric objective becomes too challenging. Second, the shape or spacing of the cornea or crystalline lens may vary between the two subjects causing the same difficulties in image quality for the target

dot pattern. More subject samples across all refractive errors would help to better understand this phenomenon.

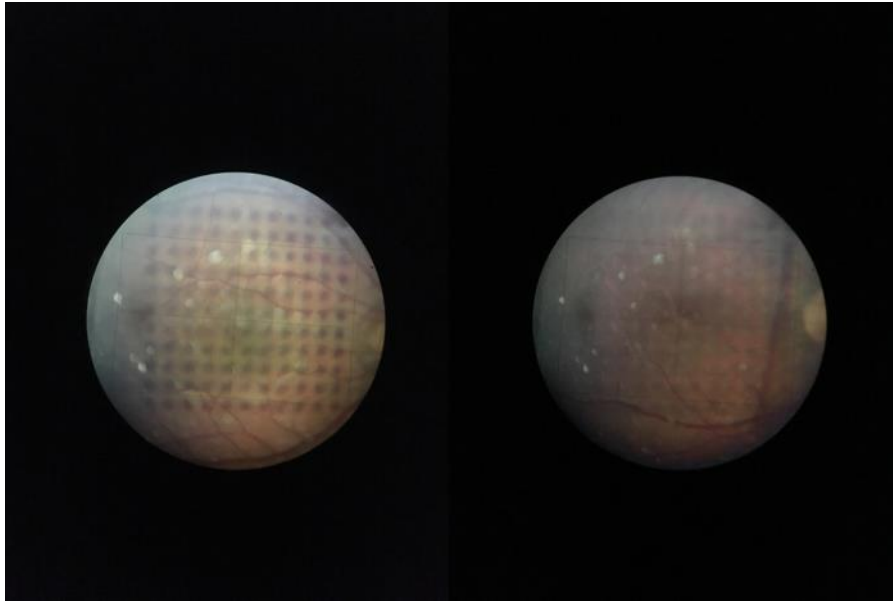


Figure 5- 6: Retinal images for two subjects with -4 D reported refractive error. The subject of the left passed the visual inspection test for well resolved target dots and the subject on the left failed this inspection due to weak contrast and blurred dots.

Dot Deviation Around Retinal Structures

In review of all subject retinal images, there were a few instances of interesting target deformations that raised questions regarding their origin. One deformation pattern that stood out were center collapsing grid points near the optical axis of the eye and camera system. High contrast and well resolved dots could be seen in the periphery of the target and retina while the central region experienced highly eroded target dots that seemed to collapse inward. The deviations seen in these subjects are quite abrupt and suggest a strong local deformation region. These deviations may be due to the foveal depression of the eye. Another intriguing deformation

lends weight to the ideal of strong local deformation sites when it was observed that for some subjects, the target dots would deform along the shape of a blood vessel.

Figure 5-7 shows an image of blood vessel spot deformation and Figure 5-8 shows two cases of central blur and deformation with strong periphery dots. In the case of central collapsing dots, this would obviously affect the central spacing metric used to determine the nominal grid points when running coefficient fitting. But this observation may have other implications as well. While yet unverified, these local deformation sites could be related to strong curvature deformation areas on the retina. Perhaps large blood vessels, strong pressure or other ocular anomalies create local deformations or stressors, similar to mounting structures imparting aberrations on optical components. A higher density target may show fine retinal structure detail if applied in this manner. With a more densely sampled grid target the possibility of measuring local retinal curvature may be possible.



Figure 5- 7: Target dot deformation around blood vessels. Dots appears to move with the meander of blood vessels in the red circled areas. Local curvature departures are the proposed cause.

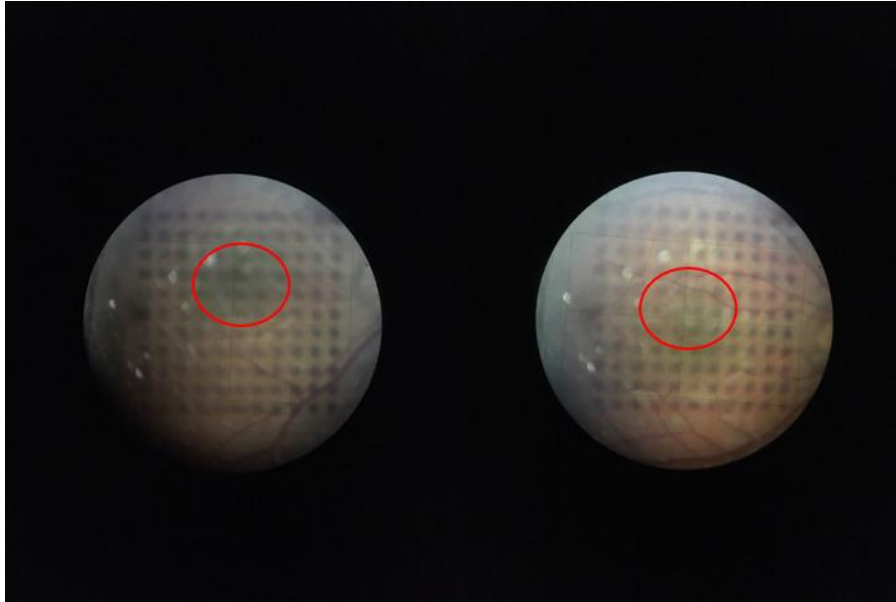


Figure 5- 8: Examples of central region dot blurring and deformation. Strong local curvature, foveal depression or perhaps strong corneal keratoconus may be responsible for these pattern deformations.

The remainder of this chapter will discuss future work and potential system improvements for a second-generation fundus camera system. A summary statement of the entire dissertation work is provided at the end of the chapter.

Fundus Camera Reverse Engineer and Second-Generation Camera

The first step toward improving the current modified fundus camera system is to reverse engineer as much of the current system as possible. Since the aspheric objective can be removed from its housing, several metrology techniques could be applied to the front and back surfaces to determine their lens prescriptions. Profilometry, coordinate measuring machine (CMM) data and Fizeau interferometer data, if the asphericity is low, can all be collected to build surface maps of the ophthalmic objective. The goal in reverse engineering the camera system would be to update the simulation software with the entire array of lens elements from illumination to imaging to verify experimental results. Furthermore, the field flattening nature of the ophthalmic objective

can be compared to the ocular distortion metric used in the simulation work. It shall be noted here that improvement to eye model simulation can also be achieved. Moving the eye model to a rotationally non-symmetric system where the retinal surface is deformed and investigating eye rotation, accommodation and corneal blink deformation would further strengthen simulation results. The ocular distortion metric would inevitably be improved or found to be inadequate with increased complexity.

Following the simulation and modeling of the current camera system, new areas to improve ocular distortion measurements in fundus camera imaging can be explored. For example, there may be a more ideal lens prescription for the ophthalmic objective or additional components that mitigate high order aberration such as off-axis astigmatism. The camera system can also be designed to reduce or eliminate inherent distortion found in either the illumination or imaging path of the camera. Efforts to understand how target plane location, conjugate to the retinal surface are affected by target translation or with refractive power of the subject. Optimal placement of the grid target can be modeled and achieved in simulation. Lastly, aberration control throughout the system needs to be investigated with respect to ocular distortion. All of the above design considerations should lead to significant system improvement for understanding ocular distortion measurements in a second-generation camera system.

Variable Intermediate Apertures for Field Curvature Control

If varied retinal curvature in meridians of the eye or different levels of asphericity of the retina contribute to eroded target patterns, then intermediate apertures could help to reduce these poor imaging conditions. Placing a variable diameter aperture inside the camera system, most likely at

the holed mirror location, could provide further control of field curvature or field flattening for large field coordinates leaving the retina. Images could be swept with several aperture diameters to create high contrast well resolved target images for a variety of refractive errors and field points.

Alternative Measurement Configurations

The fundus camera configuration allows for convenient target projection and image capture in a well understood system. This however, is just one potential configuration to measure ocular distortion. Fundamentally, this body of work proves that the process of projecting a target onto an ocular surface, imaging the resultant pattern, and post processing the image leads to useful information related to ocular distortion. Applying this process to another imaging modality loses no generality in measuring ocular distortion, rather the metric used to characterize the ocular distortion would likely change. This could lead to new areas of insight between distortion and the human eye.

One such suggestion would be the use of a scanning method. Scanning systems exist where a beam is scanned over the surface of the retina in a raster pattern. By modulating the beam at certain positions in the scanning cycle, one could conceivably measure ocular distortion. For example, if the beam is turned off when scanning over known grid positions and back on for regions not on the grid, then the resulting raster image will appear to have the projected target superimposed on the retinal surface. A scanning method would create the known grid pattern point by point during the scan and record the deviation of each point on the retina to build the

ocular distortion map. Extensions, as seen in this example, make the measurement of ocular distortion a rich environment for imaging with various alternative configurations.

Software Guided Alignment Assistance with Eye Tracking

One of the largest errors experienced in human imaging comes from camera and eye misalignment. Modifying a second-generation camera system with a more robust alignment package would be of great interest. Placing a minimally invasive eye tracking camera setup on the front of the system would be a reasonable first step. Using near infrared (NIR) radiation, the pupil of the eye can be monitored, and the center of the pupil tracked using the starburst method as one example of many eye tracking techniques. Capturing the eye in the NIR provides a nice high contrast pupil boundary for image processing while also minimizing ambient light noise during fundus imaging. Tracking pupil gaze direction would allow for some eye orientation information and consequently retinal area information.

The next implementation to an alignment system would monitor the fundus camera body location relative to the head or chin rest position. Monitoring relative distance away from these fixed datums provides useful 3D spatial information of the camera pointing direction relative to gaze direction. Using a model eye on a laboratory bench, the system could be calibrated with a known grid target pattern projected onto the retinal model eye. Translation stages and rotation stages placed at the center of rotation of the model eye could then displace the model eye in varying degrees while images of the target pattern are captured. After several runs, a database of ocular distortion images could be captured and in human imaging, the database can be accessed to correlate live images with eye model patterns. When the camera system identifies forms that

are likely due to misalignment, image capture functionality can be turned off to reduce the number of problematic or high error distortion patterns, flagged in the data set or have a compensating mechanism which drives the system back into alignment.

Finally, auto detection suites can be implemented to capture and identify retinal features. By identifying retinal features such as blood vessels, the camera system can autofocus to ensure that image capture of the retinal surface is always well resolved. Tracking of these features can also ensure alignment by tracking the movement of features between subsequent images. If the eye rotates too far, or the head shifts during imaging, the software could flag images taken during these large movements or stop image capture functionality. These improvements would update the current camera system toward a more modern fundus camera configuration.

Image Processing Improvements

Several upgrades to the image processing package used to find target centroids or marker areas can be introduced in future work. After design modifications are in place and target patterns become more readily resolved, intensity based centroid fitting can be implemented. This feature would sift the local area around a potential target center and use the available image intensity information to center the selected center location based on the mean intensity. Allowing for automated dot detection to remove the human component of center selection is desired in for both accuracy and speed improvements.

More complicated automatic detection schemes for target fiducials can be implemented.

Currently, the complex Fourier filter implemented in the software varies three parameters of a Fourier mask. More robust Fourier masks can be achieved that capture a higher percentage of

target dots by removing more spatial frequency noise from retinal structures and mismatched intensity. Lastly, iterative minimization techniques in coefficient fitting can be introduced. Currently, the least squares fit is run a single time to calculate distortion coefficients. New point fitting criterion with iteratively updated error minimization could serve to reduce fitting error while capturing the higher frequency distortion information seen in some of the retinal images.

Expanded Human Trials and Relationship to Refractive Error

The small cohort human trial served a vital role in this investigatory work related to the measurement of ocular distortion. However, the relationship to refractive error was not well understood from this small study. After improving the system error and better understanding the fundus imaging technique for ocular distortion, new larger human subject trials would be desired. The first and most simple test would be to again measure the general population for mean radial ocular distortion. One major improvement to a cohort study would be to collect biometry data for each subject before the measurement such as autorefractometer data for accurate refractive error measurements. More complex data such as corneal topography, retinal curvature or crystalline lens curvature could be coupled to simulation for improved post-processing and analysis. Adding statistical strength through a larger cohort would allow for more confident analysis of population distortion.

The original motivation for this work was to investigate whether ocular distortion played a role in refractive error development. Therefore, a future cohort study of young children could glean information on how ocular distortion presents itself in a young eye and by tracking children over a course of a few years, how ocular distortion changes with eye growth. It is possible that the

small cohort population and simulation population, built from adult biometric data, shows the result of years of eye growth on the measured ocular distortion value. For young children, the growing and malleable eye may present very different insights on how ocular distortion evolves. This study coupled with previous literature reviews of myopic progression or refractive error development could breach new insight into the mechanisms underlying human eye growth.

A continuation on the young child cohort study would be the investigation of several myopic control modalities and their effects on ocular distortion. While early simulation results suggest certain trends in ocular distortion with respect to refractive error for various correction modalities, measuring the advance or suppression of refractive error development is desired. Evaluating children who stop progressing toward myopia or hyperopia and looking at the modality with ocular distortion measurements, may provide insight as to why certain modalities are more effective at stopping refractive error development than others. Extension to eye growth mechanisms could also be inferred from such a study.

Conclusion

Motivation for characterizing and measuring ocular distortion was born from interest in understanding the causes myopic progression and refractive error development in the human population. A new imaging system was proposed to measure the amount of ocular distortion present in the human eye. Two scientific research goals were laid out at the beginning of this work. The first goal asked if it was possible to repeatably place a known target on the back of the retina that could be imaged on a detector. The second goal asked whether there was a

relationship between the refractive error and the amount or type of ocular distortion in the human eye.

This body of work demonstrates a proof of concept imaging system for ocular distortion that can repeatably image a target pattern on the retina of the human eye. No apparent trend related to ocular distortion and refractive error was seen from a small human cohort. Simulation work of a random population of model eyes and mean radial percent distortion suggest that the human population has a small variability in ocular distortion magnitude with a tendency to be slightly barrel distorted for all refractive errors. Visual inspection of retinal images shows high variability in subjects of different refractive errors. Analysis of simulation and human trial data suggest two new research postulates for future research efforts, justified by the variability in ocular distortion across the population. These postulates suggest that in older age, given a unique set of ocular lens components, the human eye tries to minimize ocular distortion to a value of zero or that there is a minimum tolerable level of ocular distortion, specific to the optical configuration of an individual's eye. Refractive error development and myopic progression remain active areas of research and the relationship with ocular distortion may yield new insights on understanding or controlling eye growth in the human population.

Appendix A: Fifth and Sixth Order Wavefront Expansion

The following are the 5th and 6th order wavefront expressions, expanded from Barakat and Houston. Applying the derivative with respect to the direction cosines (p, q) and grouping terms that depend only on (x_o, y_o) will yield the higher order distortion terms for a rotationally non-symmetric system.

$$\begin{aligned}
 W^5 = & E_1p^5 + E_2p^4q + E_3p^3q^2 + E_4p^2q^3 + E_5pq^4 + E_6q^5 + E_7p^4x_o + E_8p^3qx_o + E_9p^2q^2x_o \\
 & + E_{10}pq^3x_o + E_{11}q^4x_o + E_{12}p^3x_o^2 + E_{13}p^2qx_o^2 + E_{14}pq^2x_o^2 + E_{15}q^3x_o^2 \\
 & + E_{16}p^2x_o^3 + E_{17}pqx_o^3 + E_{18}q^2x_o^3 + E_{19}px_o^4 + E_{20}qx_o^4 + E_{21}x_o^5 + E_{22}p^4y_o \\
 & + E_{23}p^3qy_o + E_{24}p^2q^2y_o + E_{25}pq^3y_o + E_{26}q^4y_o + E_{27}p^3x_oy_o + E_{28}p^2qx_oy_o \\
 & + E_{29}pq^2x_oy_o + E_{30}q^3x_oy_o + E_{31}p^2x_o^2y_o + E_{32}pqx_o^2y_o + E_{33}q^2x_o^2y_o \\
 & + E_{34}px_o^3y_o + E_{35}qx_o^3y_o + E_{36}x_o^4y_o + E_{37}p^3y_o^2 + E_{38}p^2qy_o^2 + E_{39}pq^2y_o^2 \\
 & + E_{40}q^3y_o^2 + E_{41}p^2x_oy_o^2 + E_{42}pqx_oy_o^2 + E_{43}q^2x_oy_o^2 + E_{44}px_o^2y_o^2 + E_{45}qx_o^2y_o^2 \\
 & + E_{46}x_o^3y_o^2 + E_{47}p^2y_o^3 + E_{48}pqy_o^3 + E_{49}q^2y_o^3 + E_{50}px_oy_o^3 + E_{51}qx_oy_o^3 \\
 & + E_{52}x_o^2y_o^3 + E_{53}py_o^4 + E_{54}qy_o^4 + E_{55}x_oy_o^4 + E_{56}y_o^5
 \end{aligned}$$

$$\begin{aligned}
 W^6 = & F_1p^6 + F_2p^5q + F_3p^4q^2 + F_4p^3q^3 + F_5p^2q^4 + F_6pq^5 + F_7q^6 + F_8p^5x_o + F_9p^4qx_o \\
 & + F_{10}p^3q^2x_o + F_{11}p^2q^3x_o + F_{12}pq^4x_o + F_{13}q^5x_o + F_{14}p^4x_o^2 + F_{15}p^3qx_o^2 \\
 & + F_{16}p^2q^2x_o^2 + F_{17}pq^3x_o^2 + F_{18}q^4x_o^2 + F_{19}p^3x_o^3 + F_{20}p^2qx_o^3 + F_{21}pq^2x_o^3 \\
 & + F_{22}q^3x_o^3 + F_{23}p^2x_o^4 + F_{24}pqx_o^4 + F_{25}q^2x_o^4 + F_{26}px_o^5 + F_{27}qx_o^5 + F_{28}x_o^6 \\
 & + F_{29}p^5y_o + F_{30}p^4qy_o + F_{31}p^3q^2y_o + F_{32}p^2q^3y_o + F_{33}pq^4y_o + F_{34}q^5y_o \\
 & + F_{35}p^4x_oy_o + F_{36}p^3qx_oy_o + F_{37}p^2q^2x_oy_o + F_{38}pq^3x_oy_o + F_{39}q^4x_oy_o \\
 & + F_{40}p^3x_o^2y_o + F_{41}p^2qx_o^2y_o + F_{42}pq^2x_o^2y_o + F_{43}q^3x_o^2y_o + F_{44}p^2x_o^3y_o \\
 & + F_{45}pqx_o^3y_o + F_{46}q^2x_o^3y_o + F_{47}px_o^4y_o + F_{48}qx_o^4y_o + F_{49}x_o^5y_o + F_{50}p^4y_o^2 \\
 & + F_{51}p^3qy_o^2 + F_{52}p^2q^2y_o^2 + F_{53}pq^3y_o^2 + F_{54}q^4y_o^2 + F_{55}p^3x_oy_o^2 + F_{56}p^2qx_oy_o^2 \\
 & + F_{57}pq^2x_oy_o^2 + F_{58}q^3x_oy_o^2 + F_{59}p^2x_o^2y_o^2 + F_{60}pqx_o^2y_o^2 + F_{61}q^2x_o^2y_o^2 \\
 & + F_{62}px_o^3y_o^2 + F_{63}qx_o^3y_o^2 + F_{64}x_o^4y_o^2 + F_{65}p^3y_o^3 + F_{66}p^2qy_o^3 + F_{67}pq^2y_o^3 \\
 & + F_{68}q^3y_o^3 + F_{69}p^2x_oy_o^3 + F_{70}pqx_oy_o^3 + F_{71}q^2x_oy_o^3 + F_{72}px_o^2y_o^3 + F_{73}qx_o^2y_o^3 \\
 & + F_{74}x_o^3y_o^3 + F_{75}p^2y_o^4 + F_{76}pqy_o^4 + F_{77}q^2y_o^4 + F_{78}px_oy_o^4 + F_{79}qx_oy_o^4 \\
 & + F_{80}x_o^2y_o^4 + F_{81}py_o^5 + F_{82}qy_o^5 + F_{83}x_oy_o^5 + F_{84}y_o^6
 \end{aligned}$$

Appendix B: Crude Eye Model Verification

To ensure the validity of the calibration process for the fundus camera, a simulation and experiment verification was conducted. The following section details the experimental setup, assumptions, results and error analysis of this verification process.

The use of a crude eye model was made possible through an off the shelf achromatic doublet and a custom curved fiber bundle (CFB) donated by SCHOTT. Imaging of the test target would be captured on the posterior surface of the CFB. The achromatic doublet from Thorlabs featured an 8 mm diameter open aperture and a 16 mm focal length that served as the corneal and crystalline lens surfaces, adding power to the crude eye model. A suspended matrix of 6.5 μm fiber cores was machined to provide radius of curvature of -16.928 mm on the anterior surface and a polished flat surface on the posterior surface. To ensure an accurate radius of curvature for the anterior surface of the CFB, a spherometer and ZYGO Verifire Fizeau interferometer were used to measure the surface with the results from each averaged together. Knowledge of this radius of curvature will strongly impact the resulting distortion measurement as the CFB serves as the retinal imaging surface. The CFB open aperture was approximately 20 mm with the spacing between the doublet posterior surface and the CFB was 15.858 mm on axis. The materials of the achromatic doublet were N-BAF10 and N-SF6HT, while the suspension matrix or fiber core index was unknown. Since incident light rays on the fiber bundle would experience total internal reflection (TIR) before exiting the posterior surface, refraction effects and thus, knowledge of the index was not needed. Further explanation related to target imaging shall be presented later.

A grid target pattern was created using a large cardboard aperture with poked holes spaced 1 inch apart and backlit by a set of fluorescent tubes from an eye chart. The holes were referenced to a known mechanical datum to ensure a uniform array of points and the target was placed approximately 405 mm from the anterior surface of the achromatic doublet. However, due to the mismatched dimensions of the cardboard, the grid pattern is inherently skewed relative to the imaging plane. A point grey color camera with a zoom lens system was connected to the MATLAB Image Processing Toolbox to capture the image of the grid pattern through the crude eye model on the posterior CFB surface. The experimental setup and accompanying schematic of optical elements can be seen in Figure B-1.



Figure B-1: Pegboard experimental setup. Note that this section used a cardboard aperture with 1" holes placed over the diffuse light source in place of the pegboard shown in the image. Spot patterns on the back of CFB are captured with a RGB Point Grey camera for processing.

To compare point locations on the CFB from the experimental setup, the above described system was implemented and analyzed using Zemax raytracing software. A target consisted of an object with dimensions 254 mm x 254 mm placed 405 mm away from the anterior surface of the doublet. Rays emanating from the holes of the experimental grid target were modeled using chief

rays ($p_x, p_y = 0$) defined by normalized object coordinates h_x, h_y from $[-1,1]$. The field coordinates were divided into 11 equal spaced positions corresponding to a 1 inch or 25.4 mm spacing between each field point. Merit function values for the x and y chief ray position were recorded on the curved retinal image plane. The Zemax model with defined field positions can be seen in Figure B-2.

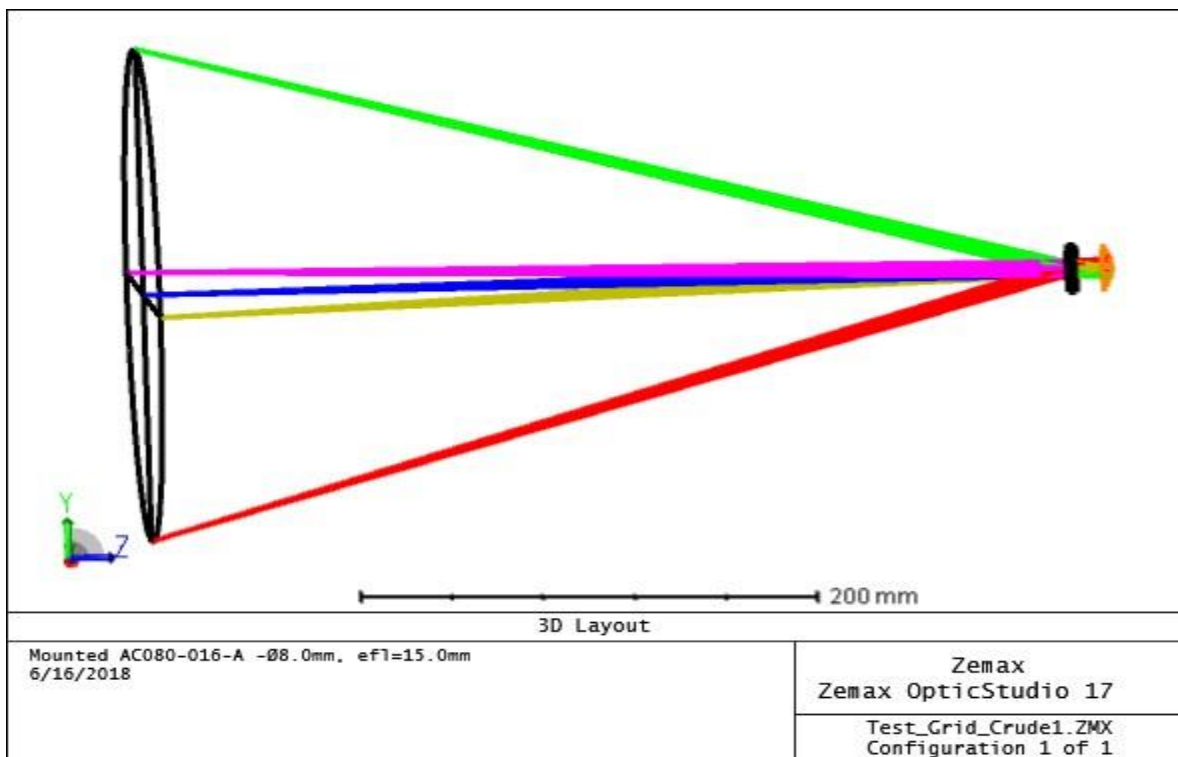


Figure B-2: Object definition and crude eye model raytracing through Zemax.

The aim of the validation process was to verify that this crude eye model could serve as a characterization tool for the modified fundus camera. Furthermore, using the chief ray height from Zemax simulation as a comparative to the centroid of dot patterns in the experimental setup was investigated for validity. Imaging results of the grid pattern were analyzed in MATLAB and can be seen in Figure B-3.

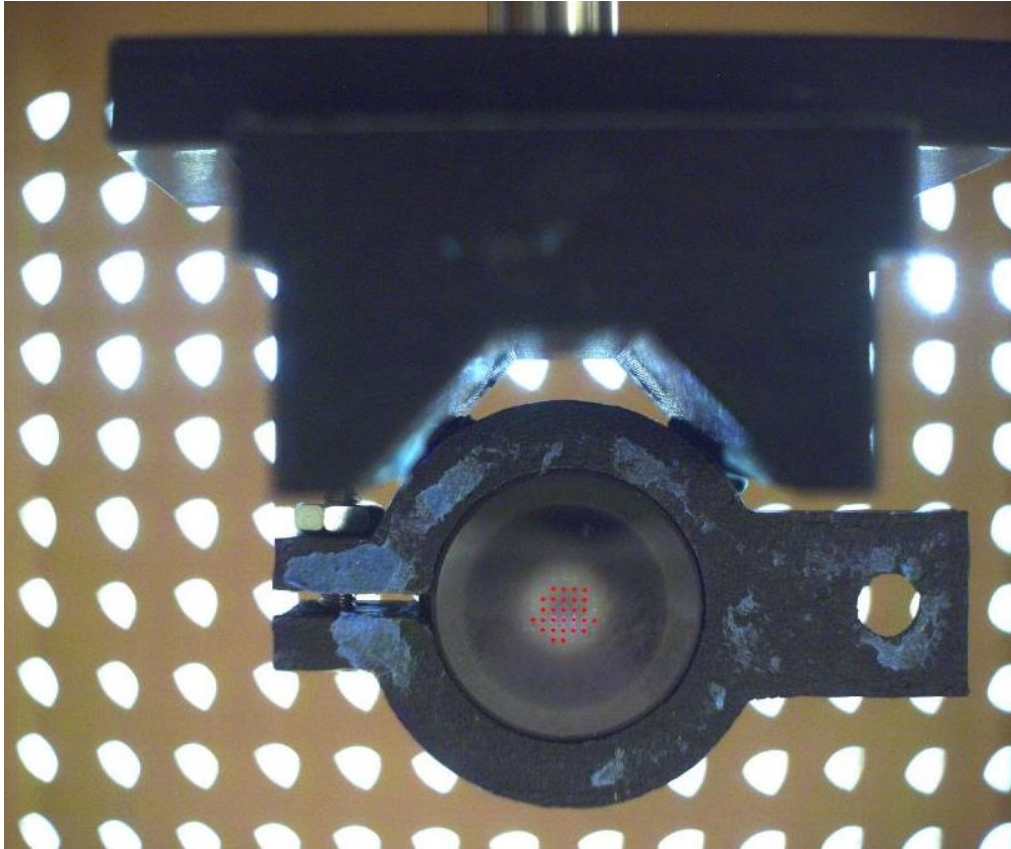


Figure B-3: Imaging and dot fit results of the CFB from MATLAB

The centers of the grid pattern formed on the anterior surface of the CFB were found using a centroid detection function in MATLAB which reports centers to a fraction of a pixel, leading to increased accuracy. A region of interest was defined around the illuminated ring on the CFB and filtered to remove noise and gain artifacts from the camera while boosting the bright centers of the dot pattern. Figure B-4 illustrates the accuracy of the centroiding function on bright centers of the processed binary image.

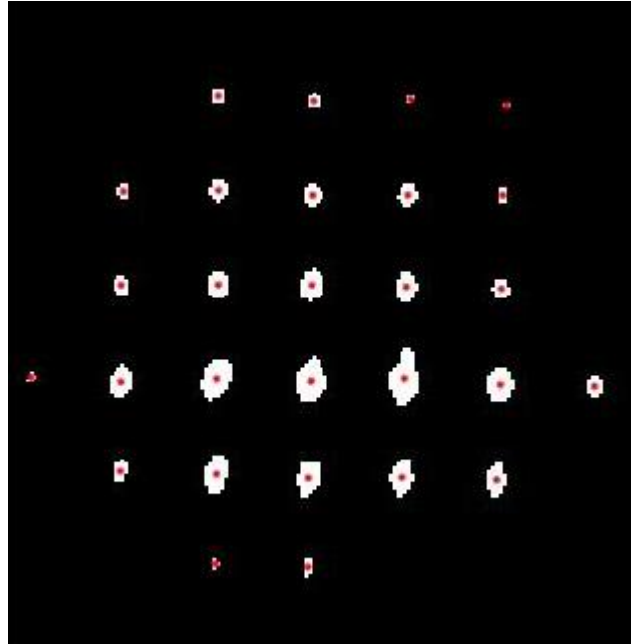


Figure B-4: Centers of grid pattern are shown in red as determined by the centroiding function

A ruler placed in the plane of the posterior CFB surface was used to calibrate the resulting pixel space of the image to real space coordinate for comparison to Zemax simulation results. This calibration image can be seen in Figure B-5 and details that approximately 26 pixels corresponds to 1 mm in real space coordinates.

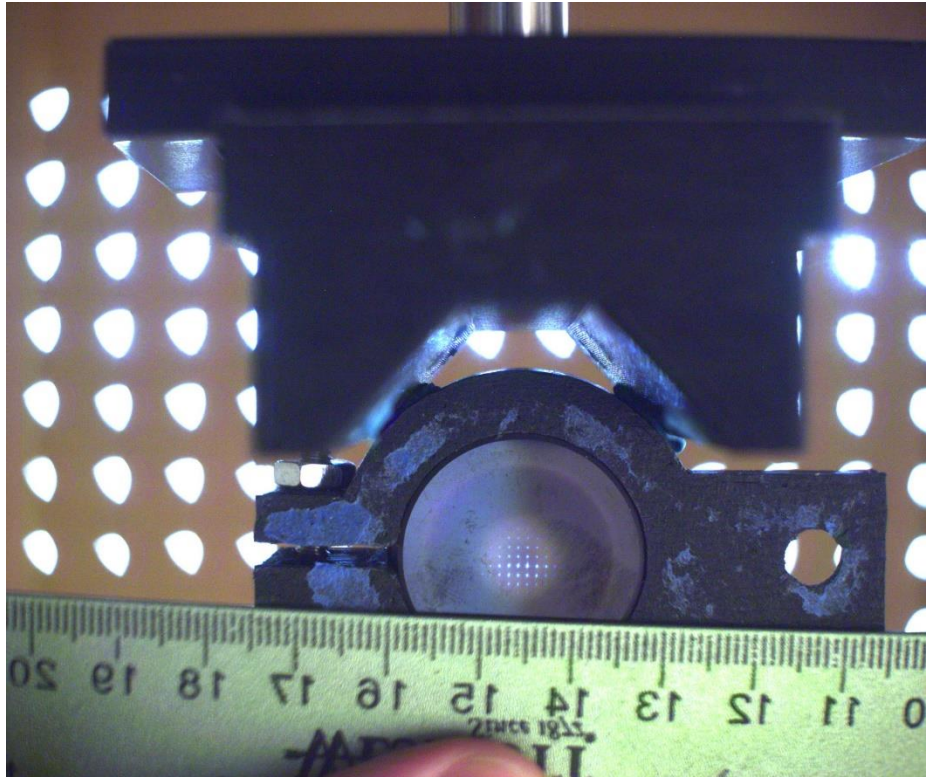


Figure 5: Ruler calibration for converting image space pixel coordinates to real space image coordinates

A nominal grid image on the CFB image plane was defined as the paraxial image of the grid target scaled by the paraxial magnification of the crude eye model system as reported by Zemax. Comparing the separation from the center coordinate point (0,0) to the first vertically displaced point in the nominal, simulated and experimental image was used to quantify the accuracy of this verification process. The center (0,0) location point for the experimental image was assumed to be the largest bright spot or point (4,4) in Figure B-4. The following Y heights were determined to be 0.9772 mm, 1.045 mm, and 1.21 mm for the experimental, nominal and simulated cases respectively. The plot of centroid points for each case can be seen in Figure B-6.

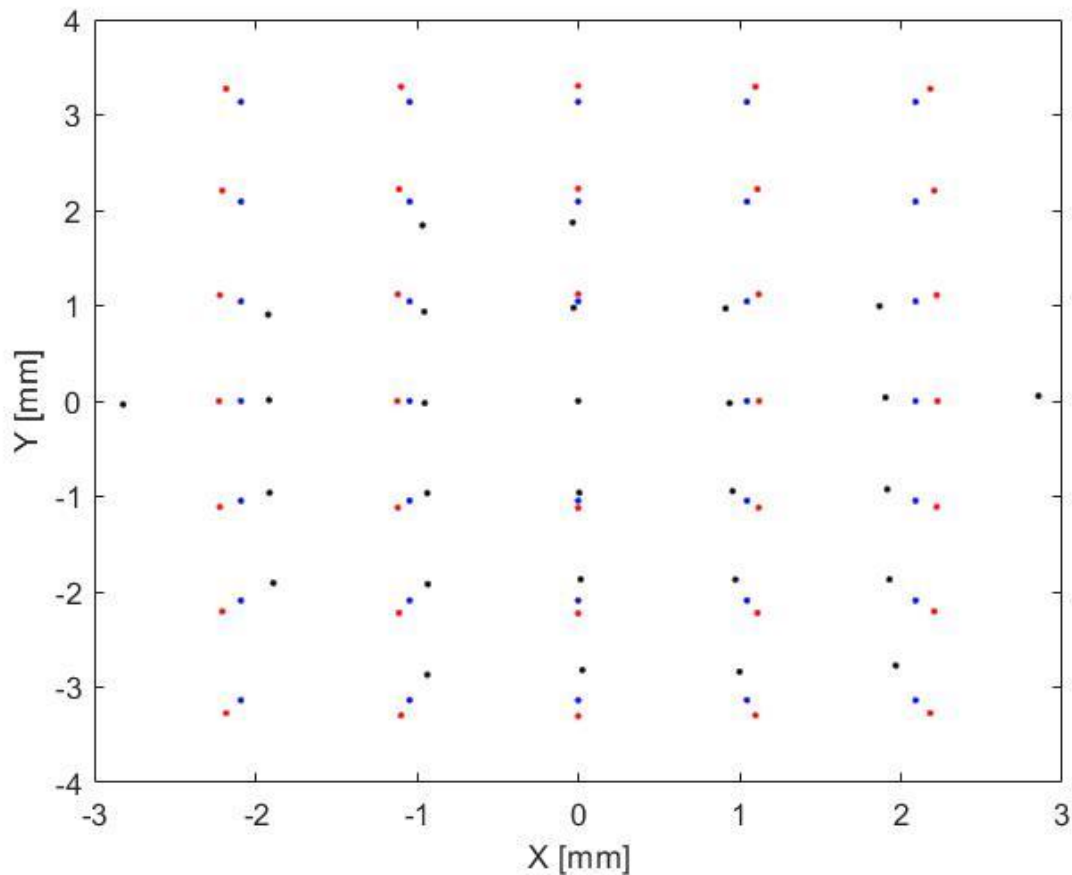


Figure 6: The experimental centroids (black), nominal paraxial centroids (blue), and simulated chief ray centroids (red). A slight barrel distortion can be seen in the resulting patterns along with a skew angle imposed on the experimental pattern (black) due to the imposed skew in target construction

A major limitation in the use of this CFB was discovered during experimental trials that relates to potential sources of error in the measurement process. The numerical aperture (NA) of the crude eye model dictates the acceptance or emittance angles of the system where the NA is defined by Equation B-1, where f is the focal length of the achromatic doublet and D is the open aperture diameter of the doublet.

$$NA = \frac{1}{2 * \frac{f}{D}} \quad \text{B-1}$$

The above approximation is valid for systems in air, giving the system and NA of 0.25. As mentioned previously, the cores of the fibers have a diameter of $6.5\ \mu\text{m}$ and thus are limited in acceptance angle of light focused by the doublet. A detailed image of the fiber cores was recorded using a ZYGO NewView 8300 optical profiler and can be seen in Figure B-7.

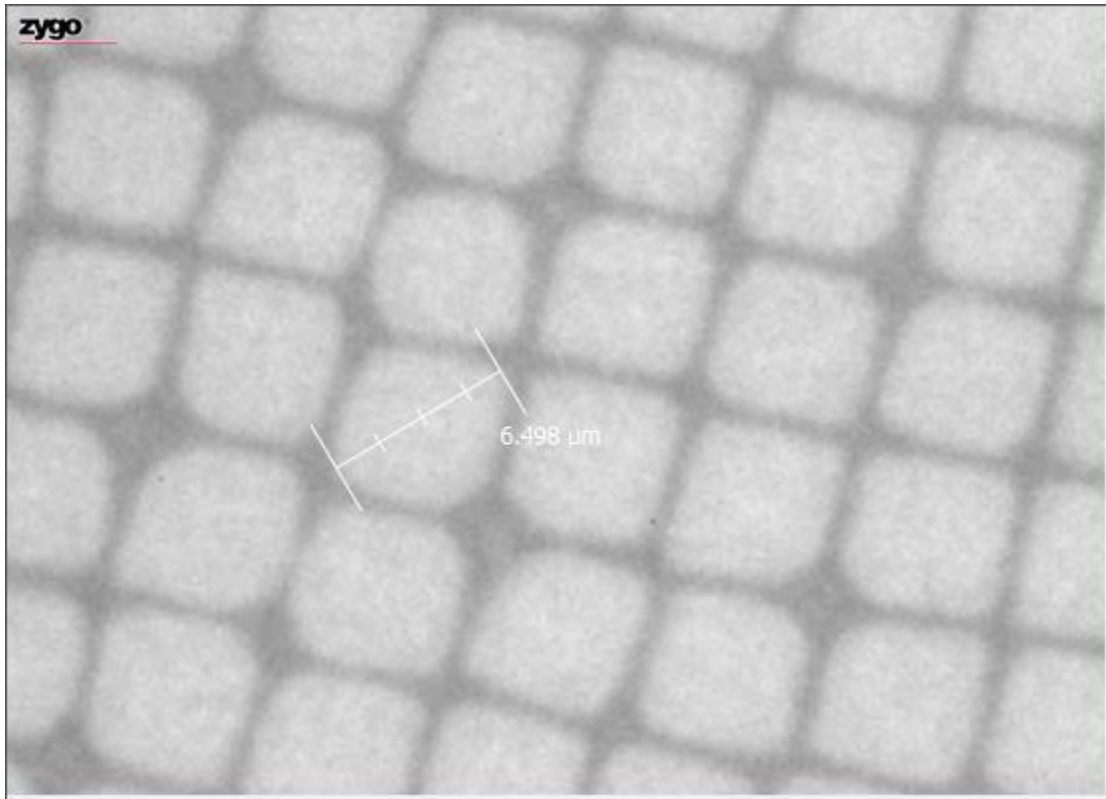


Figure 7: 50x magnification of posterior CFB surface detailing the fiber core matrix

While the index of refraction for the fiber cores is unknown, it is clear to understand that the TIR condition is broken at certain incident field angles on the CFB. This leads to the relatively small illumination area ($\sim 10\ \text{mm}$ in diameter) compared to clear open aperture of the CFB which is $20\ \text{mm}$ diameter.

Error Analysis and Conclusion

The centroid fitting done in MATLAB will have some built in error after filtering and boosting related to the resolving capabilities of the camera as well as the performance of the CFB as an imaging plane. Therefore, an assumption of the error in pixel space related to the true chief ray location is estimated to be within a 5x5 pixel region or in-other-words two-pixel spans in both the horizontal and vertical directions from center pixel (0,0), consistent with Nyquist sampling theorem. Thus, a max deviation in any meridian corresponds to a real space coordinate error of 0.077 mm. The simulation and experimental results deviate by twice this error estimation. It is plausible that in the experimental setup, the distance between the posterior doublet surface and the CFB is less than or equal to 15.858 mm, resulting in a significant change in chief ray location from the simulation. A -2 mm defocus, corresponding to a 13.858 mm separation, moves the first vertically displaced chief ray point from 1.121 mm to 0.996 mm. Therefore, with known limitations to the CFB illumination area and optical parameters defining the crude eye model, analysis of this verification process suggests that simulated results and the use of this crude eye model are sufficient for characterizing the modified fundus camera system.

Appendix C: Retinal Irradiance Calculation for Modified Fundus Camera

Following ISO Standard 15004-2 for Ophthalmic Instruments, the retinal irradiance was calculated for a modified fundus camera using Cree XLamp XP-G2 LED's as the input source. The standard places a limit of $220 \frac{\mu W}{cm^2}$ as the upper limit for retinal irradiance based on a two-hour exposure period. The following documentation will discuss the ISO Standard, measurement method and analysis for this modified fundus camera system.

Procedure:

Following Annex D in the ISO Standard, classification of the instrument as Group 1 or Group 2 is done following the method described in Annex D or an equivalent method to calculate the spectral irradiance or spectral radiant power used in the limiting condition. For instruments classified in Group 1, the limiting condition for retinal aphakic irradiance, found in Section 5.4.1.3a, follows Equation C-1.

$$E_{AR} = \sum_{305}^{700} E_{\lambda} * A(\lambda) * \Delta\lambda \quad \text{C-1}$$

In Equation C-1, the spectral irradiance [E_{λ}] is multiplied by the aphakic photochemical hazard weighting function [$A(\lambda)$] defined in Annex A, and the spectral bandwidth [$\Delta\lambda$]. The upper limit for the retinal aphakic irradiance E_{AR} is $220 \frac{\mu W}{cm^2}$ which is found by summing all of the spectral contributions of the source, weighted by the hazard curves at each respective wavelength.

To find the retina aphakic irradiance, the method in Annex D.2 provides the parameters and measurements needed to qualify the instrument. First, the solid angle defining the exit pupil of the ophthalmic system and the corneal plane is found. Equation C-2 uses the exit pupil aperture (A_{exit}) and the distance from the exit pupil to the corneal plane (D_p) to calculate the solid angle (Ω_e).

$$\Omega_e = \frac{A_{exit}}{D_p^2} \quad \text{C-2}$$

The radiance at the corneal plane (L_λ) is found using Equation C-3 and requires a measurement of the spectral irradiance at the corneal plane ($E_{\lambda-c}$).

$$L_\lambda = \frac{E_{\lambda-c}}{\Omega_e} \quad \text{C-3}$$

Measurement of Corneal Spectral Irradiance

Measurement of the corneal irradiance was chosen to characterize the retinal aphakic irradiance given by Section 5.4.13a. To find the corneal spectral irradiance, the spectral content of the source as well as the measured detector irradiance must be considered.

A Gentec EO MAESTRO monitor with a 380nm-1080nm silicon photodetector were used to measure the corneal irradiance. The detector can work in irradiance mode, where the irradiance is reported per input beam diameter. In operation of the fundus camera, an in-focus annulus of illumination is located at the eye system stop. Therefore, the Si-detector was placed approximately 3 mm before the annulus focus position to simulate the position of the corneal surface. The measured beam diameter at this position was 0.9 cm and used as the input diameter

needed for the irradiance measurement. The photodiode was set to 440 nm as the central wavelength of detection.

The LED suite of Cree XLamp CW 3700K-5000K LEDs functions using a simple constant current circuit. Thus, the output flux of the LED suite is related to the driving current that is controlled by a potentiometer in the circuit. A power source monitors the input current, while a BuckPuck regulates the voltage drop across the LED suite, controlling the brightness or output flux. Table C-1 summarizes a step through of various driving currents and the measured irradiance for each driving current.

CURRENT [A]	IRRADIANCE $\left[\frac{\mu W}{cm^2}\right]$
0.1	241
0.2	450
0.3	692
0.4	806
0.5	971
0.6	1130
0.7	1250
0.8	1390
0.9	1450

Table C-1: Current and Si-detector measured irradiance values at the corneal plane

To find the spectral corneal irradiance $E_{\lambda-c}$, the measured irradiance must be weighted by the source spectrum. The LED suite spectrum is the green curve shown in Figure C-1 from the manufacturer reported data sheet and was digitized to perform the spectral weighting in MATLAB.

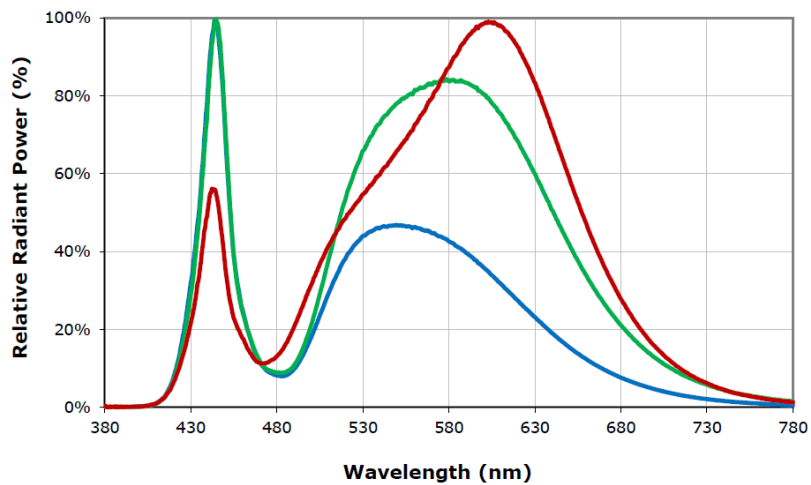


Figure C-8: LED suite relative power spectrum

Since the curve is given as the relative radiant power, a normalization must be completed on the curve. To do this, the percentage values are converted to decimal values in the range of [0,1], summed across the curve, and each individual data point on the curve is divided by this sum. Therefore, adding the irradiance contributions from each wavelength returns the total measured irradiance given by the Si-detector.

Procedure Continued:

Now that the corneal spectral irradiance $E_{\lambda-c}$ is known and the spectral radiance L_{λ} can be calculated, the remaining steps to determine the retinal aphakic irradiance E_{AR} can be completed.

The pupil aperture that passes light from the cornea to the retina, may be defined if information is known about the instrument. As mentioned previously, the operation of the fundus requires a well-focused annulus of illumination to be located at the eye system stop. By measuring the outer and inner diameter of the annulus at the focal plane, the effective area of illumination at the pupil can be determined. The outer diameter of the annulus was measured to be 6 mm and the inner

obscuration diameter was measured to be 2 mm. Thus, the pupil illumination area A_p is found by taking the difference between the outer and inner annulus areas.

A reasonable assumption presented in the ISO Standard is the optical distance between the pupil plane of the eye and the retina D_o is set to be 17 mm. The retinal spectral irradiance E_λ , is then readily found by applying Equation C-4.

$$E_\lambda = \frac{L_\lambda A_p}{D_o^2} \quad \text{C-4}$$

Following Equation C-1, it is straightforward to find the retinal aphakic irradiance E_{AR} .

Results:

It can be concluded that the range of input currents to the LED suite does not produce a retinal aphakic irradiance above the upper limit set by section 5.4.1.3a of ISO Standard 15004-2, classifying this modified fundus camera as a Group 1 ophthalmic instrument. Table C-2 reports the calculated retinal aphakic irradiance values for each input current and Figure C-2 shows this same information graphically.

CURRENT[A]	IRRADIANCE $\left[\frac{\mu W}{cm^2}\right]$
0.1	16.0
0.2	29.8
0.3	45.8
0.4	53.4
0.5	64.3
0.6	74.8
0.7	82.8
0.8	92.0
0.9	96.0

Table C-2: Calculated retinal aphakic irradiance values by LED suite driver current

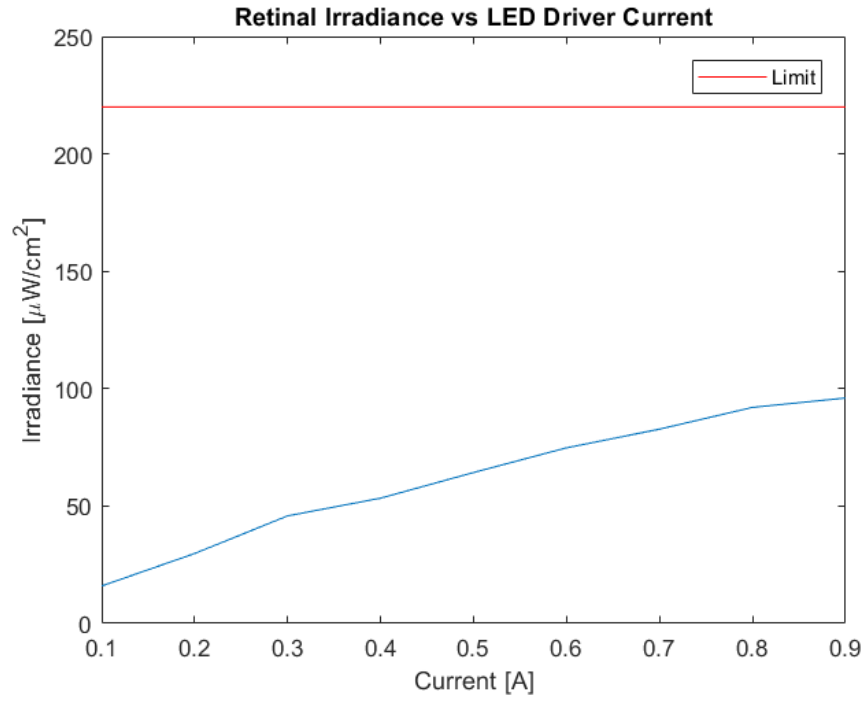


Figure C-9: Retinal aphakic irradiance vs. LED driver current

Appendix D: Distortion Coefficient Values for All Human Trial Subjects

The following appendix provides supplemental data regarding ocular distortion measurements from the small human trial cohort. Contained within this appendix are illustrations of distortion coefficients along with the mean value measured plotted against refractive error for all subjects. Coefficient values for all three processed images are also shown in bar charts in this appendix. Lastly, a summary table contains values indicating if a distortion coefficient spanned zero, meaning low confidence in the measured coefficient values, is presented for all subjects.

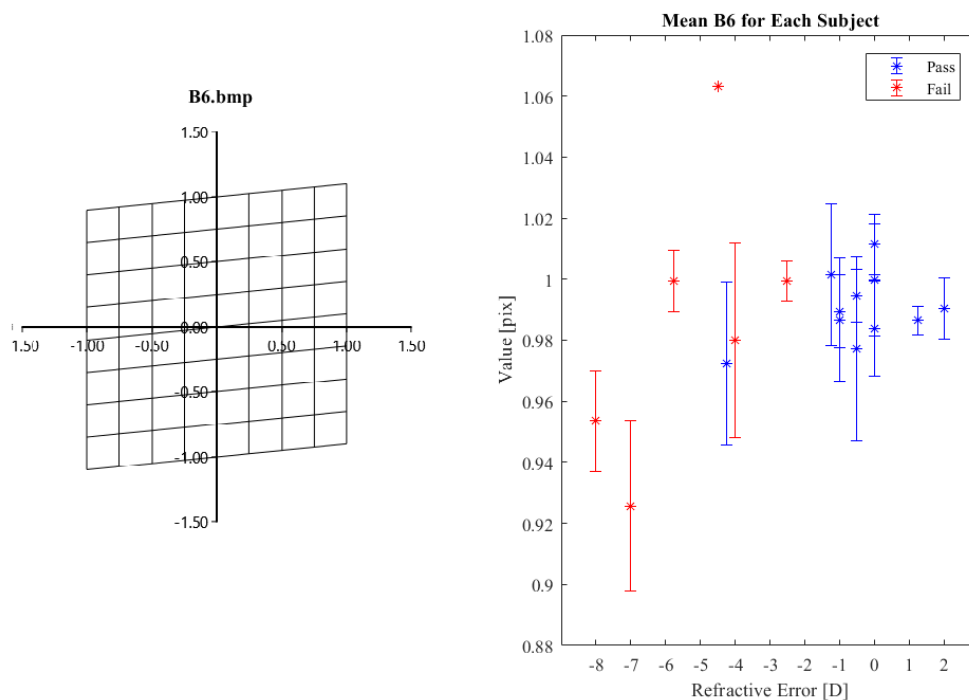


Figure D- 1: An illustration of B_6 distortion (left) along with the mean measured values for B_6 plotted against refractive error for all cohort subjects (right).

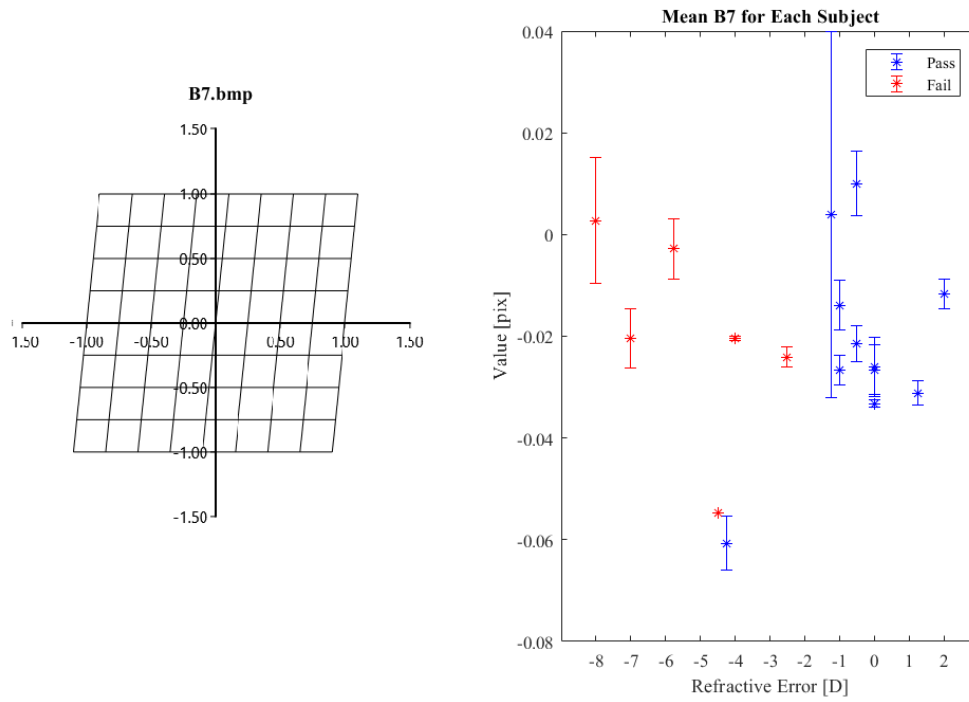


Figure D- 2: An illustration of B_7 distortion (left) along with the mean measured values for B_7 plotted against refractive error for all cohort subjects (right).

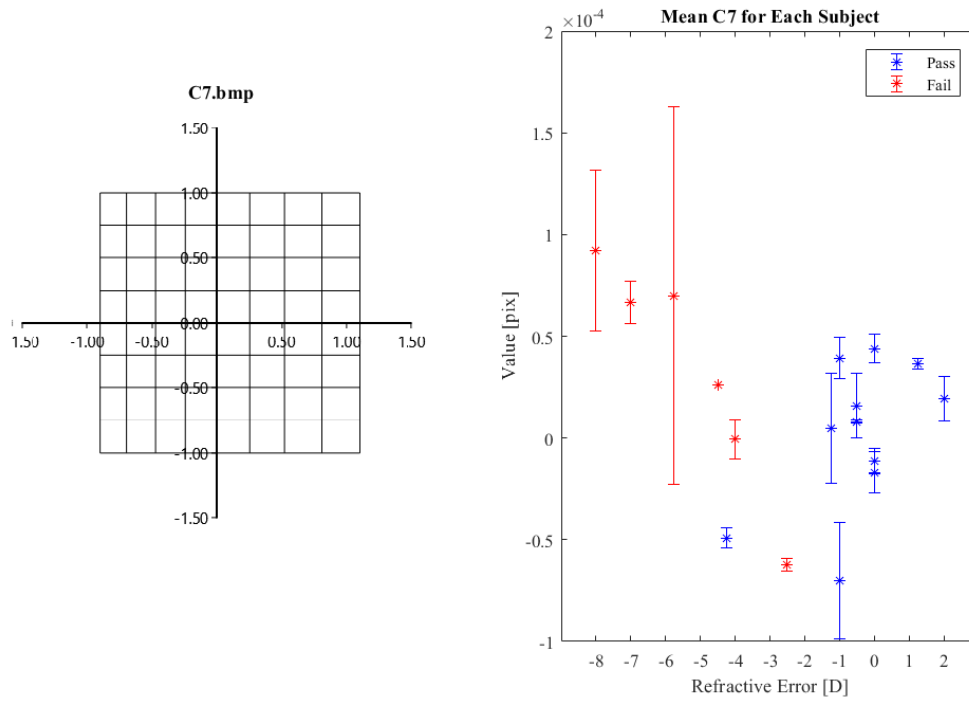


Figure D- 3: An illustration of C_7 distortion (left) along with the mean measured values for C_7 plotted against refractive error for all cohort subjects (right).

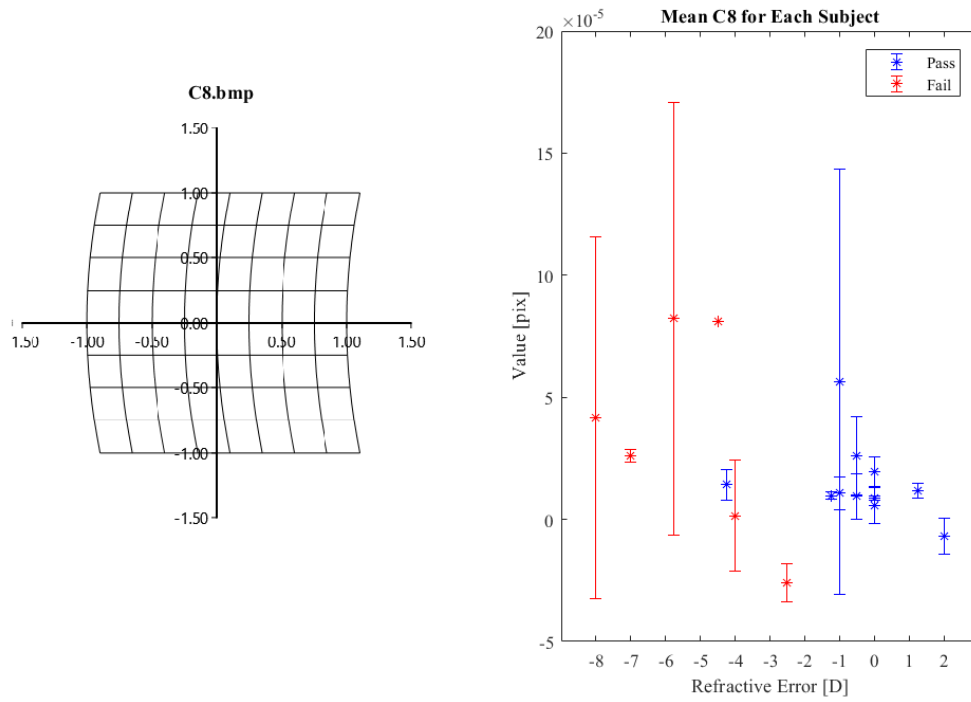


Figure D- 4: An illustration of C_8 distortion (left) along with the mean measured values for C_8 plotted against refractive error for all cohort subjects (right).

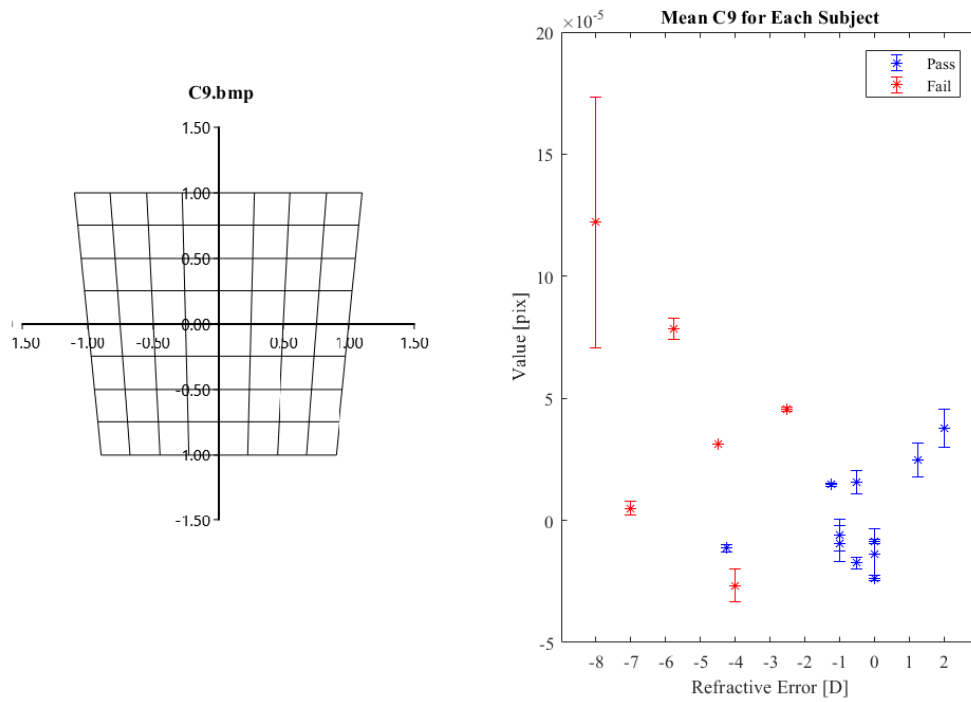


Figure D- 5: An illustration of C_9 distortion (left) along with the mean measured values for C_9 plotted against refractive error for all cohort subjects (right).

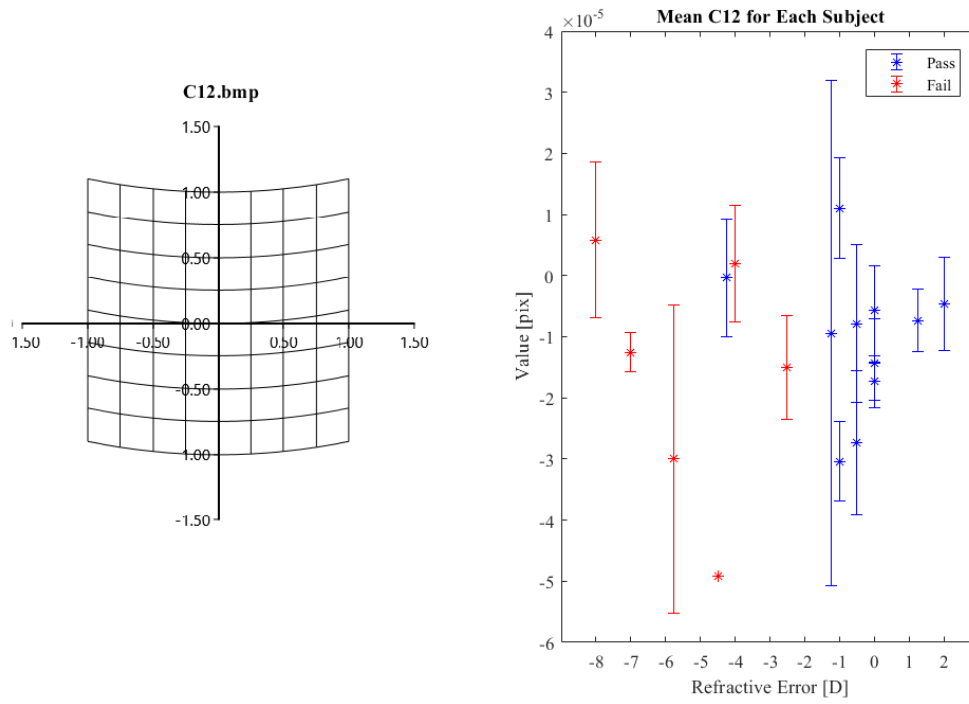


Figure D- 6: An illustration of C_{12} distortion (left) along with the mean measured values for C_{12} plotted against refractive error for all cohort subjects (right).

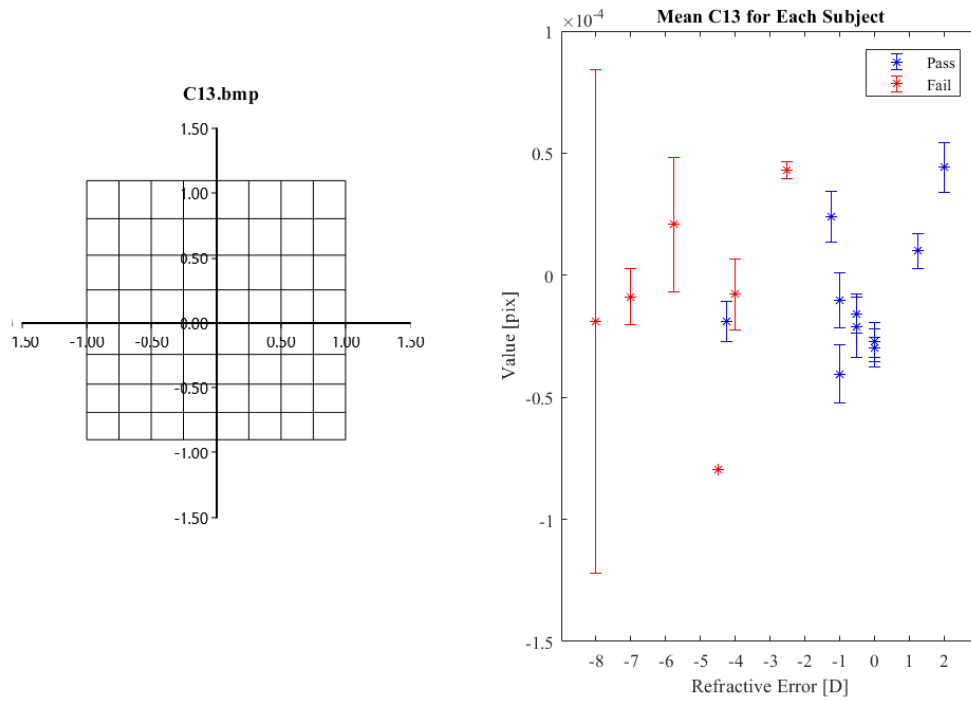


Figure D- 7: An illustration of C_{13} distortion (left) along with the mean measured values for C_{13} plotted against refractive error for all cohort subjects (right).

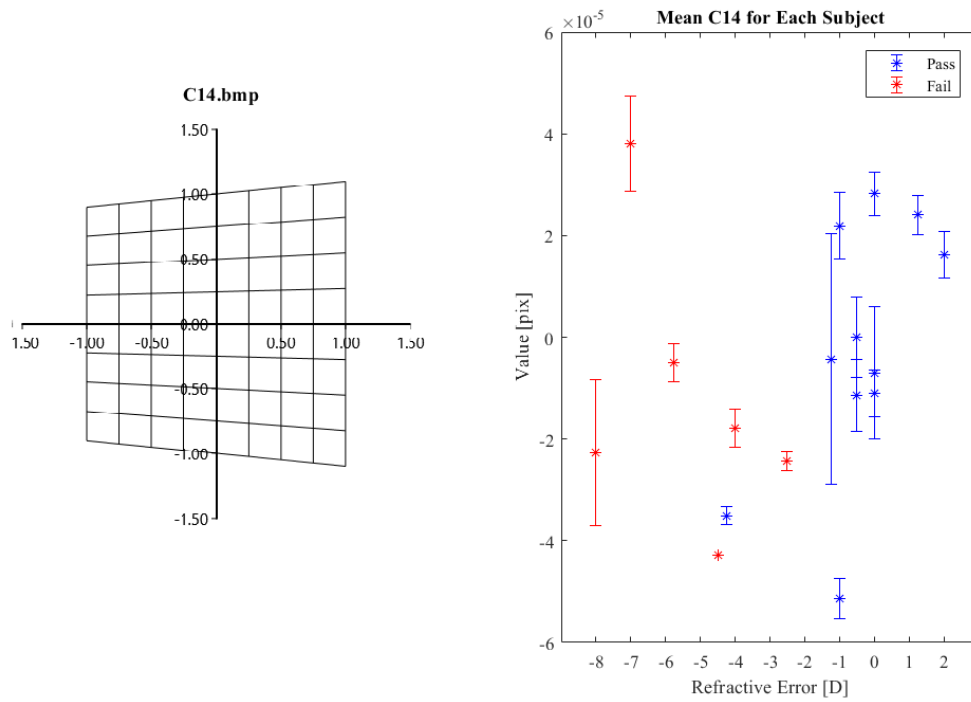


Figure D- 8: An illustration of C_{14} distortion (left) along with the mean measured values for C_{14} plotted against refractive error for all cohort subjects (right).

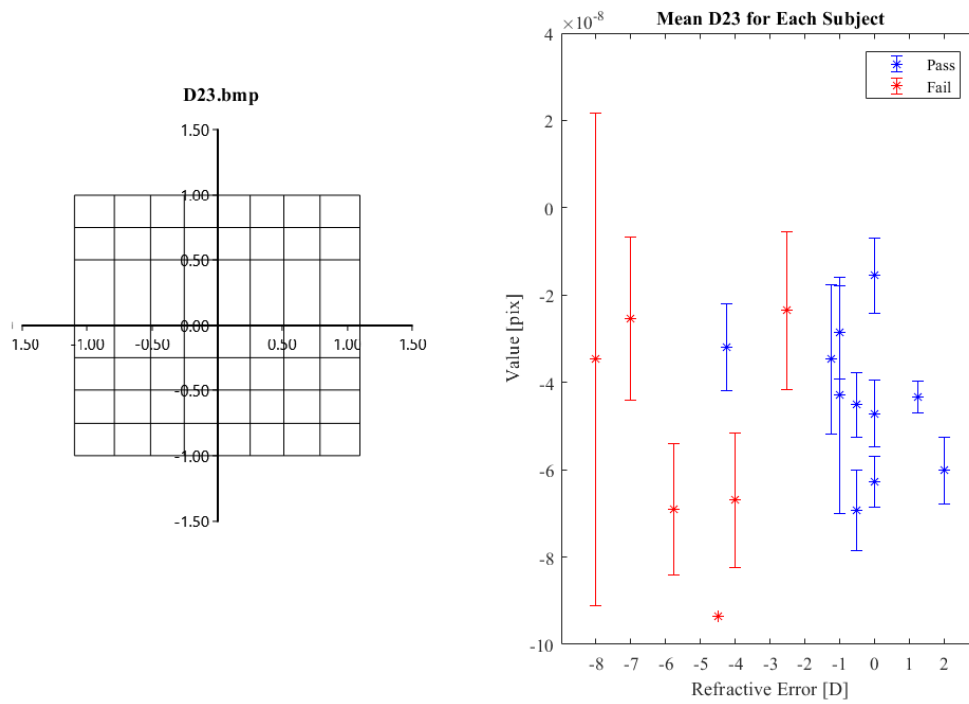


Figure D- 9: An illustration of D_{23} distortion (left) along with the mean measured values for D_{23} plotted against refractive error for all cohort subjects (right).

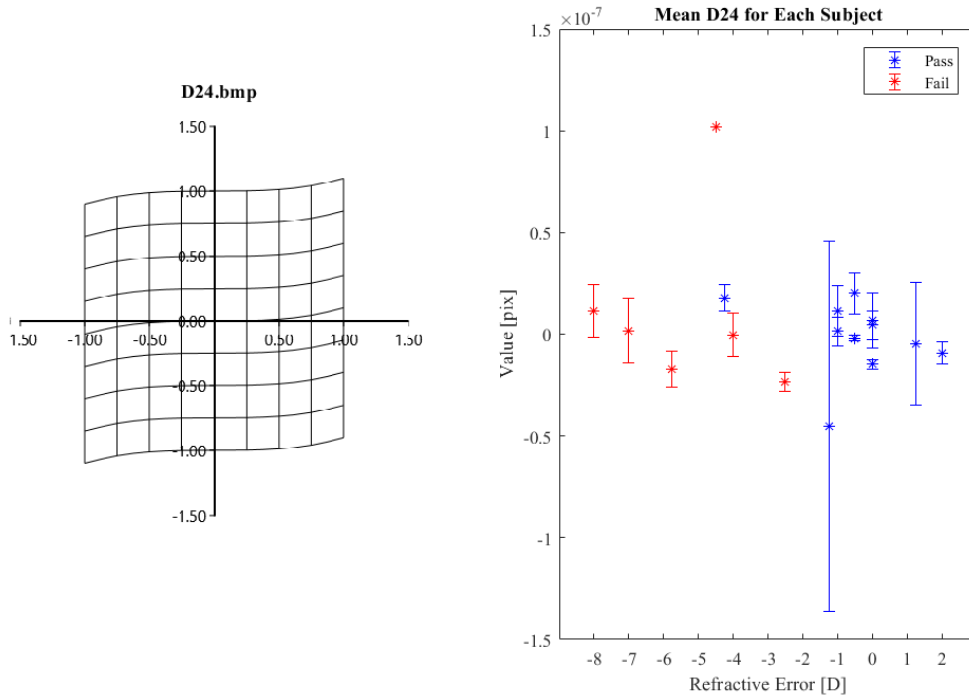


Figure D- 10: An illustration of D_{24} distortion (left) along with the mean measured values for D_{24} plotted against refractive error for all cohort subjects (right).

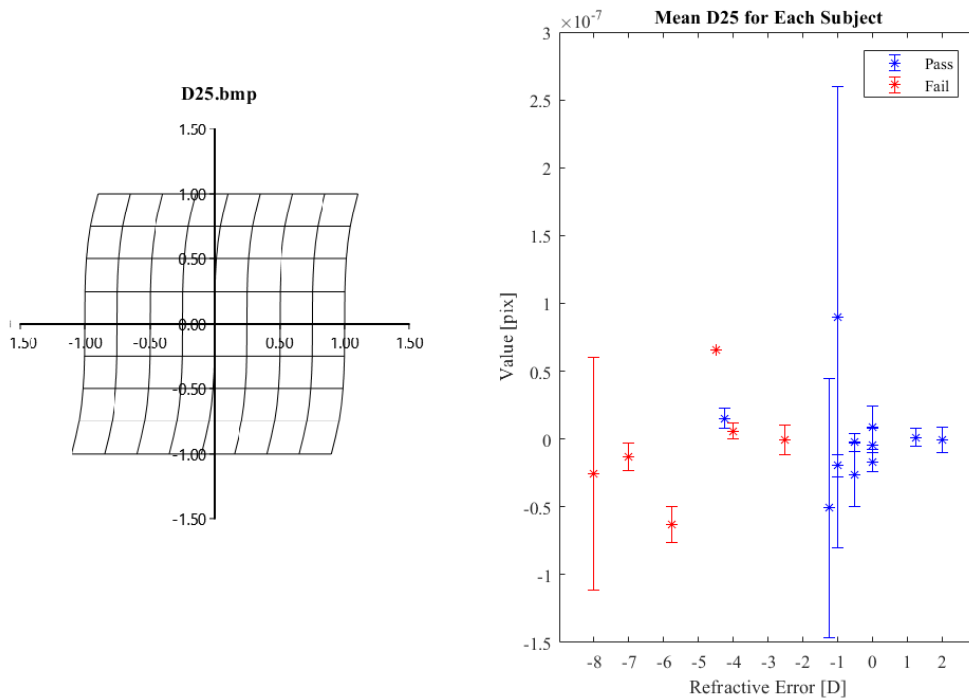


Figure D- 11: An illustration of D_{25} distortion (left) along with the mean measured values for D_{25} plotted against refractive error for all cohort subjects (right).

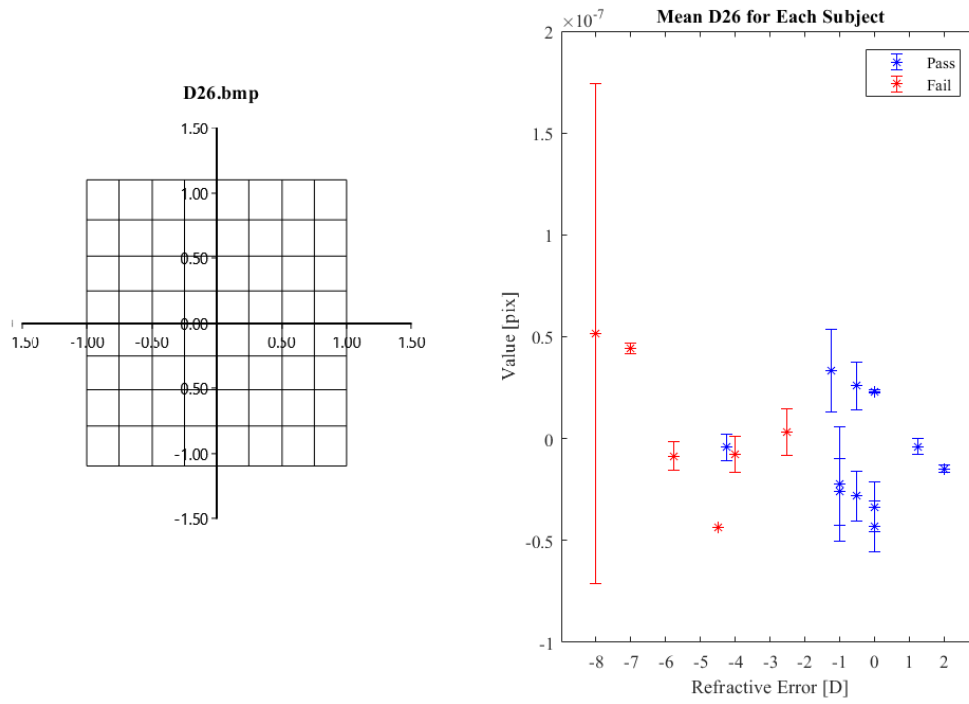


Figure D- 12: An illustration of D_{26} distortion (left) along with the mean measured values for D_{26} plotted against refractive error for all cohort subjects (right).

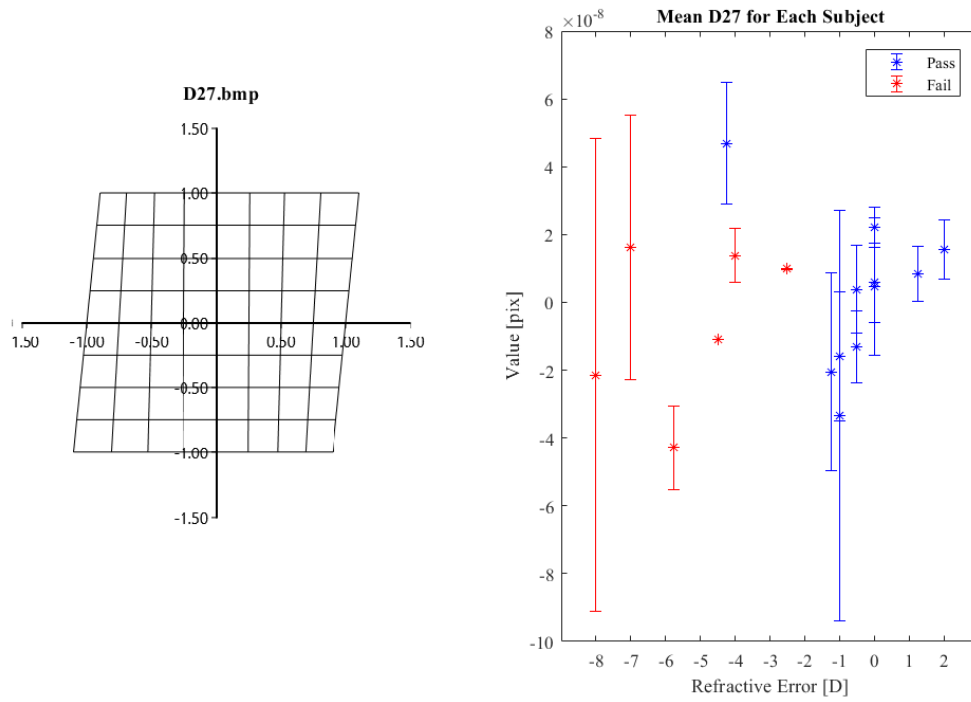


Figure D- 13: An illustration of D_{27} distortion (left) along with the mean measured values for D_{27} plotted against refractive error for all cohort subjects (right).

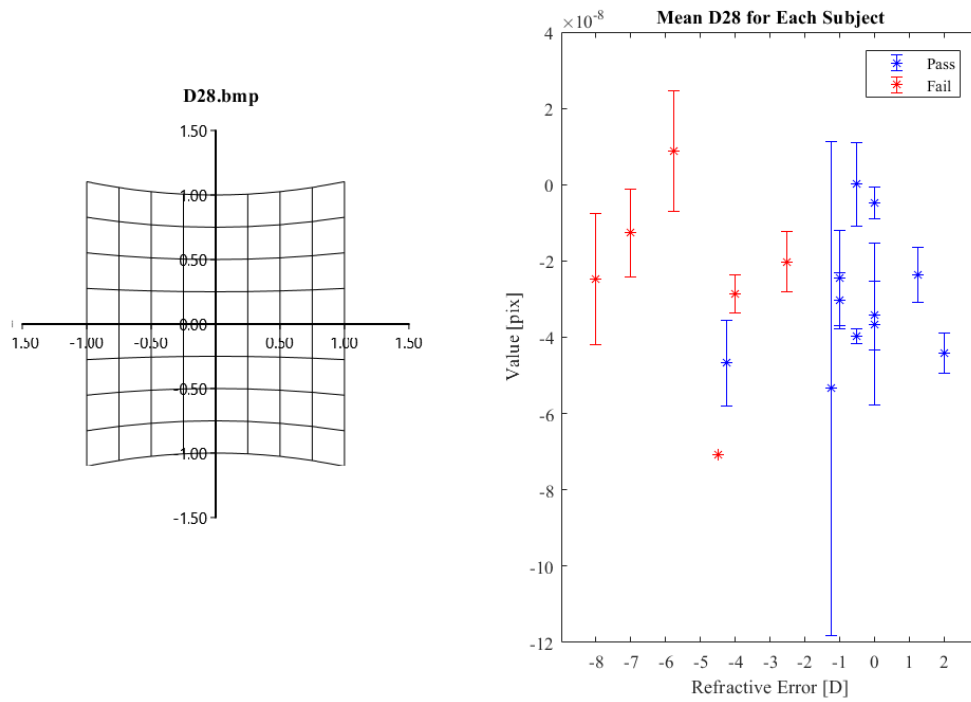


Figure D- 14: An illustration of D_{28} distortion (left) along with the mean measured values for D_{28} plotted against refractive error for all cohort subjects (right).

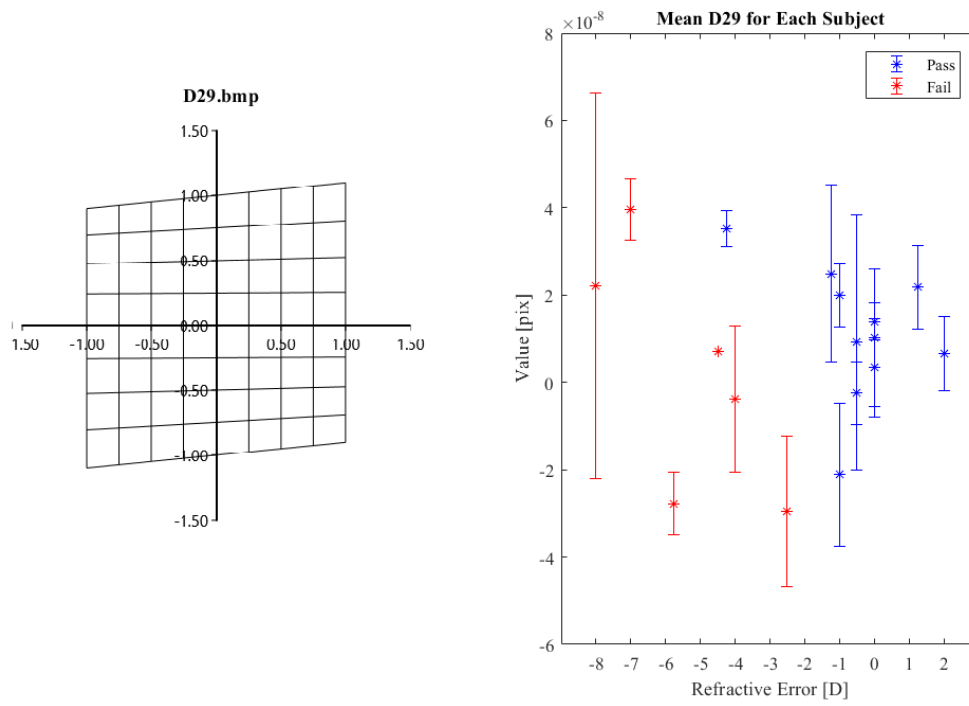


Figure D- 15: An illustration of D_{29} distortion (left) along with the mean measured values for D_{29} plotted against refractive error for all cohort subjects (right).

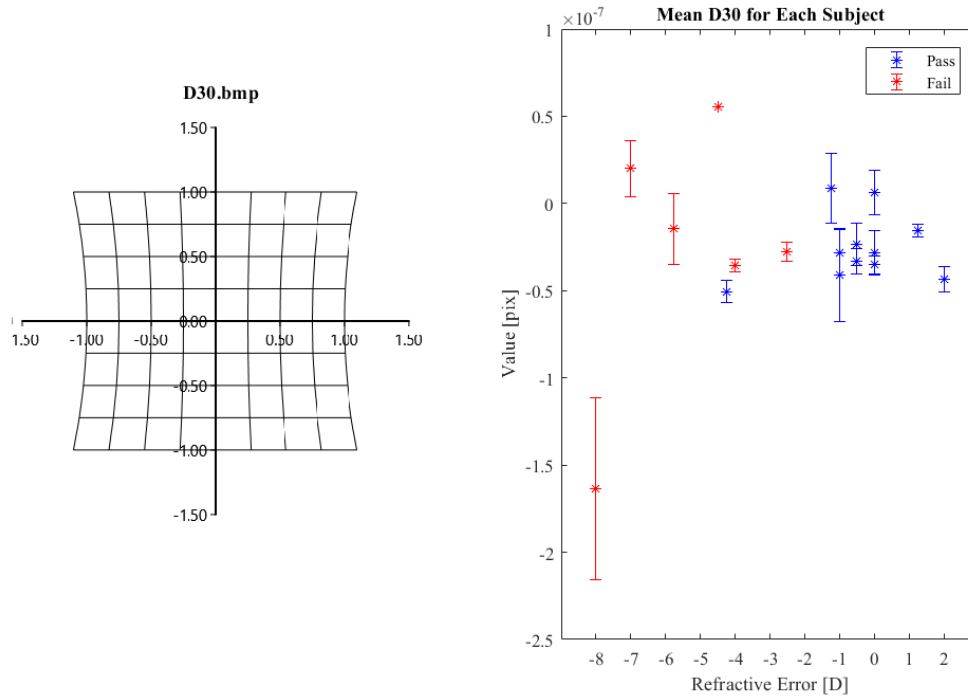


Figure D- 16: An illustration of D_{30} distortion (left) along with the mean measured values for D_{30} plotted against refractive error for all cohort subjects (right).

Subject	1	2	3	4	5	6	7	8	9	10	11	12	13	14	15*	16	17
B2	0	0	0	0	0	0	0	0	0	0	0	0	0	0	0	0	0
B7	0	0	1	1	0	0	0	0	0	0	0	1	0	0	0	0	0
C7	0	0	0	1	0	0	0	0	0	0	0	0	0	1	0	0	0
C9	0	0	0	0	0	0	0	1	0	0	0	0	0	0	0	0	0
C8	0	0	1	0	0	0	0	0	1	0	1	0	0	1	0	0	0
D23	0	0	1	0	0	0	0	0	0	0	0	0	0	0	0	0	0
D27	0	1	1	0	1	1	0	0	1	0	0	0	0	0	0	0	0
D30	0	0	0	0	0	0	0	0	0	0	0	1	0	0	0	0	0
D25	1	0	0	1	0	1	1	0	0	1	1	0	0	0	0	1	1

Table D- 1: X distortion coefficient confidence matrix. A value of 0 indicated that in three processed images the given coefficient maintained consistent sign of positive or negative. A value of 1 indicates that one or more of the measured values flipped sign and thus low confidence measurements. Subject 15 only had one image processed.

Subject	1	2	3	4	5	6	7	8	9	10	11	12	13	14	15*	16	17
B6	0	0	0	0	0	0	0	0	0	0	0	0	0	0	0	0	0
B3	0	0	0	0	0	0	0	0	0	0	0	0	0	0	0	0	0
C12	1	0	1	1	0	0	0	0	0	1	0	0	0	1	0	0	1
C14	0	0	0	1	0	0	0	0	0	0	0	0	0	0	0	0	0
C13	0	1	0	0	0	0	0	1	0	0	0	1	0	1	0	0	0
D24	0	0	1	1	0	0	1	1	0	1	1	0	0	1	0	0	0
D28	0	0	0	0	0	0	0	0	0	0	0	0	0	0	0	0	0
D29	1	0	1	0	1	0	0	0	1	1	0	0	0	1	0	0	1
D26	0	0	1	0	0	0	0	0	0	0	0	0	1	1	0	1	0

Table D- 2: Y distortion coefficient confidence matrix. A value of 0 indicated that in three processed images the given coefficient maintained consistent sign of positive or negative. A value of 1 indicates that one or more of the measured values flipped sign and thus low confidence measurements. Subject 15 only had one image processed.

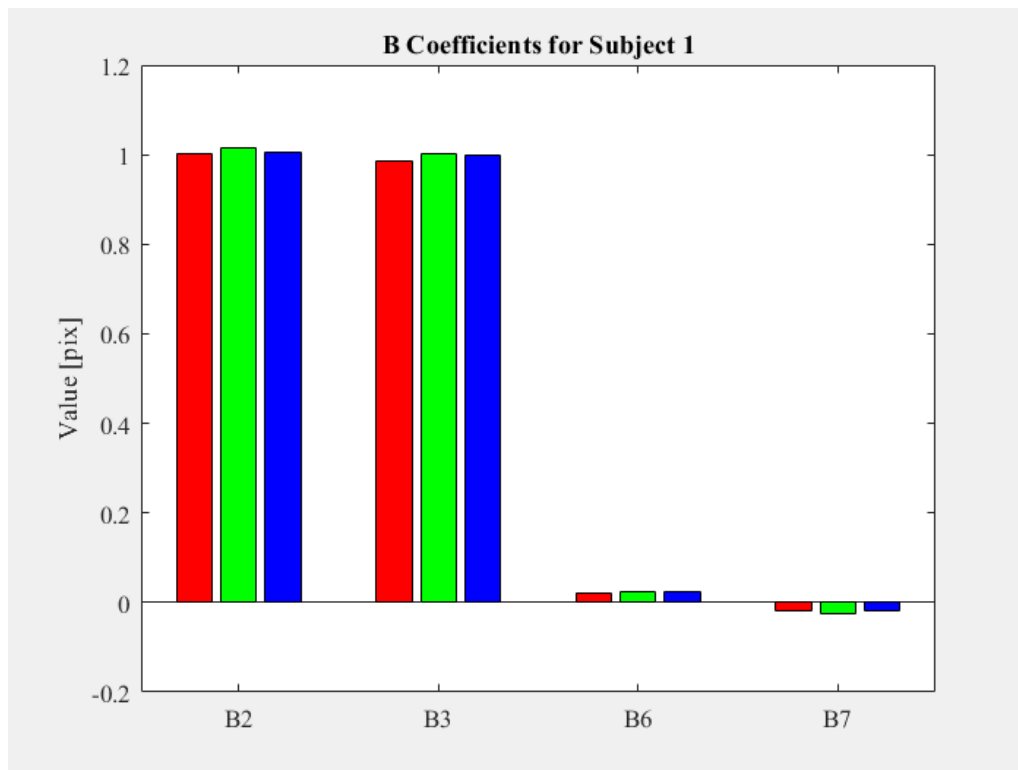


Figure D- 17: Second order distortion coefficient values for all processed retinal images of subject 1.

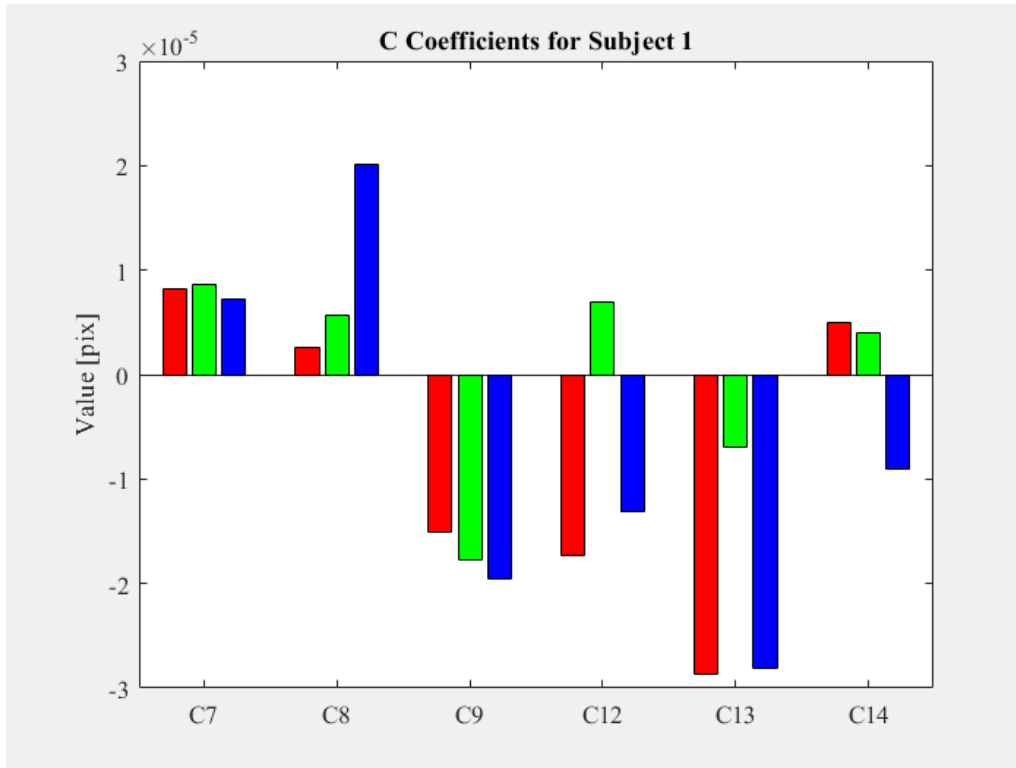


Figure D- 18: Third order distortion coefficient values for all processed retinal images of subject 1.

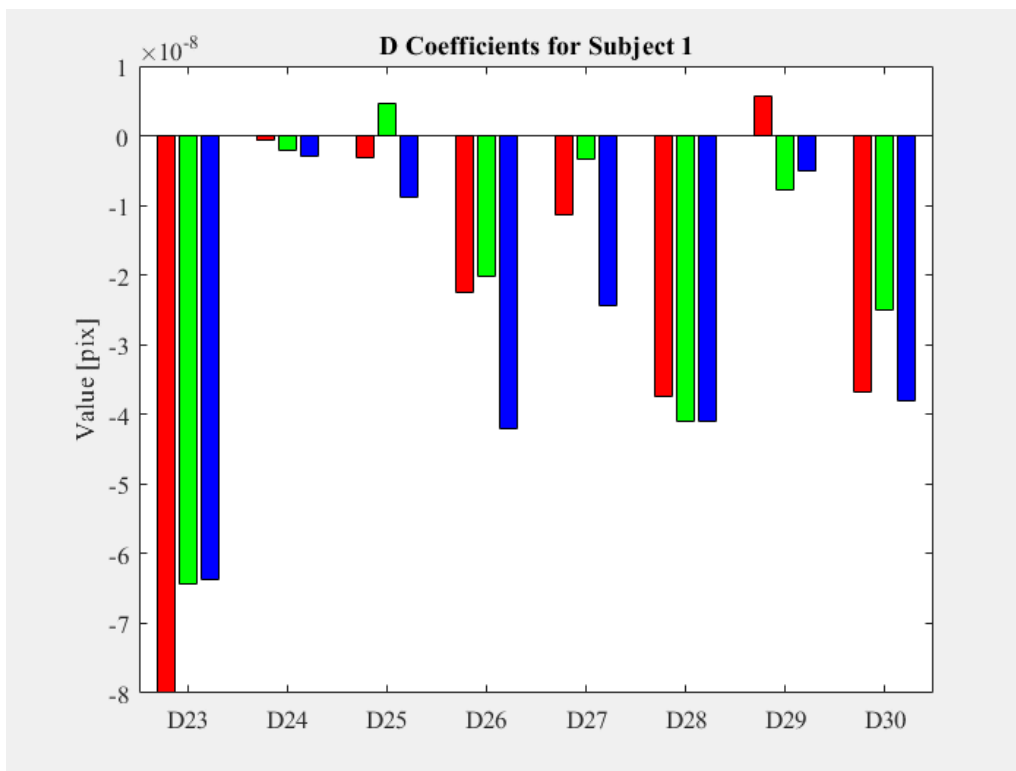


Figure D- 19: Fourth order distortion coefficient values for all processed retinal images of subject 1.

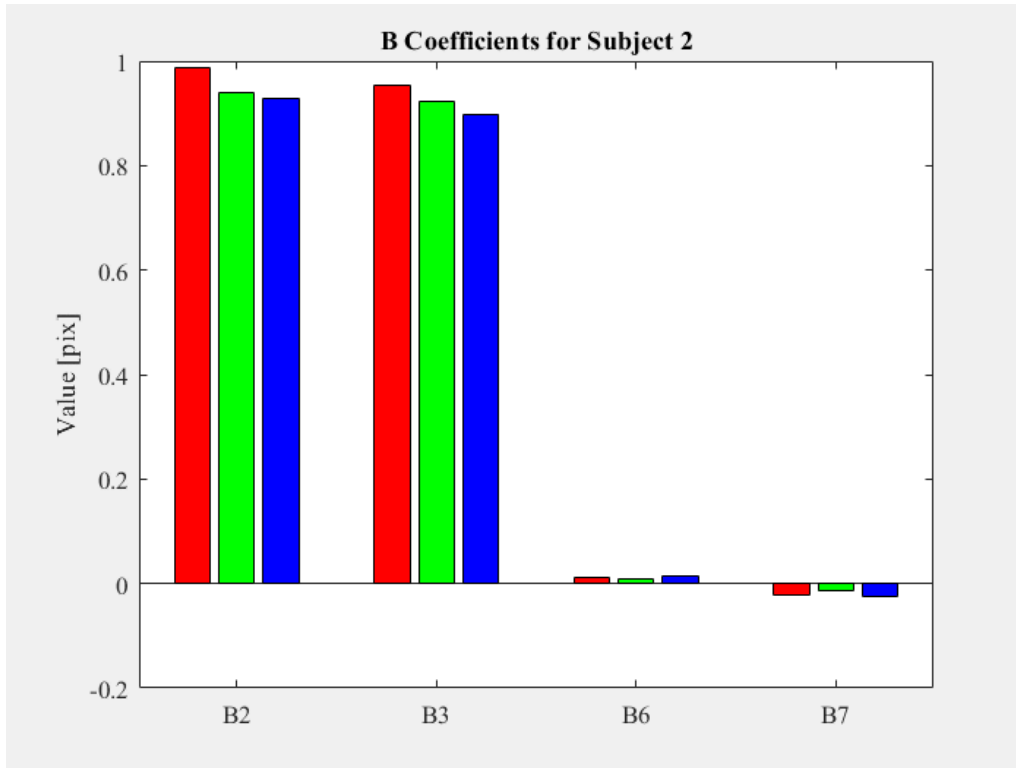


Figure D- 20: Second order distortion coefficient values for all processed retinal images of subject 2.

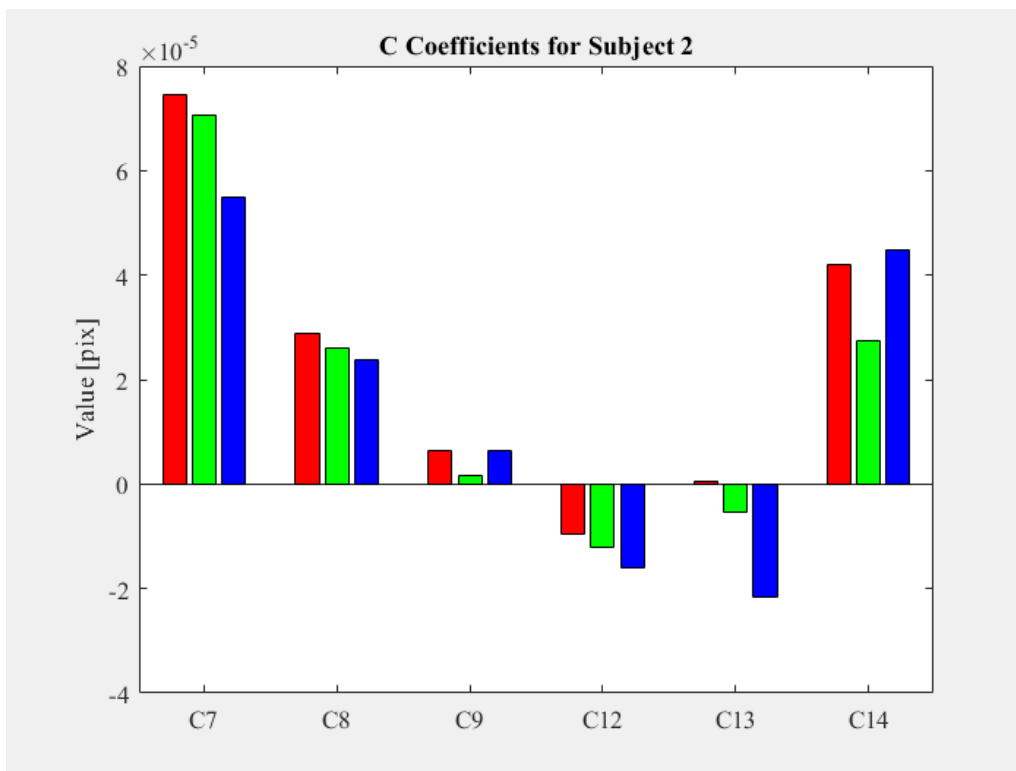


Figure D- 21: Third order distortion coefficient values for all processed retinal images of subject 2.

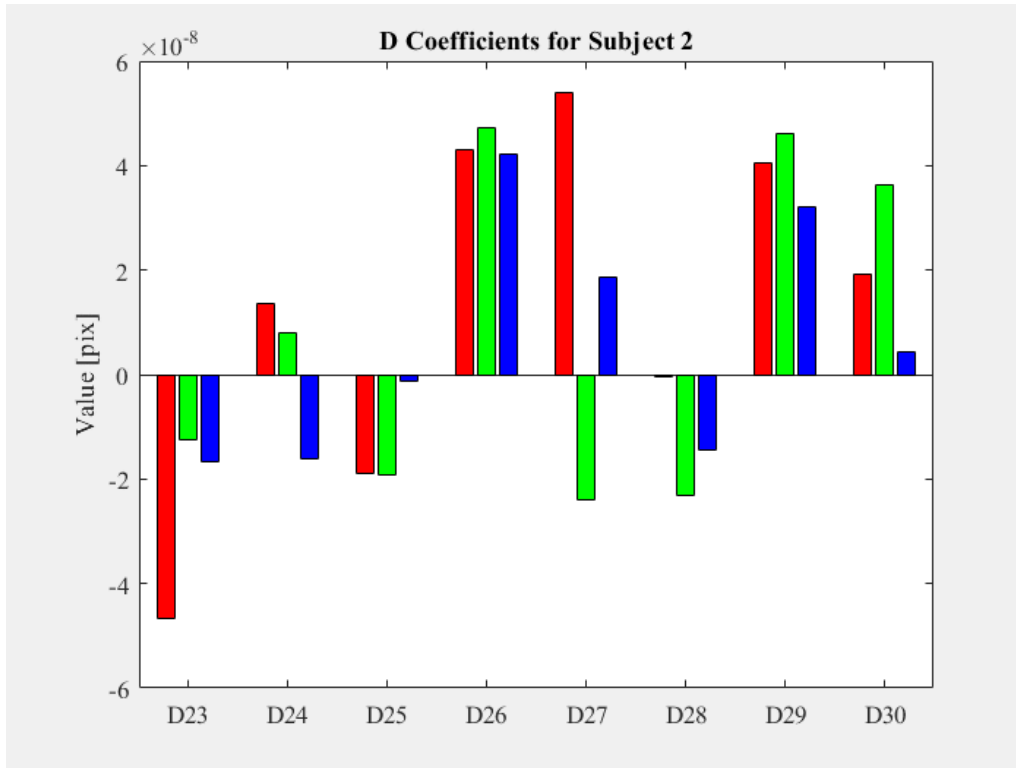


Figure D- 22: Fourth order distortion coefficient values for all processed retinal images of subject 2.

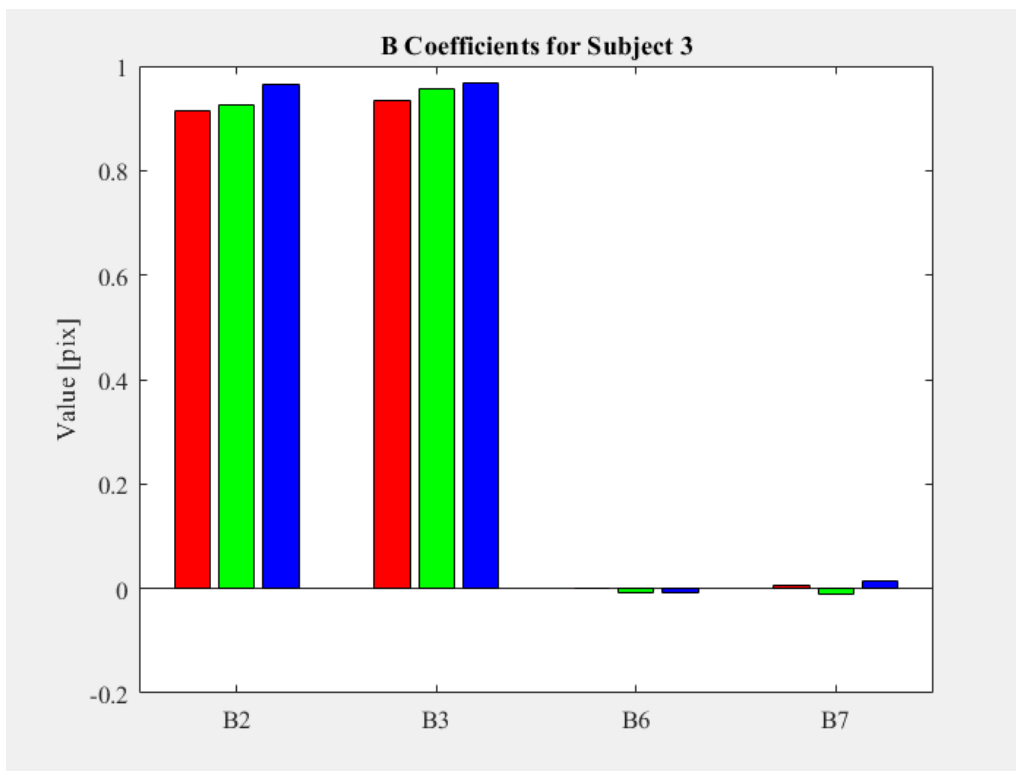


Figure D- 23: Second order distortion coefficient values for all processed retinal images of subject 3.

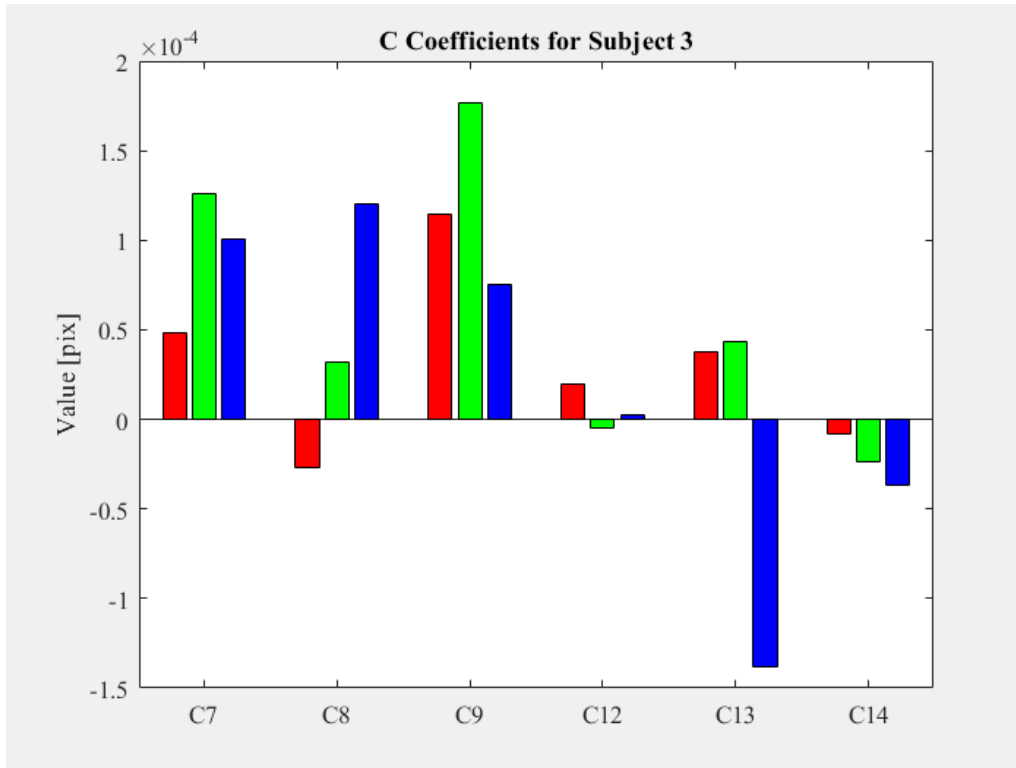


Figure D- 24: Third order distortion coefficient values for all processed retinal images of subject 3.

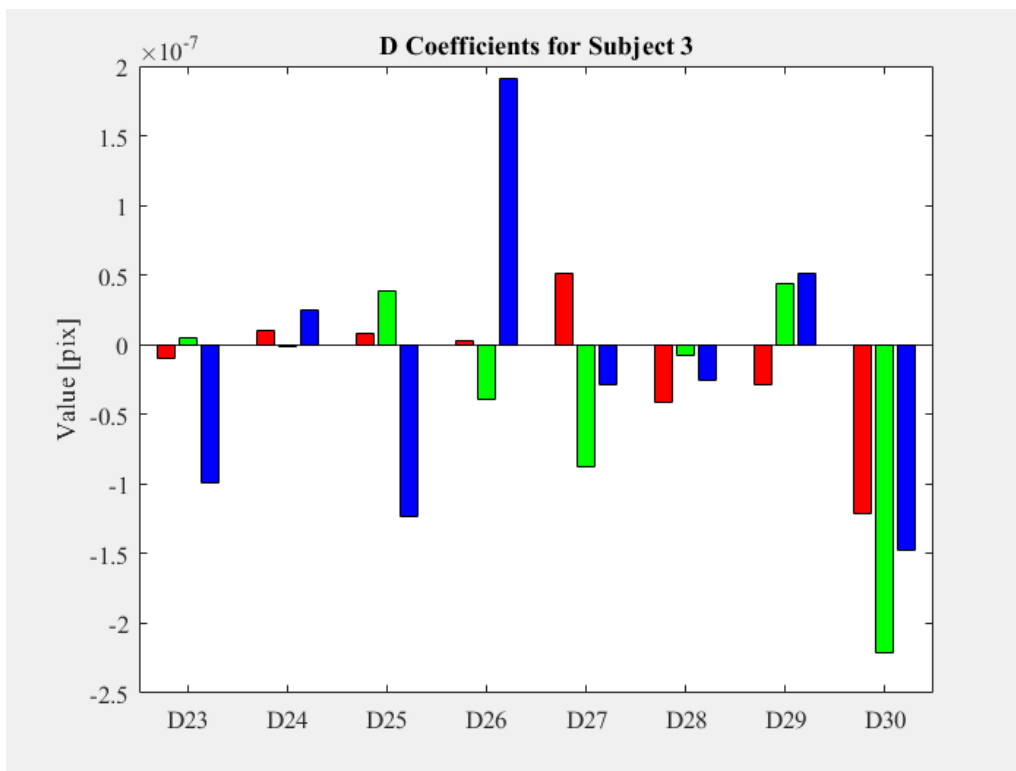


Figure D- 25: Fourth order distortion coefficient values for all processed retinal images of subject 3.

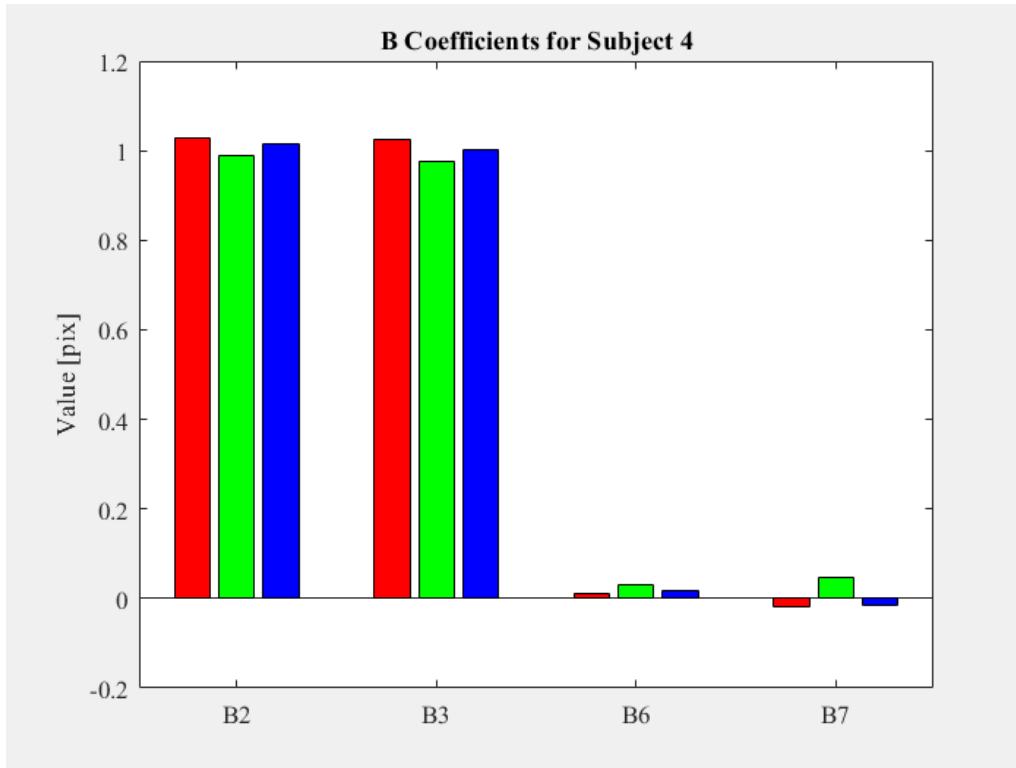


Figure D- 26: Second order distortion coefficient values for all processed retinal images of subject 4.

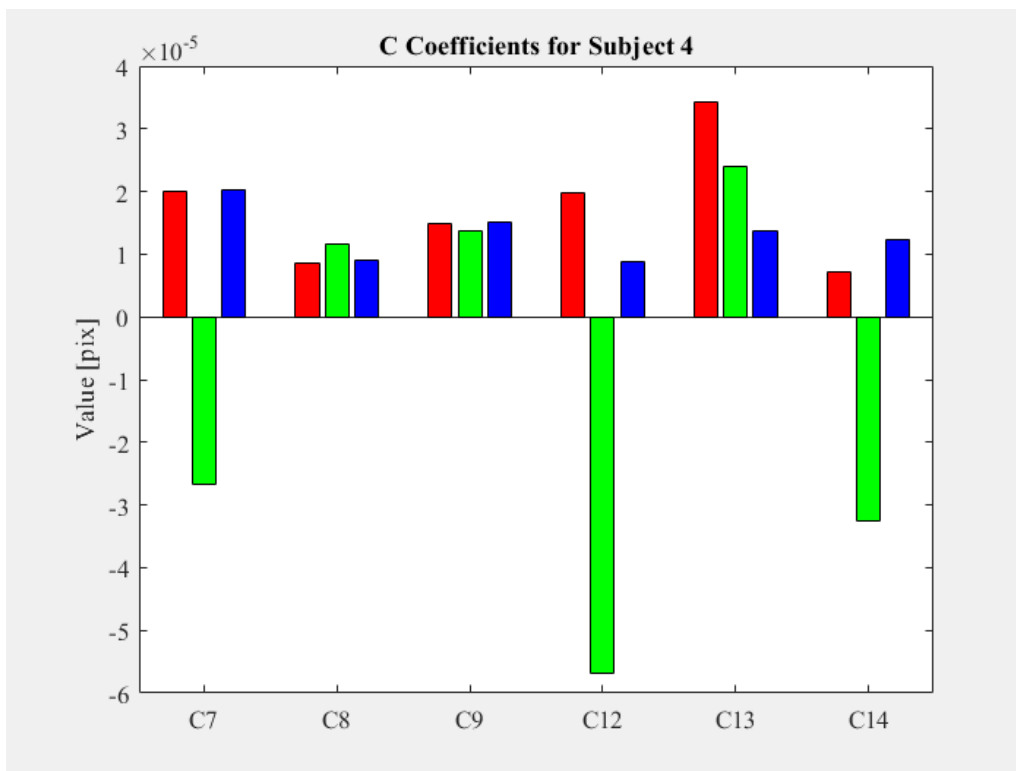


Figure D- 27: Third order distortion coefficient values for all processed retinal images of subject 4.

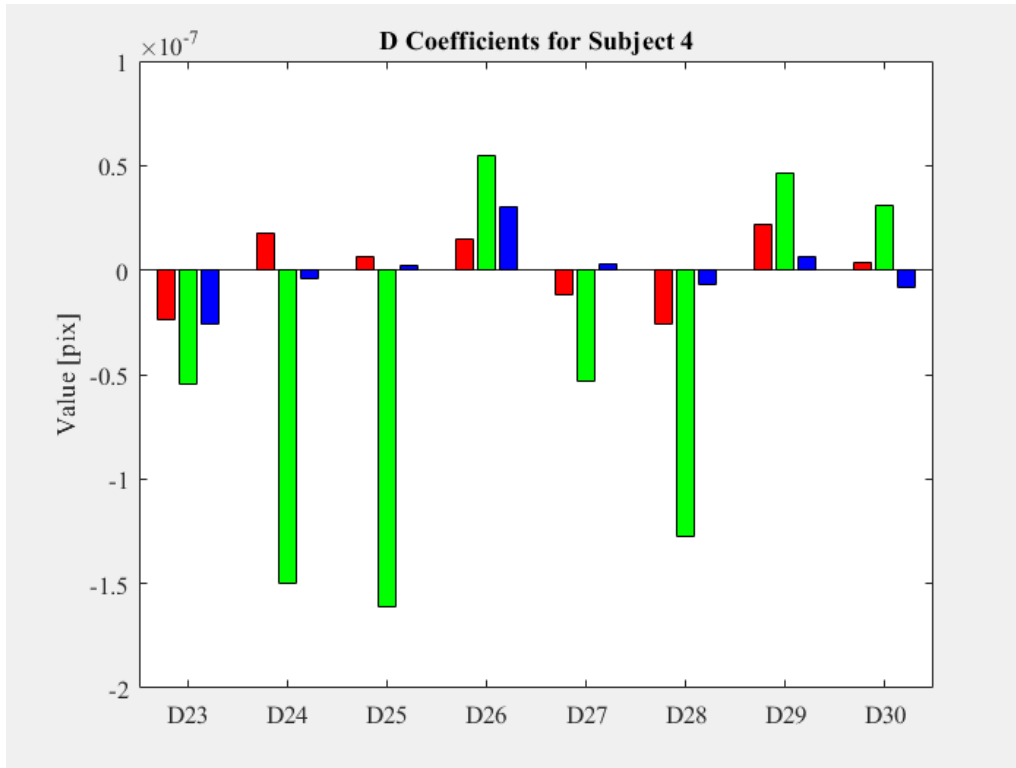


Figure D- 28: Fourth order distortion coefficient values for all processed retinal images of subject 4.

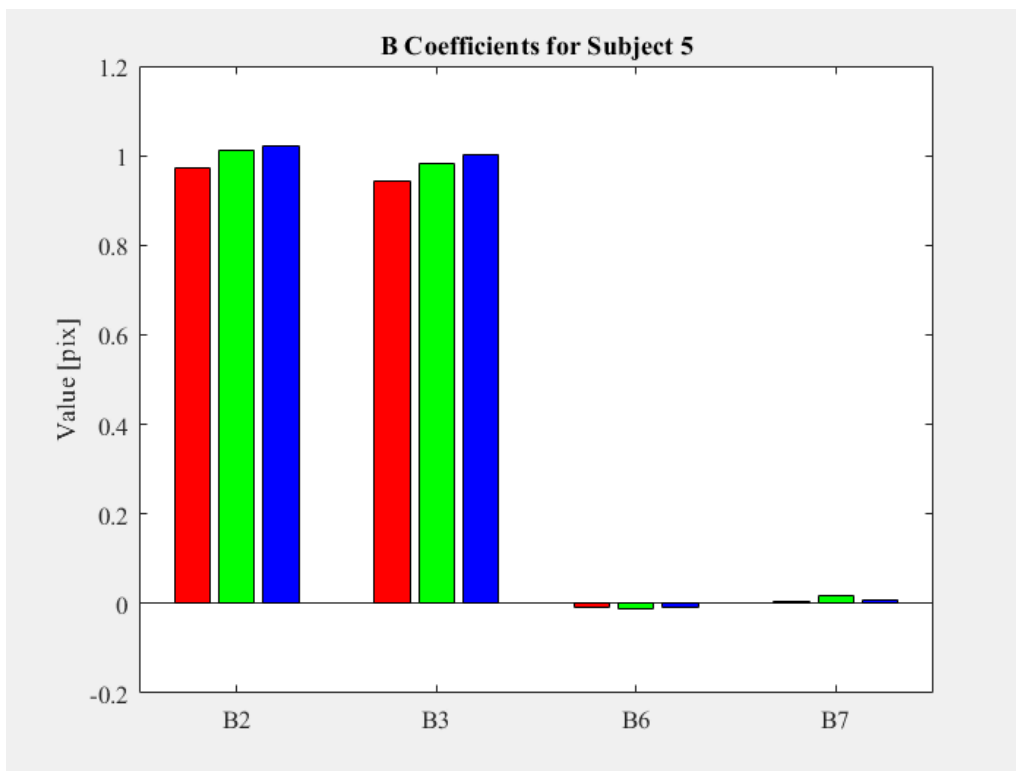


Figure D- 29: Second order distortion coefficient values for all processed retinal images of subject 5.

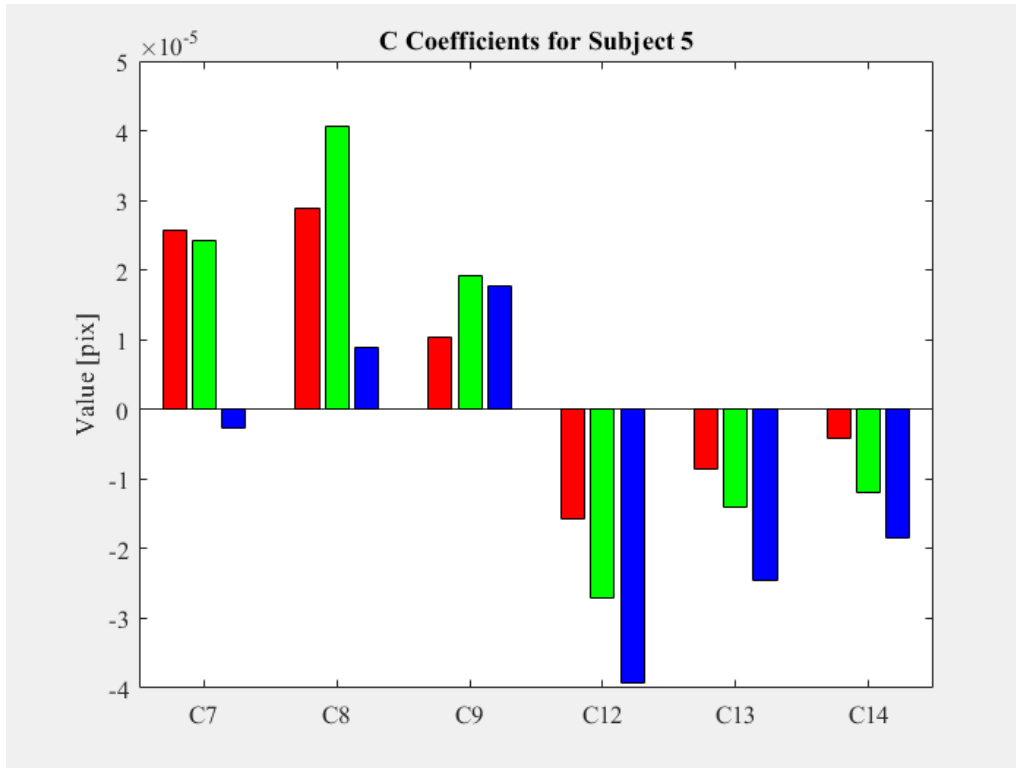


Figure D- 30: Third order distortion coefficient values for all processed retinal images of subject 5.

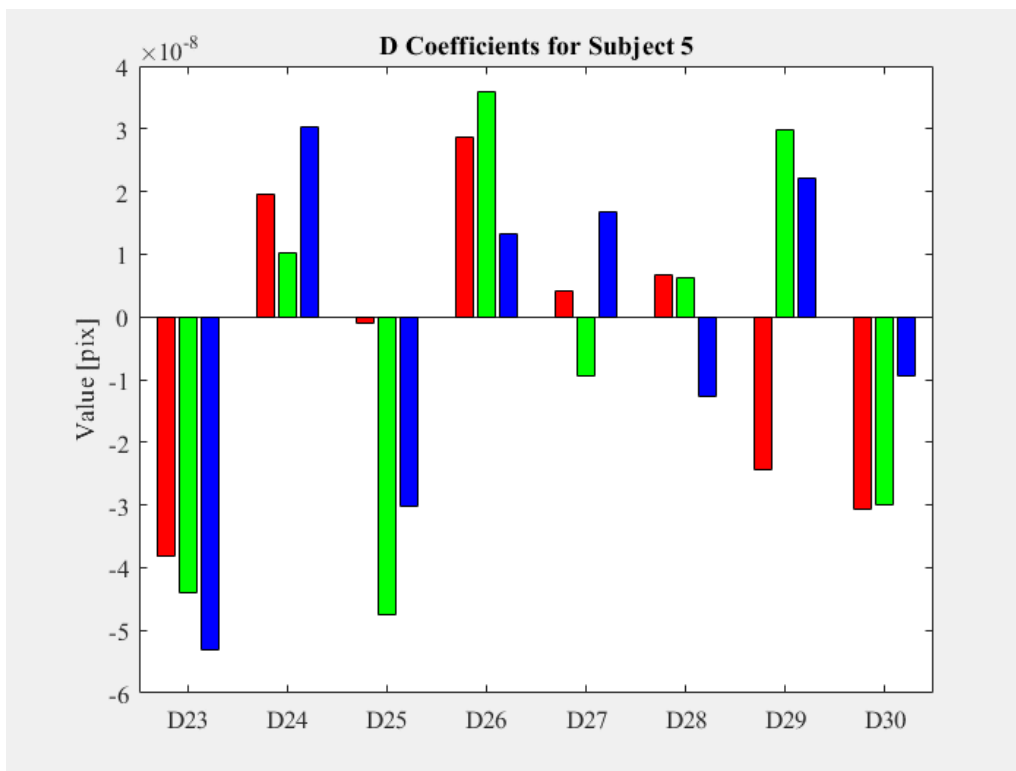


Figure D- 31: Fourth order distortion coefficient values for all processed retinal images of subject 5.

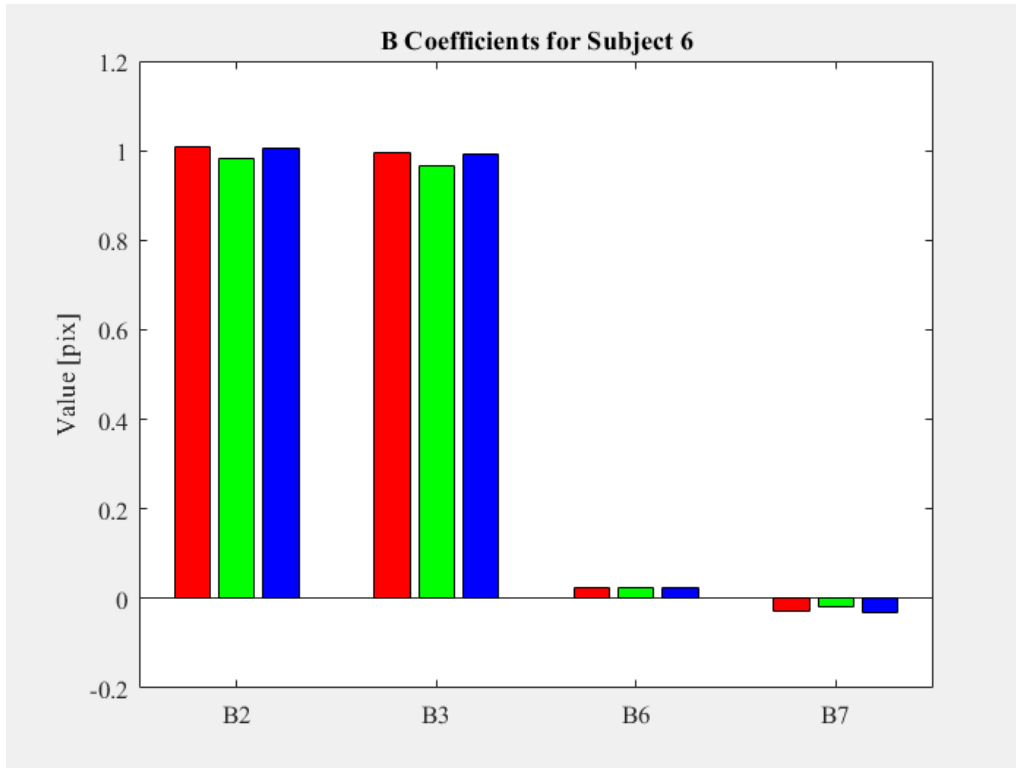


Figure D- 32: Second order distortion coefficient values for all processed retinal images of subject 6.

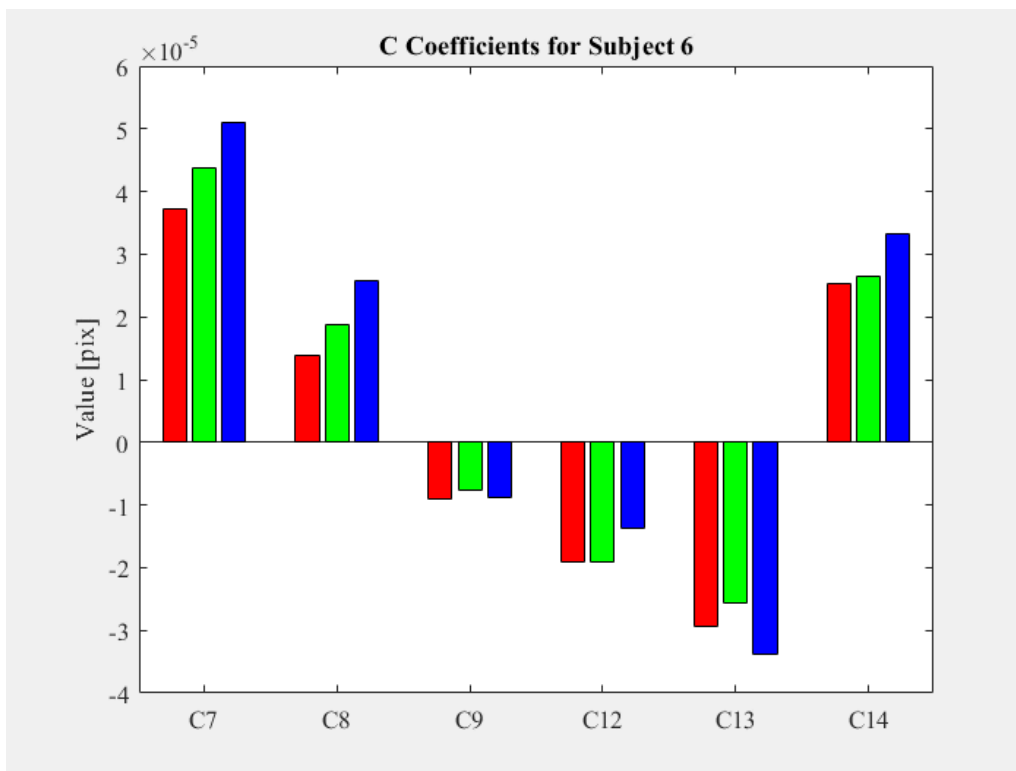


Figure D- 33: Third order distortion coefficient values for all processed retinal images of subject 6.

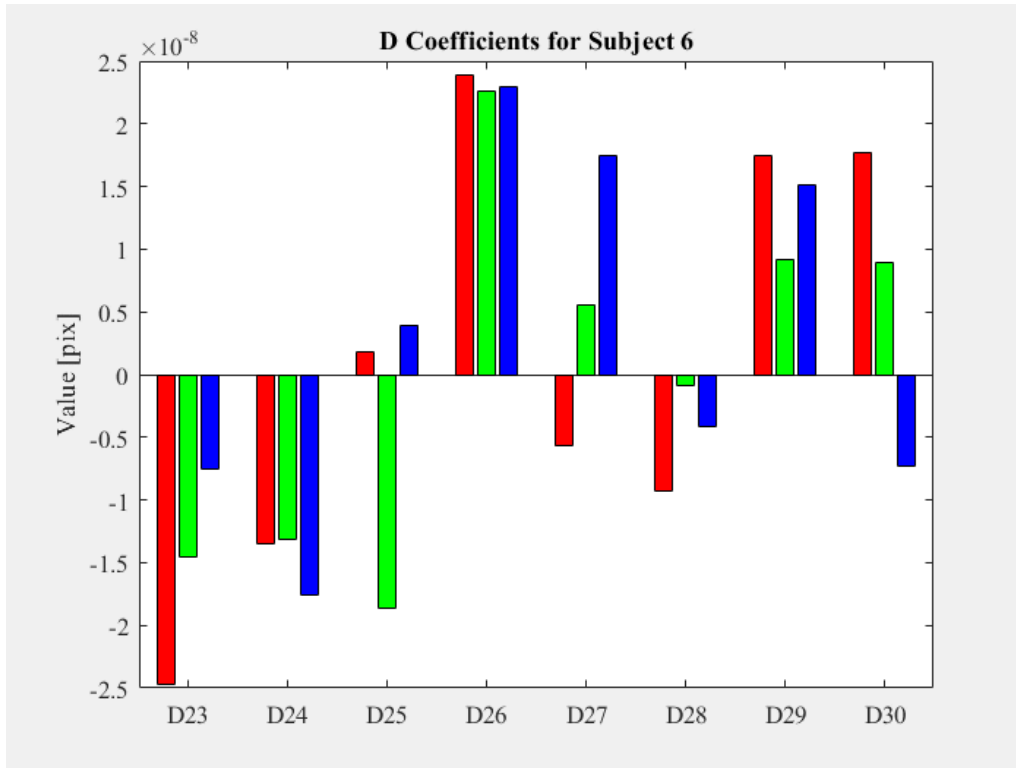


Figure D- 34: Fourth order distortion coefficient values for all processed retinal images of subject 6.

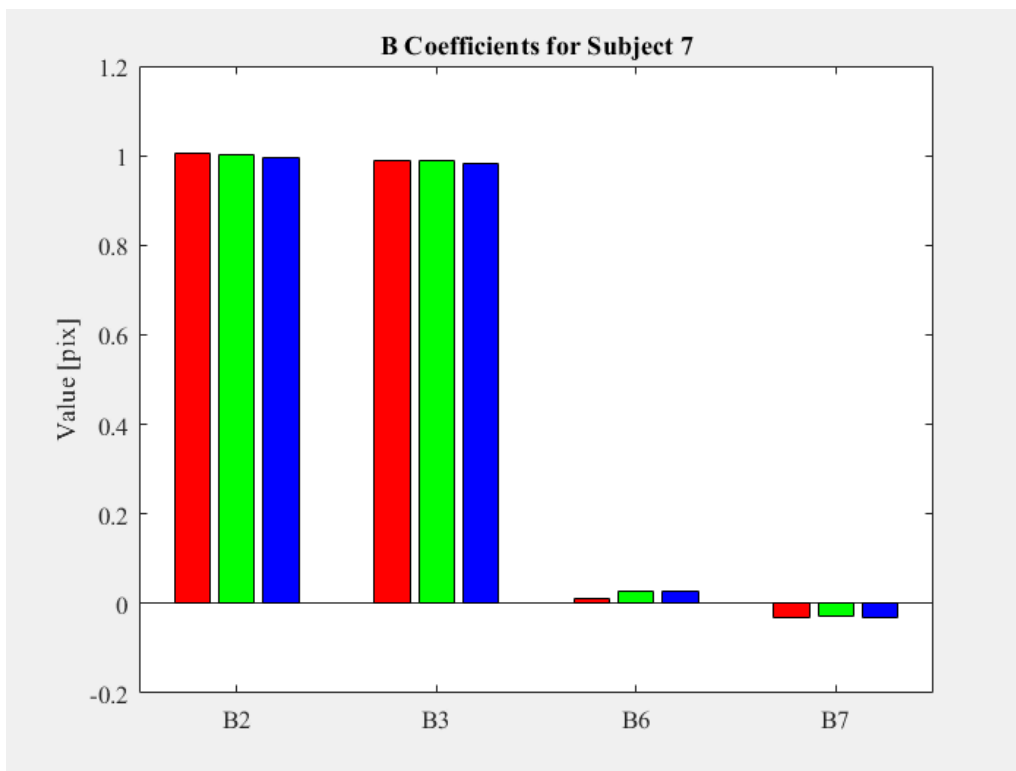


Figure D- 35: Second order distortion coefficient values for all processed retinal images of subject 7.

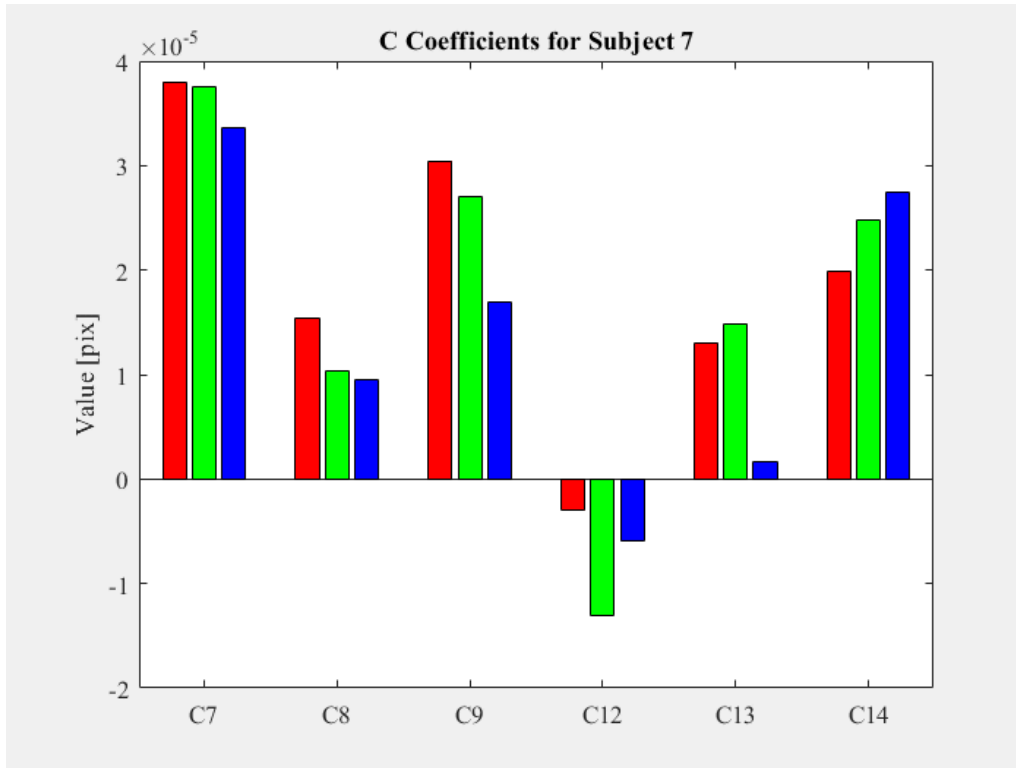


Figure D- 36: Third order distortion coefficient values for all processed retinal images of subject 7.

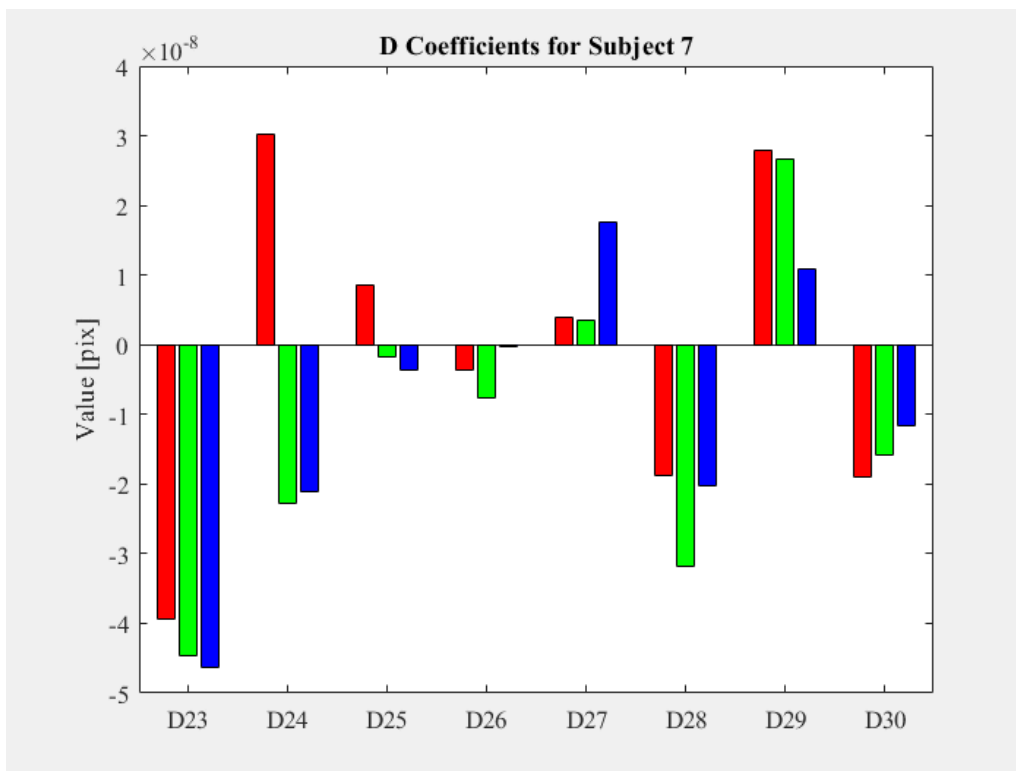


Figure D- 37: Fourth order distortion coefficient values for all processed retinal images of subject 7.

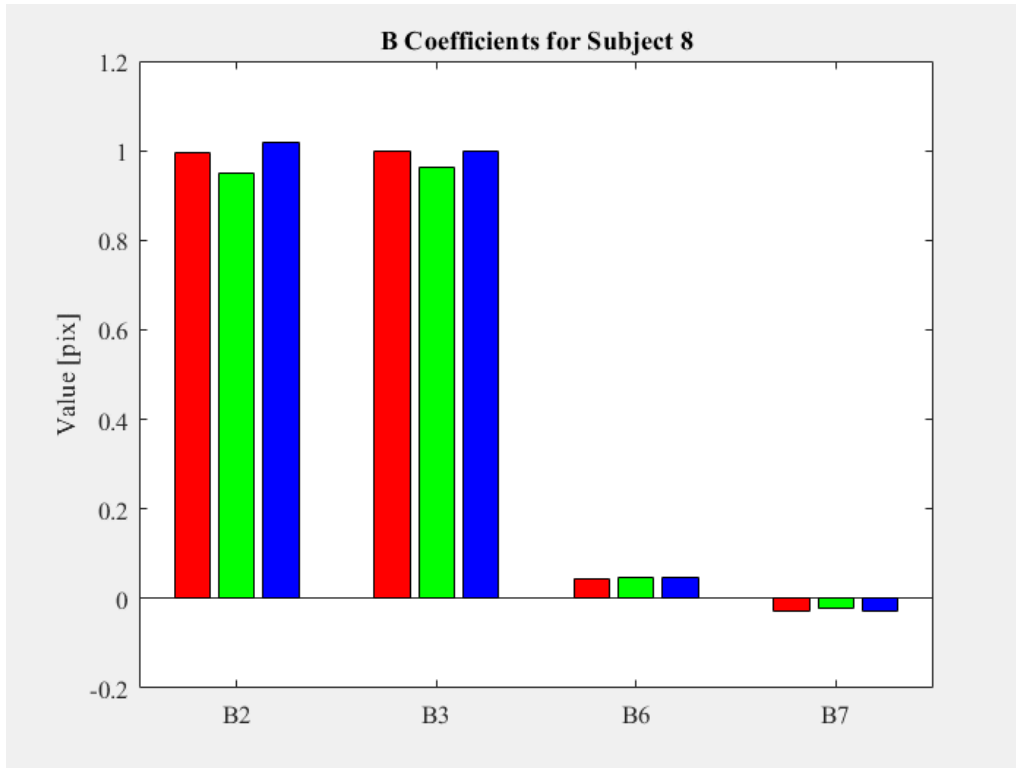


Figure D- 38: Second order distortion coefficient values for all processed retinal images of subject 8.

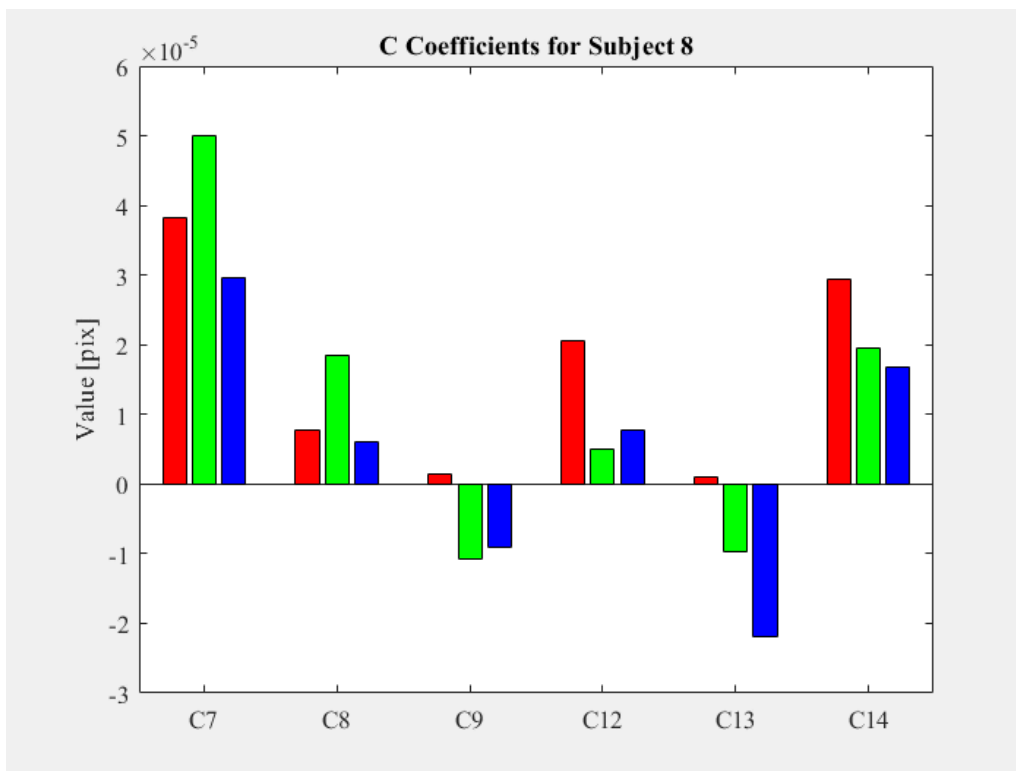


Figure D- 39: Third order distortion coefficient values for all processed retinal images of subject 8.

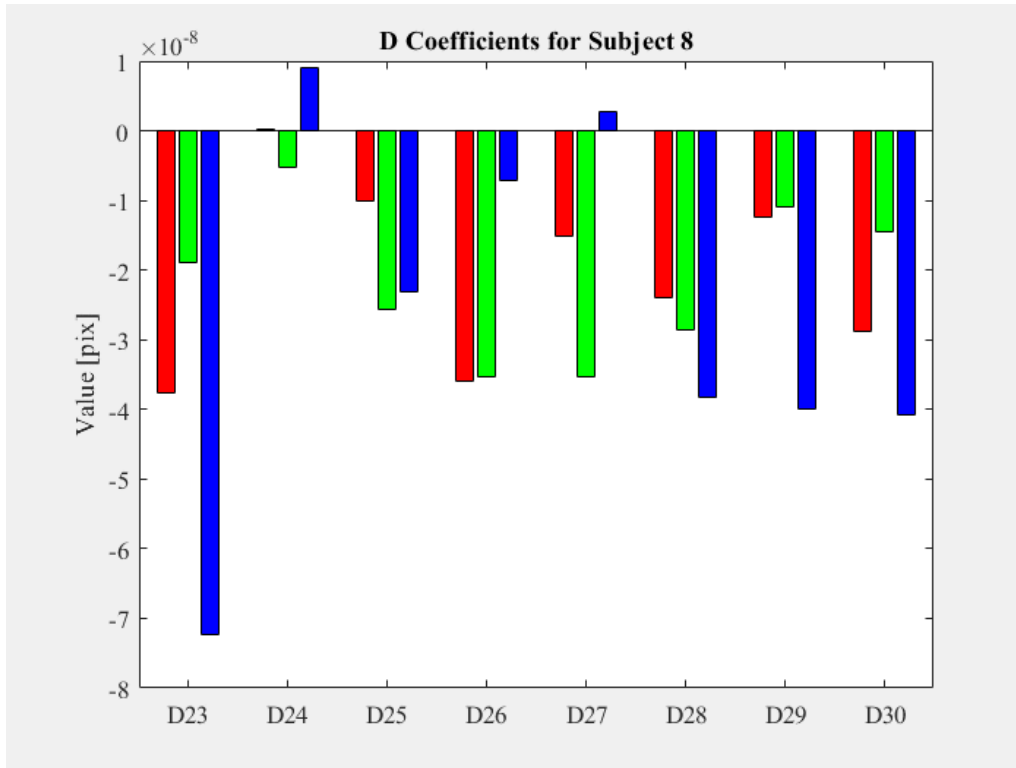


Figure D- 40: Fourth order distortion coefficient values for all processed retinal images of subject 8.

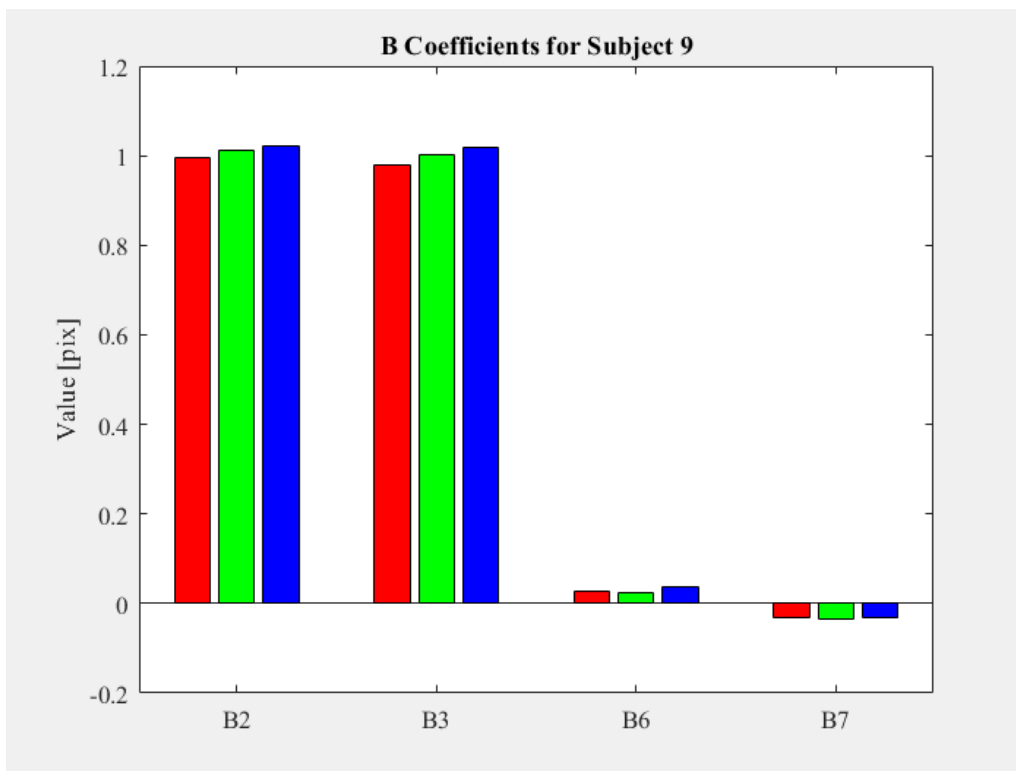


Figure D- 41: Second order distortion coefficient values for all processed retinal images of subject 9.

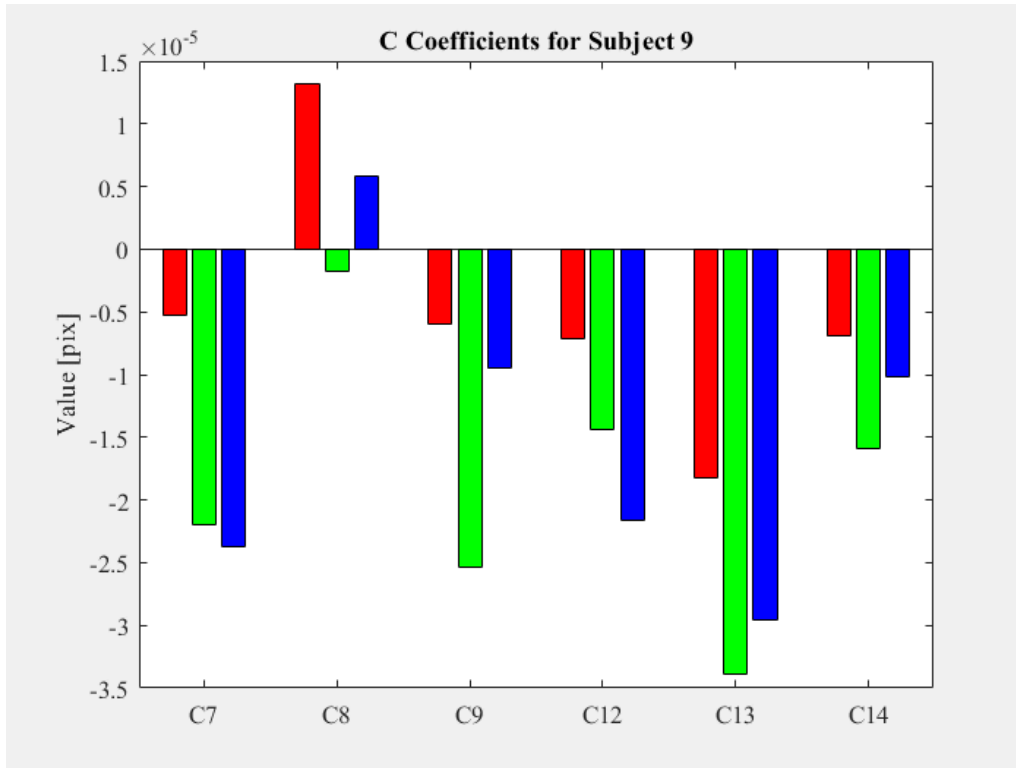


Figure D- 42: Third order distortion coefficient values for all processed retinal images of subject 9.

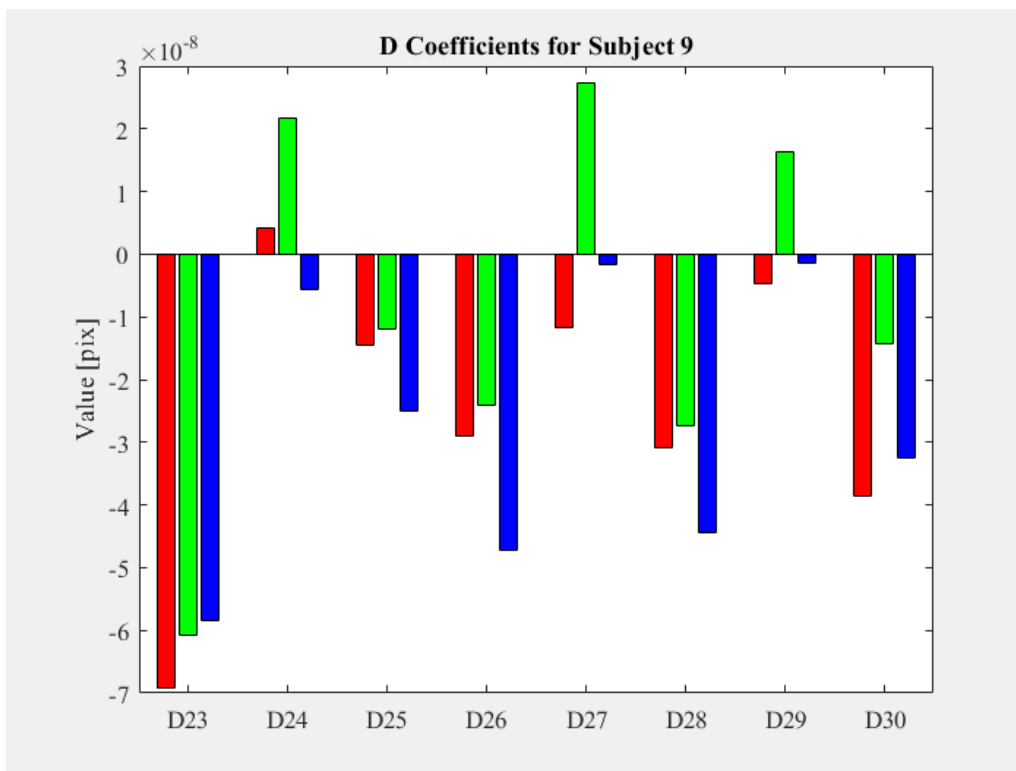


Figure D- 43: Fourth order distortion coefficient values for all processed retinal images of subject 9.

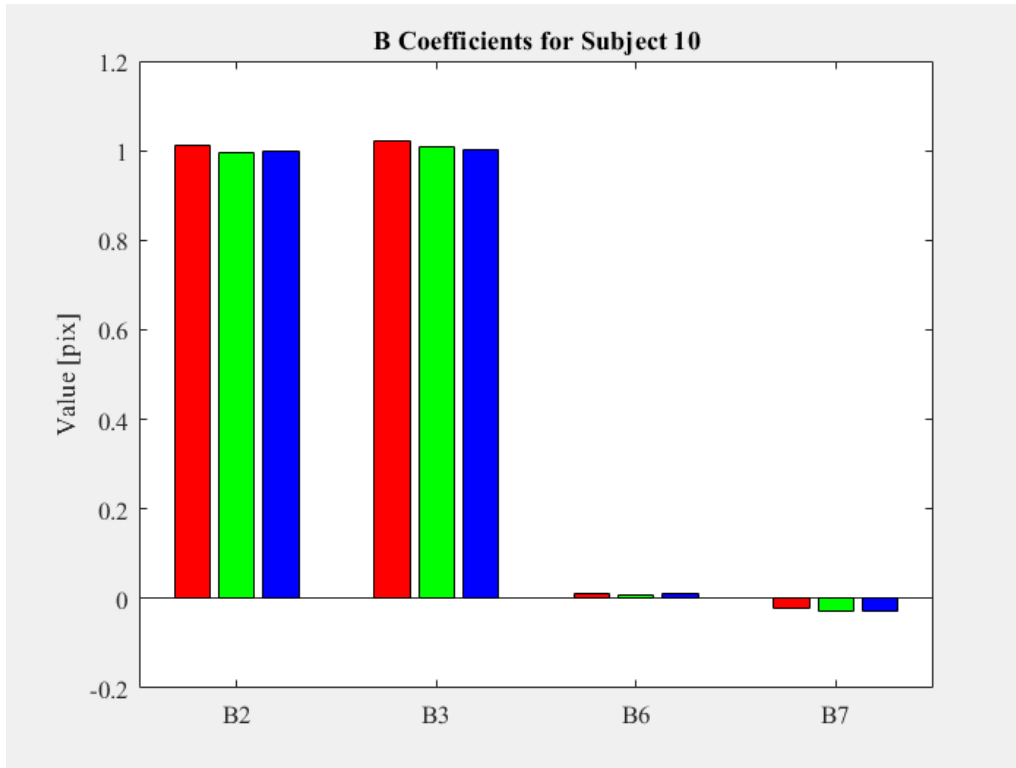


Figure D- 44: Second order distortion coefficient values for all processed retinal images of subject 10.

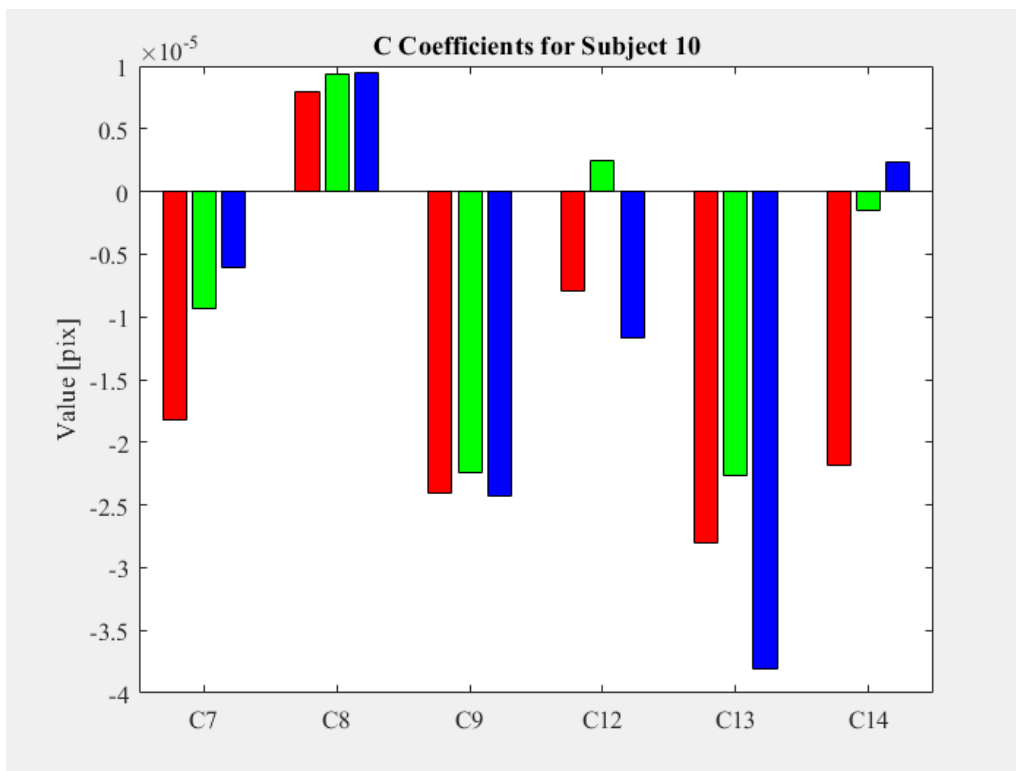


Figure D- 45: Third order distortion coefficient values for all processed retinal images of subject 10.

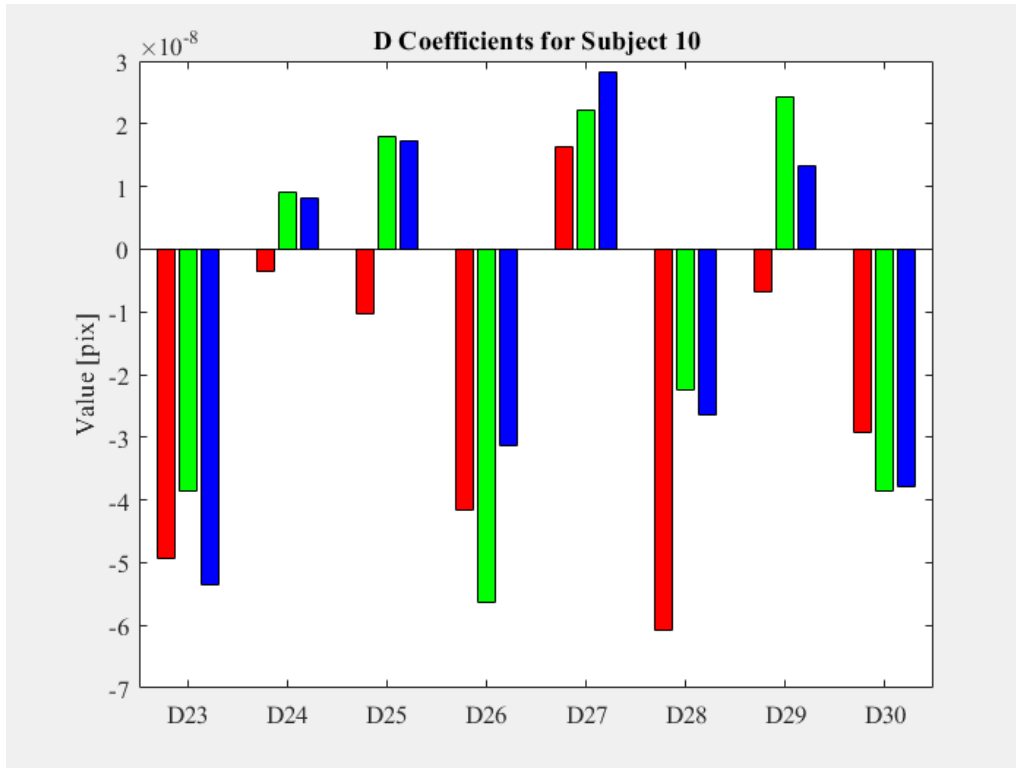


Figure D- 46: Fourth order distortion coefficient values for all processed retinal images of subject 10.

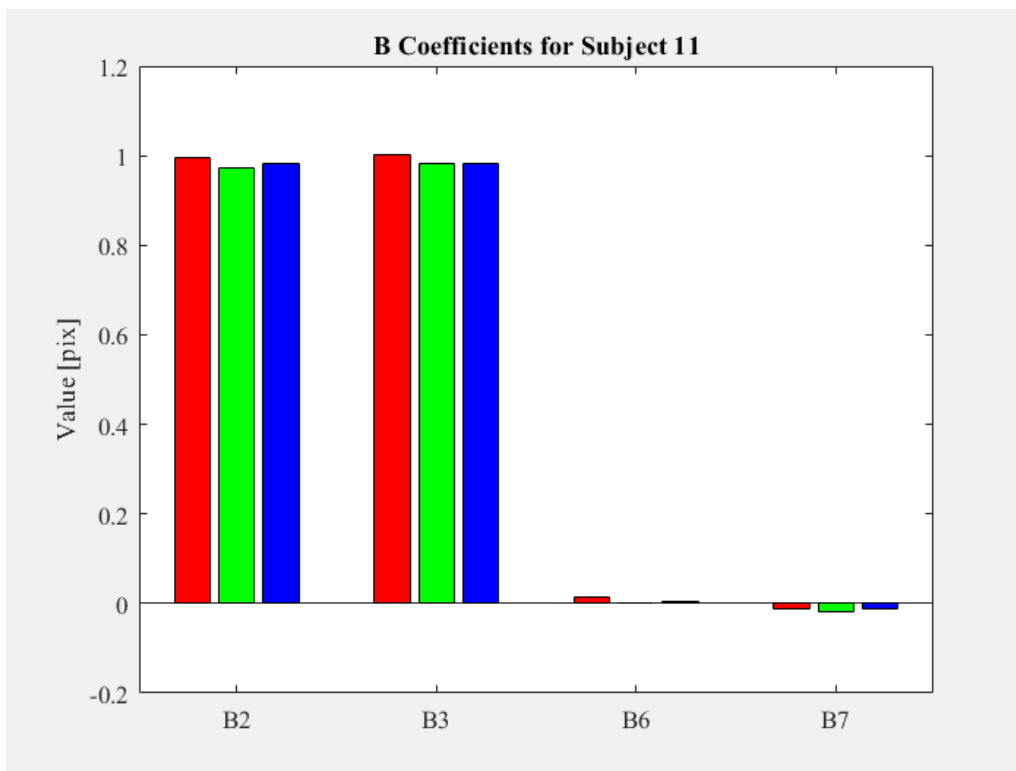


Figure D- 47: Second order distortion coefficient values for all processed retinal images of subject 11.

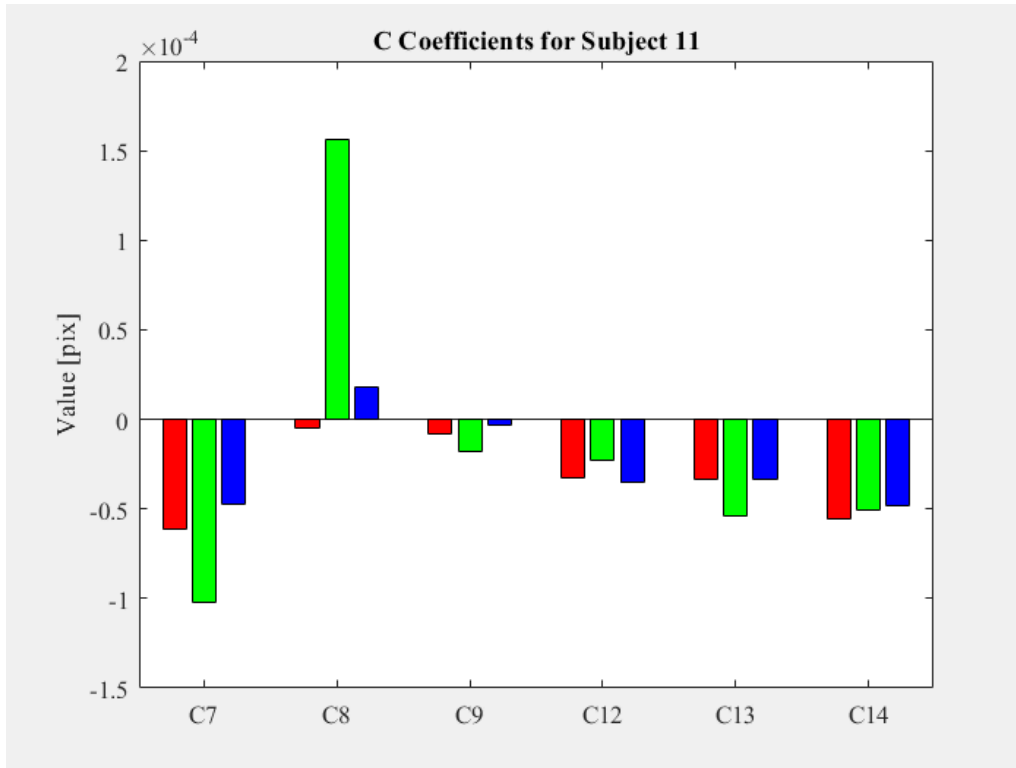


Figure D- 48: Third order distortion coefficient values for all processed retinal images of subject 11.

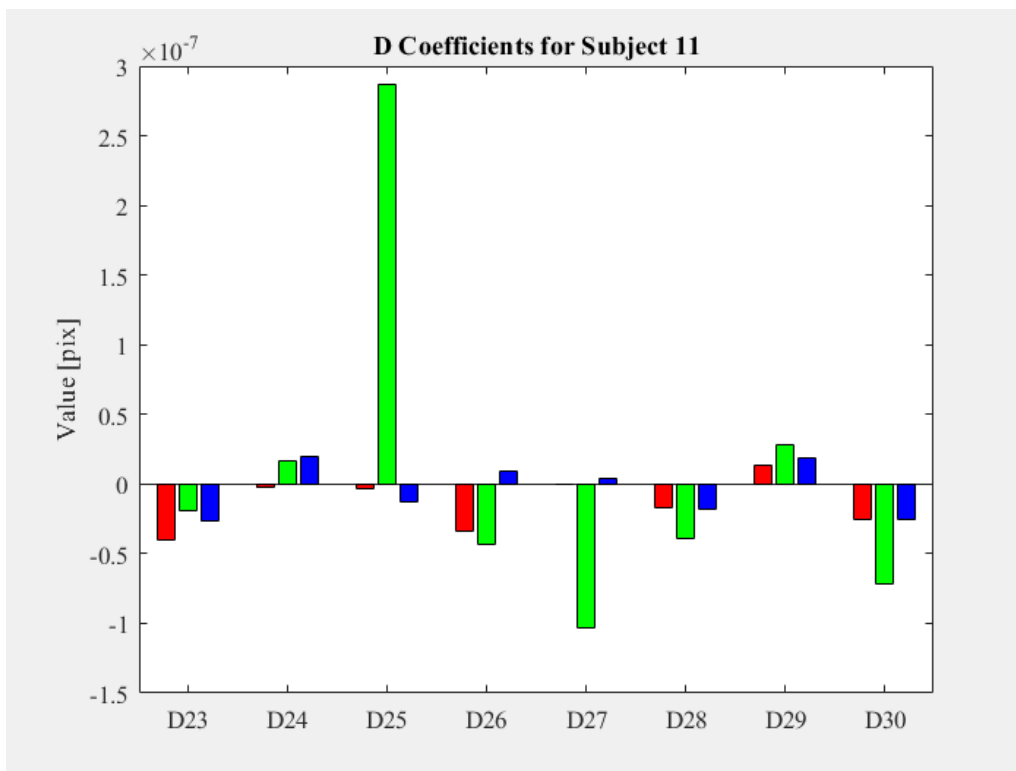


Figure D- 49: Fourth order distortion coefficient values for all processed retinal images of subject 11.

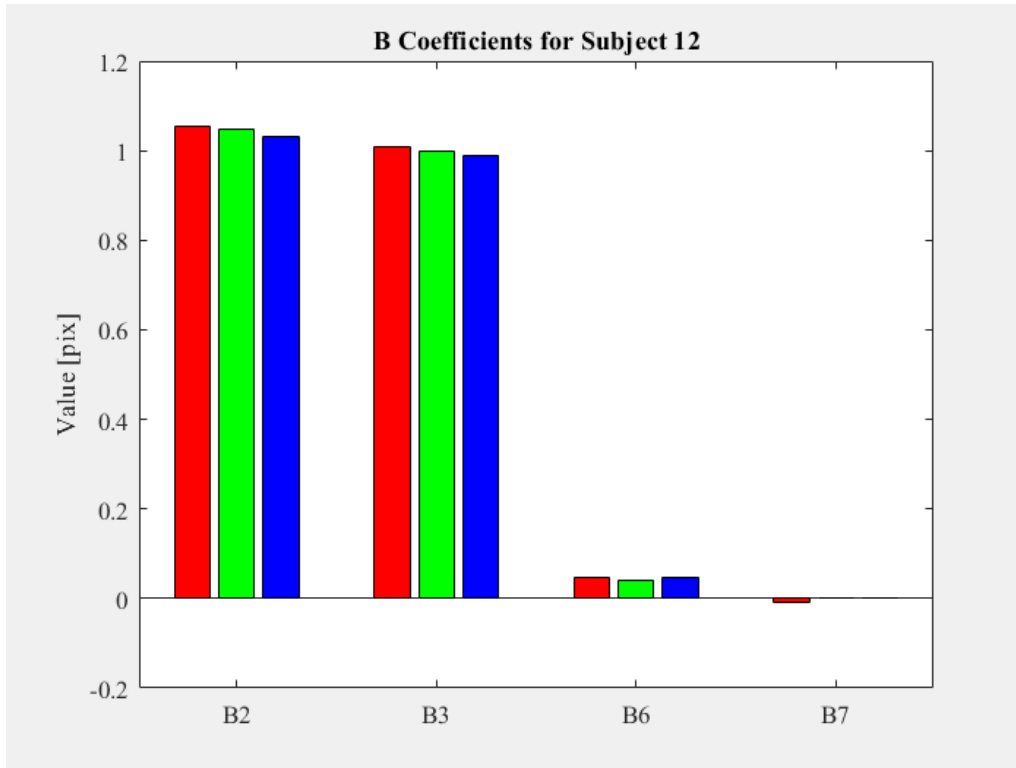


Figure D- 50: Second order distortion coefficient values for all processed retinal images of subject 12.

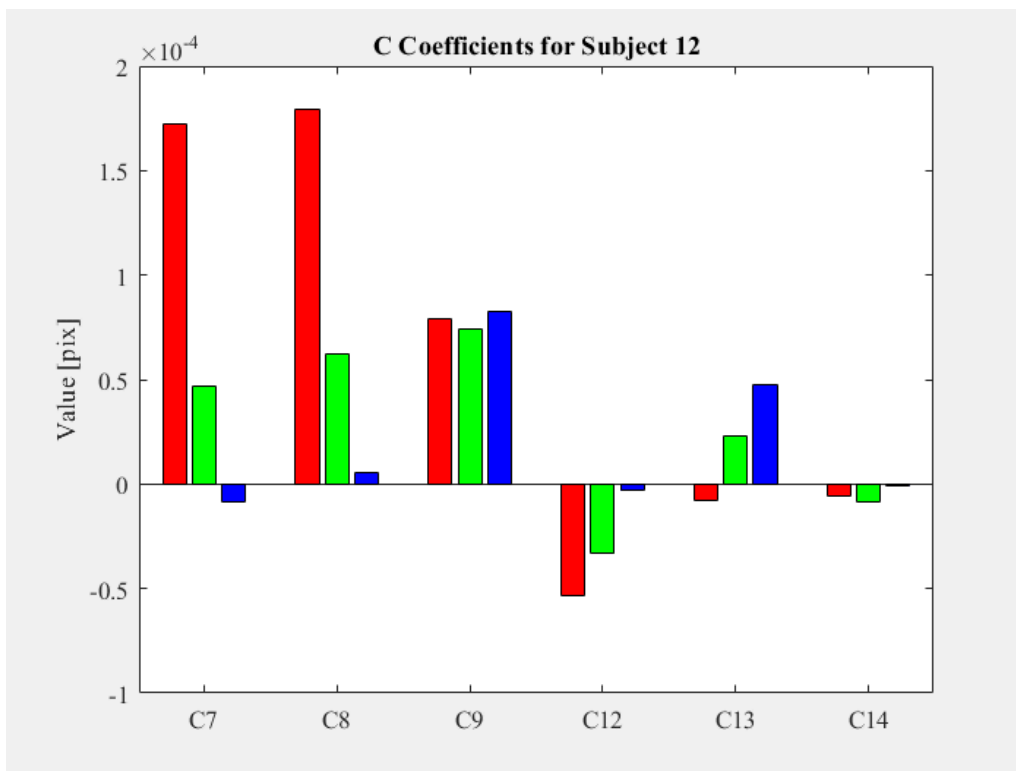


Figure D- 51: Third order distortion coefficient values for all processed retinal images of subject 12.

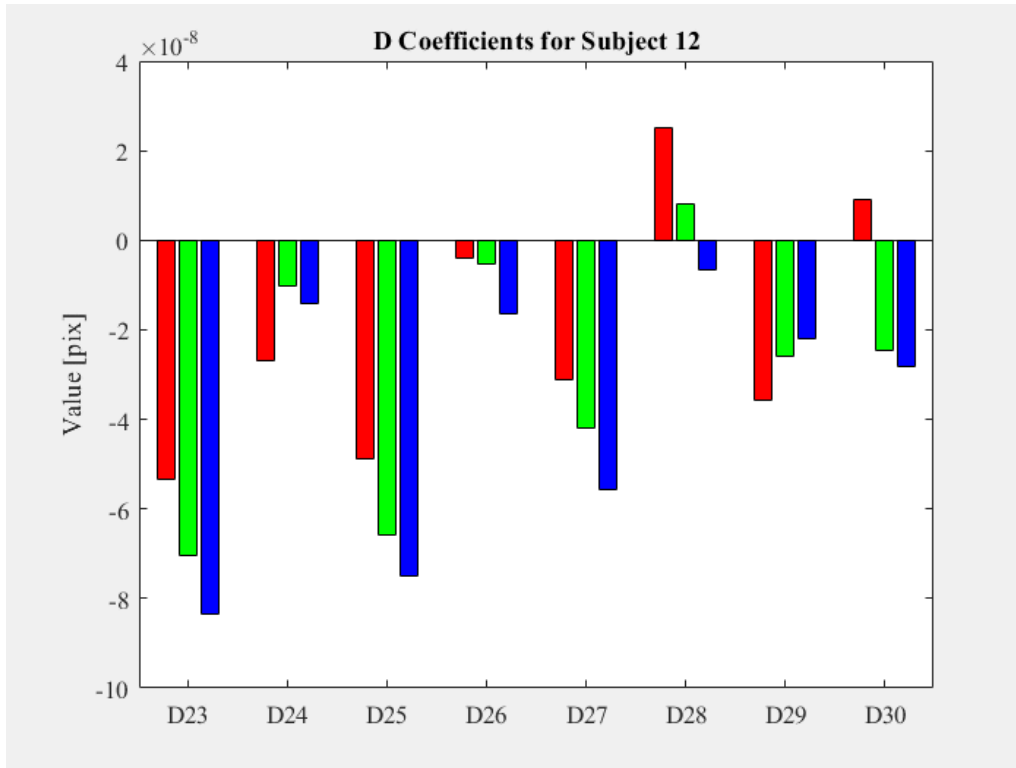


Figure D- 52: Fourth order distortion coefficient values for all processed retinal images of subject 12.

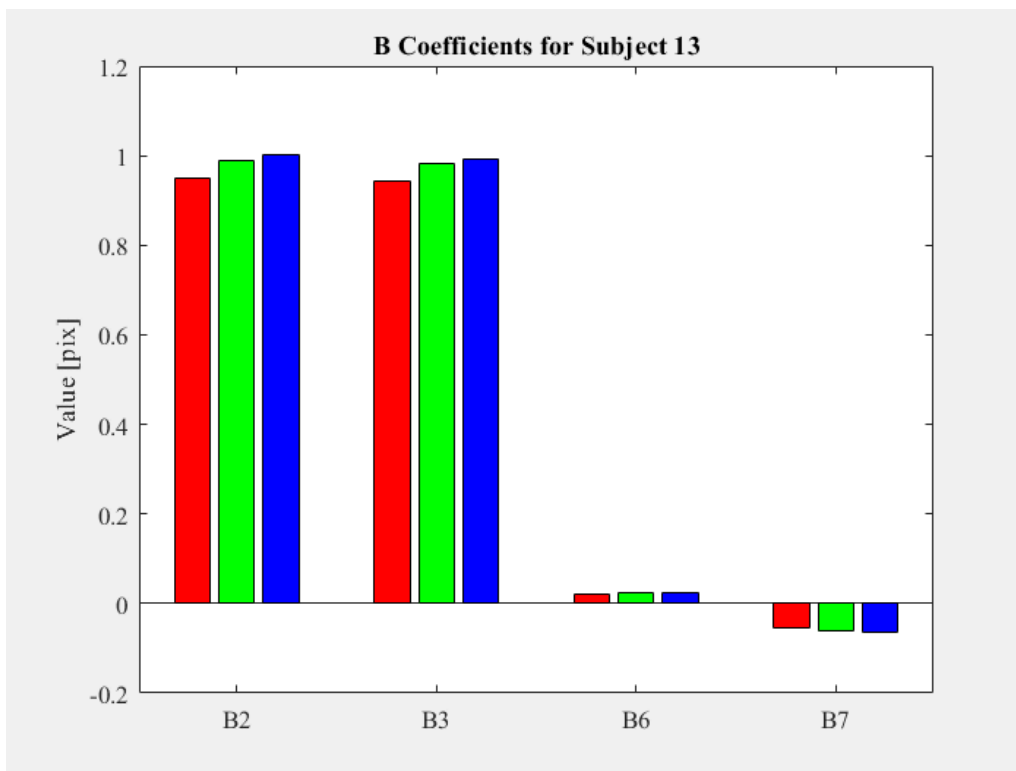


Figure D- 53: Second order distortion coefficient values for all processed retinal images of subject 13.

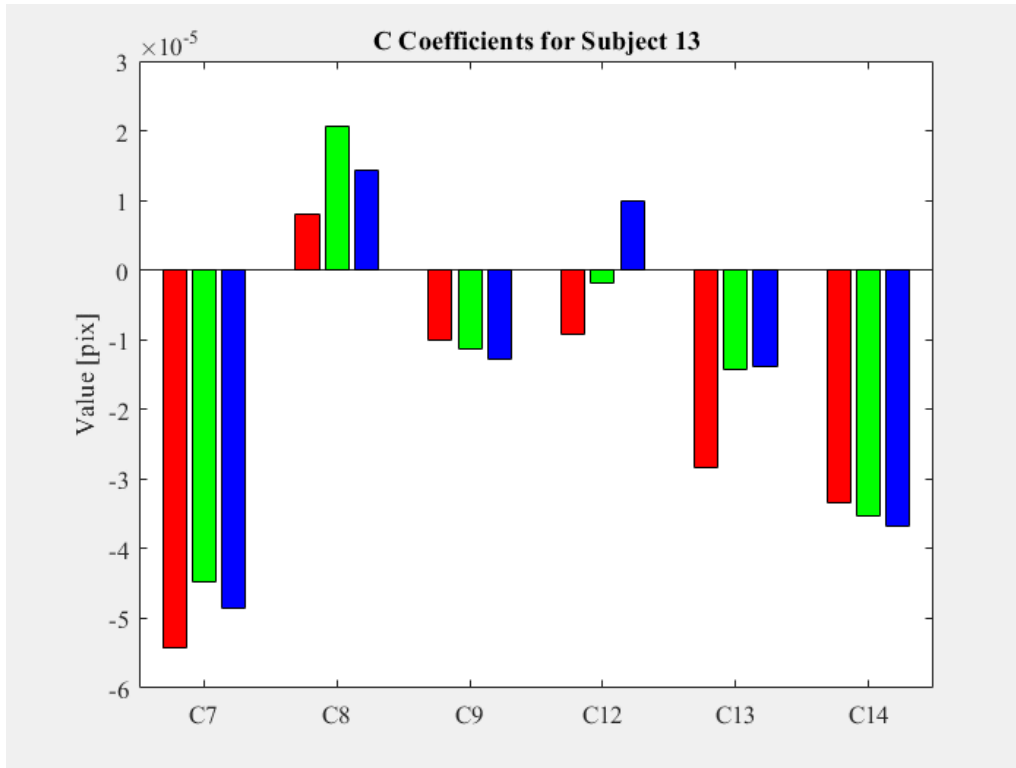


Figure D- 54: Third order distortion coefficient values for all processed retinal images of subject 13.

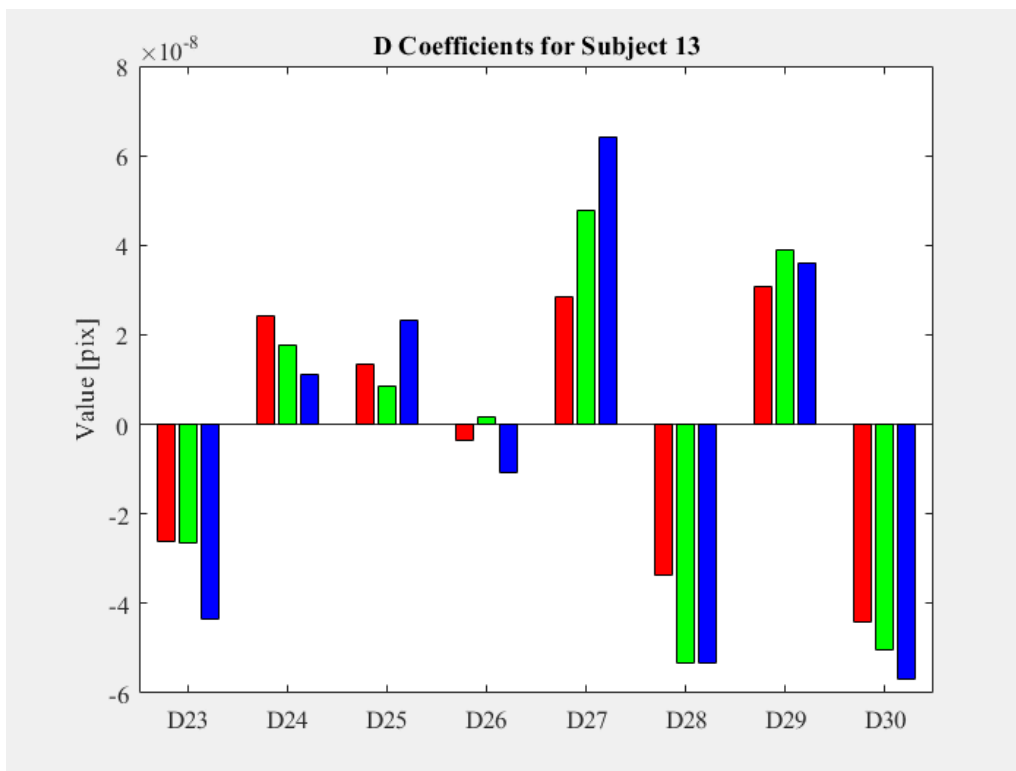


Figure D- 55: Fourth order distortion coefficient values for all processed retinal images of subject 13.

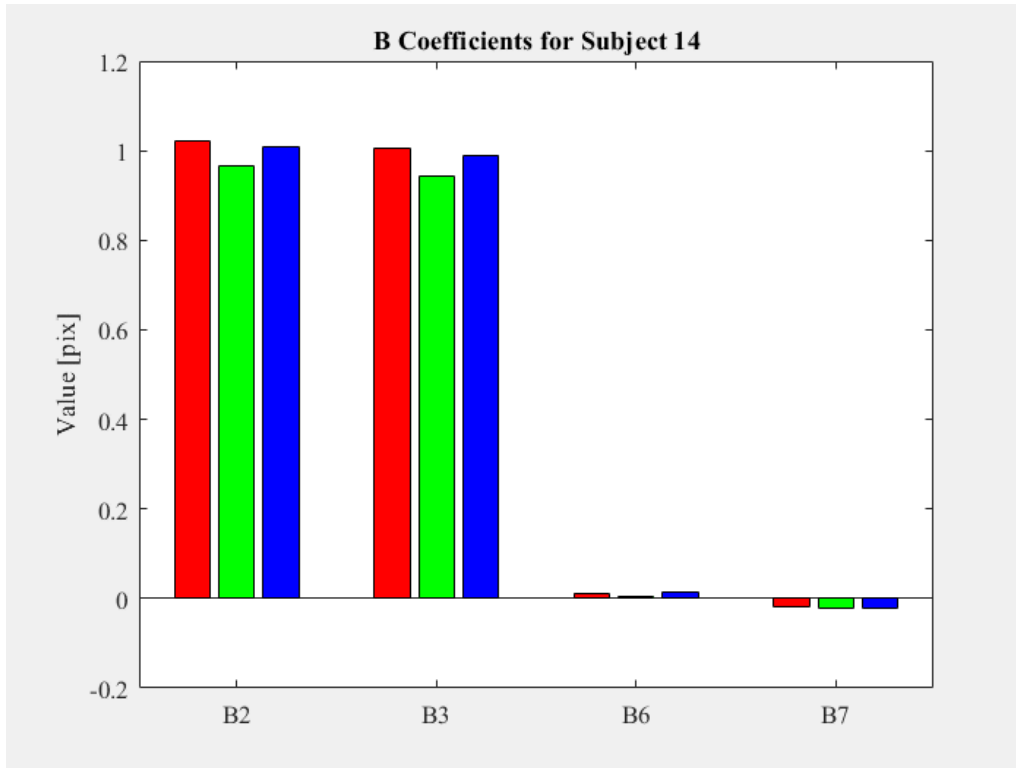


Figure D- 56: Second order distortion coefficient values for all processed retinal images of subject 14.

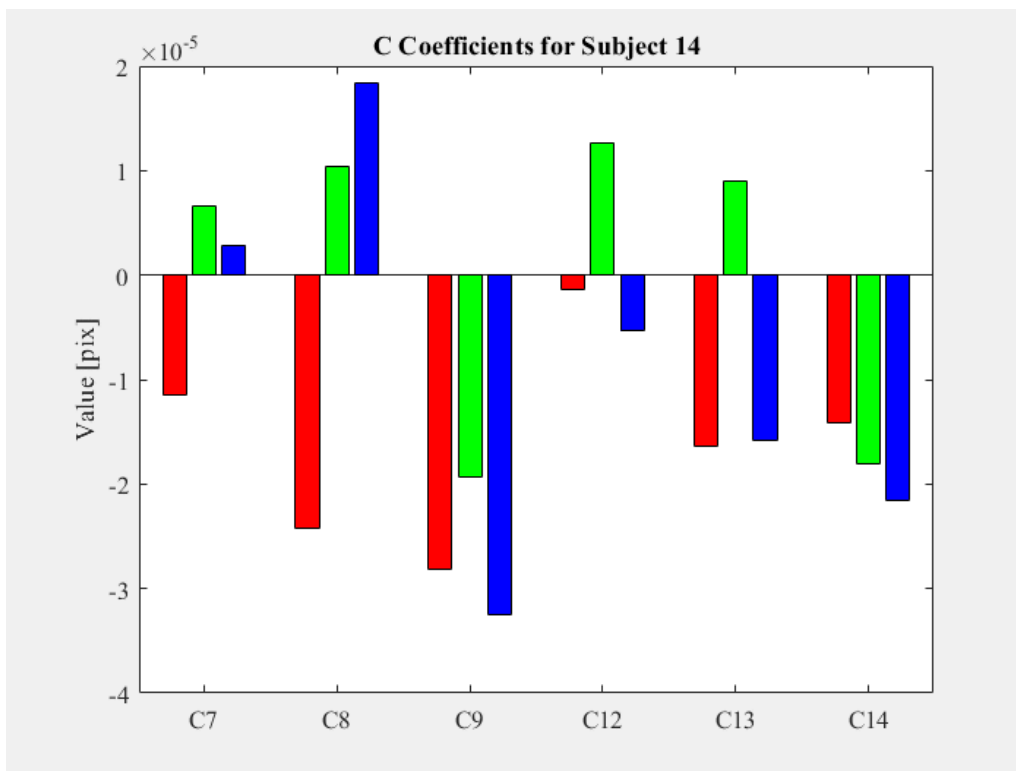


Figure D- 57: Third order distortion coefficient values for all processed retinal images of subject 14.

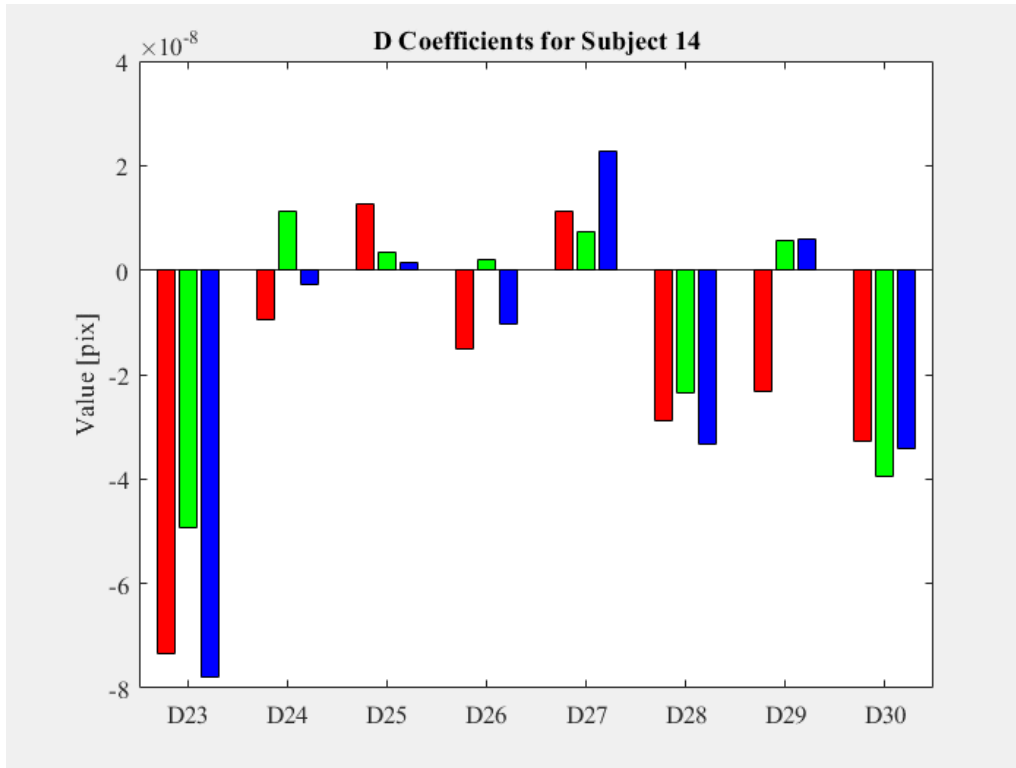


Figure D- 58: Fourth order distortion coefficient values for all processed retinal images of subject 14.

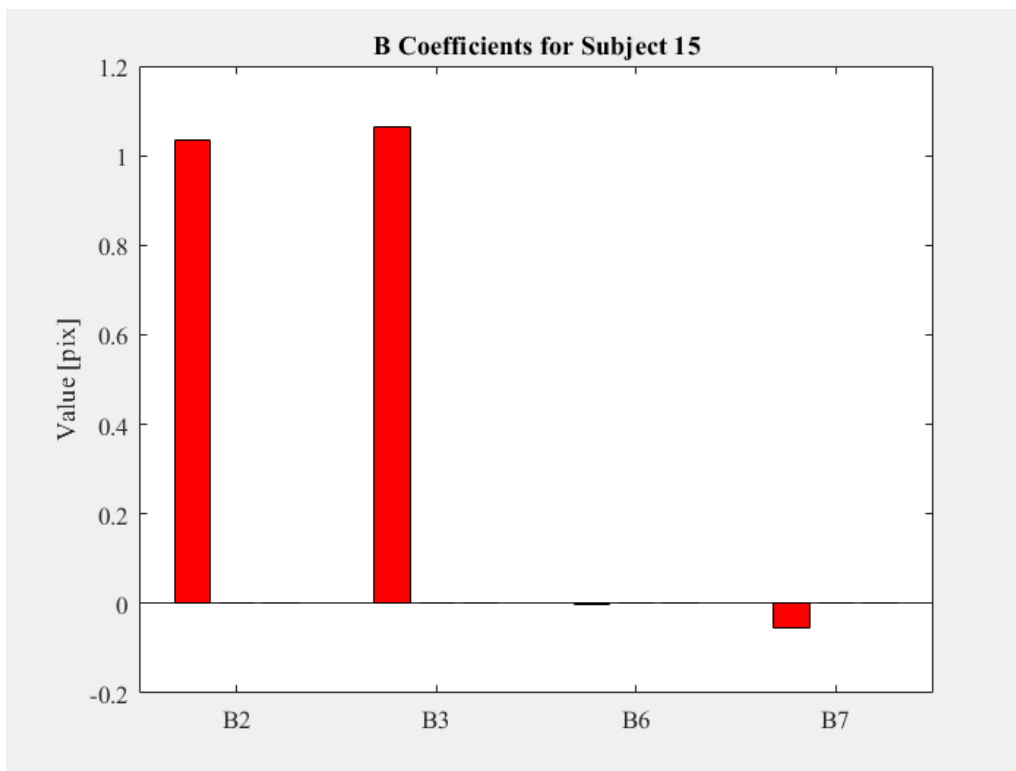


Figure D- 59: Second order distortion coefficient values for all processed retinal images of subject 15.

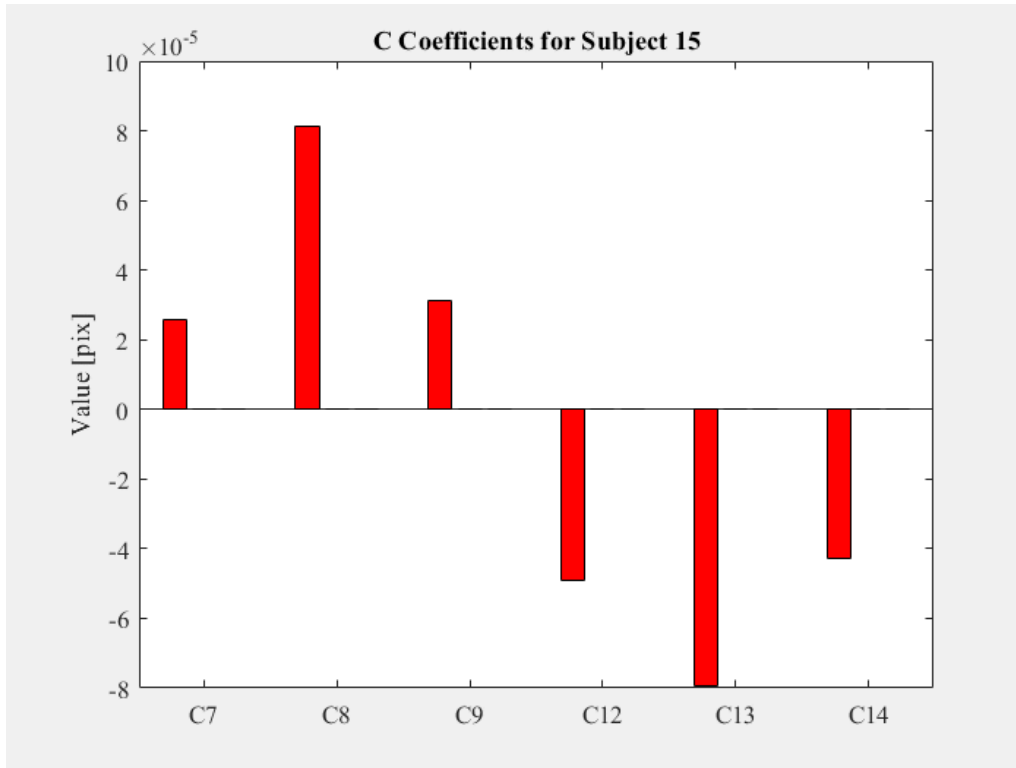


Figure D- 60: Third order distortion coefficient values for all processed retinal images of subject 15.

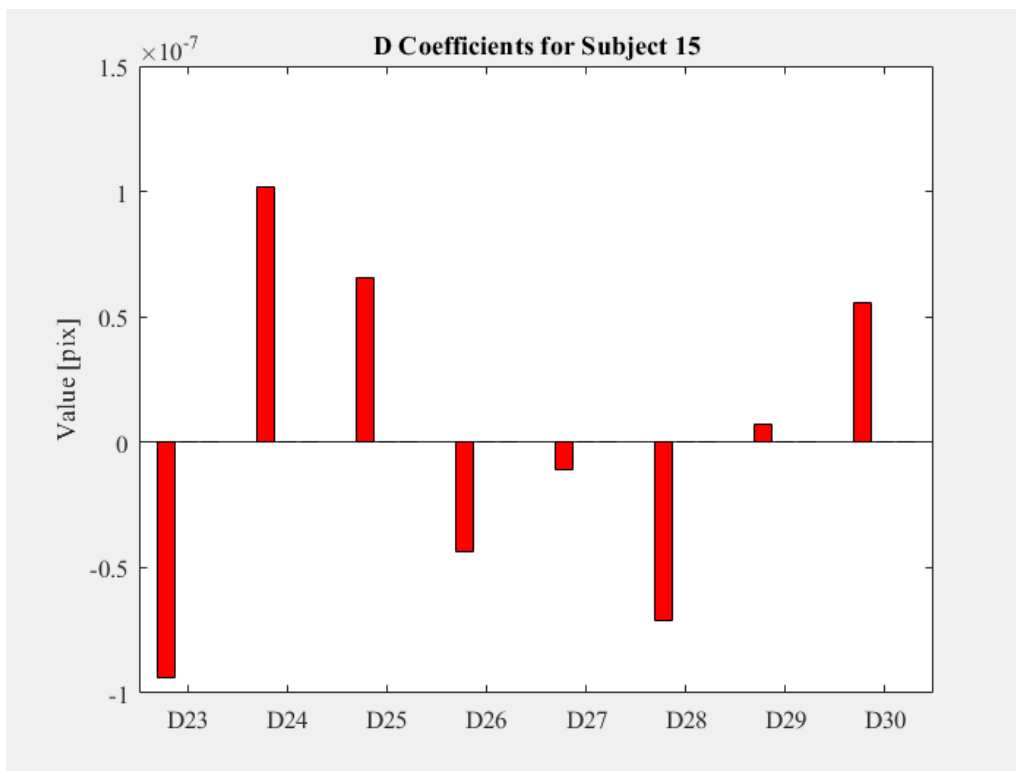


Figure D- 61: Fourth order distortion coefficient values for all processed retinal images of subject 15.

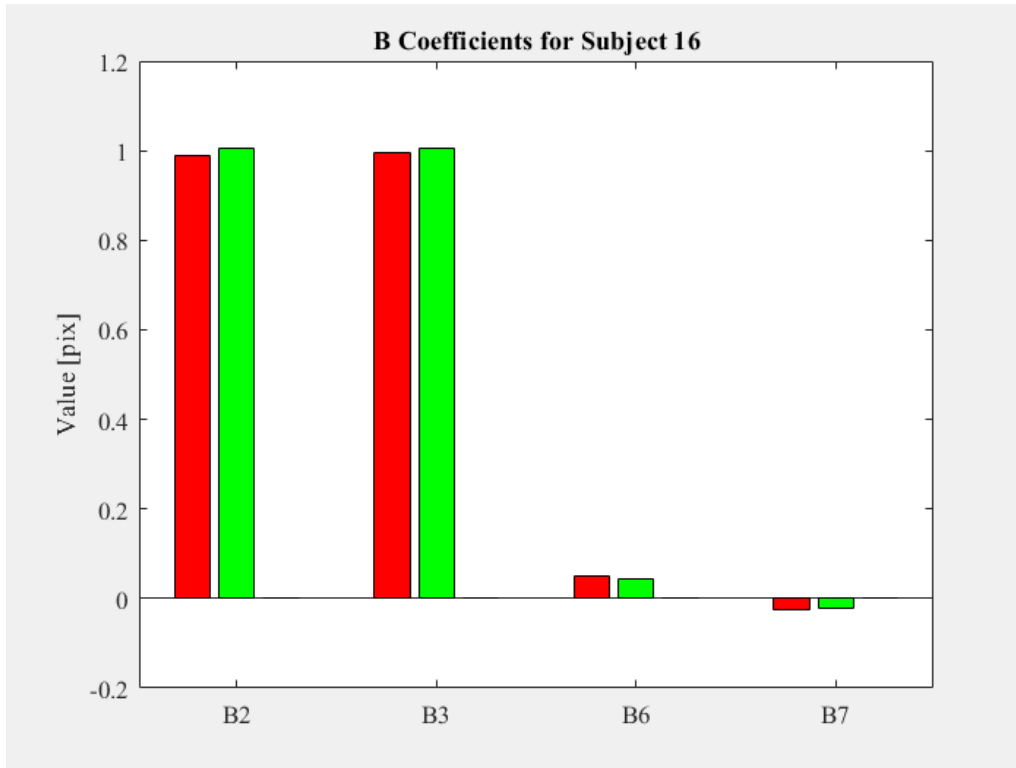


Figure D- 62: Second order distortion coefficient values for all processed retinal images of subject 16.

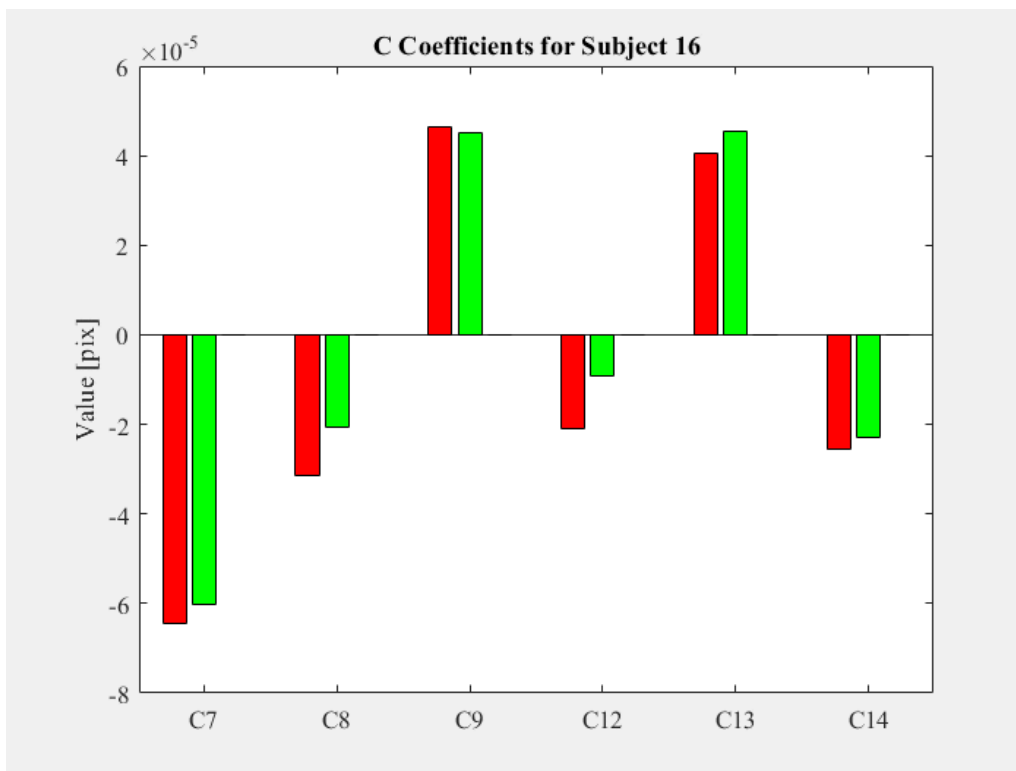


Figure D- 63: Third order distortion coefficient values for all processed retinal images of subject 16.

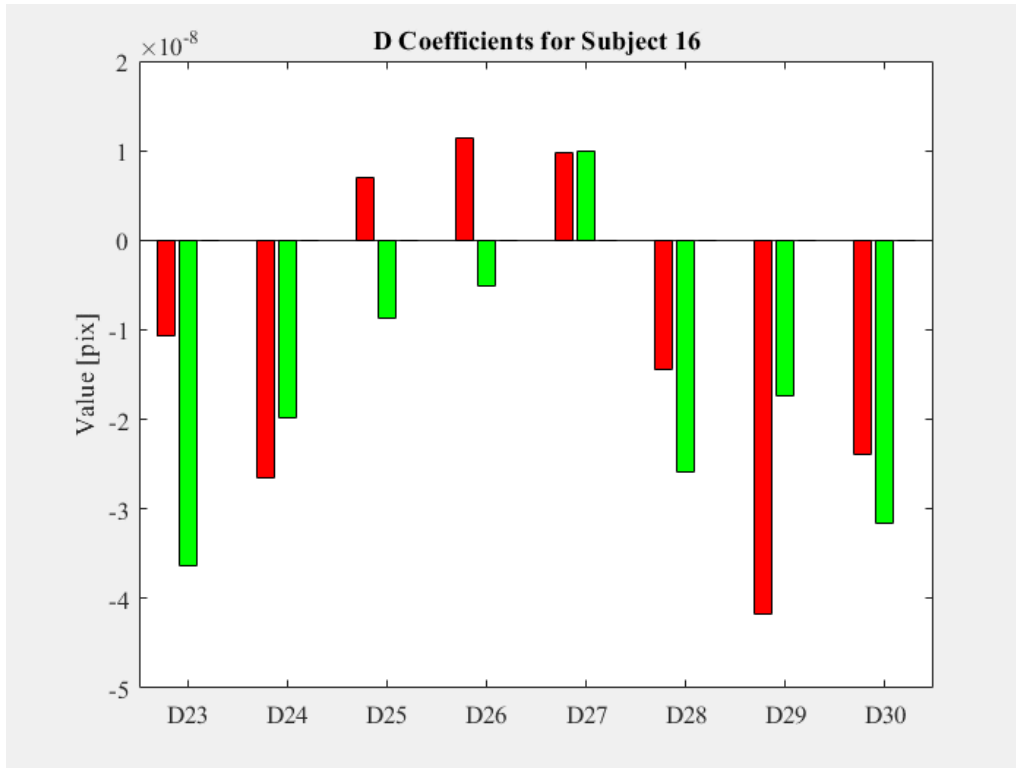


Figure D- 64: Fourth order distortion coefficient values for all processed retinal images of subject 16.

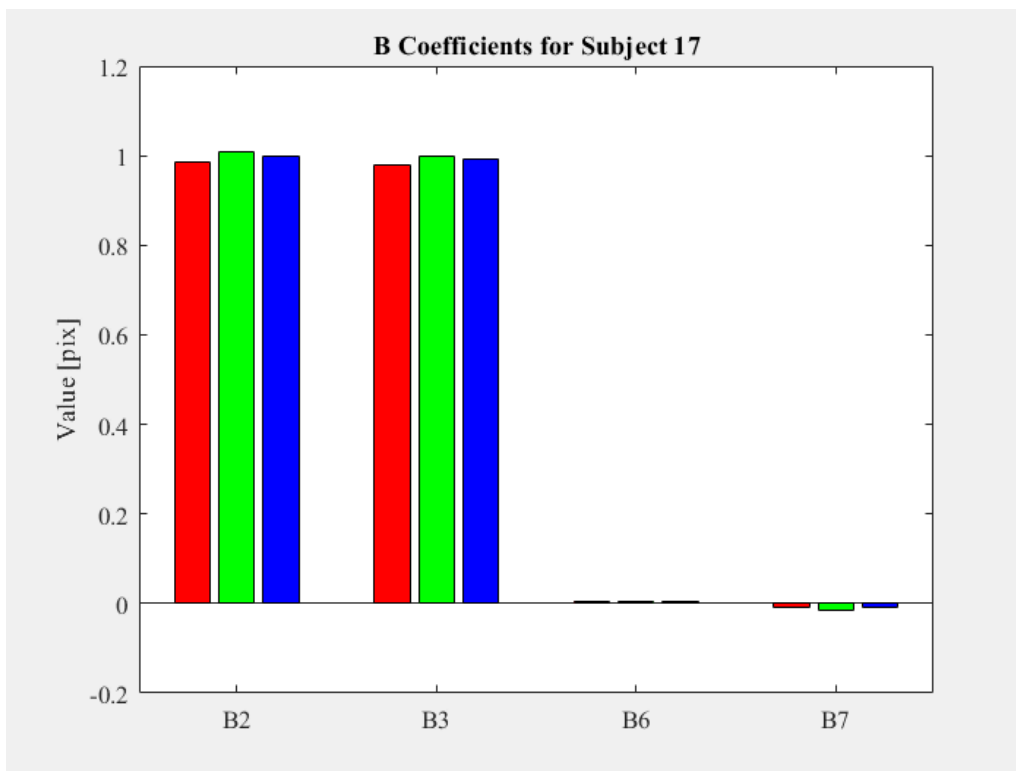


Figure D- 65: Second order distortion coefficient values for all processed retinal images of subject 17.

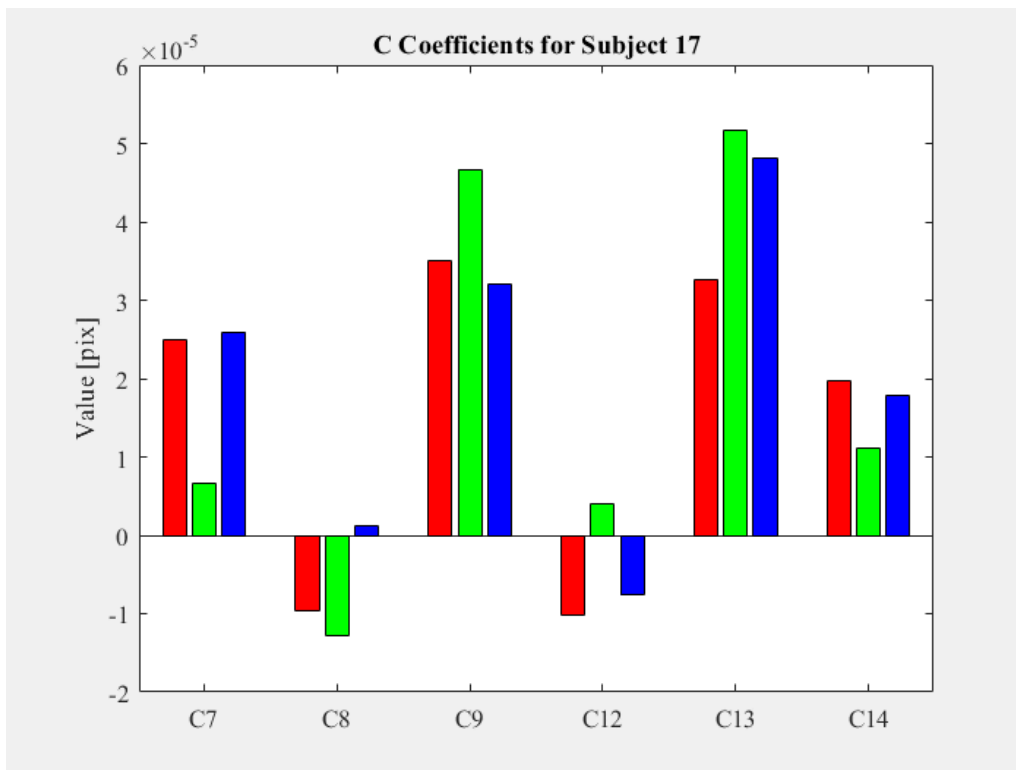


Figure D- 66: Third order distortion coefficient values for all processed retinal images of subject 17.

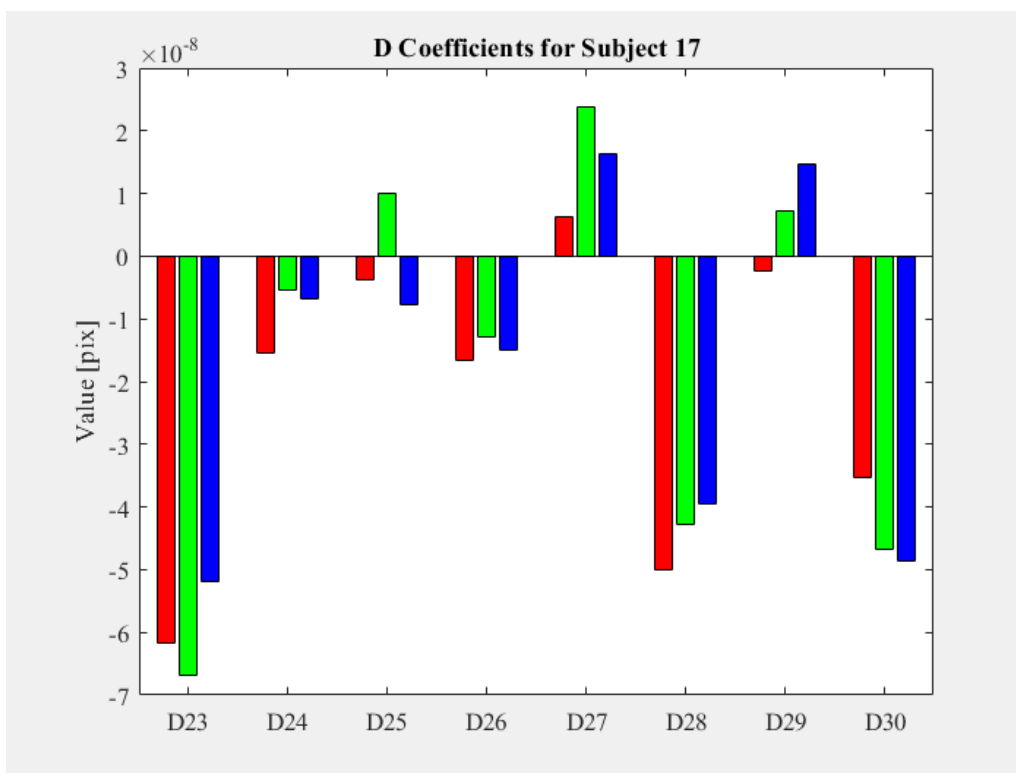


Figure D- 67: Fourth order distortion coefficient values for all processed retinal images of subject 17.

References

- [1] F. DR, "Myopia," *Bmj*, vol. 324, no. May, pp. 1195–1199, 2002.
- [2] I. G. Morgan, K. Ohno-Matsui, and S.-M. Saw, "Myopia," in *The Lancet*, vol. 379, 2012, pp. 1739–1748.
- [3] L. L. K. Lin, Y. F. Shih, C. K. Hsiao, and C. J. Chen, "Prevalence of Myopia in Taiwanese Schoolchildren: 1983 to 2000," *Ann. Acad. Med. Singapore*, vol. 33, no. 1, pp. 27–33, 2004.
- [4] I. G. Morgan, K. A. Rose, L. B. Ellwein, and the R. E. S. in C. S. Refractive Error Study in Children Survey Group, "Is emmetropia the natural endpoint for human refractive development? An analysis of population-based data from the refractive error study in children (RESC)," *Acta Ophthalmol.*, vol. 88, no. 8, pp. 877–84, Dec. 2010.
- [5] S. Vitale, R. D. Sperduto, and F. L. Ferris, "Increased Prevalence of Myopia in the United States Between 1971-1972 and 1999-2004," *Arch. Ophthalmol.*, vol. 127, no. 12, p. 1632, Dec. 2009.
- [6] S.-M. Saw, G. Gazzard, E. C. Shih-Yen, and W.-H. Chua, "Myopia and associated pathological complications," *Ophthalmic Physiol. Opt.*, vol. 25, no. 5, pp. 381–391, Sep. 2005.
- [7] F. Schaeffel and M. Feldkaemper, "Animal models in myopia research," *Clin. Exp. Optom.*, vol. 98, no. 6, pp. 507–517, 2015.
- [8] J. Wallman, J. Turkel, and J. Trachtman, "Extreme myopia produced by modest change in early visual experience," *Science*, vol. 201, no. 4362, pp. 1249–51, Sep. 1978.
- [9] S. M. Sherman, T. T. Norton, and V. A. Casagrande, "Myopia in the lid-sutured tree shrew (*Tupaia glis*)," *Brain Res.*, vol. 124, no. 1, pp. 154–7, Mar. 1977.
- [10] D. Trolio, D. L. Nickla, and C. F. Wildsoet, "Investigative ophthalmology & visual science," *Invest. Ophthalmol. Vis. Sci.*, vol. 41, no. 8, pp. 2043–2049, Jul. 2000.
- [11] E. Raviola and T. N. Wiesel, "Effect of dark-rearing on experimental myopia in monkeys," *Invest. Ophthalmol. Vis. Sci.*, vol. 17, no. 6, pp. 485–8, Jun. 1978.
- [12] F. Schaeffel, A. Glasser, and H. C. Howland, "Accommodation, refractive error and eye growth in chickens," *Vision Res.*, vol. 28, no. 5, pp. 639–57, 1988.
- [13] A. W. Shaikh, J. T. Siegart, and T. T. Norton, "Effect of interrupted lens wear on compensation for a minus lens in tree shrews," *Optom. Vis. Sci.*, vol. 76, no. 5, pp. 308–15, May 1999.
- [14] B. Graham and S. J. Judge, "Normal development of refractive state and ocular component dimensions in the marmoset (*Callithrix jacchus*)," *Vision Res.*, vol. 39, no. 2, pp. 177–87, Jan. 1999.

- [15] L. F. Hung, M. L. Crawford, and E. L. Smith, "Spectacle lenses alter eye growth and the refractive status of young monkeys.," *Nat. Med.*, vol. 1, no. 8, pp. 761–5, Aug. 1995.
- [16] J. Wallman, M. D. Gottlieb, V. Rajaram, and L. A. Fugate-Wentzek, "Local retinal regions control local eye growth and myopia.," *Science*, vol. 237, no. 4810, pp. 73–7, Jul. 1987.
- [17] Norton, T T and J. S., "Local myopia produced by partial visual field deprivation in tree shrew," *Soc. Neurosci. Abstr.*, vol. 17, p. 577, 1991.
- [18] A. Benavente-Perez, A. Nour, and D. Troilo, "Axial Eye Growth and Refractive Error Development Can Be Modified by Exposing the Peripheral Retina to Relative Myopic or Hyperopic Defocus," *Invest. Ophthalmol. Vis. Sci.*, vol. 55, no. 10, pp. 6765–6773, Oct. 2014.
- [19] E. L. Smith, L.-F. Hung, J. Huang, and J. Huang, "Relative peripheral hyperopic defocus alters central refractive development in infant monkeys.," *Vision Res.*, vol. 49, no. 19, pp. 2386–92, Sep. 2009.
- [20] D. Troilo, M. D. Gottlieb, and J. Wallman, "Visual deprivation causes myopia in chicks with optic nerve section," *Curr. Eye Res.*, vol. 6, no. 8, pp. 993–999, Jan. 1987.
- [21] T. T. Norton, J. A. Essinger, and N. A. McBrien, "Lid-suture myopia in tree shrews with retinal ganglion cell blockade.," *Vis. Neurosci.*, vol. 11, no. 1, pp. 143–53.
- [22] L. He, M. R. Frost, and T. T. Norton, "Differential gene expression in tree shrew retina compared with retinal pigment epithelium (RPE) in response to six hours of minus-lens wear," *Invest. Ophthalmol. Vis. Sci.*, vol. 55, no. 13, pp. 3037–3037, Apr. 2014.
- [23] X. Zhong, J. Ge, E. L. Smith, and W. K. Stell, "Image defocus modulates activity of bipolar and amacrine cells in macaque retina.," *Invest. Ophthalmol. Vis. Sci.*, vol. 45, no. 7, pp. 2065–74, Jul. 2004.
- [24] R. A. Stone, T. Lin, A. M. Laties, and P. M. Iuvone, "Retinal dopamine and form-deprivation myopia.," *Proc. Natl. Acad. Sci. U. S. A.*, vol. 86, no. 2, pp. 704–6, Jan. 1989.
- [25] N. A. McBrien, L. M. Cornell, and A. Gentle, "Structural and ultrastructural changes to the sclera in a mammalian model of high myopia.," *Invest. Ophthalmol. Vis. Sci.*, vol. 42, no. 10, pp. 2179–87, Sep. 2001.
- [26] P. M. Iuvone, M. Tigges, R. A. Stone, S. Lambert, and A. M. Laties, "Effects of apomorphine, a dopamine receptor agonist, on ocular refraction and axial elongation in a primate model of myopia.," *Invest. Ophthalmol. Vis. Sci.*, vol. 32, no. 5, pp. 1674–7, Apr. 1991.
- [27] M. FELDKAEMPER, S. DIETHER, G. KLEINE, and F. SCHAEFFEL, "Interactions of Spatial and Luminance Information in the Retina of Chickens During Myopia Development," *Exp. Eye Res.*, vol. 68, no. 1, pp. 105–115, Jan. 1999.
- [28] A. J. Fischer, J. J. McGuire, F. Schaeffel, and W. K. Stell, "Light- and focus-dependent expression of the transcription factor ZENK in the chick retina," *Nat. Neurosci.*, vol. 2, no. 8, pp. 706–712, Aug. 1999.

- [29] J. Winawer and J. Wallman, "Temporal constraints on lens compensation in chicks.," *Vision Res.*, vol. 42, no. 24, pp. 2651–68, Nov. 2002.
- [30] E. L. Smith *et al.*, "Effects of Foveal Ablation on Emmetropization and Form-Deprivation Myopia," *Investig. Ophthalmology Vis. Sci.*, vol. 48, no. 9, p. 3914, Sep. 2007.
- [31] R. Ashby, A. Ohlendorf, and F. Schaeffel, "The Effect of Ambient Illuminance on the Development of Deprivation Myopia in Chicks," *Investig. Ophthalmology Vis. Sci.*, vol. 50, no. 11, p. 5348, Nov. 2009.
- [32] R. S. Ashby and F. Schaeffel, "The Effect of Bright Light on Lens Compensation in Chicks," *Investig. Ophthalmology Vis. Sci.*, vol. 51, no. 10, p. 5247, Oct. 2010.
- [33] J. T. Siegwart, Jr., A. H. Ward, and T. T. Norton, "Moderately Elevated Fluorescent Light Levels Slow Form Deprivation and Minus Lens-Induced Myopia Development in Tree Shrews," *Invest. Ophthalmol. Vis. Sci.*, vol. 53, no. 14, pp. 3457–3457, Mar. 2012.
- [34] T. T. Norton and J. T. Siegwart, "Light levels, refractive development, and myopia – A speculative review," *Exp. Eye Res.*, vol. 114, pp. 48–57, Sep. 2013.
- [35] E. L. Smith, L.-F. Hung, B. Arumugam, J. Huang, and J. Huang, "Negative lens-induced myopia in infant monkeys: effects of high ambient lighting.," *Invest. Ophthalmol. Vis. Sci.*, vol. 54, no. 4, pp. 2959–69, Apr. 2013.
- [36] E. L. Smith, L.-F. Hung, and J. Huang, "Protective Effects of High Ambient Lighting on the Development of Form-Deprivation Myopia in Rhesus Monkeys," *Investig. Ophthalmology Vis. Sci.*, vol. 53, no. 1, p. 421, Jan. 2012.
- [37] D. O. Mutti *et al.*, "Corneal and Crystalline Lens Dimensions Before and After Myopia Onset," *Optom. Vis. Sci.*, vol. 89, no. 3, pp. 251–262, Mar. 2012.
- [38] T. Y. P. Chui, D. Bissig, B. A. Berkowitz, and J. D. Akula, "Refractive Development in the "ROP Rat"," *J. Ophthalmol.*, vol. 2012, p. 956705, 2012.
- [39] D. I. Flitcroft, "The complex interactions of retinal, optical and environmental factors in myopia aetiology," *Prog. Retin. Eye Res.*, vol. 31, no. 6, pp. 622–660, 2012.
- [40] E. L. Smith, C. Kee, R. Ramamirtham, Y. Qiao-Grider, and L.-F. Hung, "Peripheral Vision Can Influence Eye Growth and Refractive Development in Infant Monkeys," *Investig. Ophthalmology Vis. Sci.*, vol. 46, no. 11, p. 3965, Nov. 2005.
- [41] J. Wallman and J. Winawer, "Homeostasis of Eye Growth and the Question of Myopia," *Neuron*, vol. 43, no. 4, pp. 447–468, Aug. 2004.
- [42] D. O. Mutti, R. I. Sholtz, N. E. Friedman, and K. Zadnik, "Peripheral Refraction and Ocular Shape in Children," *Invest. Ophthalmol. Vis. Sci.*, vol. 41, no. 5, pp. 1022–1030, Apr. 2000.
- [43] D. A. Atchison *et al.*, "Eye Shape in Emmetropia and Myopia," *Investig. Ophthalmology Vis. Sci.*, vol. 45, no. 10, p. 3380, Oct. 2004.
- [44] D. A. Atchison, N. Pritchard, K. L. Schmid, D. H. Scott, C. E. Jones, and J. M. Pope, "Shape of the retinal surface in emmetropia and myopia," *Investig. Ophthalmol. Vis. Sci.*,

- vol. 46, no. 8, pp. 2698–2707, 2005.
- [45] J. Gwiazda, F. Thorn, J. Bauer, and R. Held, “Myopic children show insufficient accommodative response to blur,” *Invest. Ophthalmol. Vis. Sci.*, vol. 34, no. 3, pp. 690–694, Mar. 1993.
- [46] J. Gwiazda, J. Bauer, F. Thorn, and R. Held, “A dynamic relationship between myopia and blur-driven accommodation in school-aged children,” *Vision Res.*, vol. 35, no. 9, pp. 1299–1304, May 1995.
- [47] D. O. Mutti *et al.*, “The response AC/A ratio before and after the onset of myopia,” *Investig. Ophthalmol. Vis. Sci.*, vol. 58, no. 3, pp. 1594–1602, 2017.
- [48] D. O. Mutti *et al.*, “Refractive Error, Axial Length, and Relative Peripheral Refractive Error before and after the Onset of Myopia,” *Investig. Ophthalmology Vis. Sci.*, vol. 48, no. 6, p. 2510, Jun. 2007.
- [49] D. O. Mutti *et al.*, “Accommodative lag before and after the onset of myopia,” *Investig. Ophthalmol. Vis. Sci.*, vol. 47, no. 3, pp. 837–846, 2006.
- [50] L. A. Jones-Jordan *et al.*, “Early childhood refractive error and parental history of myopia as predictors of myopia,” *Invest. Ophthalmol. Vis. Sci.*, vol. 51, no. 1, pp. 115–21, Jan. 2010.
- [51] I. Morgan and K. Rose, “How genetic is school myopia?,” *Prog. Retin. Eye Res.*, vol. 24, no. 1, pp. 1–38, Jan. 2005.
- [52] R. Pacella, J. McLellan, K. Grice, E. A. Del Bono, J. L. Wiggs, and J. E. Gwiazda, “Role of genetic factors in the etiology of juvenile-onset myopia based on a longitudinal study of refractive error,” *Optom. Vis. Sci.*, vol. 76, no. 6, pp. 381–6, Jun. 1999.
- [53] R. Chakraborty, L. A. Ostrin, D. L. Nickla, P. M. Iuvone, M. T. Pardue, and R. A. Stone, “Circadian rhythms, refractive development, and myopia,” *Ophthalmic Physiol. Opt.*, vol. 38, no. 3, pp. 217–245, 2018.
- [54] P. Kang *et al.*, “Peripheral refraction in different ethnicities,” *Investig. Ophthalmol. Vis. Sci.*, vol. 51, no. 11, pp. 6059–6065, 2010.
- [55] S. A. Read, M. J. Collins, and B. P. Sander, “Human Optical Axial Length and Defocus,” *Investig. Ophthalmology Vis. Sci.*, vol. 51, no. 12, p. 6262, Dec. 2010.
- [56] J. Wallman *et al.*, “Moving the retina: choroidal modulation of refractive state,” *Vision Res.*, vol. 35, no. 1, pp. 37–50, Jan. 1995.
- [57] B. P. Sander, M. J. Collins, and S. A. Read, “The interaction between homatropine and optical blur on choroidal thickness,” *Ophthalmic Physiol. Opt.*, vol. 38, no. 3, pp. 257–265, 2018.
- [58] X. Zhu, T. W. Park, J. Winawer, and J. Wallman, “In a Matter of Minutes, the Eye Can Know Which Way to Grow,” *Investig. Ophthalmology Vis. Sci.*, vol. 46, no. 7, p. 2238, Jul. 2005.
- [59] D. Carlson, “Anatomy of the Human Eye - Infographic.” [Online]. Available:

- <https://owlcation.com/stem/Anatomy-of-the-Eye-Human-Eye-Anatomy>. [Accessed: 30-May-2018].
- [60] A. J. Fischer, P. Miethke, I. G. Morgan, and W. K. Stell, "Cholinergic amacrine cells are not required for the progression and atropine-mediated suppression of form-deprivation myopia.," *Brain Res.*, vol. 794, no. 1, pp. 48–60, May 1998.
- [61] G. J. Lind, S. J. Chew, D. Marzani, and J. Wallman, "Muscarinic acetylcholine receptor antagonists inhibit chick scleral chondrocytes.," *Invest. Ophthalmol. Vis. Sci.*, vol. 39, no. 12, pp. 2217–31, Nov. 1998.
- [62] W. A. Luft, Y. Ming, and W. K. Stell, "Variable effects of previously untested muscarinic receptor antagonists on experimental myopia.," *Invest. Ophthalmol. Vis. Sci.*, vol. 44, no. 3, pp. 1330–8, Mar. 2003.
- [63] N. A. McBrien, H. O. Moghaddam, and A. P. Reeder, "Atropine reduces experimental myopia and eye enlargement via a nonaccommodative mechanism.," *Invest. Ophthalmol. Vis. Sci.*, vol. 34, no. 1, pp. 205–15, Jan. 1993.
- [64] L. B. Wilson *et al.*, "The Relation of Axial Length and Intraocular Pressure Fluctuations in Human Eyes," *Investig. Ophthalmology Vis. Sci.*, vol. 47, no. 5, p. 1778, May 2006.
- [65] R. Chakraborty, S. A. Read, and M. J. Collins, "Diurnal Variations in Axial Length, Choroidal Thickness, Intraocular Pressure, and Ocular Biometrics," *Investig. Ophthalmology Vis. Sci.*, vol. 52, no. 8, p. 5121, Jul. 2011.
- [66] R. B. Rabbetts, *Bennett & Rabbetts' clinical visual optics*. Elsevier/Butterworth Heinemann, 2007.
- [67] S. Weiss and F. Schaeffel, "Diurnal growth rhythms in the chicken eye: relation to myopia development and retinal dopamine levels.," *J. Comp. Physiol. A.*, vol. 172, no. 3, pp. 263–70, Apr. 1993.
- [68] D. L. Nickla and K. Totonelly, "Brief light exposure at night disrupts the circadian rhythms in eye growth and choroidal thickness in chicks," *Exp. Eye Res.*, vol. 146, pp. 189–195, May 2016.
- [69] D. L. Nickla, K. Jordan, J. Yang, and K. Totonelly, "Brief hyperopic defocus or form deprivation have varying effects on eye growth and ocular rhythms depending on the time-of-day of exposure," *Exp. Eye Res.*, vol. 161, pp. 132–142, Aug. 2017.
- [70] K. S. Korshunov, L. J. Blakemore, and P. Q. Trombley, "Dopamine: A Modulator of Circadian Rhythms in the Central Nervous System," *Front. Cell. Neurosci.*, vol. 11, p. 91, Apr. 2017.
- [71] C. R. Jackson *et al.*, "Retinal Dopamine Mediates Multiple Dimensions of Light-Adapted Vision," *J. Neurosci.*, vol. 32, no. 27, pp. 9359–9368, Jul. 2012.
- [72] C. Ribelayga and S. C. Mangel, "Absence of circadian clock regulation of horizontal cell gap junctional coupling reveals two dopamine systems in the goldfish retina," *J. Comp. Neurol.*, vol. 467, no. 2, pp. 243–253, Dec. 2003.

- [73] B. Rohrer, P. M. Iuvone, and W. K. Stell, "Stimulation of dopaminergic amacrine cells by stroboscopic illumination or fibroblast growth factor (bFGF, FGF-2) injections: possible roles in prevention of form-deprivation myopia in the chick.," *Brain Res.*, vol. 686, no. 2, pp. 169–81, Jul. 1995.
- [74] J. Liang, B. Grimm, S. Goelz, and J. F. Bille, "Objective measurement of wave aberrations of the human eye with the use of a Hartmann-Shack wave-front sensor.," *J. Opt. Soc. Am. A. Opt. Image Sci. Vis.*, vol. 11, no. 7, pp. 1949–57, Jul. 1994.
- [75] X. Cheng, A. Bradley, X. Hong, N. Thibos, and Larry N, "Relationship between Refractive Error and Monochromatic Aber... : Optometry and Vision Science," *Optom. Vis. Sci.*, vol. 80, no. 1, pp. 43–49, 2003.
- [76] L. Llorente, S. Barbero, D. Cano, C. Dorronsoro, and S. Marcos, "Myopic versus hyperopic eyes: axial length, corneal shape and optical aberrations," *J. Vis.*, vol. 4, no. 4, p. 5, 2004.
- [77] S. Marcos, S. A. Burns, P. M. Prieto, R. Navarro, and B. Baraibar, "Investigating sources of variability of monochromatic and transverse chromatic aberrations across eyes," *Vision Res.*, vol. 41, no. 28, pp. 3861–3871, 2001.
- [78] W. N. Charman, "Aberrations and myopia," *Ophthalmic Physiol. Opt.*, vol. 25, no. 4, pp. 285–301, Jul. 2005.
- [79] A. Mathur, D. A. Atchison, and W. N. Charman, "Myopia and peripheral ocular aberrations," *J. Vis.*, vol. 9, no. 10, pp. 15–15, Sep. 2009.
- [80] A. Hartwig and D. A. Atchison, "Analysis of Higher-Order Aberrations in a Large Clinical Population," *Investig. Ophthalmology Vis. Sci.*, vol. 53, no. 12, p. 7862, Nov. 2012.
- [81] T. Buehren, M. J. Collins, D. R. Iskander, B. Davis, and B. Lingelbach, "The stability of corneal topography in the post-blink interval.," *Cornea*, vol. 20, no. 8, pp. 826–33, Nov. 2001.
- [82] P. Kang, "Optical and pharmacological strategies of myopia control," *Clin. Exp. Optom.*, vol. 101, no. 3, pp. 321–332, 2018.
- [83] J. J. Walline, K. Lindsley, S. S. Vedula, S. A. Cotter, D. O. Mutti, and J. D. Twelker, "Interventions to slow progression of myopia in children," *Cochrane Database Syst. Rev.*, no. 12, p. CD004916, Dec. 2011.
- [84] J. Katz *et al.*, "A randomized trial of rigid gas permeable contact lenses to reduce progression of children's myopia.," *Am. J. Ophthalmol.*, vol. 136, no. 1, pp. 82–90, Jul. 2003.
- [85] J. J. Walline, L. A. Jones, D. O. Mutti, and K. Zadnik, "A Randomized Trial of the Effects of Rigid Contact Lenses on Myopia Progression," *Arch. Ophthalmol.*, vol. 122, no. 12, p. 1760, Dec. 2004.
- [86] K. Chung, N. Mohidin, and D. J. O'Leary, "Undercorrection of myopia enhances rather than inhibits myopia progression.," *Vision Res.*, vol. 42, no. 22, pp. 2555–9, Oct. 2002.

- [87] S.-M. Li *et al.*, “Studies using concentric ring bifocal and peripheral add multifocal contact lenses to slow myopia progression in school-aged children: a meta-analysis,” *Ophthalmic Physiol. Opt.*, vol. 37, no. 1, pp. 51–59, Jan. 2017.
- [88] S. Barbero and M. Faria-Ribeiro, “Foveal vision power errors induced by spectacle lenses designed to correct peripheral refractive errors,” *Ophthalmic Physiol. Opt.*, vol. 38, no. 3, pp. 317–325, 2018.
- [89] D. Cheng, G. C. Woo, and K. L. Schmid, “Bifocal lens control of myopic progression in children,” *Clin. Exp. Optom.*, vol. 94, no. 1, pp. 24–32, Jan. 2011.
- [90] J. Gwiazda *et al.*, “A randomized clinical trial of progressive addition lenses versus single vision lenses on the progression of myopia in children,” *Invest. Ophthalmol. Vis. Sci.*, vol. 44, no. 4, pp. 1492–500, Apr. 2003.
- [91] D. Cheng, K. L. Schmid, and G. C. Woo, “The effect of positive-lens addition and base-in prism on accommodation accuracy and near horizontal phoria in Chinese myopic children,” *Ophthalmic Physiol. Opt.*, vol. 28, no. 3, pp. 225–237, Apr. 2008.
- [92] Correction of Myopia Evaluation Trial 2 Study Group for the Pediatric Eye Disease Investigator Group, “Progressive-Addition Lenses versus Single-Vision Lenses for Slowing Progression of Myopia in Children with High Accommodative Lag and Near Esophoria,” *Invest. Ophthalmol. Vis. Sci.*, vol. 52, no. 5, pp. 2749–2757, Apr. 2011.
- [93] G. W. Fulk, L. A. Cyert, and D. E. Parker, “A randomized trial of the effect of single-vision vs. bifocal lenses on myopia progression in children with esophoria,” *Optom. Vis. Sci.*, vol. 77, no. 8, pp. 395–401, Aug. 2000.
- [94] O. Pärssinen, E. Hemminki, and A. Klemetti, “Effect of spectacle use and accommodation on myopic progression: final results of a three-year randomised clinical trial among schoolchildren,” *Br. J. Ophthalmol.*, vol. 73, no. 7, pp. 547–51, Jul. 1989.
- [95] G. W. Fulk and L. A. Cyert, “Can bifocals slow myopia progression?,” *J. Am. Optom. Assoc.*, vol. 67, no. 12, pp. 749–54, Dec. 1996.
- [96] T. Grosvenor, D. M. Perrigin, J. Perrigin, and B. Maslovitz, “Houston Myopia Control Study: a randomized clinical trial. Part II. Final report by the patient care team,” *Am. J. Optom. Physiol. Opt.*, vol. 64, no. 7, pp. 482–98, Jul. 1987.
- [97] D. Cheng, G. C. Woo, B. Drobe, and K. L. Schmid, “Effect of Bifocal and Prismatic Bifocal Spectacles on Myopia Progression in Children,” *JAMA Ophthalmol.*, vol. 132, no. 3, p. 258, Mar. 2014.
- [98] T. Uemura, Y. Arai, and C. Shimazaki, “Eye-Head Coordination During Lateral Gaze in Normal Subjects,” *Acta Otolaryngol.*, vol. 90, no. 1–6, pp. 191–198, Jan. 1980.
- [99] T. Schilling, A. Ohlendorf, S. R. Varnas, and S. Wahl, “Peripheral Design of Progressive Addition Lenses and the Lag of Accommodation in Myopes,” *Investig. Ophthalmology Vis. Sci.*, vol. 58, no. 9, p. 3319, Jul. 2017.
- [100] T. A. Aller, M. Liu, and C. F. Wildsoet, “Myopia Control with Bifocal Contact Lenses,” *Optom. Vis. Sci.*, vol. 93, no. 4, pp. 344–352, 2016.

- [101] P. Sankaridurg *et al.*, “Spectacle Lenses Designed to Reduce Progression of Myopia: 12-Month Results,” *Optom. Vis. Sci.*, vol. 87, no. 9, pp. 631–641, Sep. 2010.
- [102] J. J. Walline, K. L. Greiner, M. E. McVey, and L. A. Jones-Jordan, “Multifocal contact lens myopia control,” *Optom. Vis. Sci.*, vol. 90, no. 11, pp. 1207–1214, 2013.
- [103] P. Sankaridurg *et al.*, “Decrease in Rate of Myopia Progression with a Contact Lens Designed to Reduce Relative Peripheral Hyperopia: One-Year Results,” *Investig. Ophthalmology Vis. Sci.*, vol. 52, no. 13, p. 9362, Dec. 2011.
- [104] C. S. Y. Lam, W. C. Tang, D. Y. Y. Tse, Y. Y. Tang, and C. H. To, “Defocus Incorporated Soft Contact (DISC) lens slows myopia progression in Hong Kong Chinese schoolchildren: A 2-year randomised clinical trial,” *Br. J. Ophthalmol.*, vol. 98, no. 1, pp. 40–45, 2014.
- [105] J. Pauné, H. Morales, J. Armengol, L. Quevedo, M. Faria-Ribeiro, and J. M. González-Méijome, “Myopia Control with a Novel Peripheral Gradient Soft Lens and Orthokeratology: A 2-Year Clinical Trial,” *Biomed Res. Int.*, vol. 2015, no. D, 2015.
- [106] J. Pauné, A. Queiros, D. Lopes-Ferreira, M. Faria-Ribeiro, L. Quevedo, and J. M. Gonzalez-Meijome, “Efficacy of a Gas Permeable Contact Lens to Induce Peripheral Myopic Defocus,” *Optom. Vis. Sci.*, vol. 92, no. 5, pp. 596–603, May 2015.
- [107] J. Pauné, A. Queiros, L. Quevedo, H. Neves, D. Lopes-Ferreira, and J. M. González-Méijome, “Peripheral myopization and visual performance with experimental rigid gas permeable and soft contact lens design,” *Contact Lens Anterior Eye*, vol. 37, no. 6, pp. 455–460, Dec. 2014.
- [108] N. S. Anstice and J. R. Phillips, “Effect of dual-focus soft contact lens wear on axial myopia progression in children,” *Ophthalmology*, vol. 118, no. 6, pp. 1152–1161, 2011.
- [109] B. N. Cheng X, Xu J, Chehab K, Exford J, “Soft Contact Lenses with Positive Spherical,” vol. 93, no. 4, pp. 353–366, 2016.
- [110] E. L. Smith, “Optical treatment strategies to slow myopia progression: Effects of the visual extent of the optical treatment zone,” *Exp. Eye Res.*, vol. 114, pp. 77–88, Sep. 2013.
- [111] P. Gifford and K. L. Gifford, “The future of myopia control contact lenses,” *Optom. Vis. Sci.*, vol. 93, no. 4, pp. 336–343, 2016.
- [112] P. Kang, Y. Fan, K. Oh, K. Trac, F. Zhang, and H. A. Swarbrick, “The effect of multifocal soft contact lenses on peripheral refraction,” *Optom. Vis. Sci.*, vol. 90, no. 7, pp. 658–666, 2013.
- [113] D. A. Berntsen and C. E. Kramer, “Peripheral Defocus with Spherical and Multifocal Soft Contact Lenses,” *Optom. Vis. Sci.*, vol. 90, no. 11, pp. 1215–1224, Nov. 2013.
- [114] D. Lopes-Ferreira *et al.*, “Peripheral myopization using a dominant design multifocal contact lens,” *J. Optom.*, vol. 4, no. 1, pp. 14–21, Jan. 2011.
- [115] J. Huang *et al.*, “Efficacy comparison of 16 interventions for myopia control in children: A network meta-analysis,” *Ophthalmology*, vol. 123, no. 4, pp. 697–708, 2016.

- [116] Y. Sun *et al.*, “Orthokeratology to Control Myopia Progression: A Meta-Analysis,” *PLoS One*, vol. 10, no. 4, p. e0124535, Apr. 2015.
- [117] J.-K. Si, K. Tang, H.-S. Bi, D.-D. Guo, J.-G. Guo, and X.-R. Wang, “Orthokeratology for Myopia Control,” *Optom. Vis. Sci.*, vol. 92, no. 3, pp. 252–257, Mar. 2015.
- [118] T. Hiraoka, Y. Sekine, F. Okamoto, T. Mihashi, and T. Oshika, “Safety and efficacy following 10-years of overnight orthokeratology for myopia control,” *Ophthalmic Physiol. Opt.*, vol. 38, no. 3, pp. 281–289, 2018.
- [119] P. Cho and S. W. Cheung, “Discontinuation of orthokeratology on eyeball elongation (DOEE),” *Contact Lens Anterior Eye*, vol. 40, no. 2, pp. 82–87, Apr. 2017.
- [120] D. Chen, A. K. C. Lam, and P. Cho, “Posterior corneal curvature change and recovery after 6 months of overnight orthokeratology treatment,” *Ophthalmic Physiol. Opt.*, vol. 30, no. 3, pp. 274–280, May 2010.
- [121] A. Mathur and D. A. Atchison, “Effect of Orthokeratology on Peripheral Aberrations of the Eye,” *Optom. Vis. Sci.*, vol. 86, no. 5, pp. E476–E484, May 2009.
- [122] P. Ganesan and C. F. Wildsoet, “Pharmaceutical intervention for myopia control,” *Expert Rev. Ophthalmol.*, vol. 5, no. 6, pp. 759–787, Dec. 2010.
- [123] F. Schaeffel, D. Troilo, J. Wallman, and H. C. Howland, “Developing eyes that lack accommodation grow to compensate for imposed defocus,” *Vis. Neurosci.*, vol. 4, no. 2, pp. 177–83, Feb. 1990.
- [124] C. L. Cottrill and N. A. McBrien, “The M1 muscarinic antagonist pirenzepine reduces myopia and eye enlargement in the tree shrew,” *Invest. Ophthalmol. Vis. Sci.*, vol. 37, no. 7, pp. 1368–79, Jun. 1996.
- [125] R. M. Siatkowski *et al.*, “Safety and Efficacy of 2% Pirenzepine Ophthalmic Gel in Children With Myopia,” *Arch. Ophthalmol.*, vol. 122, no. 11, p. 1667, Nov. 2004.
- [126] W. H. Chua *et al.*, “Atropine for the Treatment of Childhood Myopia,” *Ophthalmology*, vol. 113, no. 12, pp. 2285–2291, 2006.
- [127] A. Chia *et al.*, “Atropine for the treatment of childhood Myopia: Safety and efficacy of 0.5%, 0.1%, and 0.01% doses (Atropine for the Treatment of Myopia 2),” *Ophthalmology*, vol. 119, no. 2, pp. 347–354, 2012.
- [128] A. Chia, W. H. Chua, L. Wen, A. Fong, Y. Y. Goon, and D. Tan, “Atropine for the treatment of childhood myopia: Changes after stopping atropine 0.01%, 0.1% and 0.5%,” *Am. J. Ophthalmol.*, vol. 157, no. 2, p. 451–457.e1, 2014.
- [129] L. Tong, X. L. Huang, A. L. T. Koh, X. Zhang, D. T. H. Tan, and W. H. Chua, “Atropine for the Treatment of Childhood Myopia: Effect on Myopia Progression after Cessation of Atropine,” *Ophthalmology*, vol. 116, no. 3, pp. 572–579, 2009.
- [130] E. H. Leung and R. Rosen, “Atlas of Wide-Field Retinal Angiography and Imaging,” pp. 1–25, 2016.
- [131] H. Littmann, “Die Zeiss Funduskamera,” in *59th Meeting of German Ophthalmology*,

- 1955.
- [132] E. DeHoog and J. Schwiegerling, “Fundus camera systems: a comparative analysis,” *Appl. Opt.*, vol. 48, no. 2, pp. 221–228, 2009.
- [133] O. Pomerantzeff, R. H. Webb, and F. C. Delori, “Image formation in fundus cameras,” *Investig. Ophthalmol. Vis. Sci.*, vol. 18, no. 6, pp. 630–637, 1979.
- [134] M. Hammer, A. Roggan, D. Schweitzer, and G. Muller, “Optical properties of ocular fundus tissues-an in vitro study using the double-integrating-sphere technique and inverse Monte Carlo simulation,” *Phys. Med. Biol.*, vol. 40, no. 6, pp. 963–978, Jun. 1995.
- [135] N. P. A. Zagers, J. van de Kraats, T. T. J. M. Berendschot, and D. van Norren, “Simultaneous measurement of foveal spectral reflectance and cone-photoreceptor directionality,” *Appl. Opt.*, vol. 41, no. 22, p. 4686, Aug. 2002.
- [136] B. BENGTTSSON and C. E. T. KRAKAU, “Some Essential Optical Features of the Zeiss Fundus Camera,” *Acta Ophthalmol.*, vol. 55, no. 1, pp. 123–131, 1977.
- [137] W. Smith, *Modern Optical Engineering - Chapter 3 - Abberations*, Third. SPIE, 2000.
- [138] R. Barakat and A. Houston, “The Aberrations of Non-Rotationally Symmetric Systems and Their Diffraction Effects,” vol. 13, no. 1, pp. 1–30, 1966.
- [139] R. Navarro, “The optical design of the human eye: A critical review,” *J. Optom.*, vol. 2, no. 1, pp. 3–18, 2009.
- [140] J. Schwiegerling, “Arizona Eye Model,” in *Field Guide to Visual and Ophthalmic Optics*, SPIE, 2004.
- [141] D. A. Atchison and G. Smith, *Optics of the human eye*. Butterworth-Heinemann, 2000.
- [142] J. Porter, A. Guirao, I. G. Cox, and D. R. Williams, “Monochromatic aberrations of the human eye in a large population,” *J. Opt. Soc. Am. A. Opt. Image Sci. Vis.*, vol. 18, no. 8, pp. 1793–803, Aug. 2001.
- [143] J. J. Rozema, D. A. Atchison, and M. J. Tassignon, “Statistical eye model for normal eyes,” *Investig. Ophthalmol. Vis. Sci.*, vol. 52, no. 7, pp. 4525–4533, 2011.
- [144] J. Schwiegerling, “Statistical generation of normal and post-refractive surgery wavefronts,” *Clin. Exp. Optom.*, vol. 92, no. 3, pp. 223–226, 2009.
- [145] D. A. Atchison, E. L. Markwell, S. Kasthurirangan, J. M. Pope, G. Smith, and P. G. Swann, “Age-related changes in optical and biometric characteristics of emmetropic eyes,” *J. Vis.*, vol. 8, no. 4, p. 29, Apr. 2008.
- [146] J. E. Greivenkamp, *Field guide to geometrical optics*. SPIE Press, 2004.
- [147] J. Varikooty, N. Keir, C. A. Woods, and D. Fonn, “Measurement of the refractive index of soft contact lenses during wear,” *Eye Contact Lens*, vol. 36, no. 1, pp. 2–5, 2010.
- [148] E. Kim, R. C. Bakaraju, and K. Ehrmann, “Power Profiles of Commercial Multifocal Soft Contact Lenses,” *Optom. Vis. Sci.*, vol. 94, no. 2, pp. 183–196, 2017.

- [149] J. Nam, L. N. Thibos, and D. R. Iskander, “Describing ocular aberrations with wavefront vergence maps,” *Clin. Exp. Optom.*, vol. 92, no. 3, pp. 194–205, 2009.
- [150] M. Rodriguez-Vallejo, J. Benlloch, A. Pons, J. A. Monsoriu, and W. D. Furlan, “The effect of fractal contact lenses on peripheral refraction in myopic model eyes,” *Curr. Eye Res.*, vol. 39, no. 12, pp. 1151–1160, 2014.
- [151] J. Sasian, “Introduction to Aberrations & Geometrical-Optics Based Imaging - Lecture 15 - Pupil Aberrations.” pp. 1–27.